A Ph.D. Dissertation on

Kalman Filter And Its Advanced Variants For Condition Assessment Of Hysteretic Structural Systems

submitted by

Pranjal Tamuly

(156104030)

under the supervision of

Dr. Arunasis Chakraborty

Dr. Sandip Das

DEPARTMENT OF CIVIL ENGINEERING

INDIAN INSTITUTE OF TECHNOLOGY GUWAHATI

July, 2021

Certificate

It is certified that the work contained in the dissertation entitled **"Kalman Filter and Its Advanced Variants for Condition Assessment of Hysteretic Structural Systems"**, by **Pranjal Tamuly (156104030)** for the partial fulfillment of the requirements for the award of the *Doctor of Philosophy* (*Ph.D.*) in *Civil Engineering* with the specialization in *Structural Engineering* at the *Indian Institute of Technology Guwahati, India* is an authentic work. This work has been carried out under our supervision and it has not been submitted elsewhere for the award of a degree.

Date:

Dr. Arunasis Chakraborty
Associate Professor
Department of Civil Engineering
Indian Institute of Technology Guwahati
Guwahati - 781039, India

Date:

Dr. Sandip Das
Assistant Professor
Department of Civil Engineering
Indian Institute of Technology Guwahati
Guwahati - 781039, India

Acknowledgements

First and foremost, I would like to express my deep and sincere gratitude to my supervisors *Dr. Arunasis Chakraborty* and *Dr. Sandip Das*, for providing continuous support in my research through their endless guidance. I will always be grateful to them for improving my understanding regarding structural engineering right from basic to advanced level. Their important suggestions and co-operation have been a constant source of motivation while carrying out my research work. I also owe them a great tribute for improving my writing skill, which is very important to present any research work effectively.

Besides my supervisors, I would like to thank the members of the Doctoral Committee, *Prof. Anjan Dutta*, *Prof. Hemant B. Kaushik*, and *Dr. Deepak Sharma* for their valuable recommendation and insightful remarks to direct my efforts in meaningful thesis work. I wish to acknowledge the financial assistance from the Department of Civil Engineering, Indian Institute of Technology Guwahati, India, to carry out this research.

I would like to appreciate the insightful discussions and co-operation from senior research scholars, especially Dr. Swaroop Mahato, Dr. Amit Rathi, and Dr. Sulaem Musaddiq Laskar. I would like to thank all my lab-mates in the NDT laboratory: Pallab, Lavish, Subhadip, Kasturi, Sajeer, Soroj, Bonisha, Monjusha and Tori for making my stay memorable.

Last but not least, one might not stand up without the support of his/her family. Hence, I would like to take this opportunity to thank my parents Mr. Rajen Tamuly, Mrs Rita Tamuly and my brother Mr. Bishal Tamuly. Their constant guidance and support have driven me to conclude this work.

Pranjal Tamuly
(156104030)
Department of Civil Engineering
Indian Institute of Technology Guwahati
Guwahati - 781039, India

Date:

This thesis is dedicated to

my beloved parents.

Abstract

Civil infrastructures in the modern era are indispensable for basic facilities that help society function, including buildings, roads, utilities, and other systems. Its continuous development and maintenance are fundamental to the socio-economic growth of a country. These infrastructures have a specific design life span, and they deteriorate as time progresses. Natural aging, overloading, and lack of maintenance are some of the primary causes of degradation. Besides aging, a structure also experiences damage due to natural calamities such as earthquakes, storms, tsunamis that often induce substantial distress and subsequent reduction of strength and service life. Structural health monitoring and condition assessment in periodic intervals, especially after any natural calamities, are crucial to avoid any catastrophic failure, which may lead to human causalities as well as severe economic losses.

In general, the damage is incurred in a structure in the form of cracks and/or yielding of material, which often leads to non-linear hysteretic behavior. Due to the hereditary nature of hysteresis, modeling and identifying the non-linear hysteretic systems continues to be one of the challenging problems in structural health assessment. One of the efficient ways to assess structural health is using time-domain Bayesian filtering. Although several studies are available in the literature on the identification of hysteretic systems using the Bayesian algorithms, most of them focus on simulated experiments or small-scale laboratory tests. Field implementation of these algorithms experience several challenges. For example, Extended Kalman filter is often used for system identification, which linearized a non-linear system using Taylor series expansion. However, linearization of system matrices of a full-scale structure is difficult, if not impossible in many occasions. Besides linearization, predictor-corrector time-marching algorithm in Bayesian framework often face numerical instability. With these in view, a constrained minimum variance unbiased (CMVU) algorithm is developed in the light of sigma point transformation to simultaneously identify the hysteretic parameters and input excitation from noisy structural responses. In this algorithm, hysteretic behavior is modeled using a generalized Bouc-Wen model, where Bounded Input and Bounded Output (BIBO) property is preserved by novel constraint conditions to avoid any instability associated with the identification process.

Further, bounds corresponding to each hysteretic parameter are also proposed within the CMVU algorithm to obtain convergent and optimal solutions. Three different types of sigma points generation schemes (viz. unscented transformed points, cubature quadrature points, and quasi-Monte Carlo points) are presented in this study to demonstrate the efficiency of this algorithm. The proposed algorithm is validated using a simulated response of a reinforced concrete frame under seismic excitation. The hysteretic parameters are obtained by minimizing the error between the model and experimentally observed load-deformation

characteristics, including degradation and pinching effect. The rationale behind using experimentally observed hysteresis in simulation is to replicate the actual structure to maintain its realistic material behavior. Once the algorithm is validated numerically, its performance is further demonstrated using the shake table test data of a full-scale bridge pier. This test was carried out in the NEES-UCSD large High-Performance Outdoor Shake Table facility, and the data is available in the public domain, i.e., the DESIGNSAFE-CI platform. The identification results presented in this study clearly show the robustness of the proposed algorithm, which can estimate both hysteretic properties and input excitation with a sufficient level of accuracy.

Besides identifying hysteretic parameters and input excitation, the proposed CMVU algorithm can estimate the restoring force generated by the structure during ground excitation, which cannot be obtained directly using instrumentation alone. In the absence of measured restoring force, researchers often use the total inertia force acting on the structure under base excitation as the restoring force, which leads to incorrect hysteretic behaviour. It is shown that the proposed CMVU algorithm can capture the true nature of the hysteresis, which is further utilized as an engineering demand parameter to estimate the damage state of the structure. First, the proposed strategy is tested using a simulated example. Next, it is applied to the same shake table test data of the full-scale bridge pier used in parameter and input estimation to study the cumulative in-situ damage state using Park and Ang damage index. The main aim of this study is to facilitate the decision-making process based on the in-situ condition assessment from the recorded response after any seismic event.

In this context, the phenomenological models (viz. Bouc-Wen) can efficiently capture the global load-deformation behaviour of any hysteretic structure. However, they may not adequately capture the damage mechanism of complex systems that demand the information related to the presence, location, type, and extent of the damage. To address this issue, a damage estimation framework through mechanics-based non-linear finite element (FE) model updating is developed using Open System for Earthquake Engineering Simulation (OpenSees) FE package to obtain more insight into the incurred damage. The traditional unscented Kalman filter (UKF) algorithm is augmented with the parameter bounds to avoid possible instabilities, which may occur in Opensees solver during the updating process. The proposed framework is validated using the simulated noisy measurement data (i.e., acceleration, strain history, etc.) of a reinforced concrete frame. The updated parameters are subsequently used for damage estimation using Park and Ang damage index. Further, the proposed algorithm is adopted for the same reinforced bridge pier experiment, and the results show close conformity of the estimated damage to the actual one.

Each proposal in this thesis is validated both numerically and experimentally to prove its efficiency and practicality. It includes both phenomenological and mechanics-based nonlinear models of the hysteretic systems. Overall, the study shows the ability of the proposed algorithms for damage quantification that are fundamental for decision making (i.e., future retrofitting/rehabilitation).

List of Publications

Journal Articles:

1. P. Tamuly, A. Chakraborty and S. Das, "Experimental Verification of Constrained Minimum Variance Unbiased Estimator for Simultaneous Input and State Estimation of BIBO Type Bouc-Wen Hysteretic Structural System". *Structural Control and Health Monitoring*, Wiley, 2021, Volume 28, Issue 1, Pages e2648.

2. P. Tamuly, A. Chakraborty and S. Das, "Condition Assessment of Bridge Pier Using Constrained Minimum Variance Unbiased Estimator". *Structural Monitoring and Maintenance*. Technopress, 2020, Volume 7, Number 4, Pages 319-344.

3. P. Tamuly, A. Chakraborty and S. Das, "Nonlinear Finite Element Model Updating Using Constrained Unscented Kalman Filter for Condition Assessment of Reinforced Concrete Structure". *Journal of Civil Structural Health Monitoring*, Springer, https://doi.org/10.1007/s13349-021-00496-7.

4. P. Tamuly, A. Chakraborty and S. Das, "Simultaneous Input and Parameter Estimation of Hysteretic Structural Systems Using Quasi-Monte Carlo Simulation Based Minimum Variance Unbiased Estimator". *Journal of Bridge Engineering*, ASCE. https://doi.org/10.1061/(ASCE)BE.1943-5592.0001767.

Contents

List of Figures

List of Tables

List of Abbreviations

SHA	Structural health assessment
GDP	Gross domestic product
ASCE	American society of civil engineer
NDT	Non-destructive test
SI	Sys tem identification
LSE	Least square estimation
EKF	Extended Kalman filter
UKF	Unscented Kalman filter
EnKF	Ensemble Kalman filter
PF	Particle filter
MAC	Modal assurance criterion
COMAC	Coordinate modal assurance criterion
FD	Fractal dimension
MSE	Modal strain energy
MSECR	Modal strain energy change ratio
DOF	Degrees of freedom
SDOF	single degree of freedom
MDOF	Multiple degrees of freedom
KF-WGI	Kalman Filter- Weighted Global Iteration
ILS-UI	Iterative least square under unknown excitation
SNLSE	Sequential non-linear least-square
EKF-WGI	Extended Kalman filter-Weighted Global Iteration
GMSPPF	Gaussian mixture sigma-point particle filter
PBEE	performance based earthquake engineering
BIBO	Bounded input bounded output
CMVU	constrained minimum variance unbiased estimation
MCMC	Markov chain monte carlo
AKF	Augmented Kalman filter
DKF	Dual Kalman filter
URNDDR	Unscented recursive nonlinear dynamic data reconciliation
GMVU	Generalized minimum variance unbiased estimation
GHF	Gauss-Hermite filter
CKF	Cubature-Kalman filter
BWBN	Bouc-Wen-Baber-Noori
CIUKF	Constrained iterated unscented Kalman filter
CUKF	Constrained iterated unscented Kalman filter

List of Major Symbols and Their Meanings

α	Ratio of post yield to pre-yield stiffness
β,γ, n	Bouc-Wen model parameters controlling shape and size
X_β, X_γ	Auxiliary variable
$\mathbf{x}(t)$	Displacement
$\dot{\mathbf{x}}(t)$	Velocity
$\ddot{\mathbf{x}}(t)$	Acceleration
$\ddot{\mathbf{x}}_g(t)$	Ground acceleration
$\mathbf{\Phi}$	Unknown parameter vector
$\mathbf{B}$, $\mathbf{H}$	Influence matrix
$\mathbf{Z}$	Extended state vector
$\mathbf{F}$	Restoring force
$\mathbb{E}$	Expectation operator
$G(\bullet)$	State transition function
$h(\bullet)$	Nonlinear measurement function
$\mathbf{\Phi}$	Parameters with bounds
$\mathbf{P}$	Covariance matrix
$\mathbf{\Psi}$	Sigma points for State
$\mathbf{\Xi}$	Sigma points for measurements
$\mathbf{R}$	Measurements covariance
$\mathbf{L}_k$	Optimal gain matrix
$\mathbf{K}_k$	Kalman gain matrix
δ_v, δ_η	Degradation parameters of Bouc-Wen model
$q, p, \zeta_0, \psi, \delta_\psi, \lambda$	Pinching parameters of Bouc-Wen model
ϕ	Curvature
ϵ	Strain
E	Young's modulus
f_y	Yield stress of steel
f_c	Yield stress of concrete
b	Strain hardening ratio
R_0	Elasto-plastic transition parameter

Chapter 1

Introduction

Global infrastructural development experienced a thumping growth over the past decades. The present socio-economic scenario worldwide shows that around 3.17% of the Gross Domestic Product (GDP) has been spent on infrastructure and its maintenance in 2020 [1]. The global infrastructure report has estimated a substantial rise in this expenditure head up to a striking $94 trillion from 2016 to 2040 [2]. In view of this requirement, the civil engineering community has always played an important role in adopting practical inspection, monitoring, and maintenance measures to reduce the associated cost. A significant number of structural failures/collapses in the past have shown the need for regular condition assessment. It is a continuous process as every structure experiences deterioration from the moment it is exposed to its operational environment. In this context, natural calamities (viz. Earthquakes, wind, floods) are often attributed as the leading cause of damage to any structure. The earthquakes in the recent past have proved this fact (e.g., Kobe in 1995, Gujarat in 2001, L'Aquila in 2009, Chile in 2010, and Tohoku Japan in 2011). Fig. 1.1 shows the damage caused by some of these seismic events. A study has reported that more than 90% of the deaths during earthquakes in India were due to the collapse of inhabited structures [3]. Therefore, health assessment of these structures due to aging or exposure to natural hazards is essential for ensuring their safety and serviceability. This process provides critical inputs for decision-making on maintenance and rehabilitation/retrofitting.

The failure of infrastructures such as bridges, dams, power plants, and emergency response buildings comes at the cost of life imperilment, economic losses, and functional disruption. Due to this reason, many national agencies and professional bodies have made it a priority to survey the health of civil infrastructures. In 2017, the American Society of Civil Engineers (ASCE) conducted several studies regarding the health of the structures at the national level. It graded them with an overall D+ (poor) category in their Report [4]. A similar study was carried out in Canada and found that more than 40% of the bridges currently in use were built before 1977. A large number of these bridges demands immediate rehabilitation or replacements [5]. In Australia, many public bridges that have been operational for 30 to 40 years since their inception need major renovation. The maintenance of these bridges on large scales are expensive and demand new technologies to meet the practical challenges. The data reveals that around $41.8 billion is needed in the USA to maintain 45000+ bridges currently in operation [6]. Similar studies in Australia show that $270 million per year is required for condition assessment [7]. These values are quite astounding from the economic

(a)

(b)

Figure 1.1: Earthquake damage of infrastructure; (a) Bhuj earthquake dated 26^{th} January 2001 (Source: www.nicee.org), and (b) Kobe earthquake dated 17^{th} January 1995 (Source: The Wall-Street Journal)

point of view. Countries like India are yet to take significant initiatives for lifeline structural assessment at the national level except a few local measures on a case-to-case basis. Therefore, to prioritize the decision-making process for effective resource utilization, systematic, proactive planning and preventive measures must be adopted. The decision-making process incorporates efficient condition-based inspection/monitoring strategies that ultimately lead to assessing residual life, detecting any damage, and safety measures necessary at the earliest stage. Also, it facilitates in articulating the maintenance strategies to ensure uninterrupted service life and prevent catastrophic failure. Without periodic structural assessment, it may experience a loss due to continuous depletion of strength and becomes vulnerable. In general, structural degradation is quantified by the change in material and geometric properties (e.g., stiffness, damping, mass), which affect structural performance. Thus, efficient/reliable heath evaluation techniques are essential for the smooth operation of any structural ecosystem.

1.1 Structural Health Monitoring

Structural Health Monitoring (SHM) is a systematic study to evaluate the health of an in-service structure or its components. It is a multidisciplinary technique that includes observation-based analysis of a structure over a given period. Then the damage-sensitive parameters are derived from the measurements before they are interpreted to determine the in-situ health of any structure. This process is repeated periodically to track the ability of a structure to cope with evolving applied conditions, deterioration, and aging. During this process sensors are fixed on the surface or embedded inside. Depending upon the type of installation, these data collection devices are classified as integrated or surface sensors. Structural health monitoring techniques can be broadly classified into two types - offline and online depending upon the mode of data used in the identification process.

Farrar et al. [8] demonstrated that SHM is fundamentally the same as statistical pattern recognition, which aims to process and classify patterns (data) based on either previously

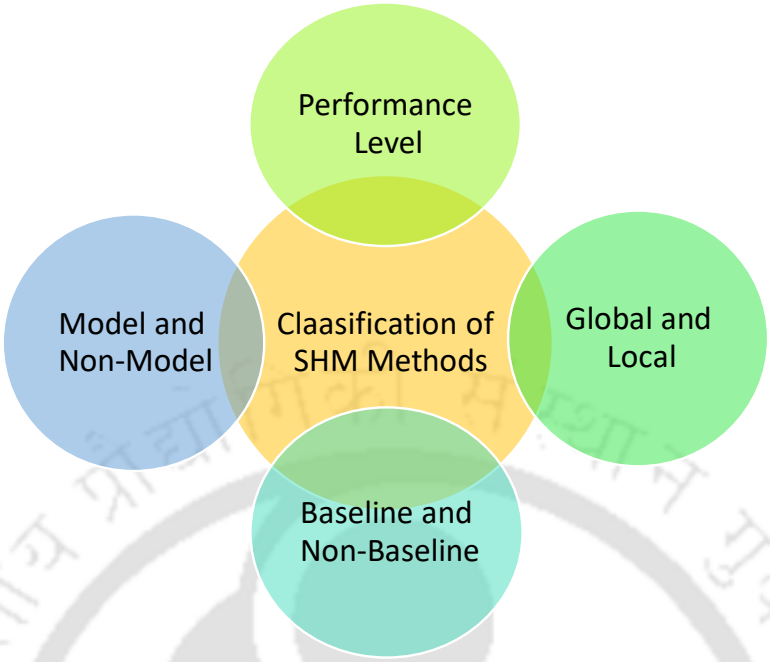

Figure 1.2: Different classification of SHM methods

available knowledge or the information obtained from the patterns. It covers different stages of problem formulation to interpret results, broadly classified into two parts, i.e., diagnosis and prognosis. The diagnosis only refers to data analysis for the current health assessment of any structure. In contrast, prognosis refers to the study of damage propagation to estimate the remaining service life [9]. The elementary classes of different SHM techniques are briefly summarized in Fig. 1.2 and explained in the following subsections.

1.1.1 Performance Based Approaches

The performance-based classification of damage detection was first introduced by Rytter [10]. It has four levels of damage detection i.e.

- Level 1 – methods only deal with the occurrence of damage
- Level 2 – methods determine the occurrence as well as the location of a damage
- Level 3 – methods quantify the severity of damage in addition to Level 2 analysis
- Level 4 – methods predict the future life in addition to analysis in Level 3

In this format, levels 1 to 3 refer to diagnosis while level 4 refers to prognosis [11–13]. Level 4 also includes fatigue life analysis and fracture mechanics-based damage quantification and prediction [9].

1.1.2 Model and Non-Model Based Approaches

Model and non-model-based damage detection methods are distinguished in this classification. In the non-model-based techniques, the response of the current state is compared with the previous measurements. The deviation in the damage-sensitive features is estimated for its detection. On the other hand, the model-based approach compares measurements (viz. acceleration, displacement, strain, etc.) with the same response of an analytical or numerical model (say, finite element model). The main advantage in model-based approach lies in its ability to quantify the extent and severity of the damage. It is challenging to develop an accurate/reliable numerical or analytical model for many complex structures. In addition, the computational cost also limits its applicability in some cases.

1.1.3 Global and Local Methods

Damage detection methods are commonly classified into the global or local approach, based on the structural model used in this process. These are distinguished based on the extent of the structure relative to the whole structure that can be analyzed [14]. The global methods study a relatively more significant portion, and their precision to identify the location and severity of damage is limited on many occasions. Therefore, only severe damages are determined with the help of this method. At the same time, local techniques can focus on every component of the structure and detect the exact location and severity of even a minor damage, e.g., cracks. However, prior information about the location of the damage is necessary. So, both these methods are often combined, utilizing their benefits. The global approach helps to verify the overall performance, while the local approach is used to pinpoint the location of damage in a structure.

1.1.4 Baseline and Non-Baseline

Worden et al. [13] proposed a fundamental axiom of SHM that any damage identification methodology must compare two states of any system. The response acquired at the initial stage is usually utilized as a reference or baseline to differentiate between the damaged and undamaged state. For model-based methods, the baseline performance can be established using a finite element model. However, there are some proposals [15, 16] that are not dependent on the baseline to classify a state, i.e., damaged or undamaged. Thus, instead of relying on the baseline measurements, non-baseline methods are based on comparing two conditions. It uses a pre-assumed behavior of the structure as a baseline. The damage, in this case, is confirmed by the deviation of the response from its pre-assumed state.

1.2 Literature Review

In this section, the literature review is presented to discuss different techniques used in SHM. The first assessment of any structure is often carried out using visual inspection, which requires only physical examination of damage. Based on the experience of the observer, the severity of the damage level is assigned. A significant drawback of this method is that the

damage remains undetected if the damage location is inaccessible. Non-structural elements are removed to uncover the potential area of damage before the inspection.

Another popular technique is the local non-destructive test (NDT), often used as a secondary step once the suspected area of damage is identified. Some examples of these methods are acoustic emissions or ultrasonic tests [17], magnetic field tests [18], and radiography [19]. The local NDT-based approach becomes inefficient for an extensive structural system, as it requires the damage location to be known beforehand, and the area should be readily accessible. Furthermore, the execution of these methods in such situations is expensive, time-consuming, and labor-intensive. Besides these practical challenges, the designer often faces difficulty in correlating the NDT results directly with the health of the structural system.

Thus, the need for cost-effective damage detection methods suitable for large structures has led to several structural health assessment techniques. Among them, the System Identification (SI) based approach is most widely used. It is based on the underlying physical process, which utilizes the input-output relationship. In a typical SI-based algorithm, the three essential components are - (i) excitation(s), (ii) mathematical representation of the structure, and (iii) measurements at a different location. The dynamic properties in terms of its mass and stiffness properties of all the elements and damping can be identified using available information, i.e., excitation and responses. Assuming mass can be estimated with sufficient accuracy, which will not change during the inspection process, structural stiffness and damping properties can be tracked for condition assessment.

Various structural health monitoring using SI techniques are currently available in the literature [20, 21]. Among them, vibration-based methods have received more attention due to their effectiveness besides advancements in computation, sensor technology, and data acquisition hardware. The basic premise of vibration-based SHM is to detect any change in the structural property (i.e., stiffness, mass, and damping) that affects the dynamic characteristics. Thus, by tracking these changes, SHM can detect structural damage, location, and extent. In general, vibration-based approach can be classified into three paradigms: frequency, time, and time-frequency domain (Fig. 1.3). Since frequency-domain modal properties represent global dynamic behaviour, it may not always be efficient to locate defects at the local element level.

In the time domain, the dynamic properties of each element (i.e., mass, stiffness, and damping) are identified using known excitation and measurements. The mass of the members are considered to be known in most cases. Thus, the vibration characteristics of a damaged structure are reflected in its stiffness and damping, whose changes are the measure of damage. Therefore, the location and extent of damage are detected by comparing the identified stiffness properties of every element with their baseline values. Here, the baseline values are mostly obtained from the structural drawings. This inspection process is carried out periodically, and the variations of sectional properties, location(s), number, and severity are monitored. The procedure can also be adapted to evaluate the performance of any rehabilitated structures to establish the effectiveness of the retrofitting measures.

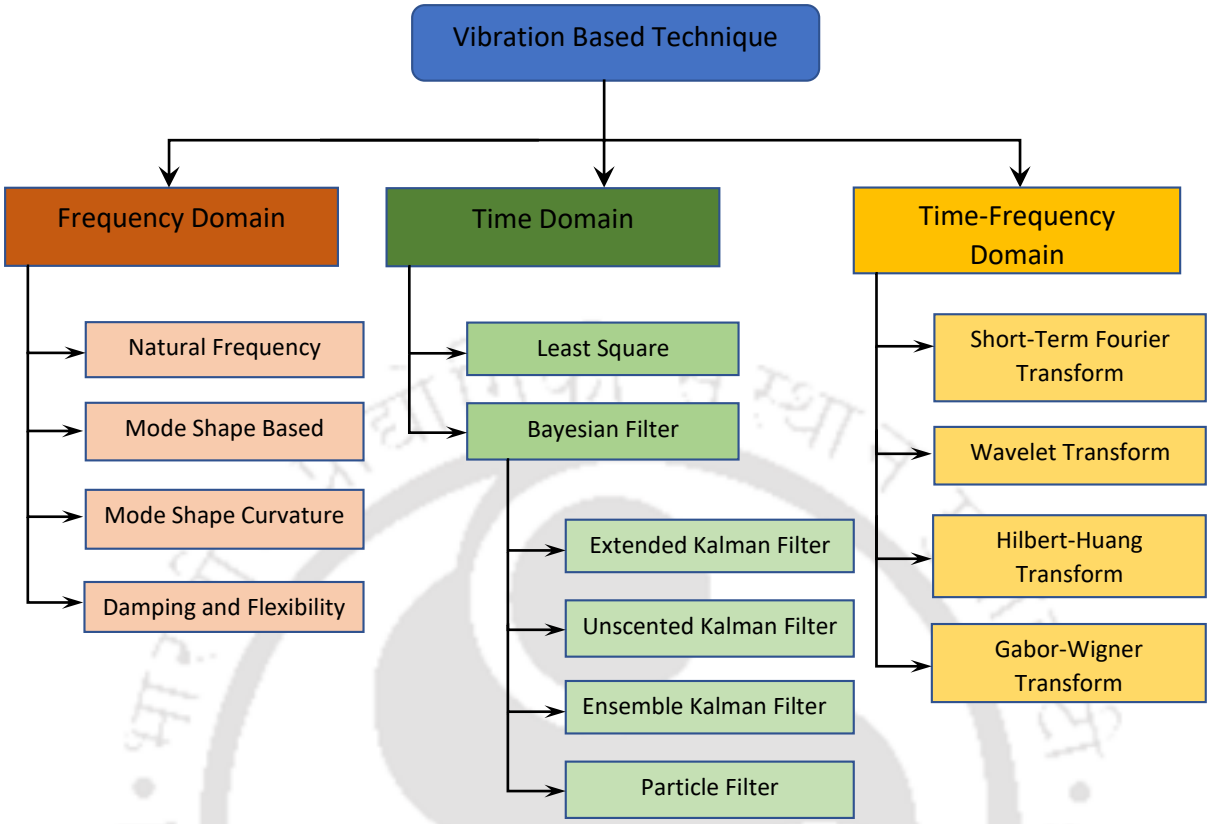

Figure 1.3: Vibration based techniques of SHM. [NB: Time-frequency domain techniques are omitted in the literature review, as the main focus is study is the development of time-domain techniques.]

1.2.1 Frequency Domain Approach

The conventional vibration-based structural damage detection is mainly based on the natural vibration characteristics, i.e., natural frequency, mode shapes, and modal damping ratio. Since any change in mass and stiffness matrix due to damage or degradation are reflected in the measured natural frequency and mode shape, they indicate the position and severity of damage inside a structure.

Doebling et al. [22] and Sohn et al. [11] presented an extensive review on different vibration-based techniques for damage identification. The details of frequency-based methods can be further subdivided into the following groups -

- natural frequency based methods
- mode shape-based methods
- modal curvature/strain energy based methods
- other methods based on modal parameters based methods

1.2.1.1 Natural Frequency-Based Methods

Natural frequency-based methods use any change in the primary feature, i.e., the natural frequency, for damage detection. These techniques are easy to implement and offer significant accuracy in most cases, which are generally categorized as forward or inverse problems. The forward problem deals with the change in frequency and its impact on the severity of damage location. On the other hand, the inverse problem deals with evaluation of damage location, size, and severity based on the identified frequencies. However, measurement alone is not sufficient to detect damage accurately as it is a global property of the structure. Moreover, the natural frequency is not so sensitive to initial cracks and can only assure extensive damage. Penny et al. [23] developed an efficient inverse strategy for damage quantification using the measured structural frequency. It was used for locating the most likely damage scenarios by simulating the frequency shifts that would occur in all possible damage cases. The simulated frequencies were updated using the measure frequencies in a least-squares sense. The minimal error indicated the actual damage case in this process. A similar procedure was also demonstrated by Lee and Chung [24] to detect the crack location using Armons Rank-order. A finite element model (FEM) was developed, and the crack size was determined to match the observed behaviour. Finally, the actual crack location and size were identified using Gudmundsons equation. Patil and Maiti [25] proposed a frequency shift-based approach to detect multiple open cracks. It was based on a transfer matrix where the cracks were modeled by the rotational springs. A beam was divided into several segments to model the damage parameter. These parameters were determined from the measured changes in the natural frequencies. Kim and Stubbs [26] proposed a single damage indicator (SDI) method to locate and quantify a crack in beams using changes in the first few natural frequencies. The crack location and size model was formulated by relating fractional changes in modal strain energy to the changes in the natural frequencies due to damage. The crack location was detected from the fractional change in the i^{th} eigenvalue, i.e., Z_i, and the modal sensitivity of the i^{th} stiffness in the j^{th} element F_{ij}. The modal curvature was obtained from a 3^{rd} order interpolation scheme, which was expressed as

$$F_{ij} = \frac{K_{ij}}{K_i} = \frac{\int_{x_j}^{x_{j+1}} \{\phi''\}^2 dx}{\int_0^L \{\phi''\}^2 dx} \tag{1.1}$$

Then, an error-index e_{ij} was introduced to represent the error in the i^{th} mode for the j^{th} location i.e.

$$e_{ij} = \frac{Z_i}{\sum_{k=1}^{N_m} Z_k} - \frac{F_{ij}}{\sum_{k=1}^{N_m} F_{kj}} \tag{1.2}$$

where N_m denotes the number of measured vibration modes. To account for all available modes, a global SDI was defined to indicate the damage location using the following form

$$SDI = \left[\sum_{i=1}^{N_m} e_{ij}^2\right]^{-1/2} \tag{1.3}$$

Zhong et al. [27] introduced a spectral center correction method (SCCM) to develop a simple solution for damage detection using the response time history. In SCCM, identified natural frequency vs. auxiliary mass location was plotted along with its derivatives up to third order to detect any crack. However, only the FE model verification was provided to illustrate their method without any experimental validation.

The natural frequency-based approaches can be categorized into two groups - the input-output approach and the output-only approach. The first approach requires knowledge of input excitation and measurements, whereas the second approach requires only measurements for system identification. Output-only procedures are quick and straightforward to adopt for inverse field application.

1.2.1.2 Mode Shape Based Methods

The advantage of using mode shape and its derivative compared to natural frequency are manifold. The local abnormal deformation of any structure is reflected in the mode shape, which helps to locate damage. Also, the mode shapes are less sensitive to the environment than natural frequencies [28]. Despite these advantages, the mode shape-based approach has several limitations [29]. For example - (i) high sampling rate is necessary for accurate estimation of mode shapes, and its curvature, (ii) mode shape has more significant statistical variation compared to the natural frequency, (iii) the mode shape-based methods, especially the curvature mode shape-based methods, are inaccurate and has inherent limitation for complex geometry or material property, and (iv) different modes undergo different levels of variation due to specific structural damage, which is not known apriori.

Over the last few decades, different direct or indirect methods are developed for damage detection. The traditional approach tries to establish a relationship between the change of mode shape, location of damage, and severity through experiment or finite element analysis. Hence, they depend on modal conditions obtained from both damaged and undamaged structures. A series of relatively new techniques have been developed, which are based on modern signal processing. These signal processing tools can be applied on the mode shape data obtained from damaged structures or their derivatives. These methods can identify the location of damage by detecting any local discontinuity or curvature of the mode shape. Thus, Coordinate Modal Assurance Criterion (COMAC) was introduced to detect damage in steel frames [30]. The sensitivity of any mode shape to a particular damage condition was computed. The modal assurance criterion (MAC) determined the correlation between the i^{th} mode of undamaged model vector $\{\phi\}_U$ and j^{th} mode of a damaged modal vector $\{\phi\}_D$, which was defined by

$$\text{MAC} = \frac{\left|\{\phi_U\}_i^T \{\phi_D\}_j\right|^2}{\{\phi_U\}_i^T \{\phi_U\}_i \{\phi_D\}_j^T \{\phi_D\}_j} \tag{1.4}$$

If the MAC numbers are arranged in a matrix, the leading diagonal elements dominate. Tatar et al. [31] demonstrated modal assurance criterion using forced vibration response of a nine-storey reinforced concrete building. In general, COMAC is developed from MAC so that the correlation can be defined using the coordinates of the modal vector rather than

the mode number. As a result, COMAC uses two sets of modal vectors, which is expressed as

$$\text{COMAC} = \frac{\left(\sum_{L=1}^{L_{\max}} \left|\left(\phi_{i,L}^{U}\right) \cdot \left(\phi_{i,L}^{D}\right)\right|\right)^2}{\sum_{L=1}^{L_{\max}} \left(\phi_{i,L}^{U}\right)^2 \sum_{L=1}^{L_{\max}} \left(\phi_{i,L}^{D}\right)^2} \tag{1.5}$$

It indicates how the coordinates of the two modal vectors deviating from each other. In the above equation, L_{max} represents the number of DOFs in a modal vector. Shi et al. [32] developed Multiple Damage Location Assurance Criterion (MDLAC) for damage localization. This two-step damage detection procedure identified the exact location of damage using incomplete mode shapes evaluated from the measurements. Then its severity was determined in the next step using the sensitivity of the identified natural frequencies. In principle, the finite element model was updated using incomplete mode shape data, which were further utilized to locate and quantify the damage. The method was validated using a simulated 2D plane truss. Comparison of the experimentally observed and numerically modeled mode shapes proved the accuracy of their proposal. Pawar et al. [33] studied the damage index of a beam where effect of damage on the mode shape was formulated using the Fourier coefficients. Hadjileontiadis et al. [34] extended the use of mode shapes to estimate Fractal Dimension (FD). The FD of a curve was calculated by

$$FD = \frac{\log_{10}(n)}{\log_{10}(d/L) + \log_{10}(n)} \tag{1.6}$$

where n is the number of discretization of the curve; d is the diameter estimated as the distance between the first point of the sequence P_1 and the i^{th} point P_i of the sequence that provides the farthest distance, and L is the total length of the curve or the sum of distances between successive points. The method developed in [34] estimated the localized FD of the fundamental mode shape directly. The damage features were extracted by employing a sliding window across the mode shape to calculate the FD at any location. Damage location and size were determined by the peak of the FD curve, which indicated the local irregularity of the fundamental mode shape. Duvnjak et al. [35] adopted FD-based DI for experimental damage detection of a reinforced concrete plate.

1.2.1.3 Modal Curvature/Strain Energy Based Method

Previous studies showed that mode shapes were less sensitive to initial damage in a complex structure [36]. The curvature of a damaged mode shape was proposed in the literature, which turned out a promising feature for damage detection. The flexural stiffness of any structure is reduced at the cracked region due to loss of sectional property. It affects mode shape in that particular region, and hence curvature of the mode shape is changed at the damaged location. The severity of damage is related to the magnitude of change in curvature, which increases with the reduction in stiffness. Wahab and De Roeck [37] showed the limitation of this method at higher modes, which inherently had multiple peaks. These peaks were not only located near cracks but also at other locations, which introduced false alarms. Thus

curvature based method is best suited for continuous structures like beams or plates and not for discrete systems like frames. Also, its use is limited to lower modes only.

Pandey et al. [38] assumed that structural damage only affected the stiffness matrix and not the mass matrix. The eigenvalue problem for a linear dynamic system can be expressed as

$$([K] - \lambda_i [M]) \{\phi_i\} = \{0\} \tag{1.7}$$

where $[K]$ and $[M]$ are stiffness and mass matrix, respectively. Other parameters in the above equation, i.e., λ_i and ϕ_i are the i^{th} eigen value and eigen vector. Similarly, the eigenvalue problem for the damaged condition is given by

$$([K^*] - \lambda_i^* [M]) \{\phi_i^*\} = \{0\} \tag{1.8}$$

where the asterisk is for the damaged elemental property. The pre and post-damage eigen vectors are the basis for damage detection. Mode shape curvature for a beam in its undamaged and damaged condition can then be estimated numerically. Consider a beam where cross-section at location x subjected to a bending moment $M(x)$. The moment-curvature relationship at this location is given by

$$v''(x) = \frac{M(x)}{EI} \tag{1.9}$$

where E is the modulus of elasticity and I the moment of inertia of the section. Thus, for a given moment acting on an undamaged and damaged beam, the reduced stiffness associated with the damaged case is bound to increase its curvature. Ratcliffe [39] presented an experimental model called the resonant gapped-smoothing method to obtain the curvature function from the frequency response function, which was further processed to get the damage location. It first converted the displacement mode shape of a damaged beam into the curvature mode shape, i.e., reciprocal of the radius of curvature. The curvature C_i at the i^{th} point on the damaged beam was estimated from the displacement y using a central difference i.e.

$$C_i = \frac{y_{i+1} + y_{i-1} - 2y_i}{h^2} \tag{1.10}$$

where h represented the uniform spatial separation adopted in the discretization. For the first and last points, the curvature was estimated using the adjacent data points. The experiment in [39] successfully located a 0.05 mm deep slot in a 6.35 mm thick beam. The natural frequencies changed by less than 0.03% due to the low level of damage. The concept of mode shape curvature was extended for simply supported and continuous bridges by Dutta and Talukdar [40] to detect and localize multiple damages. They considered standard shell elements for modeling and noticed the peaks in modal curvature changed with location, i.e., longitudinal and transverse directions of the bridge deck. They also showed that the curvatures of the lower modes were generally more accurate than the higher modes. In multiple cracks, much refinement was necessary for the precise estimation of the mode shape and the curvature.

In general, if a particular mode stores a large amount of strain energy, it is susceptible to changes in structural properties. Thus, modal strain energy helps in localizing structural damage. This idea was utilized by Shi et al. [41] to quantify damage [i.e., change in modal strain energy (MSE) before and after damag]. They defined elemental MSE as the product of the elemental stiffness matrix and the second power of the mode shape for the j^{th} element and the i^{th} mode. Thus, the MSE before and after the occurrence of damage was defined as

$$MSE_{ij} = \Phi_i^T K_j \Phi_i \tag{1.11a}$$

$$MSE_{ij}^d = \left(\Phi_i^d\right)^T K_j \left(\Phi_i^d\right) \tag{1.11b}$$

where MSE_{ij} and MSE_{ij}^d represented the undamaged and damaged case, respectively. Thus, modal strain energy change ratio (MSECR) was developed for damage localization.

$$MSECR = \frac{\left|MSE_{ij}^d - MSE_{ij}\right|}{MSE_{ij}} \tag{1.12}$$

The complete procedure was illustrated using both numerical examples and experiments on a two-story steel portal frame. Results indicated that the non-dimensional indicator in Eq. 1.12 effectively localized damages, which was also noise sensitive. Following the principle of modal strain energy, Li et al. [42] proposed damage detection based on the element-wise decomposed stiffness corresponding to axial, transverse, and rotational degrees of freedom. Strain energy was evaluated for each stiffness type corresponding to damaged and undamaged conditions using Eq. 1.11b. The damage index (β_{ij}) for the j^{th} element in the i^{th} mode was expressed as

$$\beta_{ij} = \frac{E_j}{E_j^*} \tag{1.13}$$

where the scalars E_j and E_j^* represented Young's modulus of the material strength in its undamaged and damaged state, respectively. The method required only a small number of mode shapes of a damaged and its baseline structure. A 3D 5-storey frame was studied numerically, and the results showed that the axial damage indicator was able to locate damage occurring in the horizontal elements. On the other hand, the transverse damage index could locate damage occurring in the vertical elements. However, false alarms were generated in many cases, which also failed to identify damage severity. Thus, a hybrid approach was developed using spatial Continuous Wavelet Transform (CWT) of mode shape and a Mode Shape Curvature Squares (MSCS), which helped in detecting and localizing damage in beams [43]. The approach was validated with experimental results of aluminum and carbon composite beams with different severity of the damage. A new approach was introduced using the damaged structural displacement mode shape to eliminate the necessity for undamaged structural data [44]. The findings in this paper revealed that the proposed index was as effective as the conventional mode shape curvature approach in magnifying the damage location.

1.2.1.4 Methods Based on Other Modal Parameters

Most of the studies mentioned earlier do not use damping as a parameter for damage detection. However, it has the advantage over other detection schemes based on frequencies and

mode shapes as it represents non-linear energy dissipation originating from cracks. Modena et al. [45] proposed a new approach based on modal damping ratio to address this issue. They found that small and visually unidentified cracks caused an insignificant change in resonant frequencies of the structure and required higher mode shapes for damage detection. On the other hand, the sensitivity of damping for the same crack size was measurable. Adding to this idea, Panteliou et al. [46] showed that damage identification using change in damping factor had the advantage as it was relatively insensitive to boundary conditions. The study by Yamaguchi et al. [47] used the energy-based damping analysis to quantify damage in steel and concrete bridges. They also noticed that the modal damping was a sensitive indicator against corrosion-induced damage in a reinforced concrete beams. It indicated that the local corrosion level might be detectable by measuring the modal damping ratio. Cao et al. [48] presented a review on modal damping ratio to detect deterioration in different infrastructure, with significant emphasis on reinforced concrete and fiber-reinforced composites. Ay et al. [49] developed a unique approach for vibration-induced damage identification using the probability distribution of decay rate. They analyzed the damage-induced changes in the overall damping behaviour using the free vibration of a dynamic system.

Different damage identification strategies used a dynamically measured flexibility matrix to estimate the change in its behaviour [50]. The flexibility matrix is defined as the inverse of the stiffness matrix. Hence, the flexibility matrix F relates the applied static force f and resulting structural displacement u through the following relation

$$\{u\} = [F]\{f\} \tag{1.14}$$

In this formulation, flexibility matrix is expressed as

$$[F] = [\Phi][\Omega]^{-1}[\Phi]^T = \sum_{i=1}^{n} \frac{1}{\omega_i^2}\{\phi_i\}\{\phi_i\}^T \tag{1.15}$$

where $[\Phi] = [\{\phi_1\}\{\phi_2\}....\{\phi_n\}]$ is the mode shapes matrix, where $\{\phi_i\}$ is the i^{th} mode shape. The diagonal matrix of rigidity $[\Omega]$ corresponds to ω_i i.e. i^{th} frequency. Thus, each column of the flexibility matrix $[F^*]$ represents the displacement pattern due to a unit force applied at the associated degree of freedom. Thus, measuring the flexibility matrices before and after damage, its variation $[\Delta]$can be obtained as follows

$$[\Delta] = [F^*] - [F] \tag{1.16}$$

where $[F]$ and $[F^*]$ are the flexibility matrices before and after damage, respectively. Now, for each column of Δ, let δ_j be the absolute maximum value of the elements in its j^{th} column i.e.

$$\delta_j = \max|\delta_{ij}| \quad i = 1, 2.....n \tag{1.17}$$

where δ_{ij} are elements of matrix $[\Delta]$ and represent the flexibility variation in each degree of freedom. The column of the flexibility matrix corresponding to the largest δ_{ij} indicates the degree of freedom where the maximum variation in flexibility occurs due to damage. Panday and Biswas [50] presented different examples (i.e., both numerical and experimental), which

showed that the damage and location could be obtained from the first two modes using the flexibility approach. Zhao et al. [51] reviewed different diagnostic parameters, including the mode shapes, natural frequencies, and modal flexibility. Their comparative approach was based on a perturbation coefficient in the stiffness matrix determined from the finite element analysis. The sensitivity coefficients for mode shapes, natural frequencies, and modal flexibility due to damage were derived in their study. Their results showed that modal flexibility was more likely to identify damage than the other two. Further, this flexibility-based approach was modified by Salehi et al. [52] using its curvature, which was verified using numerical and experimental data. They showed that the results in both cases were satisfactory, and hence, the technique could be adopted for damage detection of real-life structures. The main advantage of this technique was that it did not require a theoretical baseline model. Similarly, Altunisik et al. [53] presented a comparison of modal curvature and flexibility to localized damage in a steel cantilever beam. Their results showed that regardless the fracture depth, the modal curvature approach was superior to the modal flexibility approach for finding the location of a crack.

1.2.2 Time Domain Approach

Time-domain SHM refers to the methods that directly use measurement time-histories to detect structural damage. These methods typically first select a mathematical model to represent a structure. Then, the model parameters are identified by minimizing the difference between the measurement and model predicted structural response. The time-domain approach is better to locate and quantify defects at local and global levels. Recent advances in sensor technology, computational techniques, and data acquisition systems have made this approach reliable than the modal approaches discussed in the previous section.

1.2.2.1 Least Square Based Methods

The least-squares-based techniques are one of the most widely used mathematical tools for system identification. In this approach, the unknown parameters of a structural system are estimated by minimizing the sum of squared errors between the predicted and the measured outputs. Caravani et al. [54] used this technique using the recursive least-squares algorithm. This approach helped to estimate the stiffness parameters using the identified frequencies and mode shapes. The modal parameters were expanded as a function of stiffness using the Taylor series. Torkamani and Ahmadi [55] developed a least square algorithm using a lump mass model of a linear structure to identify stiffness and damping under seismic excitation applied at the base.

In this context, the solution of the inverse problem becomes more challenging if the input is unknown. Wang and Halder [56] provided a brief review of different techniques of parameter estimation under unknown excitation, e.g., Kalman Filter with a Weighted Global Iteration (KF-WGI) [57], stochastic adaptive techniques [58], free-decay analysis [59, 60], random decrement technique [61] among many others. These studies clearly showed that the least square method for parameter estimation was more suitable for unknown input. In this context, iterative least-square using unknown excitation (ILS-UI) has proved its ability for parameter estimation of any structure. In this process, the forces in the first few

time steps were assumed to be zero, and parameters of the structures were estimated using the recursive least square (RLS) algorithm. The iterative procedure continued until the algorithm converged to the desired level of accuracy. Later, Ling and Haldar [62] studied the performance of the least square algorithm considering Rayleigh damping. ILS-UI approach was adopted to find the stiffness and the proportional damping. The algorithm was successfully implemented using different models to identify structural parameters under white noise excitation. This approach was more efficient in terms of the total number of unknown parameters, which were $(n+2)$ (i.e., n stiffness terms plus 2 for proportional damping) compared to 2n for the viscous damping. Katkhuda et al. [63, 64] implemented a similar algorithm for inverse estimation of the degraded elemental stiffness using noisy and noise-free measurements. Other studies also investigated the potential of ILS-UI for parameter estimation and used experimental data for verification [65]. Besides offline use of least square-based parameter estimation, online use of sequential non-linear least-square (SNLSE) also received attention from researchers [66]. In this format, state and parameter vectors were estimated sequentially by minimizing a non-linear objective function linearized in every step. The SNLSE approach in [66] was demonstrated using different examples, i.e., Phase I ASCE benchmark building [67], a non-linear elastic structure, and non-linear hysteretic structures. Simulation results indicated that their approach could track the changes of structural parameters accurately, leading to the identification of structural damages. Yang et al. [68] extended the SNLSE algorithm for incomplete measurements. A similar approach in two steps was demonstrated by Wang and Cui [69] for simultaneous parameter and input estimation. Their proposal first identified the structural parameters using least-squares error minimization from the free vibration. Once the parameters were estimated, the input excitation was evaluated. The external excitation was transformed into nodal forces in i^{th} DOF at j^{th} time step as

$$f_{i,j} = m_i \ddot{x}_{g,j} \quad i = 1, 2....n \quad j = 0, 1, 2....s \tag{1.18}$$

where $f_{i,j}$ denoted external load and n was the number of DOF and s represents number of sample points. Input time history was evaluated utilizing the response of all DOF by statistical averaging i.e.

$$\ddot{x}_{g,j} = \frac{1}{n} \sum_{i=1}^{n} \frac{f_{i,j}}{m_i} \tag{1.19}$$

Thus, the measurements along the limited DOF were utilized to evaluate the input. Wang and Cui [69] implemented this method in a 10-storey building to estimate its stiffness and damping parameters with a significant level of accuracy. This iterative procedure of least square was further modified using Multiple QR Decomposition (MQRD) [70]. Chen and Li [71] further developed this technique for parameter estimation under excitation with spatial variation. First, the unknown force vector was modeled through the equation of motion using the initial guess of the unknown parameters and measurements. The estimated input force vector was then modified to comply with the spatial distribution of the external excitations. It was further used to update the already estimated parameters. The procedure was repeated until the structural parameters satisfied the convergence criterion. Sandesh and Shankar [72] presented a sub-structural approach for simultaneous evaluation

of parameter and input time history to accommodate a large structure in the least square framework. The main objective was to discretize the structure into several sub-structures to reduce computational cost. The efficiency of the least square technique was further demonstrated for hysteretic structure by Garrido et al. [73], where hysteresis was characterized Bouc-Wen model. First, the system was decoupled, and a stability analysis was performed with two different non-linear systems, i.e., SDOF and MDOF. The algorithm could identify the Bouc-Wen parameters besides other unknown system parameters with a significant level of accuracy. One of the advantages of this algorithm was that it did not require a *priori* knowledge of unknown parameters of the hysteretic component. However, the algorithm needed complete measurements to estimate hysteretic parameters. Thus, the weighted adaptive least-squares [74] algorithm was introduced to identify unknown parameters and input. The performance of this algorithm was demonstrated using (i) numerical simulation of a 6-DOF shear building model and (ii) experimental data for a 4-storey frame structure excited by impulse. In general, weighted adaptiveness consumed a limited number of iteration for convergence with a significant level of accuracy. It also provided robustness against noisy measurements. Aloisio et al. [75] used ordinary least square (OLS) to identify the dynamic properties of a masonry facade under seismic input. The performance of the proposed input-output-based identification technique under operational conditions was investigated to accurately identify different dynamic features, i.e., mode shapes, natural frequencies, and damping factors.

1.2.2.2 Extended Kalman Filter

The Extended Kalman filter (EKF) has been one of the most commonly used time-domain techniques for non-linear state and parameter estimation using vibration data. It approximates the probability density function of the state and parameters in its parametric form conditioned on the sequential measurements. The conditional probability density that provides minimum mean square estimate does not remain Gaussian when either the system or the measurement equation is non-linear. The Extended Kalman filter provides the solution for such systems by linearizing the non-linear equations using Taylor series expansion around its prior states. Then, the KF based prediction-correction procedure is applied to the linearized system.

Yun and Shinozuka [76] developed EKF to identify the parameters of non-linear multiple degree-of-freedom models of an offshore tower, where measurements of all DOF were available. Analytical studies were performed for structural systems based on artificially generated input and output for different conditions. They showed that EKF offered a good estimate even under moderate to the high noise level. A weighted global iteration (WGI) was introduced to stabilize the algorithm within the EKF algorithm [77]. The weight played an important role in tracking the unknown parameters of different structural systems, i.e., MDOF linear system, bilinear hysteretic system, and equivalent linearization of bilinear hysteretic system. Toki et al. [78] augmented the EKF-WGI scheme with additional variables for the ground motion identification. This improvisation of adopting the EKF algorithm was investigated by other researchers for input and parameter estimation, e.g., Ott and Meder [79]. Lin and Zhang [80] also adopted a similar approach for non-linear estimation of SDOF Bouc-Wen system excited by simulated earthquake ground motion. Their algorithm

offered an excellent estimate of non-linear parameters for noise-free measurements. The performance of the algorithm was also satisfactory under moderate noise and low-intensity ground motion. In this context, substructuring was also adopted by many researchers [81]. Their attention was focused on a particular region of the complete structure, which was expected to have damage. The algorithm was illustrated using a shear building model, and the result showed that the EKF-WGI method worked well even for poor initial guesses. However, the EKF-WGI required known input to initiate parameter estimation. To overcome this issue, Wang and Haldar [82] developed a two-stage procedure, which was denoted as iterative least-squares extended Kalman filter with unknown input (ILS-EKF-UI). In the first part of this algorithm, input was estimated, which was used in the next phase to identify the structural parameters. The method was verified using two examples (viz. 6-storey shear building with known and unknown input), which worked satisfactorily with limited measurements. Later, Ling and Haldar [62] and Katkhuda and Haldar [83] improved this algorithm to detect the damage accumulated in the structure, which was assumed to affect stiffness only. The damping in this inverse formulation was characterized as Rayleighs model. Das and Haldar [84] extended the procedure further for three-dimensional systems and demonstrated its performance. Martinez-Flores [85] verified EKF-UI experimentally using a two-dimensional frame. Ma and Ho [86] proposed an inverse method comprising two parts; the extended Kalman filter and a recursive least-squares estimator. It was used to identify the input force acting on a non-linear lumped mass model. They found that the selection of process and measurement noise covariance significantly impacted the estimated parameters. Thus, Yang et al. [87] developed an adaptive tracking technique so that the residual error was contributed only by the noise. This criterion was presented to determine an optimal solution for tracking the changes of structural parameters using constrained optimization. The idea was demonstrated using different cases, e.g., Phase I ASCE structural health monitoring benchmark building, non-linear elastic, and hysteretic system. Simulation results indicated that their approach was particularly suitable for tracking abrupt changes, i.e., damage. This algorithm was also adopted by other researchers for damage quantification [88]. However, above mentioned adaptive tracking required two specific measurement conditions, i.e., (i) measurements in multiple channels and (ii) measurements along the DOFs where the external excitations acted. All these studies had one common ground in their investigation, i.e., the convergence of extended Kalman filter algorithm, which experienced numerical instability in many cases. To address this issue, parameter bounds were introduced by Sen and Bhattacharya [89] that kept them within feasible limits. The algorithm was subsequently used to show its robustness and efficacy in identifying structural damage in a 6-storey shear frame and a 3D space truss. A similar approach was adopted by Li and Wang [90] to identify the parameters of a Bouc-Wen hysteretic system. However, the EKF algorithm and its different variants discussed above were highly dependent on the initial guess of the unknown parameters. Thus, a hybrid extended Kalman filter (HEKF) was proposed by Yun et al. [91] by using genetic algorithm-based optimization within the EKF framework, whose performance was demonstrated using a 3-storey steel frame.

1.2.2.3 Unscented Kalman Filter

Extended Kalman filter uses Taylor series approximation to linearize a non-linear system around its current state. In this process, the series is truncated after the first order term leading to significant numerical error. Besides truncation, estimation of gradient vector in the approximate representation of the Taylor series also contributes to numerical stability and convergence. Thus, the linearization process in the predictor-corrector framework of the Kalman filter is bypassed using the approximate solution of the original non-linear system around its current state. Therefore, a few points are generated around the last estimate using Gaussian assumption, which are called sigma points. The error covariance is minimized using the response at these sigma points in the corrector step, which gives rise to a new and improved algorithm, i.e., the Unscented Kalman filter [92]. In this context, Sitz et al. [93] demonstrated this technique to evaluate simultaneous state and parameter from incomplete measurements of various non-linear dynamical (i.e., Lotka-Volterra, chaotic Lorenz, and stochastic Van-der-pol oscillator) systems with a relatively large magnitude of measurement noise. Besides parameters, unobserved states were also estimated with high accuracy. However, their algorithm depended on the choice of the initial covariance, which was the most critical parameter for the convergence. Pepescu and Wong [94] proved that UKF was significantly superior to the EKF. Mariani and Ghisi [95] also derived a similar conclusion, where EKF and UKF were needed for joint state and parameter estimation of a non-linear system. Wu and Smyth [96] implemented EKF and UKF for non-linear system identification. They also observed that UKF was more accurate than EKF for non-linear systems. Besides accuracy, their study also proved that the UKF algorithm was robust in dealing with measurement noise.

Chatzi and Smyth [97] compared UKF with particle filter where unmeasured state and model parameters of a Bouc-Wen oscillator were used as a reference. They proved that UKF and Gaussian mixture sigma-point particle filter (GMSPPF) were the most efficient algorithm for inverse parameter estimation. Moreover, the computational cost of UKF was considerably lower than other algorithms. The efficiency of the UKF algorithm was further demonstrated for online parameter estimation of non-linear hysteretic systems by Chatzi et al. [98]. The state-space formulation incorporated a Bouc-Wen oscillator with additional polynomial or exponential non-linear terms that were properly weighted throughout the filtering process. An adaptive gain was introduced to tackle the parameter boundaries, and the algorithm was validated using experimental data involving displacement and strain measurements. In this context, it may be noted that UKF offered satisfactory results for systems with degradation and pinching and hence, was more general than EKF or a similar algorithm. To improve its performance further, iterated cubature unscented Kalman filter was developed by combining the unscented transformation with the cubature integration scheme to generate improved sigma point configuration [99]. This research work demonstrated the impact of the cubature scheme on overall efficiency in the presence of noisy measurements. All these improvisations augmented the efficiency of the original UKF algorithm. However, the impact of initial guesses remained a primary factor behind numerical convergence. Thus, to reduce the effect of initial guesses, a Bayesian optimization was proposed to incorporate the level of confidence on the initial guesses [100]. This approach was validated using the shake table test data of a 5-storey shear frame. Cheng and Beker [101] developed a weighted adaptive

constrained unscented Kalman filter (WACUKF) by combining the adaptive evaluation of measurement noise and the sigma point projection strategy for constrained parameters. They used a genetic algorithm to find the correct initial guess and demonstrated its performance using a bi-directional hysteretic system.

1.2.2.4 Ensemble Kalman Filter

The ensemble Kalman filter (EnKF) assimilates measurements sequentially in a Monte Carlo simulation framework. In this process, the actual covariance matrix in the Kalman filter algorithm is replaced by the covariance matrix computed from the ensemble, where the filtering algorithm propagates the samples using the exact non-linear model. Evensen [102] first introduced this method [102] to resolve the issue of poor covariance associated with the EKF. In this proposal, a finite number of Monte Carlo samples of the state vector x_k are propagated in time to estimate the *pdf* of x_k. The performance of this algorithm was demonstrated by Ghanem and Ferro [103] for non-linear systems identification in presence of Gaussian noise. It was illustrated using a 4-storey shear building model with constant stiffness and 5% damping ratio in all modes. The hysteretic behaviour was modelled to identify any change in its parameter, i.e., damage. Both location and time of occurrence of damage were accurately detected in the presence of measurement and modeling noise. A comparison between ensemble and extended Kalman filters was also presented to show the robustness of the EnKF under severe non-linearities. Slika and Saad [104] used EnKF to predict the parameters of a reinforced concrete structure exposed to chloride-induced damage to predict its remaining service life.

1.2.2.5 Particle Filter

In cases of classical non-linear filtering like EKF, the conditional probability density is represented parametrically, e.g., Gaussian *pdf*. Each iteration involves updating the parameters (e.g., mean and covariance) that fully characterize the states. These methods are capable of handling general forms of non-linearities and Gaussian additive noise. In Particle filtering, modeling of conditional probability is straightforward as the filter does not seek an approximate analytical representation of the probability density function in its parametric form. It represents the distribution by a set of samples (i.e., particles) distributed according to the *pdf*. The particle filter propagates a collection of weighted samples so that the particles in each iteration represent the distribution. It is done recursively by changing the state and weight of each particle according to the model-predicted response and measurement. Thus, it directly compares the Kalman-based filters where the estimated state and covariance are updated recursively. However, one critical difference between these algorithms is worth noting. The forecasting involves propagating each sample within the ensemble by integrating the full non-linear model. Therefore, the performance of the filter depends on the style of predicting.

Manohar and Roy [105] investigated different Monte Carlo-based methods to construct the posterior pdf of the augmented state vector based on available information. The *pdf* was evaluated using random samples with associated weights, which were used to compute the desired estimates. The attention was focused on investigating the utility of three different

Monte Carlo filters, namely, a density-based Monte Carlo filter, a bootstrap filter, and a sequential importance-sampling filter. The unknown parameters were treated as the additional dynamic state variables, where two different oscillators were used to verify their efficiency (viz. Duffing and Coulomb oscillators). Nasrellah and Manohar [106] further investigated dynamic state and parameter estimation based on a finite element model in the particle filter algorithm. In this study, non-Gaussian noise was modeled for non-linear systems. They used commercially available FEM software and combined it with a particle filter algorithm in the Matlab platform. A key feature of their method was introducing a dummy independent variable to assimilate the static and dynamic measurements from multiple sensors in a unified manner. They illustrated their proposal using a single-span beam and multi-span masonry arch bridge subjected to diagnostic moving load. The substructuring approach to estimate the hidden state was presented by Radhika and Manohar [107] based on both the Kalman filter and Sequential Monte Carlo filter. They divided the structure into linear and non-linear substructures and estimated the linear part using Kalman filter and the same for the non-linear part using particle filter. It was illustrated using different numerical examples, and the performance was compared with the exact solution and approximate solution, which did not employ sub-structuring. Chatzi and Smyth [108] presented an innovative technique for non-linear, non-Gaussian online state and parameter identification problems in the presence of strong process noise. They proposed a mutation of particles that outperformed both the traditional particle filter and the unscented Kalman filter. Sen and Nagarajaiah [109] used particle-based stochastic filters to localize the acoustic emission sources in plates. The algorithm used flight time measurements of guided waves using triangulation to estimate source coordinates in a Bayesian framework to incorporate material properties, noise measurements, and geometry of the system. Wan et al. [110] proposed a particle filter with unknown input to identify the augmented states, including parameters and unknown excitation. The standard particle filter technique was used to determine the extended states, while the least-square approximation was used to identify the unknown excitation simultaneously.

1.2.3 State Estimation under Unknown Input Force

Besides monitoring and damage prognosis, estimation of unknown external force has remained an active area of research. The identified input enables an assessment of the damage after any extreme events to forecast the remaining life span. In practice, the external force is often kept outside the measurement scheme due to various reasons. Therefore, these forces need to be determined indirectly from the measurements. Thus, accurate characterization of input forces is vital for decision making, e.g., rehabilitation/retrofitting. It leads to a greater reliance on numerical simulation-based analytical models and reduces the need for a costly array of sensors for recording the input/excitation. Due to this reason, there is a constant need to reconstruct the input forces based on the available measurements. Thus, an instrumented structure becomes its load transducer for the estimation of excitation.

The need for input characterization is even more justified as measuring input for every structure is practically impossible. In this context, the identification of ground motion from structural measurement offers a promising alternative. The input ground motion obtained from the structural measurement is less dependent on the assumption and the empirical formulae of the ground motion model [111]. Inspired by these reasons, Lourens et al. [112]

proposed an augmented Kalman filter for joint estimation of input and state. The input force was considered unknown without any regularization. Its applicability was separately demonstrated with the help of laboratory experiments and field tests. A dual implementation of the Kalman filter was proposed to identify the unknown input and states from a linear state-space model [113]. They demonstrated the performance of their method using the simulated response of a high-rise building. This model was further adopted by Maes et al. [114] for joint input and state estimation using noisy data. Gillijns and De Moor [115,116] proposed minimum variance unbiased solution of joint input and state estimation of a linear discrete-time dynamic system in a different approach. It was an extension of Kitanidis [117] proposal for joint input and state estimation. They proposed a minimum variance unbiased estimator as a recursive filter where state and input estimation were interconnected. The resulting filter had the structure of the Kalman filter, except the input was replaced by the optimal estimate at each time step. A modified version of this algorithm was proposed by Song [118] using unscented sigma points for joint input and state estimation of a non-linear system. They conducted an extensive numerical study on linear and non-linear systems to show the robustness of their proposal.

1.3 Objectives

Several identification approaches have been presented in the literature review. In this context, the Kalman filters and their advanced variants for recursive time-domain estimation are more efficient in incorporating measurements. Different identification algorithms are available in the literature based on known inputs, which may not be the case for many structures. Thus, researchers have attempted input identification, which is an advantage for the structures having no option for input measurement. However, most identification algorithms face difficulty in dealing with non-linear systems excited by non-stationary input. Previous studies on hysteretic system identification using Gaussian filtering algorithm were focused on its performance using simulated experiments or small-scale laboratory tests. Synthetic experiments used in these studies considered hypothetical values of hysteretic parameters and other structural properties. Only a few studies were focused on the inverse problem dealing with large structures exhibiting non-linear hysteresis. In particular, the identification of full-scale hysteretic reinforced concrete structure under earthquake excitation needs further attention to study the efficiency of the recursive time marching algorithms. This gap area motivates the author of this thesis to develop different variants of Kalman filters suitable for non-linear system identification of actual structures and subsequently estimate the damage state. With these in view, the primary objectives of this work are discussed below

- In general, recursive inverse problems suffer numerical instabilities while dealing with hysteretic systems, which demands specific measures to avoid computational difficulties. In this work, appropriate bounded input bounded output (i.e., BIBO) properties are introduced to suitably augment the Bouc-Wen model for parameter and input estimation.
- Develop different sigma point generation schemes for constrained minimum variance

unbiased estimation (CMVU) algorithm to study their performance in non-linear system identification. In this format, the parameter bounds and BIBO properties mentioned above are introduced into the sigma points generation scheme.

- Validate the objectives mentioned above numerically using actual hysteretic behaviour obtained from the pseudo-dynamic test of a reinforced concrete frame. This realistic Bouc-Wen model includes degradation and pinching. The synthetic experiment is focused at tuning the identification algorithm for both parameter and input. Furthermore, the study aims to investigate the performance of different sigma point generation schemes.

- Demonstrate the efficiency of the improved CMVU algorithm using experimental results on a full-scale bridge pier specimen. The specimen is exposed to non-stationary excitations, which leads the yielding of reinforcements.

- Obtain the restoring force generated by the non-linear system to evaluate the dissipated hysteretic energy, which is an engineering damage parameter. This hysteretic energy is used to quantify the damage state of the structure that provides the basis for decision-making on rehabilitation/retrofitting.

- Develop a damage estimation framework through a mechanics-based non-linear FE model using a sigma point filter to capture the damage mechanism of a complex system that involves identifying the presence, location, type, and extent of any damage. Apply this condition assessment framework on a bridge pier test data and quantify the in-situ damage using modified Park and Ang damage index.

1.4 Organization of Thesis

This thesis contributes to developing recursive time-domain techniques based on non-linear Kalman filter theory for condition assessment of hysteretic structures. The road map of this thesis starts with the first chapter, which presents the motivation and literature review. The remaining part of this thesis is given below

- The second chapter provides a brief introduction to the development of linear Kalman filter theory. The extension of Kalman filter theory for non-linear systems is discussed in terms of Extended Kalman filter and Unscented Kalman filter. Finally, a comparative study is performed to show the effectiveness of these algorithms using an SDOF hysteretic structural system.

- In Chapter 3, the constrained minimum variance unbiased (CMVU) estimation algorithm has been developed in the light of Bouc-Wen hysteresis for simultaneous parameters and input identification. The performance of the proposed method is discussed with the help of various numerical examples corresponding to different types of Bouc-Wen models attributing degradation and pinching. Further, the applicability of the proposed algorithm is experimentally validated using full-scale test data of a bridge pier.

- The efficiency of the Kalman filter-based algorithm is demonstrated in Chapter 4 for damage assessment of a hysteretic system. First, the constrained iterative unscented Kalman filter is developed for condition assessment of a RC bridge pier using known input. The identified parameters are utilized for damage quantification of the same structure using the Park and Ang damage index.
- Chapter 5 deals with developing a new framework for material level system identification for the condition assessment of reinforced concrete structures using a novel constrained version of the unscented Kalman filtering technique. The proposed algorithm is demonstrated both numerically and experimentally to show its applicability.
- Finally, the salient contributions of this study are concluded in Chapter 6, along with the discussion of possible avenues of future development of this work.

Chapter 2

Kalman Filter

Statistical inference is a popular mathematical tool for decision-making, which is used in different applications. It can be broadly categorized into two types based on probability - Frequentist inference and Bayesian inference. Frequentist derives statistical inference from the random experiment, while Bayesian inference assigns probabilities to any hypothesis. It uses Baye's rule to represent the probability as a degree of belief based on the available evidence. Using this concept, Kalman [119] proposed a new estimation technique that could estimate the underlying probability density of an unknown random variable recursively over time by utilizing a mathematical model of the system and available measurements. Over the years, Kalman Filter has become a benchmark for estimating the state of dynamic systems. It operates in a predictor-corrector framework that does not demand complete past history and evolve in every time as soon as measurements are available. The information gained in successive time steps are incorporated into the latest prediction. It tries to obtain an optimal estimate of variables using the noisy measurement [120]. It has been extensively used in many problems, e.g., robotics (tracking, navigation), environmental simulations, econometrics and others. The Bayesian inference used in Kalman filtering is shown in Fig. 2.1, which has three steps - (1) the prediction is obtained based on initial conditions and mathematical model, (2) the measurements are collected to enhance the prediction confidence, and (3) finally, the corrected optimal estimate is obtained based on the prediction and measurement resulting in an improved outcome.

2.1 Baye's Rule

The Bayesian estimation process starts with a series of observable data that usually comes from the response of a dynamic system. Based on the measurement, the underlying state of a system is estimated, which may not be observable directly. A similar concept can also be applied to estimate the parameters of a system. Usually, this estimation considers both system state and parameters as stochastic entities. Finally, an analytical link is established between the observed data and the system state to be estimated. It provides a unified recursive framework to evaluate the current state in terms of a density function conditioned using the current state and prior observation. Consider a dynamic system whose parameter vector $\mathbf{x}$ is to be estimated from the observation vector $\mathbf{y}$. It is assumed that the random

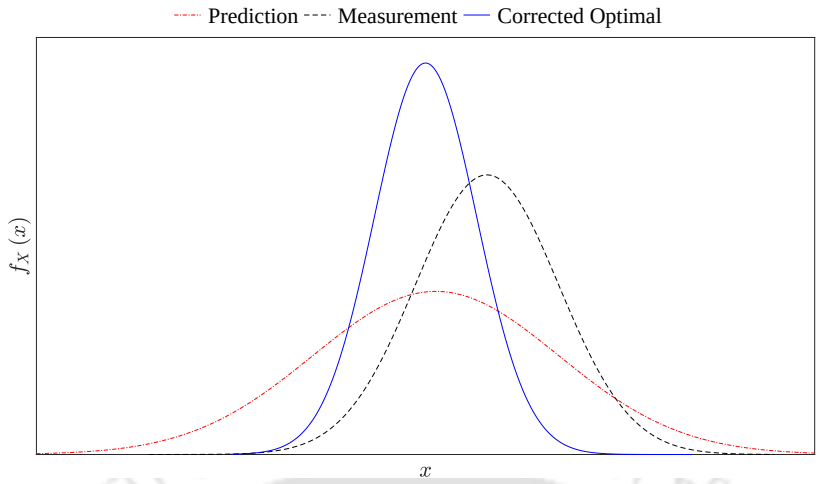

Figure 2.1: Schematic diagram of Bayesian inference

vector $\mathbf{x}$ has a known prior density $p(\mathbf{x})$. Once the value of the parameter $\mathbf{x}$ is known, the statistical properties of $\mathbf{y}$ can be expressed by the likelihood function $p(\mathbf{y}|\mathbf{x})$. As soon as the observations are available, the posterior conditional density can be obtained using Baye's law as follows

$$p(\mathbf{x}|\mathbf{y}) = \frac{p(\mathbf{y}|\mathbf{x})\, p(\mathbf{x})}{p(\mathbf{y})} \tag{2.1}$$

Here, the posterior density $p(\mathbf{x}|\mathbf{y})$ has all the information about $\mathbf{x}$ considering $\mathbf{y}$. The denominator of Eq. 2.1 is just a scalar normalizing constant, which can be obtained as

$$p(\mathbf{y}) = \int p(\mathbf{y}|\mathbf{x})\, p(\mathbf{x})\, d\mathbf{x} \tag{2.2}$$

In general, a statistical model for estimation is defined by the likelihood and posterior where the joint density of parameter and observation can be expressed as follows

$$p(\mathbf{x}, \mathbf{y}) = p(\mathbf{x}|\mathbf{y})\, p(\mathbf{y}) \tag{2.3}$$

In most of the cases, the posterior density in Eq. 2.1 is regarded as the general solution to the estimation problem.

2.1.1 Recursive Bayesian Filtering of Probability Density Functions

Consider a 1^{st} order Markov process whose current state is dependent on the previous state. A discrete random Markov process can be expressed as follows

$$\mathbf{x}_n = \mathbf{f}_{n-1}(\mathbf{x}_{n-1}, \mathbf{u}_n, \mathbf{w}_{n-1}) = \mathbf{f}_{n-1}(\mathbf{x}_{n-1}) + \mathbf{u}_n + \mathbf{w}_{n-1} \tag{2.4}$$

where $\mathbf{x}_n$ is the state vector at time t_n, $\mathbf{f}_n$ is the state transition matrix, which transforms the state from t_{n-1} to t_n and $\mathbf{u}_n$ is the external input, which drives the system dynamics. The process noise $\mathbf{w}$ is an additive zero-mean Gaussian white noise, which represent the part

of the transition function that is not modeled. The objective of the filtering is to estimate the state vector based on the experimental observation $\mathbf{y}_{1:n} = \{\mathbf{y}_1, \mathbf{y}_2 \ldots\ldots\ldots \mathbf{y}_n\}$. The link between the state vector and the observation vector can be expressed through a nonlinear function $\mathbf{h}()$ as follows

$$\mathbf{y}_n = \mathbf{h}_n\left(\mathbf{x}_n\right) + \mathbf{v}_n \tag{2.5}$$

Here, $\mathbf{v}_n$ denotes the additive zero-mean Gaussian white noise associated with the measurement to mimic the actual experimental data. The functions $\mathbf{f}_{n-1}$ and $\mathbf{h}_n$ are considered to be time-independent or changing very slowly, i.e., $\mathbf{f}_{n-1} \approx \mathbf{f}$ and $\mathbf{h}_n \approx \mathbf{h}$. The estimation of $\mathbf{x}_n$ based on the series of measurements $\mathbf{y}_{1:n}$ can be obtained in terms of posterior distribution $\mathbf{p}\left(\mathbf{x}_n|\mathbf{y}_{1:n}\right)$ from Eq.2.1 as follows

$$p\left(\mathbf{x}_n|\mathbf{y}_{1:n}\right) = \frac{p\left(\mathbf{y}_{1:n}|\mathbf{x}_n\right) p\left(\mathbf{x}_n\right)}{p\left(\mathbf{y}_{1:n}\right)} \tag{2.6}$$

Replacing $\{\mathbf{y}_{1:n}\} = \{\mathbf{y}_n, \mathbf{y}_{1:n-1}\}$ in the above equation leads to

$$p\left(\mathbf{x}_n|\mathbf{y}_{1:n}\right) = \frac{p\left(\mathbf{y}_n, \mathbf{y}_{1:n-1}|\mathbf{x}_n\right) p\left(\mathbf{x}_n\right)}{p\left(\mathbf{y}_n, \mathbf{y}_{1:n-1}\right)} \tag{2.7}$$

Using Eq. 2.3 in both numerator and denominator of Eq. 2.7 can be expressed as

$$p\left(\mathbf{x}_n|\mathbf{y}_{1:n}\right) = \frac{p\left(\mathbf{y}_n|\mathbf{y}_{1:n-1}, \mathbf{x}_n\right) p\left(\mathbf{y}_{1:n-1}|\mathbf{x}_n\right) p\left(\mathbf{x}_n\right)}{p\left(\mathbf{y}_n|\mathbf{y}_{1:n-1}\right) p\left(\mathbf{y}_{1:n-1}\right)} \tag{2.8}$$

Applying Baye's rule to $p\left(\mathbf{y}_{1:n-1}|\mathbf{x}_n\right)$ results in the following expression

$$\begin{aligned} p\left(\mathbf{x}_n|\mathbf{y}_{1:n}\right) &= \frac{p\left(\mathbf{y}_n|\mathbf{y}_{1:n-1}, \mathbf{x_n}\right) p\left(\mathbf{x}_n|\mathbf{y}_{1:n-1}\right) p\left(\mathbf{y}_{1:n-1}\right) p\left(\mathbf{x}_n\right)}{p\left(\mathbf{y}_n|\mathbf{y}_{1:n-1}\right) p\left(\mathbf{y}_{1:n-1}\right) p\left(\mathbf{x}_n\right)} \\ &= \frac{p\left(\mathbf{y}_n|\mathbf{y}_{1:n-1}, \mathbf{x}_n\right) p\left(\mathbf{x}_n|\mathbf{y}_{1:n-1}\right)}{p\left(\mathbf{y}_n|\mathbf{y}_{1:n-1}\right)} \\ &= \frac{p\left(\mathbf{y}_n|\mathbf{x}_n\right) p\left(\mathbf{x}_n|\mathbf{y}_{1:n-1}\right)}{p\left(\mathbf{y}_n|\mathbf{y}_{1:n-1}\right)} \end{aligned} \tag{2.9}$$

where $p\left(\mathbf{y}_n|\mathbf{y}_{1:n-1}, \mathbf{x}_n\right) \approx p\left(\mathbf{y}_n|\mathbf{x}_n\right)$ as the observation at t_n does not depends on same at t_{n-1}. To develop a recursive framework, the Chapman-Kolmogorov equation [121] is used as a link between the prior density and posterior density as follows

$$\begin{aligned} p\left(\mathbf{x}_n|\mathbf{y}_{1:n-1}\right) &= \int p\left(\mathbf{x}_n|\mathbf{x}_{n-1}, \mathbf{y}_{1:n-1}\right) p\left(\mathbf{x}_{n-1}|\mathbf{y}_{1:n-1}\right) d\mathbf{x}_{n-1} \\ &= \int p\left(\mathbf{x}_n|\mathbf{x}_{n-1}\right) p\left(\mathbf{x}_{n-1}|\mathbf{y}_{1:n-1}\right) d\mathbf{x}_{n-1} \end{aligned} \tag{2.10}$$

In the above expression $p\left(\mathbf{x}_n|\mathbf{x}_{n-1}\right)$ is replaced by $p\left(\mathbf{x}_n|\mathbf{x}_{n-1}, \mathbf{y}_{1:n-1}\right)$ as the predictive density $p\left(\mathbf{x}_n|\mathbf{x}_{n-1}\right)$ defined by Eq. 2.5 does not depend on the observation $\mathbf{y}_{1:n-1}$. Now, the recursive link is established between the previous posterior density function and the current posterior density function with the help of Eq. 2.9 and Eq. 2.10. This recursive framework produces successive posterior density function based on the current observation. It has been

shown that the recursive Bayesian solution can be easily inferred using this chain rule of the probability density function. However, direct application of the above method is difficult for most practical problems as the optimal solution demands parametric multi-dimensional integration, which is often impractical for large problems. This motivates the researchers to develop various simplification/approximations. One of the efficient solutions is Kalman filtering, which is described in the next section.

2.2 Kalman Filter

The Kalman filter [122] involves strong assumptions, which simplify the optimal Bayesian solution into a sequence of algebraic operations with matrices. The exact estimate of $p(\mathbf{x}_n|\mathbf{y}_{1:n})$ can be found when all these requirements are fulfilled. It estimates the statistical properties of the optimal state in terms of mean and covariance in a recursive framework. The additional assumptions associated with the Kalman filter are

- The state transition matrix $\mathbf{f}$ in Eq. 2.4 is a linear function $\mathbf{x}$ and $\mathbf{w}$.
- The observation model $\mathbf{h}$ in Eq. 2.5 is a linear function $\mathbf{x}$ and $\mathbf{v}$.
- The measurement noise $\mathbf{v}$ is an unwanted disturbance that corrupts the structural response recorded by a sensor. The sources of this disturbance are (i) Electrical interference within the sensor architecture, (ii) wear and tear of the sensor, and (iii) physical obstructions in the communication between the sensor and the recorder. It is often assumed to be Normally distributed with zero mean and known covariance $\mathbf{R}$, i.e., $\mathbf{v} \sim N(0, \mathbf{R})$.
- The process noise $\mathbf{w}$ is introduced in the formulation cater modeling approximations. For example, the baseline model used in the model-based identification approach may not be the actual representation of the phenomenological behavior of the structure. Unlike measurement noise, quantification of process noise is complex. It is assumed to be a Normally distributed with zero mean and known covariance $\mathbf{Q}$, i.e., $\mathbf{w} \sim N(0, \mathbf{Q})$ for simplicity.

Also, the initial state probability density function is Gaussian. It can be proved that if the above assumptions hold, $p(\mathbf{x}_n|\mathbf{y}_{1:n})$ is also Gaussian for all $t > 0$. With these in view, the estimation problem is defined with the following equations

$$\mathbf{x}_{k+1} = \mathbf{A}_k\mathbf{x}_k + \mathbf{B}_k\mathbf{u}_k + \mathbf{w}_k \tag{2.11a}$$

$$\mathbf{y}_{k+1} = \mathbf{C}_{k+1}\mathbf{x}_{k+1} + \mathbf{v}_{k+1} \tag{2.11b}$$

where $\mathbf{x}_{k+1}$ and $\mathbf{B}_k$ represents the state vector and transition matrix. $\mathbf{B}_k$ is the influence matrix associated with the deterministic input vector $\mathbf{u}_k$, and $\mathbf{w}_k$ is the process noise vector, accounting for model uncertainty. Further, for the measurement $\mathbf{y}_k$, $\mathbf{C}_{k+1}$ is the observation matrix that maps the actual state with the observed state while $\mathbf{v}_k$ represents the measurement uncertainty.

As stated earlier, Kalman filtering is a predictor-corrector algorithm, which can be simplified into three steps (i) initialization, (ii) prediction and (iii) correction. A brief description of these three steps are given below

- **Initialization**
  Estimate initial state $\hat{\mathbf{x}}_0^+$ and covariance matrix $\hat{\mathbf{P}}_{x,0}^+$

$$\hat{\mathbf{x}}_0^+ = \mathbb{E}\left[\mathbf{x}_0\right], \tag{2.12}$$
$$\hat{\mathbf{P}}_{x,0}^+ = \mathbb{E}\left[\left(\mathbf{x}_0 - \hat{\mathbf{x}}_0^+\right)\left(\mathbf{x}_0 - \hat{\mathbf{x}}_0^+\right)^T\right] \tag{2.13}$$

- **Prediction**
  A prior estimate of the state can be made by computing the expected value of $\mathbf{x}_{k+1}$ conditioned by the measurements upto k^{th} time step i.e.

$$\hat{\mathbf{x}}_{k+1}^- = \mathbb{E}\left[\mathbf{x}_{k+1}\left|\mathbf{y}_1, \mathbf{y}_2, ...\mathbf{y}_k\right.\right] = \mathbf{A}_k\hat{\mathbf{x}}_k^+ + \mathbf{B}_k\mathbf{u}_k \tag{2.14}$$

  It is worth mentioning that the superscript '+' denotes the optimal estimate of mean and covariance at any time step whereas superscript '-' represents the same for the prediction step. Similarly, the prior state covariance matrix is obtained by taking the expectation of the estimation error, which is given by

$$\hat{\mathbf{P}}_{\mathbf{x},k+1}^- = \mathbb{E}\left[\left(\mathbf{x}_{k+1} - \hat{\mathbf{x}}_{k+1}^-\right)\left(\mathbf{x}_{k+1} - \hat{\mathbf{x}}_{k+1}^-\right)^T\left|\mathbf{y}_1, \mathbf{y}_2, ...\mathbf{y}_k\right.\right] = \mathbf{A}_k\hat{\mathbf{P}}_{x,k}^-\mathbf{A}_k^T + \mathbf{Q}_k \tag{2.15}$$

  The measurements from the predicted state can be expressed using the following form

$$\hat{\mathbf{y}}_{k+1}^- = \mathbb{E}\left[\mathbf{y}_{k+1}\left|\mathbf{y}_1, \mathbf{y}_2, ...\mathbf{y}_k\right.\right] = \mathbf{C}_{k+1}\hat{\mathbf{x}}_{k+1}^- \tag{2.16}$$

- **Correction (upon arrival of measurement at time $k+1$)**
  The expression for Kalman gain matrix $\mathbf{K}$ at time t_{k+1} can be expressed as

$$\mathbf{K}_{k+1} = \hat{\mathbf{P}}_{\mathbf{x},k+1}^-\mathbf{C}_{k+1}^T\left(\mathbf{C}_{k+1}\hat{\mathbf{P}}_{\mathbf{x},k+1}^-\mathbf{C}_{k+1}^T + \mathbf{R}_{k+1}\right)^{-1} \tag{2.17}$$

  The posterior state $\hat{\mathbf{x}}_{k+1}^+$ and the covariance $\hat{\mathbf{P}}_{\mathbf{x},k+1}^+$ are estimated using the Kalman gain matrix $\mathbf{K}_{k+1}$ and recorded measurement $\mathbf{y}_{k+1}$ as follows

$$\hat{\mathbf{x}}_{k+1}^+ = \mathbb{E}\left[\mathbf{x}_{k+1}\left|\mathbf{y}_1, \mathbf{y}_2, ...\mathbf{y}_{k+1}\right.\right] = \hat{\mathbf{x}}_{k+1}^- + \mathbf{K}_{k+1}\left(\mathbf{y}_{k+1} - \hat{\mathbf{y}}_{k+1}^-\right) \tag{2.18a}$$
$$\hat{\mathbf{P}}_{\mathbf{x},k+1}^+ = \mathbb{E}\left[\left(\mathbf{x}_{k+1} - \hat{\mathbf{x}}_{k+1}^+\right)\left(\mathbf{x}_{k+1} - \hat{\mathbf{x}}_{k+1}^+\right)^T\left|\mathbf{y}_1, \mathbf{y}_2, ...\mathbf{y}_{k+1}\right.\right]$$
$$= \left(\mathbf{I} - \mathbf{K}_{k+1}\mathbf{C}_{k+1}\right)\hat{\mathbf{P}}_{x,k+1}^-\left(\mathbf{I} - \mathbf{K}_{k+1}\mathbf{C}_{k+1}\right)^T + \mathbf{K}_{k+1}\mathbf{R}_{k+1}\mathbf{K}_{k+1}^T \tag{2.18b}$$

2.3 Extended Kalman Filter

The Kalman filter discussed in the previous sub-section faces difficulty in dealing with non-linear dynamic systems. It may have either state or measurement or both characterized by non-linear relations. The time evolution of the state probability distribution in the case of a non-linear system can be addressed by the extended Kalman filter (EKF) [123]. In this approach, the non-linear state-space model is linearized around its latest estimated state, using a first-order Taylor series approximation. Then, the prediction-correction procedure

proposed in the Kalman filter is adopted. The posterior estimate derived in one step is used as the reference for the next time step. Thus, the discrete-time state-space representation of the non-linear dynamic system is expressed as

$$\mathbf{x}_{k+1} = \mathbf{f}_k\left(\mathbf{x}_k, \mathbf{u}_k\right) + \mathbf{w}_k \tag{2.19a}$$
$$\mathbf{y}_{k+1} = \mathbf{g}_{k+1}\left(\mathbf{x}_{k+1}, \mathbf{u}_{k+1}\right) + \mathbf{v}_{k+1} \tag{2.19b}$$

where $\mathbf{f}_k\left(.,.\right)$ and $\mathbf{g}_{k+1}\left(.,.\right)$ are the non-linear vector-valued state and measurement function, respectively. The 1^{st} order Taylor series expansion of Eq. 2.19a about the current state $\hat{\mathbf{x}}_k^+$ can be expressed as

$$\mathbf{x}_{k+1} = \left[\mathbf{f}_k\left(\hat{\mathbf{x}}_k^+, \mathbf{u}_k\right) + \left.\frac{\partial \mathbf{f}_k\left(\mathbf{x}, \mathbf{u}_k\right)}{\partial \mathbf{x}^T}\right|_{\mathbf{x}=\hat{\mathbf{x}}_k^+}\left(\mathbf{x}_k - \hat{\mathbf{x}}_k^+\right) + ...\right] + \mathbf{w}_k \tag{2.20a}$$
$$\approx \mathbf{A}_k\mathbf{x}_k + \tilde{\mathbf{u}}_k + \mathbf{w}_k \tag{2.20b}$$

where $\mathbf{A}_k = \left.\frac{\partial \mathbf{f}_k(\mathbf{x},u_k)}{\partial \mathbf{x}^T}\right|_{\mathbf{x}=\hat{\mathbf{x}}_k^+}$ and $\tilde{\mathbf{u}}_k = \mathbf{f}_k\left(\hat{\mathbf{x}}_k^+, \mathbf{u}_k\right) - \mathbf{A}_k\hat{\mathbf{x}}_k^+$. Using this 1^{st} order approximation, the prior estimate of the state vector and covariance matrix are obtained as

$$\hat{\mathbf{x}}_{k+1}^- \cong \mathbf{f}_k\left(\hat{\mathbf{x}}_k^+, \mathbf{u}_k\right) \tag{2.21a}$$
$$\hat{\mathbf{P}}_{x,k+1}^- \cong \mathbf{A}_k\hat{\mathbf{P}}_{\mathbf{x},k}^-\mathbf{A}_k^T + \mathbf{Q}_k \tag{2.21b}$$

The non-linear measurement equation is also linearized with respect to the reference point for the prior. At this point, the best available estimate of the state is given by

$$\mathbf{y}_{k+1} = \left[\mathbf{g}_{k+1}\left(\hat{\mathbf{x}}_{k+1}^-, \mathbf{u}_{k+1}\right) + \left.\frac{\partial \mathbf{g}_{k+1}\left(\mathbf{x}, \mathbf{u}_{k+1}\right)}{\partial \mathbf{x}^T}\right|_{\mathbf{x}=\hat{\mathbf{x}}_{k+1}^-}\left(\mathbf{x}_{k+1} - \hat{\mathbf{x}}_{k+1}^-\right) + ..\right] + \mathbf{v}_{k+1}$$
$$\approx \mathbf{C}_{k+1}\mathbf{x}_{k+1} + \tilde{\mathbf{z}}_{k+1} + \mathbf{v}_{k+1} \tag{2.22}$$

where $\mathbf{C}_k = \left.\frac{\partial \mathbf{g}_{k+1}(\mathbf{x},\mathbf{u}_{k+1})}{\partial \mathbf{x}^T}\right|_{\mathbf{x}=\hat{\mathbf{x}}_{k+1}^-}$ and $\tilde{\mathbf{z}}_{k+1} = \mathbf{g}_{k+1}\left(\hat{\mathbf{x}}_{k+1}^-, \mathbf{u}_{k+1}\right) - \mathbf{C}_{k+1}\hat{\mathbf{x}}_{k+1}^-$. After linearization of both state and measurement equation, the linear Kalman filter theory presented in the previous section can be applied to estimate the optimal state of the non-linear system.

2.4 Unscented Kalman Filter

The Kalman filter algorithm attempts to propagate the mean and covariance using time and measurement updates. If the system is linear, then the mean and covariance can be updated using the Kalman filter. If the system is non-linear, then the mean and covariance are approximately updated with the extended Kalman filter described in the previous subsection. To address the limited 1^{st} order accuracy of mean and covariance resulting from the truncated Taylor-series approximation in EKF, the unscented transform has been proposed in the literature [92]. Unlike the extended Kalman filter based on linearization, UKF uses the actual non-linear model and approximately estimates the Gaussian distribution describing the state variable. To do so, UKF generates several sampling points (i.e. sigma points)

around the current state based on its covariance. Then, these points are explicitly propagated through the non-linear equations to get more accurate estimates of the mean and covariance. At time $t = 0$, the estimate of the state and corresponding covariance matrix are provided to the algorithm such that

$$\hat{\mathbf{x}}_0^+ = \mathbb{E}\left[\mathbf{x}_0\right], \tag{2.23a}$$

$$\hat{\mathbf{P}}_{x,0}^+ = \mathbb{E}\left[\left(\mathbf{x}_0 - \hat{\mathbf{x}}_0^+\right)\left(\mathbf{x}_0 - \hat{\mathbf{x}}_0^+\right)^T\right] \tag{2.23b}$$

In this thesis, unscented sigma points are used to obtain the mean and covariance of the state that undergoes a non-linear transformation (e.g., a detailed FE model). This concept of sigma point generation to estimate the statistical moments was first introduced by Julier and Uhlmann [124] and became popular due to its accuracy and convenience. At any time step k, $2n+1$ number (n is the total number of states) of unscented sigma points (i.e. $\mathbf{\Psi}_k^{\mathbf{x}}$) are generated from the estimates of $\hat{\mathbf{x}}_k^-$ and covariance $\mathbf{P}_k^-$ i.e.

$$\mathbf{\Psi}_k^{\mathbf{x}} = \left[\begin{array}{ccc} \hat{\mathbf{x}}_k^- & \hat{\mathbf{x}}_k^- + \left\{\sqrt{(n+\lambda)\,\mathbf{P}_{\mathbf{x},k}^-}\right\}_i & \hat{\mathbf{x}}_k^- - \left\{\sqrt{(n+\lambda)\,\mathbf{P}_{\mathbf{x},k}}\right\}_i \end{array}\right] \tag{2.24}$$

In the above equation, $\left\{\sqrt{(n+\lambda)\,\mathbf{P}_{\mathbf{x},k}^-}\right\}_i$ is the i^{th} column of the matrix. The scaling parameter λ is defined as $\lambda = \alpha^2\,(n+\kappa) - n$. The spread of the sigma points is determined by the user-defined parameter α, whose value is less than one i.e. $0 \leq \alpha \leq 1$. At the same time, κ is a secondary scaling parameter usually set to $(3-n)$ [96]. The corresponding weights for the mean ($\mathbf{W}^m$) and covariance ($\mathbf{W}^c$) are given by

$$W_0^m = \frac{\lambda}{n+\lambda} \tag{2.25a}$$

$${W_0}^c = \frac{\lambda}{n+\lambda} + \left(1 - \alpha^2 + \rho\right) \tag{2.25b}$$

$$\mathbf{W}_i^m = \mathbf{W}_i^c = \frac{1}{2\,(n+\lambda)} \qquad i = 1, 2, 3.....2n \tag{2.25c}$$

These sigma points are transmitted through the prediction equations to obtain the new sigma points using the following expression

$$\mathbf{\Psi}_{k+1}^{\mathbf{x}} = \mathbf{f}\left(\mathbf{\Psi}_{\mathbf{k}}^{\mathbf{x}}, \mathbf{u}_k\right) + \mathbf{w}_k \tag{2.26}$$

These predicted sigma points allow for updating the FE model parameters in terms of statistical mean $\hat{\mathbf{x}}_{k|k-1}$ and covariance $\mathbf{P}_{k|k-1}^{\mathbf{x}}$ using the following equations

$$\hat{\mathbf{x}}_{k+1}^- = \sum_{i=1}^{2n+1} \mathbf{W}_i \mathbf{\Psi}_{i,k+1}^{\mathbf{x}} \tag{2.27a}$$

$$\mathbf{P}_{\mathbf{x},k+1}^- = \sum_{i=1}^{2n+1} \mathbf{W}_i \left(\mathbf{\Psi}_{i,k+1}^{\mathbf{x}} - \hat{\mathbf{x}}_{k+1}^-\right)\left(\mathbf{\Psi}_{i,k+1}^{\mathbf{x}} - \hat{\mathbf{x}}_{k+1}^-\right)^T + \mathbf{Q}_{k+1} \tag{2.27b}$$

where $\mathbf{W}$ is the weight vector associated with the sigma points. Here, it may be noted that the predicted sigma points are used to estimate the statistical mean $\hat{\mathbf{y}}_{k|k-1}$ and covariance $\mathbf{P}^{y}_{k|k-1}$ of the observation vector $\mathbf{y}_k$ as

$$\begin{aligned} \boldsymbol{\Omega}_{k+1} &= \mathbf{g}\left(\boldsymbol{\Psi}^{\mathbf{x}}_{k+1}, \mathbf{u}_{k+1}\right) + \mathbf{v}_{k+1} \\ \hat{\mathbf{y}}_{k+1} &= \sum_{i=1}^{2n+1} \mathbf{W}_i \boldsymbol{\Omega}_{i,k+1} \qquad (2.28a) \\ \mathbf{P}^{-}_{\mathbf{y},k+1} &= \sum_{i=0}^{2n+1} \mathbf{W}_i \left(\boldsymbol{\Omega}_{i,k+1} - \hat{\mathbf{y}}_{k+1}\right)\left(\boldsymbol{\Omega}_{i,k+1} - \hat{\mathbf{y}}_{k+1}\right)^T + \mathbf{R}_{k+1} \qquad (2.28b) \end{aligned}$$

Once the moments of the state and measurement vectors are obtained, Kalman gain matrix ($\mathbf{K}_k$) is evaluated by minimizing the mean square error between the estimated measurement ($\hat{\mathbf{y}}_{k+1}$) and the actual measurement ($\mathbf{y}_{k+1}$) [124] i.e.

$$\mathbf{K}_k = \mathbf{P}^{-}_{\mathbf{xy},k+1}\left(\mathbf{P}^{-}_{\mathbf{y},k+1}\right)^{-1} \qquad (2.29)$$

where $\mathbf{P}_{\mathbf{xy},k+1}$ represents the cross-covariance matrix between the parameters and the measurements, which is given by the following expression

$$\mathbf{P}^{-}_{\mathbf{xy},k+1} = \sum_{i=1}^{2n+1} \mathbf{W}_i \left(\boldsymbol{\Psi}_{i,k+1} - \hat{\mathbf{x}}^{-}_{k+1}\right)\left(\boldsymbol{\Omega}_{i,k+1} - \hat{\mathbf{y}}_{k+1}\right)^T \qquad (2.30)$$

Finally, the updated model parameters ($\mathbf{x}_k$) and their associated covariance ($\mathbf{P}^{\mathbf{x}}_k$) are obtained from the following expressions

$$\begin{aligned} \hat{\mathbf{x}}^{+}_{k+1} &= \hat{\mathbf{x}}^{-}_{k+1} + \mathbf{K}_k\left(\mathbf{y}_k - \hat{\mathbf{y}}_{k+1}\right) \qquad (2.31a) \\ \mathbf{P}^{+}_{\mathbf{x},k+1} &= \mathbf{P}^{-}_{\mathbf{x},k+1} + \mathbf{K}_k \mathbf{P}^{-}_{\mathbf{y},k+1} \mathbf{K}^T_k \qquad (2.31b) \end{aligned}$$

The flow chart of the UKF algorithm is shown in Fig. 2.2 below.

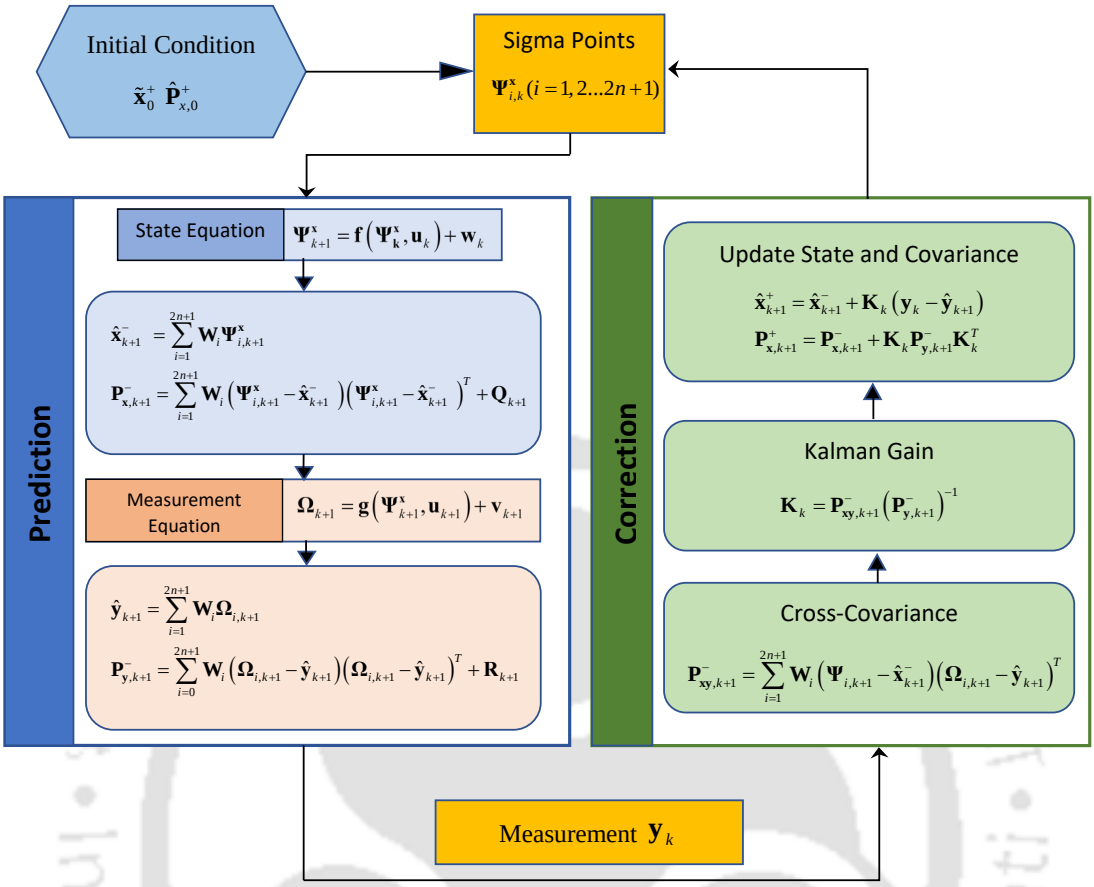

Figure 2.2: Flow chart of UKF

2.5 Joint State and Parameter Estimation

The mathematical frameworks presented above can be used for estimating the unknown parameters of a non-linear model. The unknown parameters are modeled as random variables to estimate the mean and variance of the parameters using the available set of measurements. To evaluate them, the parameters are augmented to the state vector whose differentiation with respect to time will be zero (i.e., time-invariant). Consider the state-space model with state x and parameter θ to explain this concept. The extended state vector for this system can be written as $\mathbf{Z} = \begin{bmatrix} x & \theta \end{bmatrix}^T$. The expression for augmented state-space is represented as

$$\dot{\mathbf{Z}} = \begin{bmatrix} \dot{x} \\ \dot{\theta} \end{bmatrix} = \begin{bmatrix} f(x, \theta, u) \\ 0 \end{bmatrix} \tag{2.32}$$

where $f(.)$ is the non-linear function while u denotes the input acting on the system. With this modification, the measurement equation becomes

$$y = h(\mathbf{Z}, u) + v \tag{2.33}$$

In the above equation, $h(.)$ represents the non-linear observation function with measurement noise v. This modification allows any non-linear Kalman filter technique to update recur-

sively the mean vector and covariance matrix of the parameter θ recursively. An example is presented in the following subsection to show the application of the Kalman filter for parameter estimation of a non-linear system.

2.5.1 Joint State and Parameter Estimation of a Non-linear System

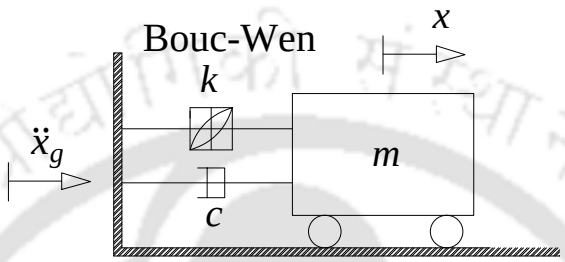

Figure 2.3: SDOF Bouc-Wen system

In this section, the performance of the Kalman filter has been verified for the joint state and parameter estimation of a hysteretic system. A single degree of freedom Bouc-Wen [125] hysteretic system is adopted for the numerical study as shown in Fig. 2.3. The equation of motion of this system can be expressed as

$$m\ddot{x}(t) + c\dot{x}(t) + kz(t) = -m\ddot{x}_g(t) \tag{2.34}$$

where $z(t)$ is the non-observable state of the Bouc-Wen model given by the following expression

$$\dot{z} = \dot{x} - \beta|\dot{x}||z|^{n-1}z - \gamma\dot{x}|z|^n \tag{2.35}$$

In the above equation, overdot signifies the derivative with respect to time. The parameter set $\{A, \beta, \gamma, n\}$ controls the overall configuration (i.e. shape and size) of the hysteresis loops. The system parameters used to simulate the response are $m = 1$ kg, $c = 0.3$ Ns/m, $k = 9$ N/m, $\beta = 2$, $\gamma = 1$, $n = 2$. To generate the responses, recorded time-history of ChiChi earthquake ground motion is applied to the oscillator (refer Fig. 2.4). The duration of the earthquake is 40 s with a sampling frequency of 250 Hz. A white noise having 2% RMS value (i.e. noise to signal ratio) is superimposed to the acceleration response to simulate the measurement noise. The system responses (i.e. displacement, velocity, and acceleration) are obtained by solving the differential (i.e., Eq. 2.34) using the 4^{th} order Runge-Kutta integration method. For identification, the extended state vector is defined as

$$\begin{aligned}\mathbf{X} &= \begin{bmatrix} x & \dot{x} & z & c & k & \beta & \gamma & n \end{bmatrix} \\ &= \begin{bmatrix} x_1 & x_2 & x_3 & x_4 & x_5 & x_6 & x_7 & x_8 \end{bmatrix}\end{aligned} \tag{2.36}$$

Thus, the state-space formulation of this non-linear hysteretic system can be expressed using Eq. 2.35 and Eq. 2.36 as follows

$$\dot{\mathbf{X}} = \begin{bmatrix} x_2 \\ -\ddot{x}_g - (x_2 x_4 + x_3 x_5)/m \\ x_2 - x_6 |x_2| |x_3|^{x_8 - 1} - x_7 x_2 |x_3|^{x_8} \\ 0 \\ 0 \\ 0 \\ 0 \\ 0 \end{bmatrix} \tag{2.37}$$

The measurement equation of the system for acceleration response can be expressed as

$$y = -(c\dot{x} + kz)/m + v \tag{2.38}$$

$$= -(x_2 x_4 + x_3 x_5)/m + v \tag{2.39}$$

The mass of the system is assumed to be known and the other parameters are estimated using both EKF and UKF algorithms. The initial guess for the unknown system parameters are $c = 0.2$ Ns/m, $k = 5$ N/m, $\beta = 0$, $\gamma = 0.5$, $n = 1$. The time histories of the estimated state vector (i.e. displacement, velocity, and acceleration) of the Bouc-Wen system obtained using both UKF and EKF are shown in Fig. 2.5. Although both EKF and UKF estimate the velocity $x(t)$ and non-observable state $z(t)$ with a satisfactory level of accuracy, there is considerable drift observed in the EKF estimate of displacement [i.e. $x(t)$]. Similarly, The identified parameters using both the EKF and UKF are shown in Fig. 2.6. A comparison of the final estimated values using the EKF and the UKF methods is shown in Table 2.1 along with their respective relative percentage errors. It is observed from this table that the UKF tracks the parameters more accurately than EKF, which can be verified from the estimated relative percentage error. For example, the percentage errors obtained using EKF for the parameters β and n are significantly higher than to UKF. In general, both these algorithm can track the state and parameters of the non-linear system in which UKF has a considerable advantage.

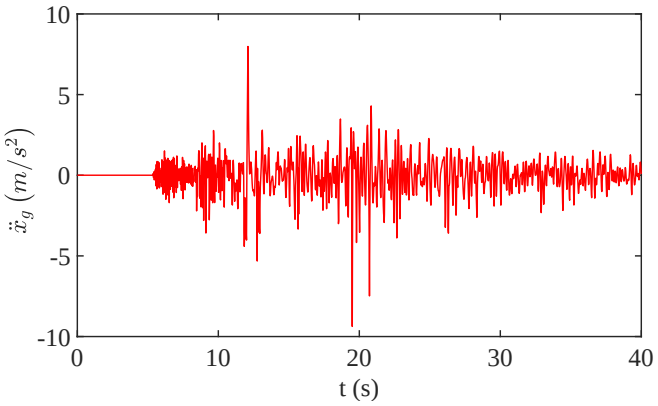

Figure 2.4: ChiChi earthquake

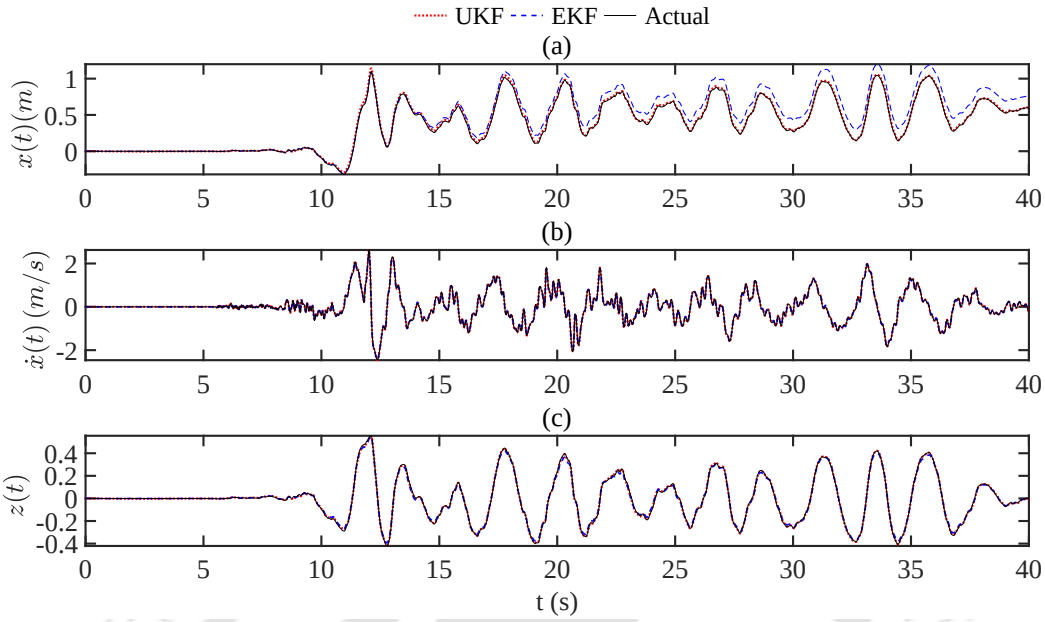

Figure 2.5: State estimation of non-linear Bouc-Wen system; (a) displacement $x(t)$, (b) velocity $\dot{x}(t)$, and (c) hysteretic displacement $z(t)$

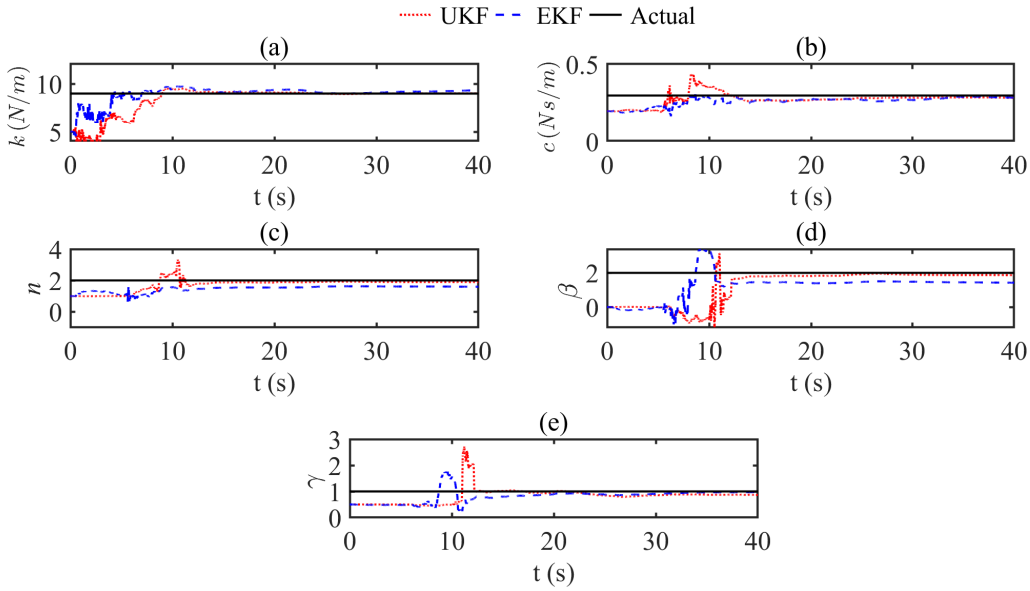

Figure 2.6: Convergence plot for estimated parameters of Bouc-Wen model; (a) initial stiffness k, (b) damping c, (c) parameter n, (d) parameter β, and (e) parameter γ

Table 2.1: Estimated parameters of Bouc-Wen model

Technique	k (N/m)	c (Ns/m)	β	γ	n
Exact	9	0.3	2	1	2
UKF	9.02(0.2%)	0.285(5%)	1.89(5.5%)	0.86(14%)	1.86(7%)
EKF	9.31(3.4%)	0.286(4%)	1.59(20%)	0.88(12%)	1.42(29%)

NB: Percentage error is mentioned within the parenthesis.

2.6 Summary

In this chapter, Kalman filtering techniques have been discussed with examples. It is primarily used for recursive estimation of the unknown state of a system in the probabilistic sense systematically using an underlying mathematical model and measurement. Kalman filter provides the optimal state estimate of a linear system under the assumption that both process and measurement noises are uncorrelated zero-mean Gaussian white noise. To overcome the assumption of a linear system, EKF uses Taylor Series approximation around the mean and then use it for prediction purpose. Due to 1^{st} order truncation of Taylor series, the prediction accuracy is sometimes affected. Unlike EKF, UKF utilizes carefully generated sample points around the current mean and uses them to propagate the non-linearity through the actual system equation. These two non-linear filters' performance has been presented for the joint state and parameter estimation of a Bouc-Wen hysteretic system. The results show that the UKF produces better estimates of states and parameters compared to the EKF.

Chapter 3

Constrained Minimum Variance Unbiased Estimator

3.1 Overview

Non-linear hysteretic behaviour is often encountered by designers in structural dynamics. When a system is subjected to severe loading, the damage is incurred in the form of cracks and/or yielding of material, which often leads to hysteretic behaviour. In general, hysteresis is manifested as a memory-based relationship between the input force acting on a system and its output. Due to its hereditary nature, the dynamic state of a system not only depends on the instantaneous values of its state variables but also on its past. Owing to this behaviour, modelling and identifying the non-linear hysteretic system continue to be one of the challenging problems in structural health monitoring. Besides health monitoring, real-time identification of the restoring force is an inevitable part of any close loop structural control algorithm [126]. Consequently, numerous attempts have been made to model the hysteretic behaviour and to identify its properties from the measured time histories [126–130].

Among different identification algorithms, the recursive time-domain estimation techniques are more efficient in incorporating measurements. Commonly used time-domain methods for non-linear system identification are least-square estimation (LSE) [131–133], extended Kalman filter (EKF) [77, 134–136] and particle filter [137, 138]. LSE is based on the minimization of error between the estimated and simulated responses, which requires many measurement channels. But in practice, it is difficult to install an extensive array of sensors to measure input and output in all degrees of freedom. For non-linear system identification, EKF is a popular technique that circumvents non-linear state and observation equations by linearizing it with the help of the Taylor series expansion. However, derivation of the gradient vector for a complex structural system is a difficult task. Moreover, linearization itself introduces significant error, which can lead to inaccurate system identification. Kalman filter based approach also assumes model and measurement errors to be Gaussian. In this context, particle filter (PF) can handle non-linear system identification problems more comprehensively by relaxing the assumption of Gaussian uncertainty associated with the measurement [139]. In this simulation-based technique, many samples are generated, which imposes a higher computational cost for large dimensional problems. To address this

issue, Julier and Uhimann [140] proposed as Unscented Kalman filter (UKF), which utilized sigma points to approximate the Gaussian distribution of the state variables accurately up to 3^{rd}-order of non-linearity [96]. Chatzi and Smyth [97] compared UKF and PF for parameter estimation of a time-invariant 3-DOF hysteretic structural system under known excitation. They observed that UKF was computationally efficient for real-time applications; however, PF provided a more accurate estimation of the structural parameters. Further, Erazo and Nagarajaiah [141] proposed the UKF-Markov Chain Monte Carlo (MCMC) method to overcome the rank deficiency of the inverse problem. They validated their technique using shake table test data, where bi-linear hysteretic model was characterized the non-linearity. Erazo and Nagarajaiah [142] also explored UKF to identify the hysteresis of a negative stiffness device, both numerically and experimentally. Recently, Astroza et al. [143] conducted a comparative study of UKF, EKF and iterated-EKF in terms of convergence, accuracy, robustness, and computational demand for non-linear finite element model updating. They concluded that UKF out-performed the other two techniques. Over the years, similar observations have been reported in the literature [94, 96, 144, 145].

However, the optimal performance of any filtering-based identification algorithm depends on the prior information of the system inputs. Usually, in the absence of known system input, a stationary Gaussian white noise model is assumed. But this assumption may not provide optimal estimation in the case of a structure subjected to non-stationary excitation. This issue can be solved by recursively updating the input and subsequently supplying it to the filtering algorithm, which leads to the development of simultaneous input and state estimation. Kitanidis [117] introduced a minimum variance state estimation filter without any assumption on input.

Further, Gillijns and De Moor [116] provided minimum variance unbiased estimation of input and state of a linear discrete-time dynamic system. Lourens et al. [112] successfully implemented a similar filter for joint input-state estimation using both experimental and numerical results. An augmented Kalman filter (AKF) was developed by Lourens et al. [146] to estimate the state and the unknown input. However, a significant drawback of the AKF algorithm was that the estimated input contained spurious low-frequency components. An alternate solution for joint input and parameter estimation was developed by Zhang et al. [147], who minimized the square of the distance between the measurements and the model responses. They utilized the virtual distortion method (VDM) to make it computationally efficient and identified any damage related changes in the mass and stiffness. Neats et al. [148] modified augmented discrete Kalman filter for joint parameter and input estimation and validated it experimentally. Later, Azam et al. [149] combined UKF with dual Kalman filter [113] to estimate the input, which UKF used for parameter estimation. Pan et al. [150] proposed a general extended Kalman filter algorithm for unknown input to tackle the problem of rank deficiency in case of limited measurements. They validated their method using the ASCE benchmark structure for both time-invariant and time-varying system parameters.

From the above studies, it can be observed that a significant amount of research work has been carried out in the field of simultaneous input and state estimation of a linear dynamic system. However, only a few efforts have been made towards simultaneous input and state estimation of a non-linear hysteretic system. Lei et al. [151] adopted EKF based joint input and parameter estimation of a four-storied hysteretic shear building model. Song [118] estimated both state and input of a 3-DOF non-linear hysteretic system using minimum

variance unbiased estimation and unscented points. Yang et al. [152] proposed an adaptive extended Kalman filter for simultaneous identification of input and time-varying parameters using numerical examples of a Bouc-Wen structure. The numerical study presented by Wu and Smyth [145] showed that UKF was efficient for real-time parameter estimation of highly non-linear systems with degradation and pinching, where the input was known. Recently, Lei et al. [153] have presented a UKF based algorithm for simultaneous identification of non-linear structural parameters and input excitation.

The literature review presented above highlights the development of Kalman filters and its modified versions for system identifications, which evolves from linear to non-linear systems. In this process, many identification algorithms are based on known inputs, which may not be the case for many structures. Thus, researchers have studied input identification, which is an advantage for the structures having no option for input measurement. However, the identification algorithm faces difficulty when a non-linear system is excited by non-stationary input. Thus, most of the studies on hysteretic system identification using Bayesian filtering algorithms focus on its performance using simulated experiments or small-scale laboratory tests. Synthetic experiments used in these studies consider hypothetical values of hysteretic parameters and other structural properties. Only a few studies are focused on the inverse problem dealing with large structures exhibiting non-linear hysteresis [154–156]. In particular, simultaneous input and parameter identification of full-scale hysteretic reinforced concrete structures under earthquake excitation need further investigation to study the efficiencies of the recursive time marching algorithms. This issue motivates the authors to examine the performance of the constrained minimum variance estimation algorithm for simultaneous parameter and input identification of a concrete bridge pier. The objectives and significant contributions of this work are discussed below.

As explained above, the study is mainly focused on the experimental validation of the constrained minimum variance estimation algorithm for reinforced structures. With these in view, the objectives of this chapter are set as follows

- In general, recursive inverse problems suffer numerical instabilities unless addressed by constrained conditions and parameter bounds. Moreover, the constrained minimum variance estimation also demands the same to avoid computational instability. In this study, appropriate bounded input bounded output (i.e. BIBO) properties are used to suitably augment the Bouc-Wen model for parameter and input estimation.

- Develop different sigma points generation schemes for constrained minimum variance unbiased estimation algorithm to study their non-linear system identification capability. In this format, the constrained conditions mentioned above are introduced in terms of parameter bounds.

- Validate the above mentioned objectives numerically using actual hysteretic behaviour obtained from the pseudo-dynamic test of a reinforced concrete frame. It provides realistic parameters of Bouc-Wen model including degradation and pinching. This synthetic experiment is aimed at tuning the identification algorithm for both parameter and input identification and also to study the performance of different sigma points generation schemes.

- Finally, Demonstrate the efficiency of the improved CMVU algorithm using experimental results on a full-scale bridge pier specimen. The specimen is exposed to non-stationary excitations, which causes the yielding of reinforcements. This experimental validation is dedicated to establishing the performance of the CMVU algorithm for field applications.

3.2 Proposed Constrained Conditions and Parameter Bound

Non-linear material behaviour is precisely described by the constitutive relationship at the micro level. Although such models exist in the literature, their integration with the gross physical model of a structure becomes too complex for practical problems. Due to this reason, phenomenological models have gained popularity among researchers and engineers. These are simple mathematical forms intended to capture the input-output relationship of the hysteretic system, which is sufficient for the purpose of its characterization at the macro level. For this reason, several models are available in the literature, which are successfully implemented in the context of system identification and structural control. A survey of different types of hysteretic models could be found in Sengupta and Li [157]. Among them, Bouc-Wen is one of the most widely used hysteresis models. Bouc [125] introduced it for the SDOF system under forced vibration and later generalized by Wen [158] in 1976. The advantage of the Bouc-Wen hysteresis is its ability to generate different loops of varying shapes and sizes. In general, the Bouc-Wen model is used as a black box whose parameters are tuned so that the output of the model produces a satisfactory resemblance with the experimental data. Although this approximate model provides a good match with the experimental data for a specific input, but the non-linear response may not be always bounded as claimed by Ikhouane et al. [159]. To resolve this issue, Ikhouane and Rodellar [160] proposed bounded input and bounded output (BIBO) property for the Bouc-Wen hysteretic model which is inherited by structural and mechanical systems. According to this proposal, the hysteretic systems following the Bouc-Wen model must have BIBO property, i.e., every bounded input to the system results in a bounded output over the time interval $[t_0, \infty)$. Also, the system dissipates energy during this process when exposed external loading cycles. Due these reasons, the stability of the Bouc-Wen model for any mechanical or structural system is ensured [160]. Chatzi et al. [98] has thoroughly demonstrated the importance of this property for the experimental identification. It is found that disregarding the BIBO property in the UKF algorithm may lead to instability, which affects the performance of the identification algorithm.

Let us consider the restoring force offered by the Bouc-Wen model, which has the following form

$$F_r(x,z,t) = \alpha k x(t) + (1-\alpha) k z(t) \tag{3.1a}$$

$$\dot{z}(t) = A\dot{x} - \beta |\dot{x}| |z|^{n-1} z - \gamma \dot{x} |z|^n \tag{3.1b}$$

In the above equation, $F_r(x,z,t)$ and $x(t)$ represent the restoring force and displacement of the hysteretic system while $\alpha \in (0,1)$ is the ratio of the post to pre-yield stiffness. The non-observable hysteretic displacement is denoted by $z(t)$ where overdot signifies the derivative

with respect to time. The set parameters $\{A, \beta, \gamma, n\}$ controls the overall configuration of the produced loops by the above equation. With respect to this system of equations (i.e. 3.1), the BIBO properties can be classified into two groups as shown in Table 3.1 [160]. In

Table 3.1: Classification of Bouc-Wen model

	Case	$\Omega_{A,\beta,\gamma,n}$	Upper bound on —z(t)—	Class
$A > 0$	$\beta + \gamma > 0$ and $\beta - \gamma \geq 0$	$\mathbb{R}$	$\max(\lvert z(0)\rvert, z_0)$	I
	$\beta + \gamma < 0$ and $\beta \geq 0$	$[-z_1, z_1]$	$\max(\lvert z(0)\rvert, z_0)$	II

this table, z_0 and z_1 are the two constants defined as $z_0 \triangleq \sqrt[n]{\frac{A}{\beta+\gamma}}$ and $z_1 \triangleq \sqrt[n]{\frac{A}{\gamma-\beta}}$. Except for these two classes, any other Bouc-Wen model does not represent hysteretic behaviour of a physical system [160]. As stated earlier, the hysteretic behaviour is history-dependent and hence the performance of non-linear state estimation algorithm can be significantly improved by prior knowledge. Researchers have proposed sub-optimal approaches in this context, which can approximate the constraint condition with reasonable accuracy. One of the popular methods for constraint handling is Moving Horizon Estimation (MHE) technique [161], where non-linear programming is solved at each time step in order to incorporate constraints conditions. However numerical optimization in this approach is computationally expensive. Likewise, unscented recursive non-linear dynamic data reconciliation (URNDDR) [162] is developed to take into account of the non-linear equality/inequality constraints in a sigma points based predictor-corrector framework. In the URNDDR, the sigma points lying outside the constraint region are projected back within the boundary and weights are assigned accordingly. One of the major drawbacks of this method is that the symmetry of the sigma point around the current position is lost after the projection. Due to this reason, the advantage of unscented transformation cannot be utilized fully. To overcome this limitation, a constrained unscented recursive estimator (CURE) was proposed by Mandela et al. [163]. In their study, optimization based projection of sigma points was proposed to deal with the constraints. It was demonstrated for both symmetric and asymmetric placement of sigma points within the constraint bounds. Further, the state updating equation was utilized to create transformed sigma points. These transformed points that violated constraints were projected back only when the updated state estimate exceeded the bounds. The experimental validation of this algorithm was carried out by Calabrese et al. [128] using a base isolated structure. The drawback of this algorithm was that at each time step needed optimization, which could be difficult for complex 3D structural problems. Yang and Ma [164] proposed a constrained EKF algorithm where the states corresponding to the system parameters were replaced by a continuous function. This idea of replacing the state vector by a function of auxiliary variables has been further extended in this thesis to develop a sigma points approach of the CMVU algorithm in the context of hysteretic systems. The way constrained conditions are imposed to the sigma points by treating them as a function of auxiliary variable has not been addressed in the literature. To explain this concept, consider the following state-space model with state X_1 and parameter θ

$$\begin{bmatrix} \dot{X}_1 \\ \dot{\theta} \end{bmatrix} = \begin{bmatrix} p(X_1, \theta) \\ 0 \end{bmatrix} \tag{3.2}$$

in which, θ is bounded between $[l_1, l_2]$. In general, the traditional Kalman filter can not take into account bounds and algebraic constraints on system variables [165]. However, a unique improvisation for this problem is provided in this study. To implement this bound, a function of auxiliary variable $[c(X_2)]$ is defined in such a way that the functional value always lies within the parameter bounds i.e $l_1 \leq c\,(X_2) \leq l_2$ while the variable remains unbounded i.e $-\infty < X_2 < \infty$. Using this concept, Eq. 3.2 can be expressed as

$$\begin{bmatrix} \dot{X}_1 \\ \dot{X}_2 \end{bmatrix} = \begin{bmatrix} p\,(X_1, c\,(X_2)) \\ 0 \end{bmatrix} \tag{3.3}$$

A sinusoidal function can be considered a good candidate for this problem. For example, the parameter θ in the above state-space model can be expressed as the function of X_2 as

$$\theta = l_1 \cos^2 X_2 + l_2 \sin^2 X_2 \tag{3.4}$$

Now, to identify the structural systems by the Bouc-Wen model, its essential BIBO property has to be ensured in the algorithm. However, between the two classes of BIBO system in Table 3.1, only class I is stable and compatible with the real systems. Also, it follows the characteristic energy dissipation and abide by the laws of Thermodynamics [166]. Hence, only BIBO class I property is relevant in this study. This property is confirmed by implicitly defining β and γ as a function of two auxiliary variables X_β and X_γ as follows

$$\beta = {X_\beta}^2 + {X_\gamma}^2 \tag{3.5a}$$
$$\gamma = {X_\beta}^2 - {X_\gamma}^2 \tag{3.5b}$$

Since both β and γ are non-dimensional parameters, the consistency of the system equation should not be hampered by the quadratic function of these auxiliary variables. The claim regarding BIBO class I property by Eq. 3.5 can be verified simply addition and subtraction of the two equations. Together with Eq. 3.4 and Eq. 3.5 provide stability to the estimator by ensuring relevant bounds for the sigma points generated. Though, the occurrence of optima outside this domain is possible, however, the probability of that occurrence is very small [164].

3.3 Constrained Minimum Variance Unbiased Estimator

The optimal minimum variance recursive filter for state and input estimation was first developed by Gillijns and Moore [116] for the discrete linear system. As the name suggests, this estimator has the lowest variance within the parameter space than any other unbiased estimator. This concept was further developed by Song [118] and proposed generalized minimum variance unbiased estimator (GMVU) to identify the non-linear systems using unscented points. In this study, the original GMVU algorithm is augmented with the constraint conditions to improve its performance and avoid instability associated with the identification of the hysteretic system. Moreover, the proposed formulation of CMVU algorithm provides a general framework that accommodate different sigma point generation schemes viz. unscented sigma points, cubature-quadrature sigma points, central difference sigma points. In

the following subsections, the sigma point based CMVU algorithm is explained for non-linear structural systems, with improvisation to adopt it for experimental identification of the actual bridge pier.

3.3.1 Sigma Points Approach For CMVU Algorithm

To demonstrate the proposed constrained minimum variance unbiased estimation algorithm, an n degree of freedom (DOF) non-linear dynamical system is considered, whose equation of motion can be expressed as

$$\mathbf{M}\ddot{\mathbf{x}}(t) + \mathbf{F}\left[\mathbf{x}(t), \dot{\mathbf{x}}(t), \mathbf{\Phi}\right] = \mathbf{B}\mathbf{u}(t) + \mathbf{D}\mathbf{f}(t) \tag{3.6}$$

In this equation, $\mathbf{x}(t)_{n\times 1} \in \mathbb{R}^n$, $\dot{\mathbf{x}}(t)_{n\times 1} \in \mathbb{R}^n$ and $\ddot{\mathbf{x}}(t)_{n\times 1} \in \mathbb{R}^n$ represent the displacement, velocity and acceleration vectors, respectively. Damping, stiffness and other non-linear hysteretic parameters are denoted by the vector $\mathbf{\Phi}_{m\times 1} \in \mathbb{R}^m$. In general, the mass of the structure remains unchanged during its lifetime, and hence the mass matrix $\mathbf{M}$ is considered to be known, which is estimated from the material and geometrical properties. $\mathbf{F}\left[\mathbf{x}(t), \dot{\mathbf{x}}(t), \mathbf{\Phi}\right]$ represents the restoring force acting on the structure, which is a function of displacement, velocity and other model parameters. Moreover, the known and unknown external forces are denoted by $\mathbf{u}(t) \in \mathbb{R}^s$ and $\mathbf{f}(t) \in \mathbb{R}^q$, respectively while $\mathbf{B}$ and $\mathbf{D}$ represent the corresponding influence matrices. The extended state vector for identification can be described as

$$\mathbf{Z}(t) = \left\{\mathbf{Z_1}\ \mathbf{Z_2}\ \mathbf{Z_3}\right\}^T \tag{3.7}$$

where $\mathbf{Z_1} = \mathbf{x}(t)^T$; $\mathbf{Z_2} = \dot{\mathbf{x}}(t)^T$ and $\mathbf{Z_3} = \mathbf{\Phi}^T$. In Eq.3.7, $\left\{\mathbf{Z_1}\ \mathbf{Z_2}\right\}^T$ represents the time-dependent state vector and $\dot{\mathbf{Z}}_\mathbf{3} = \dot{\mathbf{\Phi}}^T = \mathbf{0}$ denotes the time-invariance of the parameter vector. Substituting Eq.3.7 in Eq.3.6, the state-space model is expressed as

$$\left\{\begin{array}{c} \dot{\mathbf{Z}}_1^T \\ \dot{\mathbf{Z}}_2^T \\ \dot{\mathbf{Z}}_3^T \end{array}\right\}_{(2n+m)\times 1} = \left\{\begin{array}{c} \mathbf{Z_2}^T \\ \mathbf{M}^{-1}\left\{\mathbf{B}\mathbf{u}(t) + \mathbf{D}\mathbf{f}(t) - \mathbf{F}\left[\mathbf{Z_1}^T(t), \mathbf{Z_2}^T(t), \mathbf{Z_3}^T(t)\right]\right\} \\ \mathbf{0_{m\times 1}} \end{array}\right\} \tag{3.8}$$

The continuous-time representation of the above non-linear differential equation can be written in the following compact form

$$\dot{\mathbf{Z}}(t) = \mathbf{G}\left(\mathbf{Z}(t), \mathbf{u}(t), \mathbf{f}(t)\right) \tag{3.9}$$

The system equation (i.e. Eq. 3.9) is subsequently discretized in the time domain to implement the identification algorithm using real-time measurements, i.e.

$$\mathbf{Z}_k = \mathbf{Z}_{k-1} + \int_{(k-1)\Delta t}^{k\Delta t} \left[\mathbf{G}\left(\mathbf{Z}(t), \mathbf{u}(t), \mathbf{f}(t)\right)\right] dt = \mathbf{g}\left(\mathbf{Z}_{k-1}, \mathbf{u}_{k-1}, \mathbf{f}_{k-1}\right) \tag{3.10}$$

The non-linear observation vector $\mathbf{y}_k \in \mathbb{R}^r$ at any time $t = k\Delta t$ can be written as

$$\mathbf{y}_k = \mathbf{h}\left(\mathbf{Z}_k, \mathbf{u}_k\right) + \mathbf{H}_k\mathbf{f}_k + \mathbf{v}_k \tag{3.11}$$

In the above two equations (i.e. Eq. 3.10- Eq. 3.11), discrete-time representation of the state vector, known input vector and unknown input vector are given by $\mathbf{Z}_k$, $\mathbf{u}_k$ and $\mathbf{f}_k$, respectively. The random noise $\mathbf{v}_k$ associated with the measurement is assumed to have zero-mean Gaussian with covariance $\mathbb{E}\left[\mathbf{v}_k\mathbf{v}_k^T\right] = \mathbf{R}_k$. Also, the feed-through coefficient matrix $\mathbf{H}_k \in \mathbb{R}^{r\times q}$ in Eq.3.11, which is assumed to be full column rank i.e. $rank(\mathbf{H}_k) = q$ i.e. $r \geq q$.

In this study, the Bouc-Wen model is used to characterize the non-linear hysteretic system. With this in view, the extended state vector for complete systems can be expressed as

$$\mathbf{Z}_k = \left\{ \begin{array}{cc} \mathbf{\Lambda_k} & \mathbf{\Phi_k} \end{array} \right\}^T \tag{3.12}$$

where vector $\mathbf{\Lambda_k} = \left\{ \begin{array}{cc} \mathbf{x}_k & \dot{\mathbf{x}}_k \end{array} \right\}$ has displacement and velocity while $\mathbf{\Phi_k}$ represents the unknown parameters of the Bouc-Wen system. The prior knowledge of this system is adopted in the form of constraint conditions to maintain the stability as it is explained in Section 3.2 . For this purpose, the unknown parameters are incorporated in the vector $\mathbf{\Phi_k}$ i.e. $\mathbf{\Phi_k} = \left\{ \begin{array}{cccc} \mathbf{\Theta} & \beta & \gamma & \mathbf{w} \end{array} \right\}$, where $\mathbf{\Theta} = \{\theta_1\ \theta_2\ \theta_3 \ldots \theta_n\}$ consists of the parameters with bounds, $\mathbf{w}$ represents the parameter vector without bounds, while β and γ are the Bouc-Wen parameters. Here, stiffness and damping coefficients belong to $\mathbf{w}$, while vector $\mathbf{\Theta}$ contains Bouc-Wen parameters other than β and γ. Next, the upper and lower bounds of $\mathbf{\Theta}$ are enforced with the help of Eq. 3.4 and similarly, the BIBO properties are confirmed using Eq. 3.5.

The proposed constrained minimum variance unbiased estimator algorithm evaluates both system state $\mathbf{Z}_k$ and external unknown input force $\mathbf{f}_k$ based on the sequential measurements $\{\mathbf{y}_1, \mathbf{y}_2, ...\mathbf{y}_k\}$. At any time instant k, $\tilde{\mathbf{Z}}_\mathbf{k}$ and $\tilde{\mathbf{f}}_\mathbf{k}$ represent the estimate of state $\mathbf{Z_k}$ and unknown force $\mathbf{f_k}$, respectively. Initially (i.e. at $t = 0$), the unbiased estimate of state $\mathbf{Z}_0$ is denoted by $\tilde{\mathbf{Z}}_{0|0}$ and the same for $\mathbf{f}_0$ is given by $\tilde{\mathbf{f}}_0$. Similarly, variance matrices $\mathbf{P}^{\mathbf{Z}}_{0|0}$, $\mathbf{P}^{\mathbf{f}}_0$ and the cross-covariance matrix $\mathbf{P}^{\mathbf{Zf}}_0$ corresponding to $\mathbf{Z}_0$ and $\mathbf{f}_0$ are assumed to be known. To obtain $\tilde{\mathbf{Z}}_\mathbf{k}$ and $\tilde{\mathbf{f}}_\mathbf{k}$ simultaneously, augmented state vector $\mathbf{X}_0$ is formed, whose initial estimate $\tilde{\mathbf{X}}_{0|0}$ and corresponding covariance matrix $\mathbf{P}^{X_0}_{0|0}$ can be expressed as follows

$$\tilde{\mathbf{X}}_{0|0} = \left[\begin{array}{cc} \tilde{\mathbf{Z}}^T_{0|0} & \tilde{\mathbf{f}}^T_0 \end{array} \right]^T \tag{3.13}$$

$$\mathbf{P}^{\mathbf{X}}_{0|0} = \mathbb{E}\left[\left(\mathbf{X}_0 - \tilde{\mathbf{X}}_{0|0}\right)\left(\mathbf{X}_0 - \tilde{\mathbf{X}}_{0|0}\right)^T\right] = \left[\begin{array}{cc} \mathbf{P}^{\mathbf{Z}}_{\mathbf{0|0}} & \mathbf{P}^{\mathbf{Zf}}_{\mathbf{0}} \\ \left(\mathbf{P}^{\mathbf{Zf}}_0\right)^T & \mathbf{P}^{\mathbf{f}}_0 \end{array} \right] \tag{3.14}$$

It may be noted that the estimation of $\tilde{\mathbf{Z}}_{k|k-1}$, $\mathbf{P}^{\mathbf{Z}}_{k|k-1}$ $\mathbf{P}^{\mathbf{Zf}}_{k|k-1}$ are difficult in the statistical sense, since both $\mathbf{g}(.)$ and $\mathbf{h}(.)$ in Eq. 3.10 and Eq. 3.11 are non-linear functions. Here, it is worth noting that subscript $k|k-1$ represents the estimate at time step k provided the measurements are available up to $(k-1)$ time step. To deal with this problem, Song [118] used the unscented transformation technique proposed by Julier and Uhlmann [124], where statistical moments are estimated with the help of deterministic sampling points, known as unscented sigma points. However, instead of using only unscented sigma points, the proposed algorithm in this study provides a generalized framework to adopt any sigma

points generation scheme. For demonstration, two different types of sigma points generation schemes (i.e. unscented sigma points and cubature quadrature sigma points) to propagate the system state through $\mathbf{g}(.)$ and $\mathbf{h}(.)$ functions have been presented here. A brief description of these schemes is provided in the next subsection. At at any time step k, N numbers of sigma points $\mathbf{\Psi}_{k-1|k-1}$ and corresponding weights $\mathbf{W}$ are generated from the estimates of $\tilde{\mathbf{X}}_{k-1|k-1}$ and covariance $\mathbf{P}^{\mathbf{X}}{}_{k-1|k-1}$. These points $\mathbf{\Psi}_{k-1|k-1}$ have two components $\left(\mathbf{\Psi}^{\mathbf{Z}}_{k-1|k-1}\right)^T$ and $\left(\mathbf{\Psi}^{\mathbf{f}}_{k-1|k-1}\right)^T$ belonging to the system state and the unknown input, respectively i.e.

$$\mathbf{\Psi}_{k-1|k-1} = \left[\left(\mathbf{\Psi}^{\mathbf{Z}}_{k-1|k-1}\right)^T \left(\mathbf{\Psi}^{\mathbf{f}}_{k-1|k-1}\right)^T \right]^T \tag{3.15}$$

Now, they are propagated through the non-linear system equation [i.e. Eq. 3.10] to obtain the predicted sigma points $\mathbf{\Psi}_{k|k-1}$ as follows

$$\mathbf{\Psi}^{\mathbf{Z}}_{k|k-1} = \mathbf{g}\left(\mathbf{\Psi}^{\mathbf{Z}}_{k-1|k-1}, \mathbf{u}_{k-1}, \mathbf{\Psi}^{\mathbf{f}}_{k-1|k-1}\right) \tag{3.16}$$

These predicted sigma points help to estimate the statistical properties in terms of the system state $\tilde{\mathbf{Z}}_{k|k-1}$ and the covariance $\mathbf{P}^{\mathbf{Z}}_{k|k-1}$ as follows

$$\tilde{\mathbf{Z}}_{k|k-1} = \mathbb{E}\left[\mathbf{g}\left(\mathbf{Z}_{k-1},\mathbf{u}_{k-1},\mathbf{f}_{k-1}\right)\right] \approx \sum_{i=1}^{N} \mathbf{W}_i \mathbf{\Psi}^{\mathbf{Z}}_{i,k|k-1} \tag{3.17a}$$

$$\begin{aligned} \mathbf{P}^{\mathbf{Z}}_{k|k-1} &= \mathbb{E}\left[\left(\mathbf{Z}_k - \tilde{\mathbf{Z}}_{k|k-1}\right)\left(\mathbf{Z}_k - \tilde{\mathbf{Z}}_{k|k-1}\right)^{\mathbf{T}}\right] \\ &\approx \sum_{i=1}^{N} \mathbf{W}_i \left(\mathbf{\Psi}^{\mathbf{Z}}_{i,k|k-1} - \tilde{\mathbf{Z}}_{k|k-1}\right)\left(\mathbf{\Psi}^{\mathbf{Z}}_{i,k|k-1} - \tilde{\mathbf{Z}}_{k|k-1}\right)^T \end{aligned} \tag{3.17b}$$

where $\mathbf{\Psi}^{\mathbf{Z}}_{i,k|k-1}$ denotes the i^{th} column of the matrix $\mathbf{\Psi}^{\mathbf{Z}}_{k|k-1}$. By defining $\hat{\mathbf{y}}_k \triangleq \mathbf{y}_k - \mathbb{E}\left[\mathbf{h}\left(\mathbf{Z_k},\mathbf{u_k}\right)\right]$, Eq. 3.11 can be expressed as follows

$$\hat{\mathbf{y}}_k = \mathbf{H_k}\mathbf{f_k} + \mathbf{e_k} \tag{3.18a}$$

where the error $\mathbf{e_k}$ is given by

$$\mathbf{e_k} \triangleq \mathbf{h}\left(\mathbf{Z_k},\mathbf{u_k}\right) + \mathbf{v_k} - \mathbb{E}\left[\mathbf{h}\left(\mathbf{Z_k},\mathbf{u_k}\right)\right] \tag{3.18b}$$

The statistical mean of the measurement function $\tilde{\mathbf{\Xi}}_{k|k-1} = \mathbb{E}\left[\mathbf{h}\left(\mathbf{Z_k},\mathbf{u_k}\right)\right]$ and the error covariance $\mathbf{P}^{\mathbf{e}}_k = \mathbb{E}\left[\mathbf{e}_k\mathbf{e}_k^T\right]$ can be obtained from $\mathbf{\Psi}^{\mathbf{Z}}_{k|k-1}$ as follows

$$\tilde{\mathbf{\Xi}}_{k|k-1} \approx \sum_{i=i}^{N} \mathbf{W}_i \mathbf{\Omega}_{i,k|k-1} \tag{3.19a}$$

$$\mathbf{P}^{\mathbf{e}}_k \approx \sum_{i=1}^{N} \mathbf{W}_i \left(\mathbf{\Omega}_{i,k|k-1} - \tilde{\mathbf{\Xi}}_{k|k-1}\right)\left(\mathbf{\Omega}_{i,k|k-1} - \tilde{\mathbf{\Xi}}_{k|k-1}\right)^T + \mathbf{R}_k \tag{3.19b}$$

where $\mathbf{\Omega}_{k|k-1} = \mathbf{h}\left(\mathbf{\Psi}^{\mathbf{Z}}_{k|k-1}, \mathbf{u}_k\right)$ represents sigma points transmitted through the non-linear function $\mathbf{h}(.)$, while covariance of the additive noise $\mathbf{v}_k$ is denoted by $\mathbf{R}_k$. Now, it is assumed that estimate of the unknown input $\tilde{\mathbf{f}}_k$ can be obtained from Eq. 3.18a by applying a scaling matrix $\mathbf{C}_k$ as follows

$$\tilde{\mathbf{f}}_{\mathbf{k}} = \mathbf{C}_k \hat{\mathbf{y}}_k = \mathbf{C}_k \left(\mathbf{H}_k \mathbf{f}_k + \mathbf{e}_k\right) \tag{3.20}$$

Taking expectations on both sides of the above equation and using $\mathbb{E}\left(\mathbf{e}_k\right) = 0$ lead to

$$\mathbb{E}\left[\tilde{\mathbf{f}}_{\mathbf{k}}\right] = \mathbf{C}_k \mathbf{H}_k \mathbb{E}\left[\mathbf{f}_k\right] \tag{3.21}$$

The above equation indicates that $\tilde{\mathbf{f}}_k$ can be defined as an unbiased estimate, if and only if, $\mathbf{C}_k\mathbf{H}_k = \mathbf{I}$, where, $\mathbf{I}$ is the identity matrix. The earlier assumption of $rank(\mathbf{H}_k) = p$ is a necessary and sufficient condition for the existence of an unbiased estimator in Eq. 3.21 [118]. However, an expression of optimal $\mathbf{C}_k$ is also required for the minimum variance estimate of $\tilde{\mathbf{f}}_k$. For this purpose, an assumption is made that $\mathbf{P}^e_k$ is a positive definite matrix and there exists an invertible matrix $\mathbf{\Upsilon_k}$ such that $\mathbf{\Upsilon}_k\mathbf{\Upsilon}_k^T = \mathbf{P}^e_k$. The expression obtained by pre-multiplying both sides of Eq. 3.18a with $\mathbf{\Upsilon_k^{-1}}$ is given below

$$\mathbf{\Upsilon_k}^{-1}\hat{\mathbf{y}}_k = \mathbf{\Upsilon_k}^{-1}\mathbf{H}_k\mathbf{f}_k + \mathbf{\Upsilon_k}^{-1}\mathbf{e}_k \tag{3.22}$$

Using Gauss-Markov theorem, the expression for the minimum variance estimation of $\tilde{\mathbf{f}}_k$ is obtained from Eq. 3.22 under the assumption that $\mathbf{\Upsilon_k}^{-1}\mathbf{H}_k$ having full column rank as follows [115]

$$\begin{aligned} \tilde{\mathbf{f}}_k &= \left[\left(\mathbf{\Upsilon_k}^{-1}\mathbf{H}_k\right)^T\left(\mathbf{\Upsilon_k}^{-1}\mathbf{H}_k\right)\right]^{-1}\left(\mathbf{\Upsilon_k}^{-1}\mathbf{H}_k\right)^T\left(\mathbf{\Upsilon_k}^{-1}\hat{\mathbf{y}}_k\right) \\ &= \left[\mathbf{H}_k^T(\mathbf{P}^{\mathbf{e}}_k)^{-1}\mathbf{H}_k\right]^{-1}\mathbf{H}_k^T(\mathbf{P}^{\mathbf{e}}_k)^{-1}\hat{\mathbf{y}}_k = \mathbf{C}_k\hat{\mathbf{y}}_k \end{aligned} \tag{3.23}$$

Further simplification of the above expression leads to

$$\tilde{\mathbf{f}}_k = \mathbf{C}_k\tilde{\mathbf{y}}_k = \mathbf{C}_k\left\{\mathbf{y}_k - \mathbb{E}\left[\mathbf{h}\left(\mathbf{Z}_k, \mathbf{u}_k\right)\right]\right\} \approx \mathbf{C}_k\left(\mathbf{y}_k - \sum_{i=1}^{N}\mathbf{W}^{\mathbf{m}}_i\mathbf{\Omega}_{i,k|k-1}\right) \tag{3.24}$$

From Eq. 3.18a and Eq. 3.23, the estimation error for $\tilde{\mathbf{f}}_k$ can be expressed as

$$\mathbf{f}^{er}_k = \mathbf{f}_k - \tilde{\mathbf{f}}_k = -\mathbf{C}_k\mathbf{e}_k \tag{3.25}$$

Also, the input error covariance $\mathbf{P}^{\mathbf{f}}_k$ is obtained after substituting $\mathbf{C}_k$ from Eq. 3.23 using the following expression

$$\mathbf{P}^{\mathbf{f}}_k \triangleq \mathbb{E}\left[\mathbf{f}^{er}_k(\mathbf{f}^{er}_k)^T\right] = \mathbf{C}_k\mathbf{P}^{\mathbf{e}}_k\mathbf{C}_k^T = \left[\mathbf{H}_k^T\left(\mathbf{P}^{\mathbf{e}}_k\right)^{-1}\mathbf{H}_k\right]^{-1} \tag{3.26}$$

$$\begin{aligned} \tilde{\mathbf{Z}}_{k|k} &= \tilde{\mathbf{Z}}_{k|k-1} + \mathbf{L}_k\left\{\mathbf{y}_k - \mathbb{E}\left[\mathbf{h}\left(\mathbf{Z}_k, \mathbf{u}_k\right)\right]\right\} \\ &\approx \sum_{i=1}^{N}\mathbf{W}_i\mathbf{\Psi}^{\mathbf{Z}}_{i,k|k-1} + \mathbf{L}_k\left(\mathbf{y}_k - \sum_{i=1}^{N}\mathbf{W}_i\mathbf{\Omega}^{\mathbf{Z}}_{i,k|k-1}\right) \end{aligned} \tag{3.27}$$

where $\mathbf{L}_k$ represents the optimal gain matrix which yields minimum variance unbiased estimate of state $\mathbf{Z}_k$. The corresponding state estimation error $\tilde{\mathbf{Z}}^{er}_{k|k}$ can be expressed from Eq. 3.18a and Eq. 3.27 as follows

$$\tilde{\mathbf{Z}}^{er}_{k|k} \triangleq \mathbf{Z}_k - \tilde{\mathbf{Z}}_{k|k} = \tilde{\mathbf{Z}}^{er}_{k|k-1} - \mathbf{L}_k\mathbf{e}_k - \mathbf{L}_k\mathbf{H}_k\mathbf{f}_k \tag{3.28}$$

Taking expectations on both sides of Eq. 3.28 leads to $\mathbb{E}\left[\tilde{\mathbf{Z}}^{er}_{k|k}\right] = \mathbf{L}_k\mathbf{H}_k\mathbb{E}\left[\mathbf{f}_k\right]$. It indicates that the existence of an unbiased estimate $\tilde{\mathbf{Z}}_{k|k}$ is possible for any feasible value of $\mathbf{f}_k$, if and only if, $\mathbf{L}_k\mathbf{H}_k = 0$. Considering this assumption is satisfied, the updated covariance $\mathbf{P}^{\mathbf{Z}}_{k|k}$ associated with the state $\tilde{\mathbf{Z}}_{k|k}$ can be obtained from Eq. 3.28 as follows

$$\mathbf{P}^{\mathbf{Z}}_{k|k} \triangleq \mathbb{E}\left[\tilde{\mathbf{Z}}^{er}_{k|k}\left(\tilde{\mathbf{Z}}^{er}_{k|k}\right)^T\right] = \mathbf{P}^{\mathbf{Z}}_{k|k-1} - \mathbf{L}_k\mathbf{P}^{\mathbf{eZ}}_{k|k-1} - \mathbf{P}^{\mathbf{Ze}}_{k|k-1}\mathbf{L}_k^T + \mathbf{L}_k\mathbf{P}^{\mathbf{e}}_{k|k-1}\mathbf{L}_k^T \tag{3.29}$$

In the above equation, $\mathbf{P}^{\mathbf{Ze}}_{k|k-1}$ denotes the corresponding cross-covariance matrix which takes the following form

$$\begin{aligned}\mathbf{P}^{\mathbf{Ze}}_{k|k-1} \triangleq \mathbb{E}\left(\tilde{\mathbf{Z}}^{er}_{k|k-1}\mathbf{e}_k^T\right) &= \mathbb{E}\left[\tilde{\mathbf{Z}}^{er}_{k|k-1}\{\mathbf{h}\left(\mathbf{Z}_k,\mathbf{u}_k\right) - \mathbb{E}\left[\mathbf{h}\left(\mathbf{Z}_k,\mathbf{u}_k\right)\right]\}^T\right] \\ &\approx \sum_{i=1}^{N}\mathbf{W_i}\left(\mathbf{\Omega}_{i,k|k-1} - \tilde{\mathbf{\Xi}}_{k|k-1}\right)\left(\mathbf{\Psi}^{\mathbf{Z}}_{i,k|k-1} - \tilde{\mathbf{Z}}_{k|k-1}\right)^T\end{aligned} \tag{3.30}$$

Next, the optimal gain matrix $\mathbf{L}_k$ is obtained by minimizing the trace of $\mathbf{P}^{\mathbf{Z}}_{k|k}$ under the constrained condition $\mathbf{L}_k\mathbf{H}_k = 0$. Its optimal value is given by (refer to Appendix A)

$$\mathbf{L}_k = \mathbf{K}_k\left(\mathbf{I} - \mathbf{H}_k\mathbf{C}_k\right) \tag{3.31}$$

In which, $\mathbf{K}_k$ is similar to the Kalman gain matrix of the form

$$\mathbf{K}_k = \mathbf{P}^{\mathbf{Ze}}_{k|k-1}(\mathbf{P}^{\mathbf{e}}_k)^{-1} \tag{3.32}$$

By substituting $\mathbf{L}_k$ from Eq. 3.31 in Eq. 3.29 and rearranging them, the updated covariance matrix $\mathbf{P}^{\mathbf{Z}}_{k|k}$ can be expressed as follows (refer Appendix A)

$$\mathbf{P}^{\mathbf{Z}}_{k|k} = \mathbf{P}^{\mathbf{Z}}_{k|k-1} - \mathbf{K}_k\left(\mathbf{P}^{\mathbf{e}}_k - \mathbf{H}_k\mathbf{P}^{\mathbf{f}}_k\mathbf{H}_k^T\right)\mathbf{K}_k^T \tag{3.33}$$

Similarly, the updated cross-covariance matrix $\mathbf{P}^{\mathbf{Zf}}_k \triangleq \mathbb{E}\left[\tilde{\mathbf{Z}}^{er}_k(\mathbf{f}^{er}_k)^T\right]$ is obtained using Eq. 3.23, Eq. 3.25 and Eq. 3.28 in following form [118]

$$\mathbf{P}^{\mathbf{Zf}}_k = -\mathbf{P}^{\mathbf{Ze}}_{k|k-1}(\mathbf{C}_k)^T \tag{3.34}$$

For the next time step, the estimated states $\tilde{\mathbf{Z}}_{k|k}$, $\tilde{\mathbf{f}}_k$ and the corresponding covariance matrices $\mathbf{P}^{\mathbf{Z}}_{k|k}$, $\mathbf{P}^{\mathbf{f}}_k$ and $\mathbf{P}^{\mathbf{Zf}}_k$ are substituted into Eq. 3.13 and Eq. 3.14 and the iteration continues.

3.3.2 Sigma Points Generation Schemes

In this section, a brief overview of the sigma points generation scheme is presented. The motivation behind this scheme is to transform a probability density function when propagating through a general non-linear function. In this context, it may be noted that EKF works on the principle of linearization using the Taylor series expansion for mean and covariance to estimate from non-linear function. But, the accuracy obtained from this approach is unsatisfactory compared to sigma point approach [96]. In this process, the state is represented by a carefully generated fixed number of deterministically chosen sampling points called the sigma points. The sigma points approach for a non-linear system is based on two principles - (i) it is convenient to transform a single point through a non-linear transformation rather than compute the *pdf* and (ii) it is easy to sample from the *pdf*. Several methods are available in the literature to estimate the mean and covariance of the state propagating through a non-linear function. Julier and Uhlmann [124] first introduced unscented transformation to calculate these statistics where input-output relation undergoes a non-linear transformation. Unscented transformation utilizes some carefully selected sigma points around the predicted mean position to represent the state distribution. This approach for moment estimation is more convenient to implement, as it does not need to evaluate the gradient [124]. As a result, many sigma points based estimation techniques are developed such as Unscented Kalman filter (UKF), Gauss-Hermite filter (GHF) [167], Cubature-Kalman filter(CKF) [168], Cubature-quadrature Kalman filter [169]. Among them, unscented transformed sigma points and cubature quadrature sigma points are considered in this study. A brief description of the two schemes are presented below -

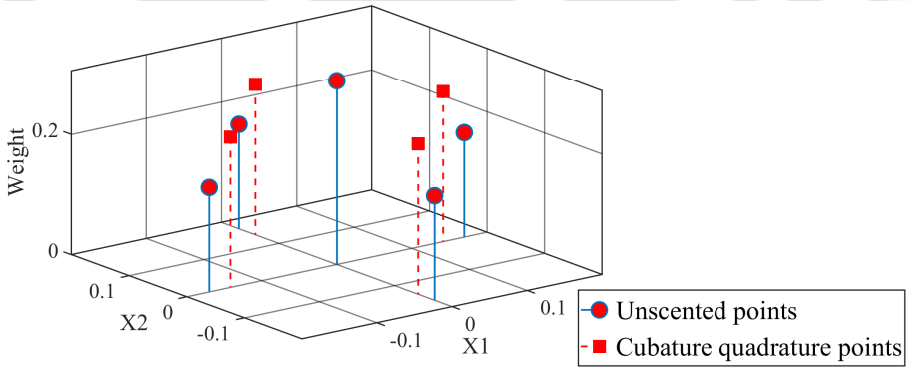

Figure 3.1: Configuration and weights of sigma points for 2-dimensional case

3.3.3 Unscented Transformed Points

In this study, unscented sigma points are utilized to calculate the mean and covariance of states that are subjected to a non-linear transformation. It was introduced by Julier and Uhlmann [124] and became popular due to its accuracy and convenience. The description of unscented points has been discussed in section 2.4. To show the configuration of sigma points, a plot of weight against the orientation of the points for a 2D case is shown in the Fig. 3.1.

3.3.4 Cubature Quadrature Points

Cubature points are used to solve the intractable integral where a closed-form solution can not be obtained. The support points and the corresponding weights approximate an integral by the weighted sum of the functions evaluated at these points. To compute the intractable integral, it is transformed into surface and line integrals. The surface integral can be calculated using the spherical cubature rule over a hyper sphere and line integral can be evaluated using the Gauss-Laguerre quadrature rule [169].

3.3.4.1 Generation of Cubature Points

For an arbitrary function $f(x)$, $X \in \mathbb{R}^n$

$$I(f) = \frac{1}{\sqrt{|\Sigma|}(2\pi)^n} \int_{\mathbb{R}^n} f(x)\, e^{-(1/2)(X-\mu)^T \Sigma^{-1}(X-\mu)} dX \tag{3.35}$$

can be expressed in spherical coordinate system as

$$I(f) = \frac{1}{\sqrt{(2\pi)^n}} \int_{r=0}^{\infty} \int_{U_n} \left[f(CrZ+\mu)\, ds(Z) \right] r^{n-1} e^{-r^2/2} dr \tag{3.36}$$

where $X = CrZ + \mu$, C is the Cholesky decomposition of the covariance matrix, Σ, $\|Z\| = 1$, μ is the mean of Gaussian distribution and U_n is the surface of a unit hyper-sphere. Now, any integral of a function $f(.)$ in the form of $\int_{\lambda=0}^{\infty} f(\lambda)\, \lambda^{\alpha} e^{-\lambda} d\lambda$ can be approximately evaluated using quadrature points and weight associated with them. The error associated with approximation of the integral depends on the number of quadrature points. The quadrature points can be determined from the roots of the n' order of Chebyshev-Laguerre polynomial

$$L_{n'}^{\alpha}(\lambda) = (-1)^{n'} \lambda^{-\alpha} e^{\lambda} \frac{d^{n'}}{d\lambda^{n'}} \lambda^{\alpha+n'} e^{-\lambda} = 0 \tag{3.37}$$

Let us assume the quadrature points be $\lambda_{i'}$. The corresponding weights can be determined as

$$w_{i'} = \frac{n'\Gamma(\alpha + n' + 1)}{\lambda_{i'} \left[\dot{L}_{n'}^{\alpha}(\lambda_{i'}) \right]^2} \tag{3.38}$$

Now to integrate the rest of the term, the Gauss-Laguerre quadrature formula is used assuming $t = r^2/2$ to cast the integral in the desired form as follows

$$I(f) = \frac{1}{\sqrt{(2\pi)^n}} \frac{2\sqrt{\pi^n}}{2n\Gamma(n/2)} \int_{r=0}^{\infty} \left(\sum_{i=1}^{2n} f\left[\sqrt{2t} u_i \right] \right) t^{n/2-1} e^{-t} dt \tag{3.39}$$

Now the integration $\int_{t=0}^{\infty} f(t)\, t^{(n/2-1)} e^{-t} dt$ is approximated using multiple quadrature points with $\alpha = n/2-1$. The solution of the problem using i' number of quadrature points denoted as $\lambda_{i'}$ can be expressed by the following equation

$$I(f) = \frac{1}{2n\Gamma(n/2)} \left[\sum_{i=1}^{2n} \sum_{i'=1}^{n'} A_{i'} f\left(\sqrt{2\lambda_{i'}}\right) [u_i] \right] \tag{3.40}$$

The above procedure is simplified into the following steps

1. Find the cubature points $u_i (i = 1, 2, 3...2n)$ located at the intersection of the unit hyper-sphere and its axes.

2. Solve the n' order Chebyshev-Laguerre polynomial Eq.3.37 for $\alpha = n/2 - 1$ to obtain the quadrature points$(\lambda_{i'})$

$$L_{n'}^{\alpha} = \lambda^{n'} - \frac{n'}{1!}(n'+\alpha)\lambda^{n'-1} + \frac{n'(n'-1)}{2!}(n'+\alpha)(n'+\alpha-1)\lambda^{n'-2} - .... = 0 \tag{3.41}$$

3. Find the CQ points as $\xi_j = \sqrt{2\lambda_{i'}}\,[u_i]$ and their corresponding weights as

$$w_j = \frac{1}{2n\Gamma(n/2)}(A_{i'}) = \frac{1}{2n\Gamma(n/2)} \frac{n'!\Gamma(\alpha+n'+1)}{\lambda_{i'}\left[\dot{L}_{n'}^{\alpha}(\lambda_{i'})\right]^2} \tag{3.42}$$

for $i = 1, 2, 3...2n, \quad i' = 1, 2, ...n'$ and $j = 1, 2, 3....2nn'$

3.4 Numerical Validation

In this section, numerical results are presented to show the performance of the CMVU algorithm proposed above for different types of Bouc-Wen systems under earthquake excitation. First, a hypothetical case of a Bouc-Wen hysteretic system is presented to verify the efficiency of the proposed algorithm

3.4.1 Validation Exercise 1

A 3-DOF structural system subjected to external ground motion is considered for numerical studies in this section as shown in Fig. 3.2. The equation motion of the system can be represented as

$$\begin{bmatrix} m_1 & 0 & 0 \\ 0 & m_2 & 0 \\ 0 & 0 & m_3 \end{bmatrix} \begin{bmatrix} \ddot{x}_1 \\ \ddot{x}_2 \\ \ddot{x}_3 \end{bmatrix} + \begin{bmatrix} c_1+c_2 & -c_2 & 0 \\ -c_2 & c_2+c_3 & -c_3 \\ 0 & -c_3 & c_3 \end{bmatrix} \begin{bmatrix} \dot{x}_1 \\ \dot{x}_2 \\ \dot{x}_3 \end{bmatrix} + \begin{bmatrix} k_1 & k_2 & -k_2 & 0 \\ 0 & -k_2 & k_2+k_3 & -k_3 \\ 0 & 0 & -k_3 & k_3 \end{bmatrix} \begin{bmatrix} z \\ x_1 \\ x_2 \\ x_3 \end{bmatrix} = \begin{bmatrix} -m_1\ddot{x}_g \\ -m_2\ddot{x}_g \\ -m_3\ddot{x}_g \end{bmatrix} \tag{3.43}$$

where $\dot{z}$ is the hysteretic component defined as

$$\dot{z} = \dot{x}_1 - \beta \left|\dot{x}_1\right| |z|^{n-1} z - \gamma \dot{x}_1 |z|^n \tag{3.44}$$

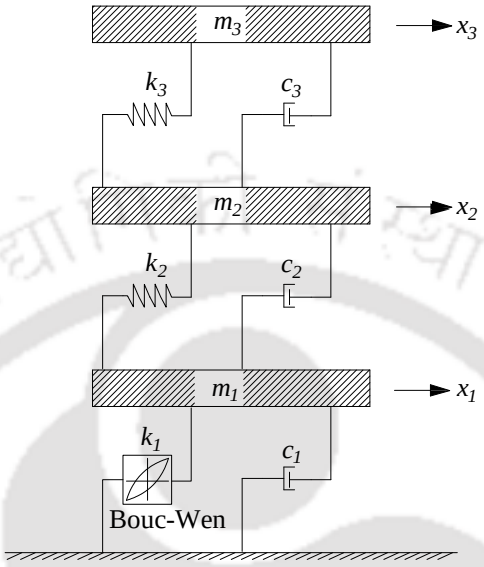

Figure 3.2: 3-DOF hysteretic structural system

Parameters β, γ and n are dimensionless quantities where the first two parameters control the shape and size of the hysteresis loop while 3^{rd} parameter controls the transition from elastic to post-elastic deformation. To generate the response of the system artificially, the values assigned in Eqs. 3.43 - Eq. 3.44 are $m_1 = m_2 = m_3 = 125$ kg, $k_1 = 24000\,\mathrm{N/m}$, $k_2 = 20000\,\mathrm{N/m}$, $k_3 = 18000\,\mathrm{N/m}$, $c_1 = 500\,\mathrm{Ns/m}$, $c_2 = 400\,\mathrm{Ns/m}$, $c_3 = 200\,\mathrm{Ns/m}$, $\beta = 2$, $\gamma = 1$ and $n = 2$. It should be noted that the Bouc-Wen system enforces an extra state variable z to model the hysteretic behaviour. The measurements of the system are generated artificially by the ground motion at the support. In this analysis, the scaled Kobe earthquake is applied at the base of the system to generate artificial measurements, i.e displacements and accelerations using the 4^{th} order Runge-Kutta Integration scheme. Different zero-mean Gaussian white noise process with three different levels (i.e. $5\%, 10\%$ and 15% noise to signal) have been added artificially. To apply the CMVU algorithm, extended state vector $\mathbf{Z}$ is formed according to Eq. 3.12. The constraint condition related to β and γ parameters can be incorporated using Eq. 3.5. In general, the parameter n is a small positive integer value, which can be ensured using the bounds according to Eq. 3.4. The identified stiffness and damping by the CMVU algorithm under different sigma point generation schemes are demonstrated in Fig. 3.3. The algorithm that utilizes unscented points is denoted as UT-Constrained. Similarly, when the algorithm uses cubature quadrature points is denoted as CQ-Constrained. It can be observed from Fig. 3.3 that both of them can successfully identify the system parameter within the reasonable level of tolerance. Here, it is worthy of noting that most of the parameters deviates from the exact value in Fig. 3.3 when the constrained conditions are not included in the algorithm which is denoted as Unconstrained. It can be

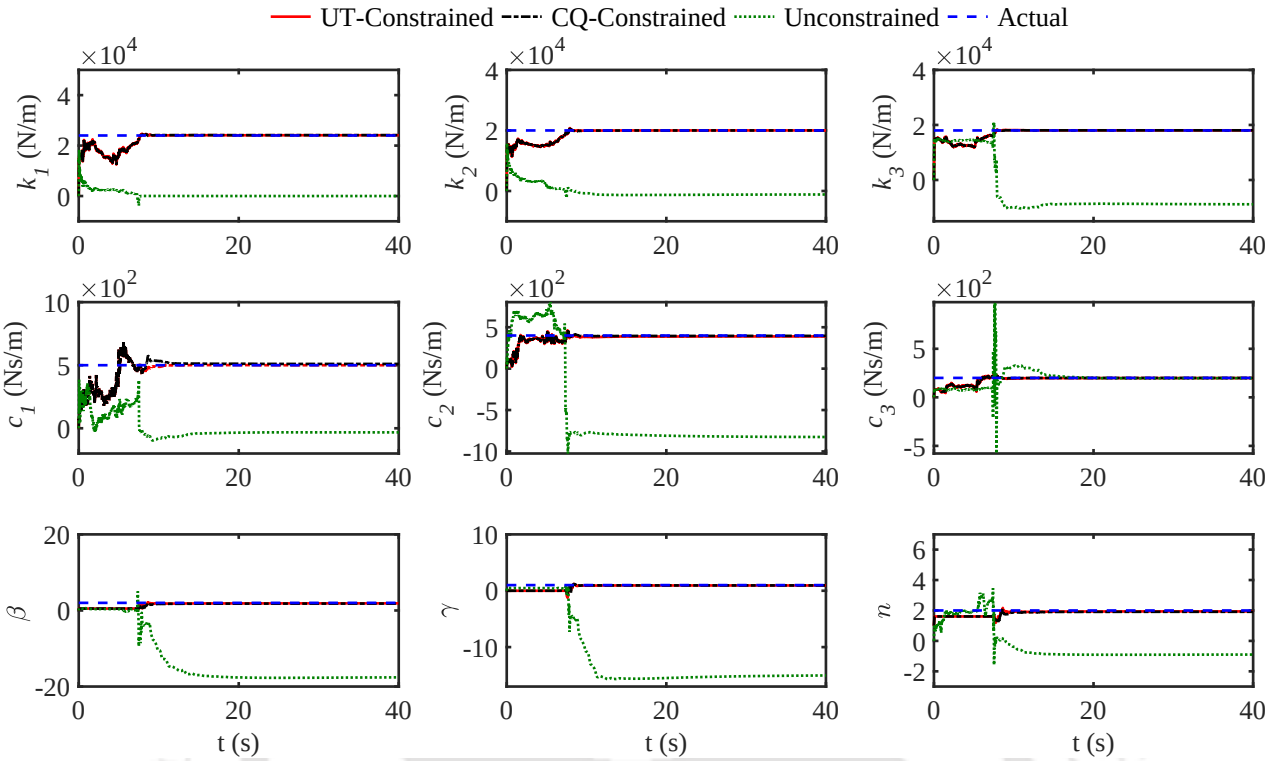

Figure 3.3: Parameter identification of 3-DOF Bouc-Wen system for 15% noise case

seen in Fig. 3.3 that at around 10 s the system parameters start converging to the exact value. At the same time, the convergence of the estimated input is also achieved (refer to Fig. 3.4a). Initially, the percentage error in input estimation is very high, which minimizes gradually as the the parameters converges to its exact value as shown in Fig. 3.4c. In this figure, as the measurements are polluted with artificial noises, its effect can be seen in terms of residual error. However, it remains within the tolerance limit (i.e. 5%). On the contrary, the parameters estimated by unconstrained CMVU diverge from their actual values, which is reflected in deviation of the input estimation. Similarly, the estimated hysteresis from constrained CMVU matches very well with the actual value (see Fig. 3.4b) as the parameters have converged to the actual values, which ultimately guarantee the satisfactory matching of the hysteresis. To further investigate the influence of noise levels and sigma point generation schemes, the relative percentage error is calculated, i.e. $\frac{|\theta_{avg}-\theta_{true}|}{\theta_{true}} \times 100$. Here, θ_{avg} is the average of the estimated parameter θ from 100 simulations i.e $\theta_{avg} = \frac{1}{100}\sum_{i=1}^{100}\theta_i$ whereas θ_{true} is the actual value of the parameter. The estimation results for a different level of noise with respect to the corresponding sigma points generation schemes are summarized in Table. 3.2. Overall performance of the two different sigma points generation schemes are comparable, as the relative estimation error for most of the parameters are below 10%. To determine the accuracy in input estimation, it is characterized by two different parameters, i.e., Arias intensity (I_A) and Peak ground acceleration (PGA). The estimated errors in input excitation for all these cases are under 5%, indicating excellent accuracy in input estimation.

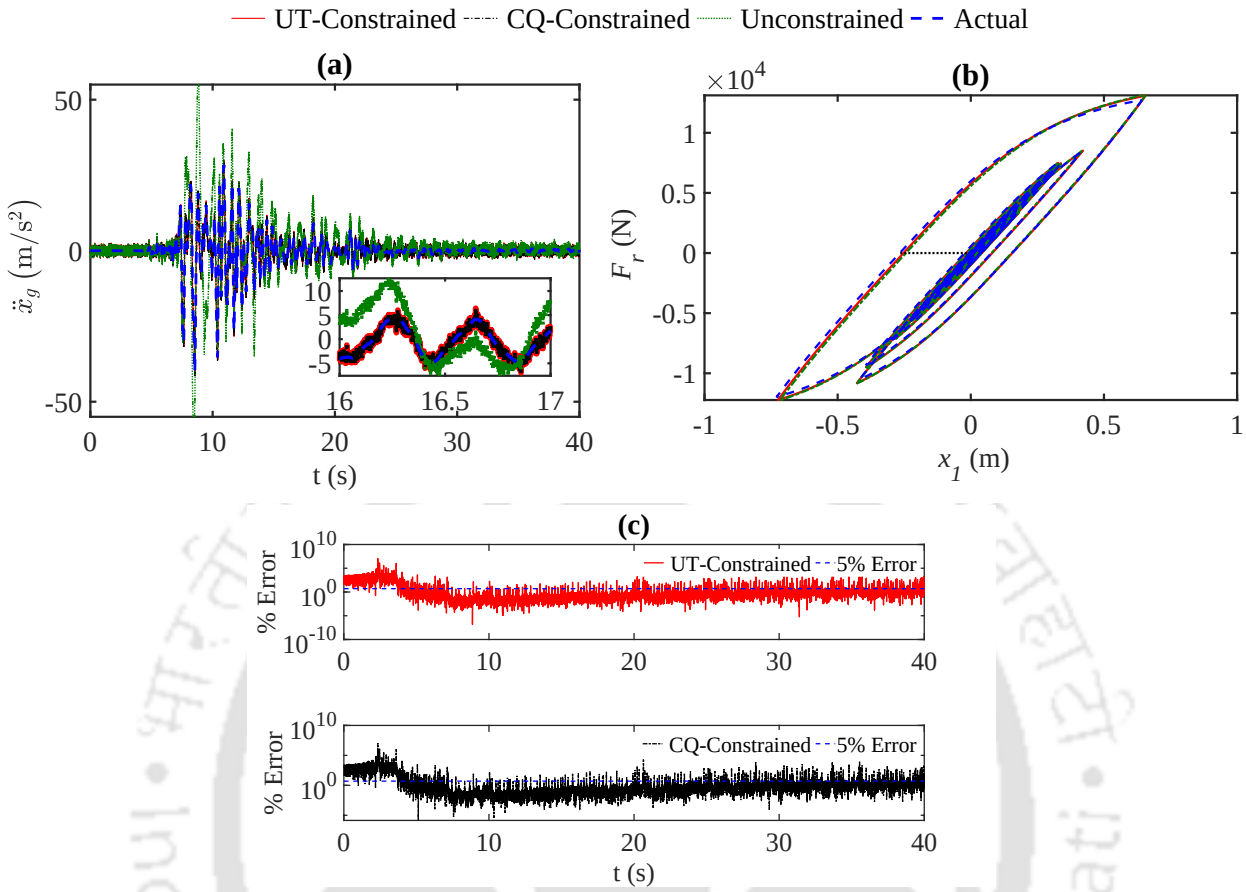

Figure 3.4: Joint parameter and input estimation for 15% noise; (a) input, (b) hysteretic behaviour, and (c) percentage error in input estimation

3.4.2 Validation Exercise 2

Once the performance of the proposed CMVU for both input and parameters of the Bouc-Wen hysteretic system is established, it is further used to identify another form of hysteresis in this validation exercise where major emphasis is given on the actual behaviour of a RC structure. In this context, civil structures designed by complying with current seismic code respond non-linearly during a seismic event. It has been observed that earthquake excitation induces repetitive cyclic deformation to the structure, causing deterioration of the material resulting in degradation of global stiffness of the structure. To take into account this behaviour, a degrading hysteresis model proposed by Baber and Wen [170] is considered here. Thus, the same 3-DOF system in Fig. 3.2 with Bouc-Wen oscillator is considered further where the time-dependent hysteresis displacement $\dot{z}$ is given by

$$\dot{z} = \frac{A(t)\,\dot{x}_1 - v(t)\,\beta\,|\dot{x}_1|\,|z|^{n-1} r - \gamma \dot{x}_1 |z|^n}{\eta(t)} \tag{3.45}$$

Table 3.2: Estimation error in % for 3-DOF Bouc-Wen system

Noise	Sigma	Parameters									Input	
	Points	k_1	k_2	k_3	c_1	c_2	c_3	β	γ	n	I_A	PGA
5%	UT	1.15	0.94	0.43	6.85	2.82	1.20	7.97	2.12	2.27	2.17	0.49
	CQ	0.97	0.9	0.47	6.98	2.83	1.25	8.38	4.67	2.18	2.23	0.47
10%	UT	0.95	0.89	0.48	6.09	3.9	1.51	10.01	5.67	3.16	1.90	1.00
	CQ	0.76	0.82	0.43	5.83	3.26	0.87	5.63	2.87	1.26	1.13	1.17
15%	UT	0.74	0.71	0.39	6.47	3.82	1.35	12.10	6.96	3.64	1.05	1.77
	CQ	0.94	0.79	0.14	5.6	1.91	0.61	11.66	2.67	3.36	0.71	0.80

In the above model, $A(t)$, $\upsilon(t)$, and $\eta(t)$ are the functions responsible for the degradation of the Bouc-Wen system. These are proportional to energy dissipation $\varepsilon(t)$ of the system, which can be written as

$$\varepsilon(t) = \int_0^t z\dot{x}\, dt \tag{3.46}$$

It should be noted that hysteretic energy is a good indication of response severity and deterioration. To include the effects of duration and severity, $A(t)$, $\upsilon(t)$, and $\eta(t)$ are defined as the function of $\varepsilon(t)$ as follows [145]

$$A(t) = 1.0 - \delta_a \varepsilon(t) \tag{3.47a}$$
$$\nu(t) = 1.0 + \delta_\nu \varepsilon(t) \tag{3.47b}$$
$$\eta(t) = 1.0 + \delta_\eta \varepsilon(t) \tag{3.47c}$$

The parameters of the 3-DOF system and the input excitation are kept unchanged. Additional parameters are considered to be $\delta_a = \delta_\nu = \delta_\eta = 0.5$. Using these parameters, the response is simulated due to the Kobe earthquake and the noise (as mentioned in the previous exercise) are added to replicate the actual measurement. However, the simulated time histories (i.e. measurements) are not shown here to avoid repetition. Using these time histories, the proposed CMVU algorithm is invoked to study its performance for a degrading system.

The estimated parameters and the input corresponding to the different noise levels and sigma point generation scheme are summarized in Table 3.3. The identified values of stiffness and damping coefficient are generally below 10% indicating good accuracy. Both the schemes are capable of identifying the stiffness and damping parameters as evident from Table 3.3. To demonstrate the performance further for the degrading systems, the hysteretic energy (E_H) dissipation during the event is also included in the same table, which is obtained from the area between the hysteretic force i.e $k_1 z$ and the total displacement. It is found that the relative estimation error of the degrading hysteretic is below 10% for all the noise levels, providing a good level of accuracy. However, when comparing the performance of UT sigma points to CQ sigma points, UT sigma points showed marginally better accuracy in estimating

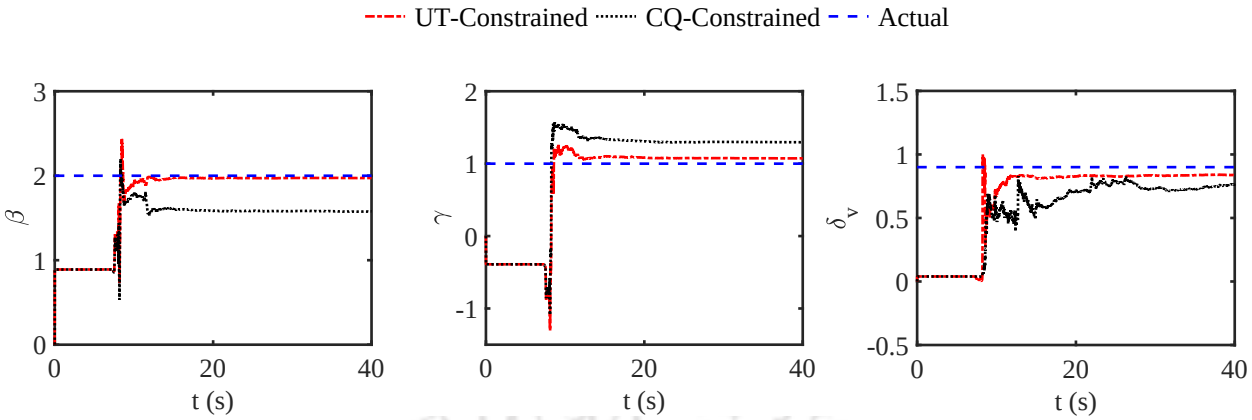

Figure 3.5: Identification of Bouc-Wen parameters of the degrading system

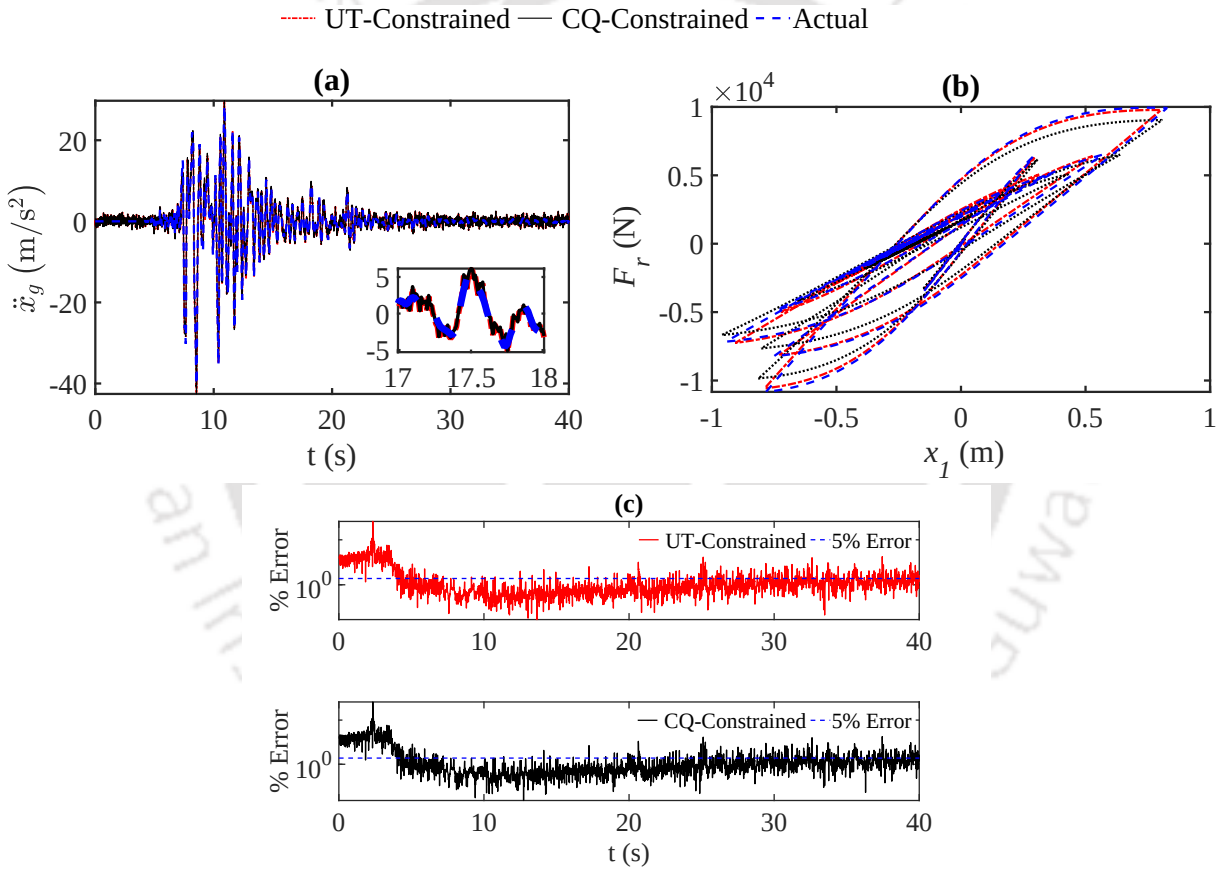

Figure 3.6: Joint parameters and input estimation of degrading Bouc-Wen system for 5% noise; (a) input (b) force deformation relationship, and (c) percentage error in input estimation

hysteretic energy (E_H) as shown in Table 3.3. Similar performance can be observed in the time-history plots of Bouc-Wen parameters (see Fig. 3.5). It is worth mentioning that the relative estimation error of E_H is showing linearly increasing behaviour with respect to the

Table 3.3: Estimation error in % for 3-DOF degrading Bouc-Wen system

Noise	Sigma	Parameter Estimation							Input Estimation	
level	points	E_H	k_1	k_2	k_3	c_1	c_2	c_3	I_A	PGA
5%	UT	4.30	2.99	1.99	0.97	8.09	3.70	1.47	1.39	1.41
	CQ	6.11	3.02	2.15	0.97	10.05	4.41	1.55	1.73	1.74
10%	UT	7.16	2.04	1.64	1.17	6.67	3.06	1.52	2.09	2.37
	CQ	8.18	2.13	1.41	1.12	7.38	4.01	2.56	1.98	1.84
15%	UT	8.48	6.52	2.72	1.01	10.95	4.61	5.37	4.59	3.24
	CQ	8.93	6.25	3.26	1.04	11.85	5.14	6.63	4.82	3.69

level of noise. A similar observation is also made for the stiffness and damping parameters, i.e 5% noise level show minimum relative percentage error while 15% noise level show maximum relative percentage error. Further, the CMVU estimation of input using both UT and CQ sigma points shows an almost identical result (Fig. 3.6a). The estimated input is converged to the actual value after a few second as implied by the error norm in Fig. 3.6c. Besides these parameters, arias intensity (I_A) and PGA are also estimated with a significant level of accuracy (i.e. the error is below 5% as shown in Table 3.3). The estimated hysteresis using CMVU is matched closely with the actual one (see Fig. 3.6b), indicating the excellent performance of the CMVU algorithm.

3.5 CMVU for Reinforced Concrete Structures

In this section, experimental results are presented to show the performance of the proposed CMVU algorithm for the input and parameter identification of a hysteretic RC structure characterized by the Bouc-Wen model. The primary emphasis of this study is to explore the scope of the proposed algorithm for hysteretic parameter estimation of the reinforced concrete structure, which is otherwise difficult by signal processing approach suitable for model characterization of a large class of dynamical systems. However, before experimental verification, a simulation exercise is carried out using actual Bouc-Wen parameters with degradation and pinching, obtained from the slow cyclic test of a reinforced concrete frame. The details of the Bouc-Wen model is presented below.

3.5.1 Bouc-Wen-Baber-Noori Model of Hysteresis

Although the Bouc-Wen model in Eq. 3.1 is capable of characterizing different hysteretic behaviour; it is not sufficient to model a reinforced concrete structure. It is because degradation and pinching are commonly associated with a reinforced concrete structure under severe loading. To accommodate these two phenomena, the Bouc-Wen-Baber-Noori (BWBN) hysteretic model was proposed in the literature [171]. Though the expression of the restoring force remains same as in Eq. 3.1a, the relationship between $z(t)$ and $x(t)$ is modified by the following expression

$$\dot{z}(t) = h(t)\,\frac{A\dot{x}(t) - \nu(t)\left(\beta\,|\dot{x}(t)|\,|z(t)|^{n-1}z(t) + \gamma\dot{x}(t)\,|z(t)|^{n}\right)}{\eta(t)} \tag{3.48}$$

In general, the effect of parameter A on the overall hysteresis is nominal and it is set to unity in most of the cases [172]. In Eq. 3.48, functions $\nu(t)$, $\eta(t)$ and $h(t)$ are responsible for strength degradation, stiffness degradation and pinching effects, respectively. Typically, strength and stiffness degradation depend on the duration and severity of the excitation, which is reflected in the cumulative hysteretic energy as follows

$$\varepsilon(t) = \int_0^t z\dot{x}\mathrm{d}t \tag{3.49}$$

Both these functions, $\nu(t)$ and $\eta(t)$ are assumed to vary linearly with $\varepsilon(t)$ as follows

$$\nu(t) = 1 + \delta_v\varepsilon(t) \tag{3.50a}$$
$$\eta(t) = 1 + \delta_\eta\varepsilon(t) \tag{3.50b}$$

where δ_v and δ_η are the constants specified for the rate at which strength and stiffness degradation take place. Finally, the pinching function $h(t)$ can be expressed as follows [173]

$$h(t) = 1 - \zeta_1(t)\exp\left(-\frac{\left(\mathrm{z}(\mathrm{t})\,\mathrm{sign}\left(\dot{\mathrm{x}}(\mathrm{t})\right) - \mathrm{qz_u}\right)^2}{\left(\zeta_2(\mathrm{t})\right)^2}\right) \tag{3.51}$$

where sign(.) represent the signum function and z_u is the ultimate value of $z(t)$ which is given by

$$z_u = \nu(t)\left(\beta + \gamma\right)^{-\frac{1}{n}} \tag{3.52}$$

The two functions $\zeta_1(t)$ and $\zeta_2(t)$ in Eq. 3.51 control the development of pinching behaviour, which are modelled by the expressions below

$$\zeta_1(t) = \left(1 - e^{-p\varepsilon(t)}\right)\zeta_0 \tag{3.53a}$$
$$\zeta_2(t) = \left(\psi_0 + \delta_\psi\varepsilon(t)\right)\left(\lambda + \zeta_1(t)\right) \tag{3.53b}$$

In the above equation, p determines the slope of the initial drop in the pinching region while ζ_0, ψ, δ_ψ and λ control the rate and amount of pinching of the hysteresis loops. Altogether, there are 12 parameters present in the BWBN model i.e. $\mathbf{C} = \{\alpha, \beta, \gamma, n, \delta_v, \delta_\eta, q, p, \zeta_0, \psi, \delta_\psi, \lambda\}$. In the forward problem, these parameters are obtained by solving an optimization problem to match the recorded load-displacement behaviour. However, this study is aimed to identify these parameters from the measured inelastic response time histories.

3.5.2 Validation Using Synthetic Experiment

In this example, a 3-DOF system is simulated using BWBN model as shown in Fig. 3.2. The hysteresis behaviour is modelled using the optimized parameters of a reinforced concrete frame. For this purpose, a single-bay single-storey reinforced concrete frame was tested in

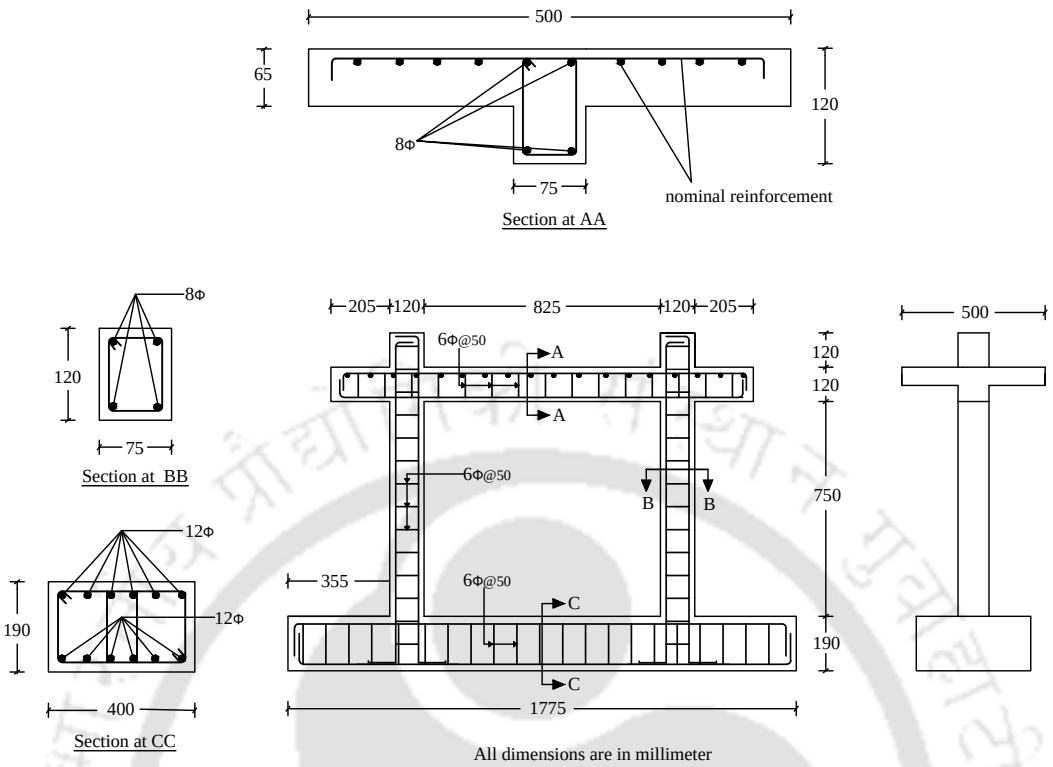

Figure 3.7: Details of frame

the Structural Engineering Laboratory of Indian Institute of Technology Guwahati by Nithin [174], which is used in this thesis only for realistic estimation of Bouc-Wen parameters for simulation. The test specimen was constructed using M25 grade of concrete and Fe500 grade steel, whose reinforcement details are given in Fig. 3.7. The overview of this experimental setup is shown in Fig. 3.8a. A Servo-hydraulic dynamic actuator (Make: MTS, USA) of capacity 250 kN with a maximum stroke of ±125 mm is used to apply lateral load as shown in Fig. 3.8b. Steel Bolts and concrete blocks are used to maintain the fixity of the base with the strong floor. A 2 tonnes weight is placed on the frame for the realistic axial load on the column. The actuator force is measured using an inbuilt load cell and displacement of the frame is obtained from a laser displacement sensor, as shown in Fig. 3.8b. The specimen is subjected to a cyclic displacement loading with a gradual increase of amplitudes and the data is recorded with a sampling frequency of 100 Hz. Fig. 3.10a and Fig. 3.10b show the time histories of displacement and force. Using these recorded responses, the BWBN model described in Section 3.5.1 is optimized to obtain its parameters. For this purpose, a multi-objective optimization is carried out using NSGA-II toolbox developed by Ortiz et al. [175]. The objective functions used in this study are given by

1. The absolute error between the displacements $\mathbf{x_n}(t)$ measured experimentally and the same $\hat{\mathbf{x}}_\mathbf{n}(t\,|\mathbf{C})$ obtained from the Bouc-Wen model of hysteresis for a given set of

parameters $\mathbf{C}$ i.e.

$$f_1(\mathbf{C}) = \sum_{i=1}^{n} |x(t_i) - \hat{x}(t_i|\mathbf{C})| \tag{3.54}$$

2. The maximum error between experimentally measured displacement $\mathbf{x_n}(t)$ and the predicted displacement responses $\hat{\mathbf{x}}_\mathbf{n}(t|\mathbf{C})$ from the model i.e.

$$f_2(\mathbf{C}) = \max_{1 \leqslant i \leqslant n} \{x(t_i) - \hat{x}(t_i|\mathbf{C})\} \tag{3.55}$$

(a)

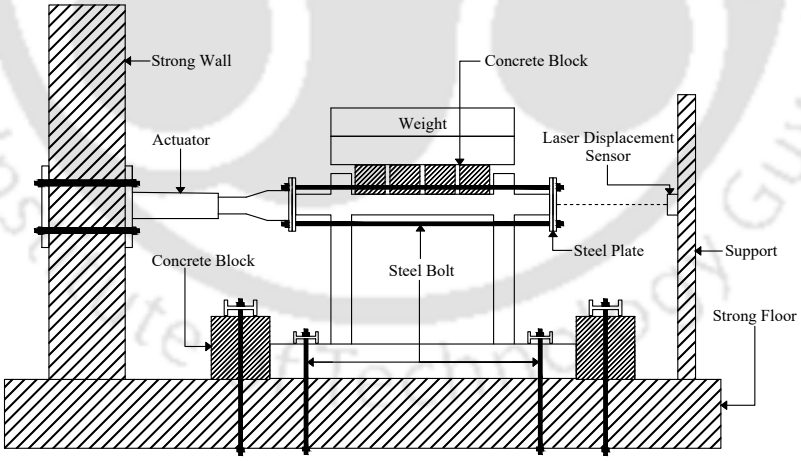

(b)

Figure 3.8: Overview of experimental setup; (a) actual test setup and (b) schematic diagram

Fig. 3.9 shows the Pareto optimal front from the set of solutions of the optimization algorithm. The solution, which corresponds to the minimum Euclidean distance from the origin,

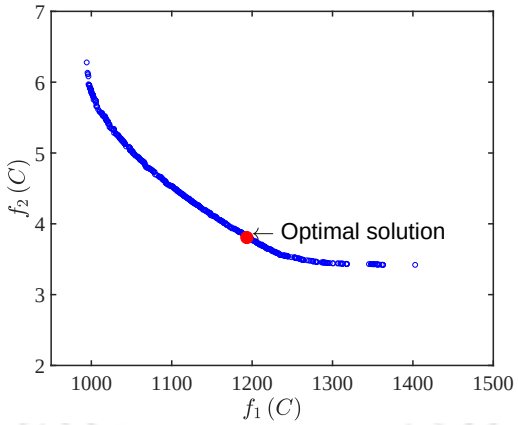

Figure 3.9: Pareto optimal solution for Bouc-Wen model

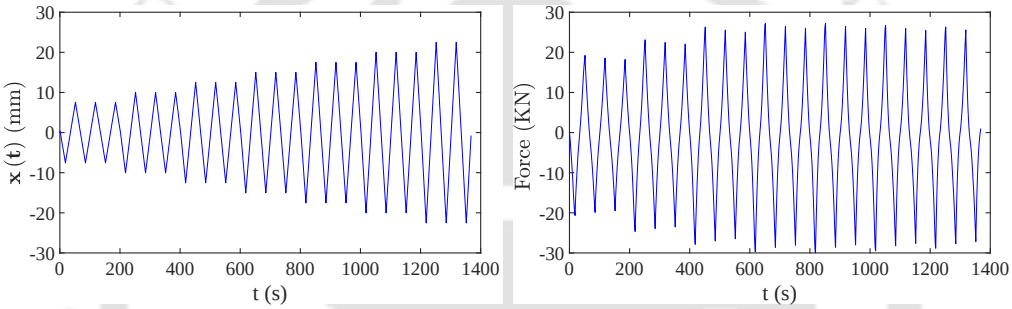

(a) **(b)**

Figure 3.10: Pseudo-dynamic test result; (a) displacement, and (b) force

is considered as the unique optimal solution satisfying both the objective functions. The parameter bounds enforced in this optimization are as proposed by Loh et al. [176]. The experimental and estimated hysteresis plots are demonstrated in Fig. 3.11, whose optimal parameters are given in Table 3.4.

Once the hysteresis model is established, response of the 3-DOF system are simulated, whose equation motion can be expressed as

$$m_1\ddot{x}_1 + c_1\dot{x}_1 + c_2\left(\dot{x}_1 - \dot{x}_2\right) + \alpha k_1 x_1 + (1-\alpha)\,k_1 z + k_2\left(x_1 - x_2\right) = -m_1\ddot{u}_g \tag{3.56a}$$

$$m_2\ddot{x}_2 + c_2\left(\dot{x}_2 - \dot{x}_1\right) + c_3\left(\dot{x}_2 - \dot{x}_3\right) + k_2\left(x_2 - x_1\right) + k_3\left(x_2 - x_3\right) = -m_2\ddot{u}_g \tag{3.56b}$$

$$m_3\ddot{x}_3 + c_3\left(\dot{x}_3 - \dot{x}_2\right) + k_3\left(x_3 - x_2\right) = -m_3\ddot{u}_g \tag{3.56c}$$

where the restoring force (F_r) for the hysteretic component can be defined as Eq. 3.1a. The additional constitutive equations needed to define the numerical model are provided by Eq. 3.48 - Eq. 3.53b. The mass for all three degrees of freedom is assumed to be same i.e. 1120 kg. Similarly, the stiffness in the two upper stories are equal i.e. 3.5×10^6 N/m. The first storey column is modelled by the Bouc-Wen hysteresis, whose parameters are given in Table 3.4. The initial stiffness of this storey is also same as the stiffness of the upper stories. Further, the damping coefficients for the second and third storey are assumed to be equal

Table 3.4: Hysteresis parameters for frame

Parameters	P_{min}	P_{max}	Optimized Values
ξ	0.02	0.2	0.1990720000
α	0.01	1	0.1530370000
β	0.3	1.3	0.3001838000
γ	-0.3	0.3	-0.2838606000
n	1	6	1.0003970000
δ_ν	0	1	0.0047967490
δ_η	0	1	0.0000000588
p	0	5	2.7916030000
ζ_0	0	1	0.9265840000
ψ_0	0	0.2	0.1999966000
δ_ψ	0	0.01	0.0021046610
λ	0	1	0.9994293000
q	0	0.03	0.0000212757

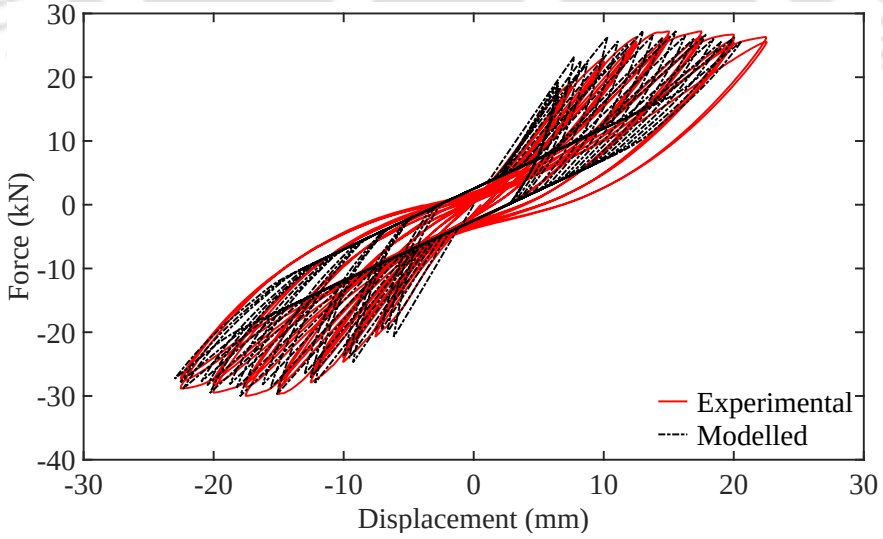

Figure 3.11: Experimental and estimated hysteretic behaviour of frame

(i.e. 6272 Ns/m), while the first storey has a damping coefficient of 24962 Ns/m. Imperial Valley earthquake record (1940) is applied to the support and measurements (displacements and accelerations) are generated using 4^{th} order the Runge-Kutta integration scheme. A zero mean Gaussian white noise is added to the measurements to replicate the actual experimental observations.

To apply the CMVU algorithm, the extended state vector is formed as in Eq. 3.12 i.e. $\mathbf{\Lambda} = \{ \; x_1 \quad x_2 \quad x_3 \quad \dot{x}_1 \quad \dot{x}_2 \quad \dot{x}_3 \quad z \; \}$, $\mathbf{\Theta} = \{ \; \alpha \quad n \quad \delta_\nu \quad \delta_\eta \quad p \quad \zeta_0 \quad \psi_0 \quad \delta_\psi \quad \lambda \quad q \; \}$ and $\mathbf{w} = \{ \; k_1 \quad k_2 \quad k_3 \quad c_1 \quad c_2 \quad c_3 \; \}$. The initial guess of the parameters in CMVU algorithm are assumed to be $k_1 = k_2 = k_3 = 2.5 \times 10^6$ N/m, $c_1 = 20000$ Ns/m and $c_2 = c_3 = 4000$ Ns/m. Similarly, initial values of the BWBN parameters are assumed to be $\alpha = 0.23, \beta = 0.04, \gamma = 0.03, n = 2, \delta_\nu = 0.0025, \delta_\eta = 4 \times 10^{-8}, p = 3, \zeta_0 = 0.51, \psi_0 = 0.08, \delta_\psi = 6 \times 10^{-4}, \lambda = 0.9, q = 6.2 \times 10^{-6}$. The bounds related to parameter $\mathbf{\Theta}$ have been incorporated as constrained conditions using Eq. 3.4, which are $0 \leq p \leq 5$; $1 \leq n \leq 6$. Except p and n, all other parameters within $\mathbf{\Theta}$ are considered to be bounded between the interval $[0, 1]$. Similarly, BIBO property is also maintained using Eq. 3.5. The displacement and acceleration responses of all three DOF i.e. $\begin{bmatrix} x_1 & x_2 & x_3 & \dot{x}_1 & \dot{x}_2 & \dot{x}_3 \end{bmatrix}^T$ are considered as measurements. In this numerical analysis, the nomenclature for the algorithm using constraints with unscented points is 'UT-Constrained' and the same with cubature quadrature points is 'CQ-Constrained'. Fig. 3.12 shows the stiffness and damping parameters obtained from the CMVU algorithm under the different sigma point generation schemes for the 2% RMS noise level. For brevity, time histories of these parameters for 5% RMS noise level are not shown. The identification results are summarized in Table 3.5 in terms of relative percentage estimation error, which is defined as $\frac{|\theta_{est} - \theta_{true}|}{\theta_{true}} \times 100$. Here, θ_{est} represents the estimate of parameter θ at the end of the iterations, whereas θ_{true} denotes the actual value of the same parameter. From Fig. 3.12, it can be concluded that both type of sigma points have converged to the actual values of parameters with reasonable accuracy i.e. within 10% relative percentage error with 2% measurement noise. It is observed that identified parameters from the cubature points have shown a significant amount of error than unscented sigma points for 5% noise level. The identified parameters related to hysteretic behaviour are shown in Fig. 3.13. In this case, it is also found that unscented points offer significantly less error as compared to cubature points.

To investigate it further, the error in hysteretic energy (E_H) dissipation between the actual and estimated is defined as a collective measure for all these hysteretic parameters. It is important to note that the hysteretic energy is computed as the area under the restoring force (F_r) and displacement (x_1), which depends on the identified parameters of the BWBN model. Although these parameters are converged within the respective bounds, unscented points have a distinct advantage over cubature points, as shown in Fig. 3.13. The under performance of cubature points is reflected in the estimated hysteresis, as shown in Fig. 3.14b. In this context, the complete set of unknown parameters of the hysteresis are listed in Table 3.6 for different noise levels. Here, it may be noted that these parameters mostly have very small numerical values. Moreover, different combinations of these parameters can provide the same level of load-deformation characteristics. Therefore, as the main objective is to identify the phenomenological model and input, the energy dissipated by the hysteresis and the ground motion characteristics have remained in the focus of this study. The relative

error in hysteretic energy also indicates better accuracy of unscented points over cubature points corresponding to both 2% and 5% noise levels, as in Table 3.5. The accuracy of the identified unknown input is characterized with the help of Arias intensity (I_A) and peak ground acceleration (PGA). The identified input matches the actual one accurately for the 2% noise level, as shown in Fig. 3.14a, where the relative estimation errors in Arias intensity and peak ground acceleration are within 5%. However, as the noise level increases (i.e. 5% noise level), the performance corresponding to cubature points is unsatisfactory, which leads to a higher percentage error in estimated input. It has been observed that at low noise level (i.e. 2% noise), both unscented and cubature points provide a good estimate with reasonable accuracy. However, unscented points out-perform the cubature points when the measurement noise is relatively high. This deterioration of the performance of cubature points is envisaged due to the omission of the central sigma point, which is the significant difference between these two sigma points generation schemes [177]. In general, the performance of CMVU is susceptible to the amount of measurement noise. In such cases, unscented points should be preferred over cubature points as it has better accuracy and more robustness to handle the complexity.

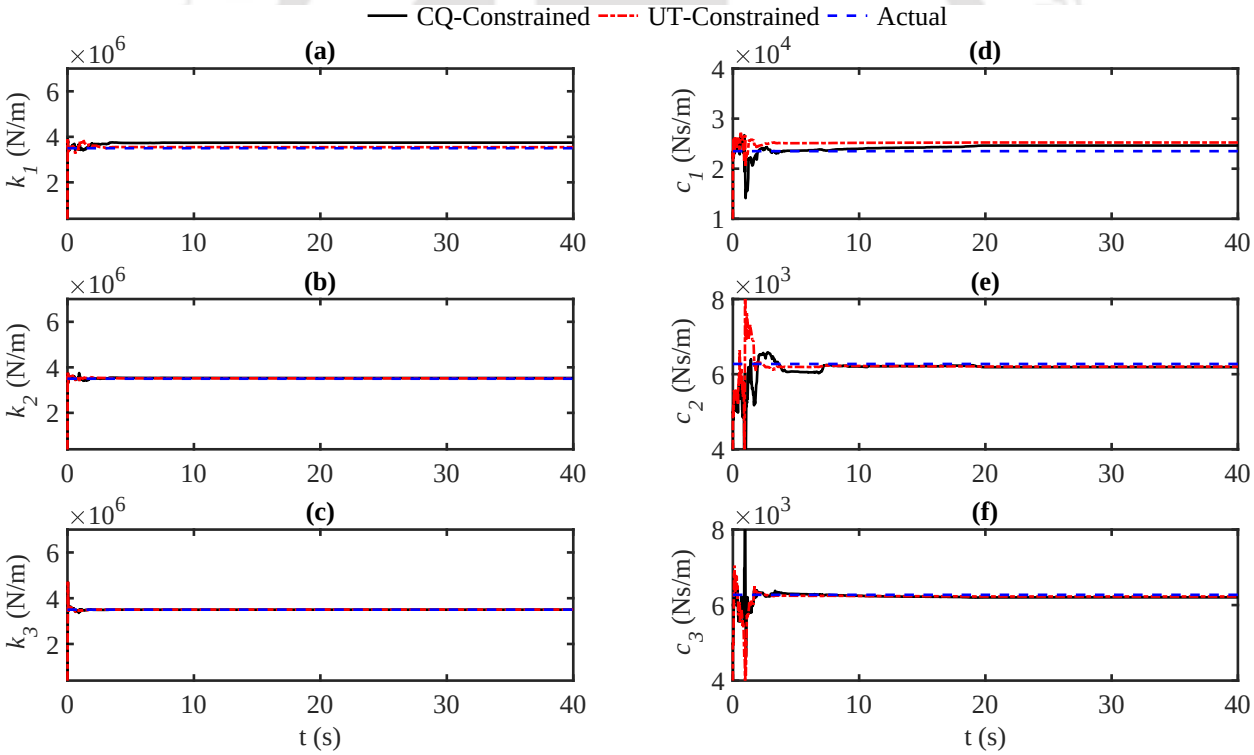

Figure 3.12: Identified stiffness and damping parameters of 3-DOF BWBN model for 2% measurement noise; (a) stiffness in storey 1, (b) stiffness in storey 2, (c) stiffness in storey 3, (d) damping in storey 1, (e) damping in storey 2 and (f) damping in storey 3

Table 3.5: Estimation error for 3-DOF BWBN model

Noise	Sigma	% Parameter Estimation							% Input	
level	points	E_H	k_1	k_2	k_3	c_1	c_2	c_3	I_A	PGA
2%	UT	2.34	1.28	0.48	0.126	0.92	1.13	0.70	0.57	1.161
	CQ	30.19	6.97	0.87	0.37	1.51	1.36	1.07	2.58	3.60
5%	UT	10.51	14.19	0.17	0.02	0.37	1.53	0.19	0.33	1.56
	CQ	44.72	26.59	24.08	3.50	113.07	106.49	2.1	162.10	67.37

Table 3.6: Summary of identified BWBN model parameters

Parameters	Exact	2% Noise		5% Noise	
	Values	UT	CQ	UT	CQ
α	0.15304	0.14541	0.10262	0.10436	0.47153
β	0.30018	0.30830	0.30184	0.32548	0.94650
γ	-0.28386	-0.28524	-0.26230	-0.22961	0.06007
n	1.00040	1.10432	1.15364	1.64235	2.56780
δ_ν	0.00480	0.00401	0.00285	0.00183	0.01168
δ_η	5.88E-08	3.88E-08	3.74E-08	3.96E-08	5.78E-08
p	2.79160	4.86572	0.21588	3.32743	0.14353
ζ_0	0.92658	0.92539	0.88995	0.90953	0.67136
ψ_0	0.20000	0.24862	0.79168	0.24295	0.06761
δ_ψ	0.00210	0.00246	0.00222	0.00269	0.10607
λ	0.99943	0.68442	0.00036	0.97471	0.19703
q	2.13E-05	4.12E-05	9.92E-06	5.55E-05	6.23E-06

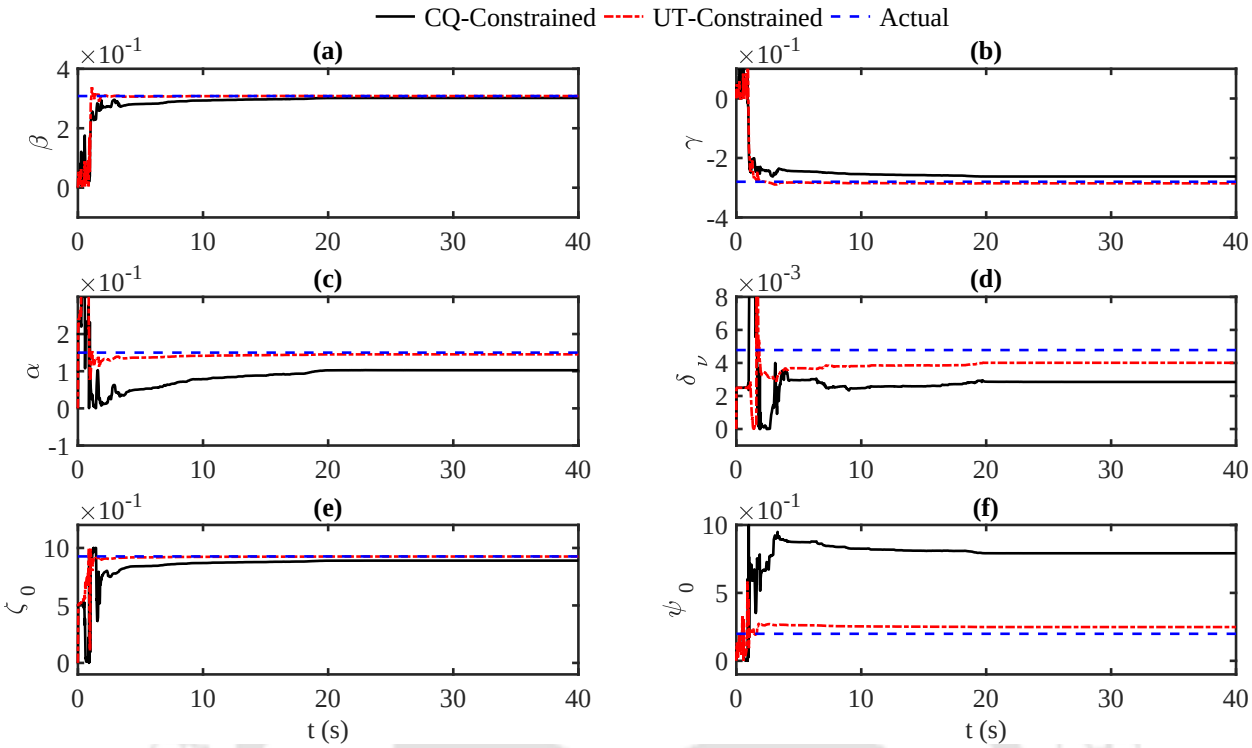

Figure 3.13: Identified hysteretic parameters for 3-DOF BWBN model for 2% measurement noise; (a) β, (b) γ, (c) α, (d) δ_ν, (e) ζ_0 and (f) ψ_0

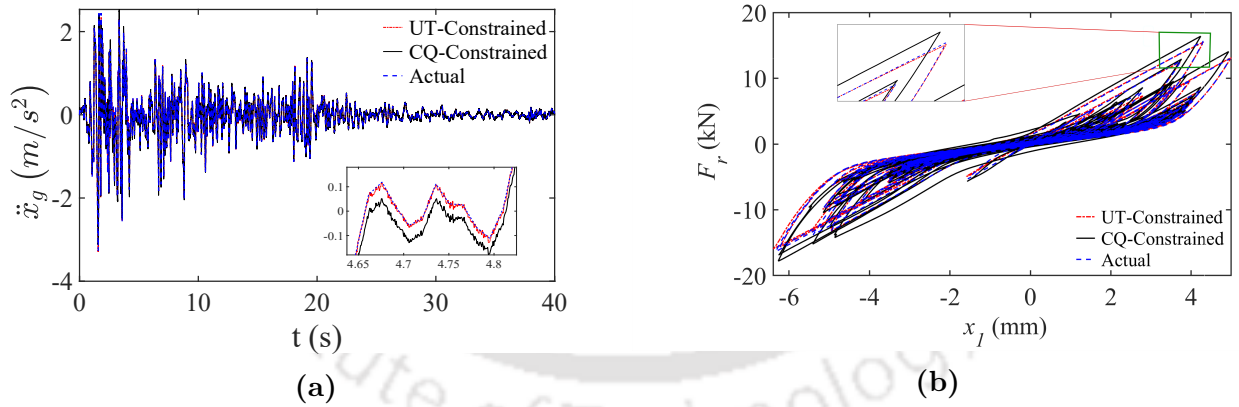

Figure 3.14: Estimation of input and BWBN parameters for 2% measurement noise; (a) support excitation and (b) hysteresis

3.5.3 Bridge Pier Test

Once the constrained minimum variance unbiased estimation algorithm is validated using synthetic experiment, its performance is further tested for full-scale reinforced concrete structure, which is the main objective of this study. For this purpose, the shake table test data of a bridge pier is used for further demonstration of the algorithm. The details of the experimental setup and the performance of this technique are described below.

3.5.3.1 Experimental Setup

The experimental details of a full-scale circular reinforced concrete bridge pier under uni-axial seismic excitation are described here. The test was carried out in NEES-UCSD large High-Performance Outdoor Shake Table as shown in Fig. 3.15a. The tests data are available in DESIGNSAFE-CI [178] platform under the project name NEES-2010-0987 [179]. The test specimen was a circular column of diameter 1.22 m and length 7.32 m. A concrete block weighing 2245 kN having the shape of cruciform was cast such that its center of mass coincided with the top of the column. The detailed information about the instrumentation and the loading protocol are available in the PEER report no. 2015/02 [180]. The structure was subjected to different earthquake excitations in succession corresponding to the different intensity levels. Among these sequences, EQ5 has been selected for this study as a distinguishable non-linear response observed during the experiment in the form of damage. The sensor placement has been shown in Fig. 3.15b in which the naming of the sensors is kept consistent with the original data file available in the DESIGNSAFE-CI platform.

3.5.3.2 Results and Discussion

The performance of the proposed CMVU algorithm on the test structure is presented here. For this purpose, the bridge pier is modelled as a 2-DOF system subjected to ground excitation, as shown in Fig. 3.15b. During the experiment, it was observed that damage was concentrated at the base of the pier and hence the material non-linearity at this location was modelled by Bouc-Wen hysteresis. As the axial load ratio is not very significant (i.e. 5.3%), stiffness degradation and pinching were unlikely to occur during the experiment. Hence, a non-degrading classical Bouc-Wen model is adopted in this case. The equation of motion of this system can be expressed as follows

$$m_1\ddot{x}_1 + c_1\dot{x}_1 + c_2\left(\dot{x}_1 - \dot{x}_2\right) + \alpha k_1 x_1 + \left(1-\alpha\right)k_1 z + k_2\left(x_1 - x_2\right) = -m_1\ddot{u}_g \tag{3.57a}$$

$$m_2\ddot{x}_2 + c_2\left(\dot{x}_2 - \dot{x}_1\right) + k_2\left(x_2 - x_1\right) = -m_2\ddot{u}_g \tag{3.57b}$$

where x_1 and x_2 represent the two degrees of freedom while the over-dot denotes the differentiation with respect to time. Also, k_1 and k_2 represent the stiffness coefficients corresponding to x_1 and x_2, respectively, whereas c_1 and c_2 denote their damping coefficients. The mass at each degree of freedom (i.e. m_1 and m_2) is known, which is calculated from the structural drawings. The hysteretic component $z(t)$ needed to define this model is the same as in Eq. 3.1b. The extended state vector is corresponding to this model using Eq. 3.12 are $\mathbf{\Lambda} = \left\{ \begin{array}{ccccc} x_1 & x_2 & \dot{x}_1 & \dot{x}_2 & z \end{array} \right\}$, $\mathbf{\Theta} = \left\{ \begin{array}{cc} n & \alpha \end{array} \right\}$ and $\mathbf{w} = \left\{ \begin{array}{cccc} k_1 & k_2 & c_1 & c_2 \end{array} \right\}$. The measurement vector is composed of recorded accelerations $\ddot{x}_1$ and $\ddot{x}_2$ (i.e. AM02E and AM09E readings) and displacement x_2 (i.e. S8E readings), which is expressed as $\left\{ \begin{array}{ccc} x_1 & \ddot{x}_1 & \ddot{x}_2 \end{array} \right\}$. The measurement noise associated with these responses are considered to be zero mean Gaussian, whose covariance matrix R_k consists of diagonal elements only. The bounds for the parameters and BIBO property of the Bouc-Wen model are kept the same as in the previous example. The initial values of the unknown parameters are assumed as $k_1 = k_2 = 5 \times 10^6$ N/m, $c_1 = 5 \times 10^4$ Ns/m, $c_2 = 1.5 \times 10^4$ Ns/m, $\alpha = 0.15, \beta = 0.04, \gamma = 0.03$ and $n = 1$.

Fig. 3.16 demonstrates the identified stiffness and damping coefficients corresponding to different types of sigma points. Moreover, a comparative study is provided to show the

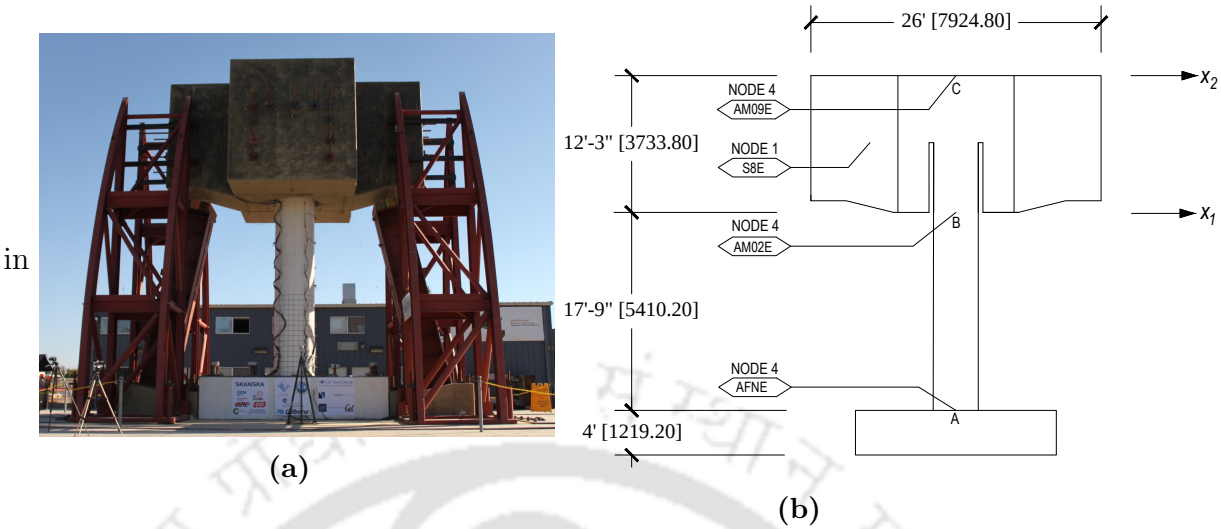

Figure 3.15: Full-scale bridge pier test; (a) Experimental test setup and (b) schematic diagram of test setup with sensor locations.

effectiveness of the proposed CMVU algorithm over generalized minimum variance unbiased estimator, where no constrained conditions are incorporated. It is denoted as 'Unconstrained' in this study. The estimates of the model parameters are presented in Table 3.7. It is observed that all variants of the unbiased estimator algorithm achieved convergence at a time around 50 s. However, the unconstrained variant provides a negative value of the identified stiffness coefficient k_1 as shown in Fig. 3.16c, which does not have any physical meaning. Also, apart from the unscented variant of the CMVU algorithm (i.e. UT-Constrained), other algorithms converged to a negative value for the damping co-efficient c_2 as shown in Fig. 3.16b. Fig. 3.17 illustrates the final estimated values of parameters of the Bouc-Wen model. The effects of these identified parameters are also reflected in the hysteretic behaviour of the system, as shown in Fig. 3.18a. This figure reveals that the true nature of the hysteretic system is captured by the unscented points while the other fails miserably. Thus, it can successfully estimate the hysteresis energy, which serves as a basis for any energy-based damage index calculation. Besides damage estimation, the proposed CMVU algorithm has a major advantage as it can also estimate the input force, which is subsequently utilized in the non-linear system identification. Fig. 3.18b depicts the estimated input time-histories for all the cases and compares them with the actual signal (i.e. AFNE sensor in Fig. 3.15b). A close match of input time-history with the actual values for unscented sigma points indicates the estimated inputs has reasonable accuracy. Here, it is worthy to be note that when constrained conditions are omitted, the estimation shows instability as reported in Chatzi et al. [98]. This instability can be clearly observed in Fig. 3.18, which shows the drift. The estimated input time-history can be used further to refine the finite element model to study the damage more comprehensively.

Table 3.7: Estimated parameters for bridge pier

Method	k_1 (N/m)	k_2 (N/m)	c_1 (Ns/m)	c_2 (Ns/m)	α	β	γ	n
UT	5.12×10^6	1.25×10^7	2.52×10^4	2.60×10^4	0.01	101.59	-9.19	2.20
CQ	3.70×10^6	9.74×10^6	1.10×10^5	-4.79×10^4	0.98	125.94	-75.01	1.01
Unc	9.72×10^6	7.11×10^6	1.37×10^5	-2.90×10^4	0.31	-0.11	2.73	0.37

NB: UT, CQ and Unc denote CMVU algorithm with Unscented points, cubature quadrature and without constrained conditions, receptively.

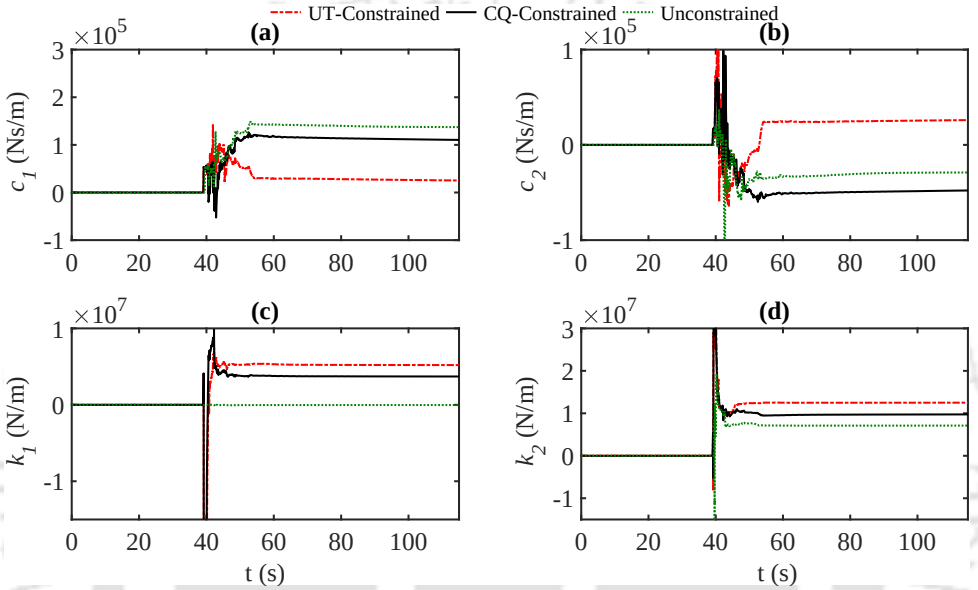

Figure 3.16: Estimated stiffness and damping coefficient of bridge pier; (a) c_1 (b) c_2 (c) k_1 and (d) k_2

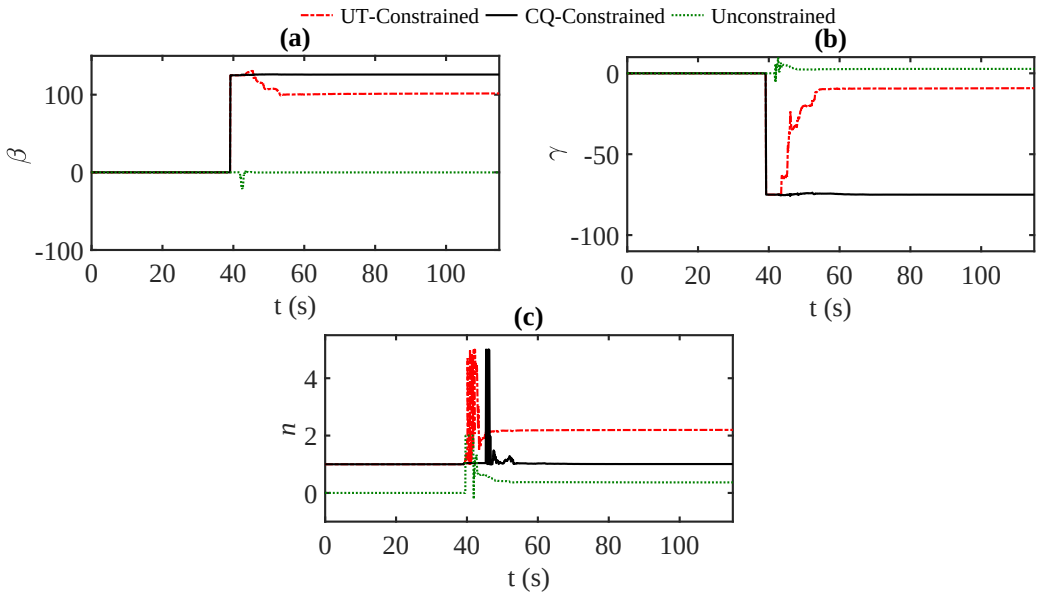

Figure 3.17: Estimated Bouc-Wen parameters for bridge pier; (a) β (b) γ and (c) n

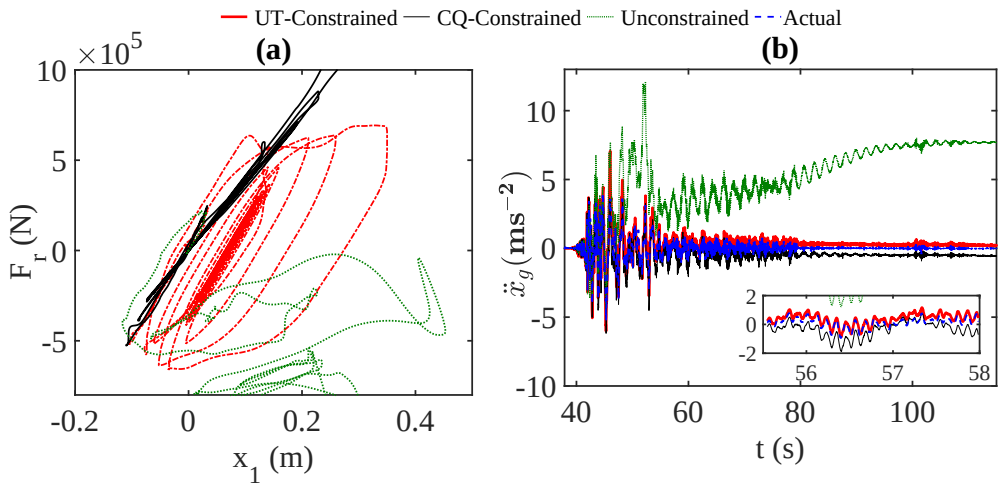

Figure 3.18: Comparison of different identification schemes; (a) hysteresis plots and (b) input time-histories

3.6 Quasi-Monte Carlo Points For Identification

The idea of approximating multidimensional Gaussian distribution through a collection of symmetric vector points centered on the mean has motivated researchers to develop different sigma point generation schemes. One such technique is quasi-Monte Carlo (QMC) scheme, which is discussed in this section. In this context, UKF may be considered as the benchmark, which performs better than EKF. However, UKF generates a few sigma points that may

not always adequate for the statistical moment estimation [181]. The systematic error is also observed in the sigma point approximation using the quadrature and cubature rules. To eliminate this error, a different point generation scheme can be adopted based on the stochastic integration rule. In this process, the expected value (μ) of a function $\varphi(\mathbf{x})$ is represented by

$$\mu = \mathbb{E}[\varphi(\mathbf{x})] = \int \varphi(\mathbf{x}) (2\pi)^{-n_x/2} e^{-\frac{1}{2}(\mathbf{x}-\tilde{\mathbf{x}})^T P_{\mathbf{x}}^{-1}(\mathbf{x}-\tilde{\mathbf{x}})} d\mathbf{x} \tag{3.58}$$

Here, it should be noted that $\mathbf{x} \sim \mathcal{N}(\tilde{\mathbf{x}}, \mathbf{P_x})$ is a multivariate Gaussian random variable. The solution of the above integral is provided by Genz and Monahan [182] based on the stochastic integration rule in the following steps

1. Select the maximum number of iteration N_{max} depending on the predefined tolerance ε
2. Initialize the iteration with $N = 0$ assuming solution of the integral $\tilde{\mu} = \mathbf{0}_{n_x \times 1}$ and error matrix $\mathbf{V} = \mathbf{0}_{n_x \times n_x}$
3. Continue the following iteration until $N = N_{max}$ or $\|V\| = \varepsilon$
   (a) Set $N = N + 1$
   (b) Generate a random number ρ from the Chi-square distribution i.e. $\rho \sim Chi(n_x + 2)$ and generate a uniformly random orthogonal matrix $\mathbf{U}$ of dimension $n_x \times n_x$
   (c) Compute the quasi-Monte Carlo points χ_i and corresponding weights w_i as

$$\chi_{\mathbf{0}} = \tilde{\mathbf{x}} \tag{3.59a}$$

$$\chi_{\mathbf{i}} = \tilde{\mathbf{x}} + \rho \mathbf{U} \left(\sqrt{\mathbf{P_x}}\right)_i \tag{3.59b}$$

$$\chi_{\mathbf{n_x+i}} = \bar{\mathbf{x}} - \rho \mathbf{U} \left(\sqrt{\mathbf{P_x}}\right)_i \tag{3.59c}$$

   In the above equation, $\left(\sqrt{\mathbf{P_x}}\right)_i$ is the i^{th} column of the matrix and $i = 1, 2, 3...n_x$. The corresponding weight may be expressed as

$$w_0 = 1 - \frac{n_x}{\rho^2} \tag{3.60a}$$

$$w_{n_x+i} = w_i = \frac{1}{2\rho^2} \tag{3.60b}$$

   (d) Finally, the solution of the integral $\tilde{\mu}$ and error matrix V after each iteration are given by

$$\tilde{\mu} = \tilde{\mu} + \mathbf{D} \tag{3.61a}$$

$$\mathbf{V} = \frac{(N-2)\mathbf{V}}{N} + \mathbf{D}\mathbf{D}^{\mathbf{T}} \tag{3.61b}$$

   In the above two equations, $\mathbf{D} = (\mathbf{S} - \tilde{\mu})/\mathbf{N}$ where $\mathbf{S}$ represents the weighted average of the integral in the current iteration i.e.

$$\mathbf{S} = \sum_{\mathbf{i=0}}^{\mathbf{2n_x}} \mathbf{w_i} \varphi(\chi_{\mathbf{i}}) \tag{3.62}$$

4. The value of the integral is approximated as $\mu = \tilde{\mu}$ at the end of step 3.

The quasi-Monte Carlo point generation scheme can be considered as a combination of cubature rule and Monte Carlo simulation. It utilizes the spherical integration rule to generate the quasi-Monte Carlo points located on n_x dimensional unit hyper-sphere. Also, the radial integration rule is used to control the spread of the points. A plot of weight vs the orientation of QMC points are compared with unscented points for a 2-dimensional case is shown in Fig. 3.19.

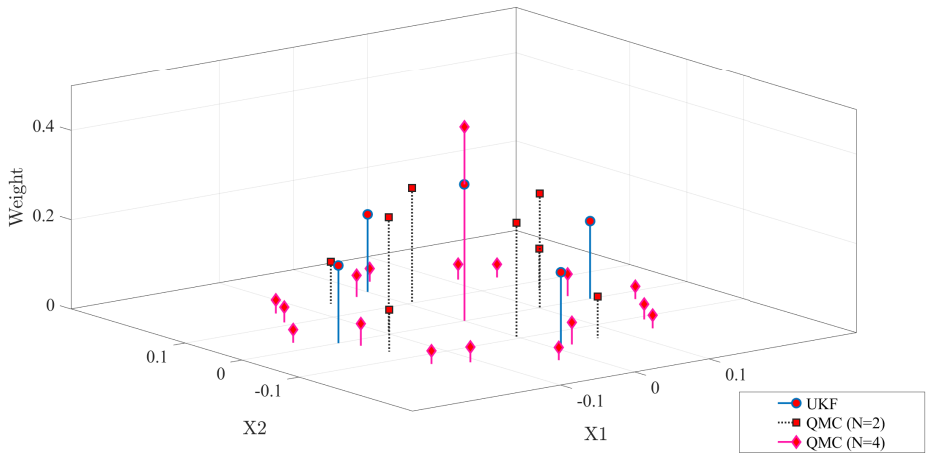

Figure 3.19: Configuration and weights of sigma points for 2-dimensional case

3.7 Numerical Results and Discussion

In this section, numerical findings are presented to demonstrate the performance of the proposed quasi-Monte Carlo Points for input-state-parameter estimation of a bridge pier characterized by the Bouc-Wen hysteresis. The aim of this investigation is to quantify the damage state of a reinforced concrete structure, which is otherwise difficult via signal processing. A simulation is carried out to establish the proposed technique with the help of actual Bouc-Wen parameters obtained from the pseudo-static experiment of a reinforced concrete frame.

3.7.1 Validation Using Synthetic Experiment

In this case, a 3-DOF system is simulated in which non-linear Bouc-Wen hysteresis is used as shown in Fig. 3.20. The non-linear response of this reinforced concrete structure is modeled with the help of the BWBN hysteretic model as explained in Section 3.5.1. The equation of motion for this system can be written as

$$m_1\ddot{x}_1 + c_1\dot{x}_1 + c_2\left(\dot{x}_1 - \dot{x}_2\right) + \alpha k_1 x_1 + (1-\alpha)\,k_1 z + k_2\left(x_1 - x_2\right) = -m_1\ddot{u}_g \tag{3.63a}$$

$$m_2\ddot{x}_2 + c_2\left(\dot{x}_2 - \dot{x}_1\right) + k_2\left(x_2 - x_1\right) = -m_2\ddot{u}_g \tag{3.63b}$$

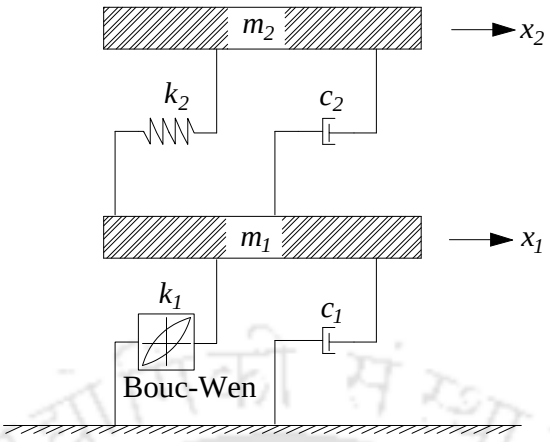

Figure 3.20: Hysteretic structural system.

The constituent equations for this computational model are given by Eq. 3.50b - Eq. 3.53b. In this analysis, $m_1 = m_2 = 1120\,\text{kg}$, $k_1 = k_2 = 3.5 \times 10^6\,\text{N/m}$, $c_1 = c_2 = 6000\,\text{Ns/m}$. The optimized values of the BWBN parameters obtained from pseudo-static test data [183] are given in Table 3.4. Measurements of this system are simulated artificially using 4^{th} order Runge-Kutta integration scheme by applying ground motion at the base. The measurements consist of displacements and accelerations time histories due to Imperial Valley 1940 ground motion. To replicate the actual measurement, the responses are polluted with additive zero-mean Gaussian white noise.

The application of the proposed technique involves the formation of an extended state vector ($\mathbf{Z}$) where unknown parameters are represented by $\mathbf{\Phi_k} = \{\ \mathbf{\Theta}\ \ \beta\ \ \gamma\ \ \mathbf{w}\ \}$. Thus, the complete unknown parameter vectors are $\mathbf{\Theta} = \{\ \alpha\ \ n\ \ \delta_\nu\ \ \delta_\eta\ \ p\ \ \zeta_0\ \ \psi_0\ \ \delta_\psi\ \ \lambda\ \ q\ \}$ and $\mathbf{w} = \{\ k_1\ \ k_2\ \ c_1\ \ c_2\ \}$. Initialization of the algorithm is carried out with the following guesses : $k_1 = k_2 = 2.5 \times 10^6\,\text{N/m}$, $c_1 = c_2 = 3000\,\text{Ns/m}$, $\alpha = 0.1$, $\beta = 0.04, \gamma = 0.03, \delta_\nu = 0.22, \delta_\eta = 0.01, p = 0.4, \zeta_0 = 1.10, \psi_0 = 0.58, \delta_\psi = 0.15, \lambda = 0.57$ and $q = 0.05$. To maintain the specific bounds of the Bouc-Wen parameters, a change of variable is performed using Eq. 3.4 while the BIBO properties are maintained using Eq. 3.5. The bounds applied to this example are $0 \leq p \leq 5$; $1 \leq n \leq 6$. All other parameters in $\mathbf{\Theta}$ are assumed to be bounded between the interval $[0, 1]$ to achieve stable convergence. To mitigate the drift in the recursive state-parameter-input identification of the non-linear systems, heterogeneous data (i.e., acceleration and displacement) are used as also proposed by Lei et al. [153]. Therefore, along with the acceleration response, displacement time histories are also included in the measurement vector, i.e. $\mathbf{y} = \left[\ x_1\ \ x_2\ \ \ddot{x}_1\ \ \ddot{x}_2\ \right]^T$.

In this numerical example, the performance of the proposed quasi-Monte Carlo algorithm is compared with the algorithm based on unscented transformed points (UT). The difference between these two approaches is insignificant at a low noise level (2%). However, as the noise level increases (i.e. 5%), the difference is evident and QMC performed better. The stiffness and damping parameters obtained from the algorithm are shown in Fig 3.21 for the 5% noise. Similarly, the convergence plot for BWBN parameters is presented in Fig. 3.22. For brevity, time histories of these parameters are not shown for 2% noise. However, Table

3.8 includes the identified model parameters for different noise levels i.e. 2% and 5%. From

Table 3.8: Summary of identified BWBN model parameters

Parameters	Exact Values	2% Noise		5% Noise	
		UT	QMC	UT	QMC
k_1	3.50E+06	3.27E+06	3.57E+06	1.75E+06	3.53E+06
k_2	3.50E+06	3.48E+06	3.51E+06	3.15E+06	3.52E+06
c_1	6000.00	5605.52	6202.95	6488.65	6199.96
c_2	6000.00	6092.87	5940.03	5675.80	5937.51
α	0.15304	0.17156	0.14689	0.42359	0.11670
β	0.30018	0.36380	0.30840	0.84304	0.26718
γ	-0.28386	-0.36353	-0.28119	-0.82559	-0.24459
n	1.00040	1.12000	1.02300	2.31000	1.18000
δ_ν	0.00480	0.00015	0.00401	9.92E-05	0.00937
δ_η	5.88E-08	8.43E-08	3.98E-08	5.13E-08	3.75E-08
p	2.79160	0.30903	1.82501	0.62290	1.42534
ζ_0	0.92658	0.93180	0.92795	0.47726	0.90147
ψ_0	0.20000	0.14312	0.21979	0.06244	0.51307
δ_ψ	0.00210	0.00304	0.00226	0.00313	0.00553
λ	0.99943	0.87906	0.84242	0.51522	0.00576
q	2.13E-05	2.60E-09	5.55E-05	0.01101	7.49E-07

this table, it is seen that two different point generation schemes have converged to the actual values of parameters without any significant divergence for 2% measurement noise with improved performance by QMC points. Also, it is found that the parameters obtained by using the UT points vary significantly from their true values as compared to those obtained by using QMC points for 5% noise as shown in Fig 3.21. The stiffness parameter (k_1) shows more than 50% relative percentage error while using UT points. On the other hand, QMC points always provide a better estimation of stiffness and damping parameters and BWBN parameters with a reasonable level of accuracy, which makes it more robust for practical applications. The superiority of the QMC points is also seen in the identified hysteretic behaviour, as shown in Fig. 3.23b. The proper pinching and degradation characteristics of the actual hysteretic behaviour are captured by the identified BWBN parameters using QMC points. In contrast, the UT points have failed to do so. The relative estimation error in hysteretic energy for both 2% and 5% noise levels is shown in Table 3.9. These values indicate that QMC points have a substantial advantage over traditional UT points. Apart from identifying the structural parameters, the input ground motions are also estimated, which is demonstrated in Fig. 3.23a. In this case, Arias intensity (I_A) and peak ground acceleration (PGA) are considered as a relative measure of accuracy between the estimated and the actual ground motions. As shown in Table 3.9, QMC scheme consistently shows lower percentage error than its counterpart i.e. UT approach. This indicates that the QMC approach is not vulnerable measurement noise and hence offers greater precision and robustness when dealing with non-linear estimation problems.

Table 3.9: Estimation error in % for 2-DOF Bouc-Wen model

Noise	Sigma Points	Hysteretic Energy	Input Ground motion PGA	I_a
2%	UT	2.42	2.12	2.33
	QMC	0.53	4.39	7.60
5%	UT	33.33	1.49	1.58
	QMC	8.54	7.07	81.28

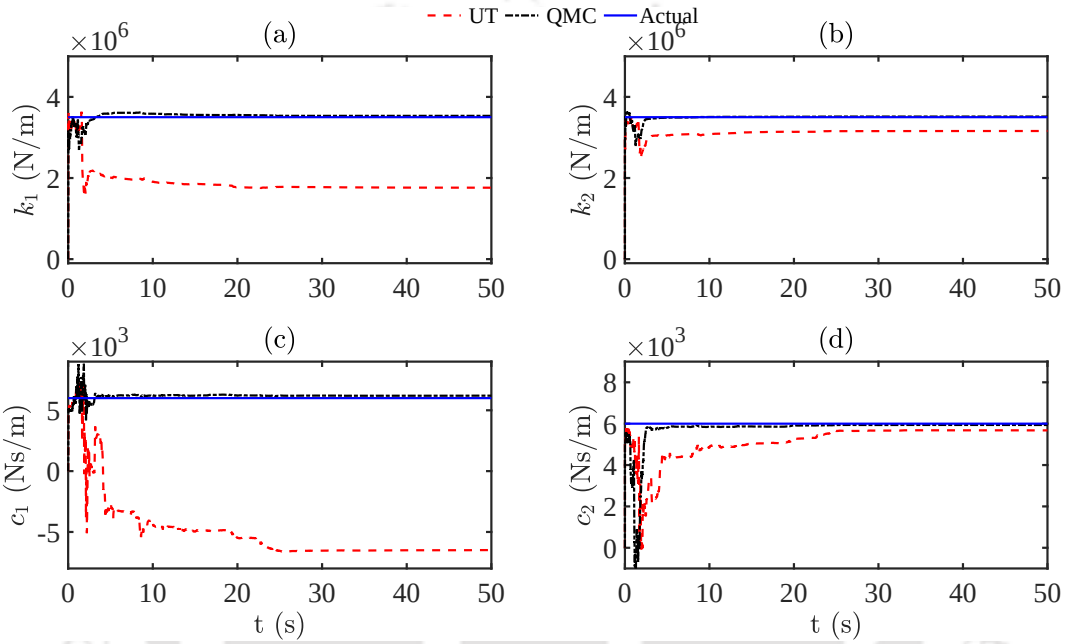

Figure 3.21: Identified stiffness and damping parameters of 2-DOF BWBN model for 5% measurement noise; (a) stiffness in storey 1, (b) stiffness in storey 2, (c) damping in storey 1 and (d) damping in storey 2

3.8 Summary

Constraint minimum variance unbiased estimator is proposed for simultaneous input and parameter estimation of the Bouc-Wen hysteretic system of a full-scale bridge pier. The essential structural properties in this case (i.e. Bounded Input and Bounded Output) are incorporated in the form of constraint conditions along with degradation and pinching effects. To demonstrate the efficiency of this algorithm, two different sigma points generation schemes (viz. unscented transformed points and cubature quadrature points) are presented here. First, the algorithm is validated using the simulated response of a Bouc-Wen model with degradation and pinching effects. Later, it is applied to the simulated response obtained from a single-bay single-storey reinforced concrete frame, whose hysteretic parameters are obtained by minimizing the error between the model and experimentally observed load-deformation characteristics. The rationale behind using experimentally observed hysteresis in simulation is to replicate the actual structure so that the realistic material behaviour is

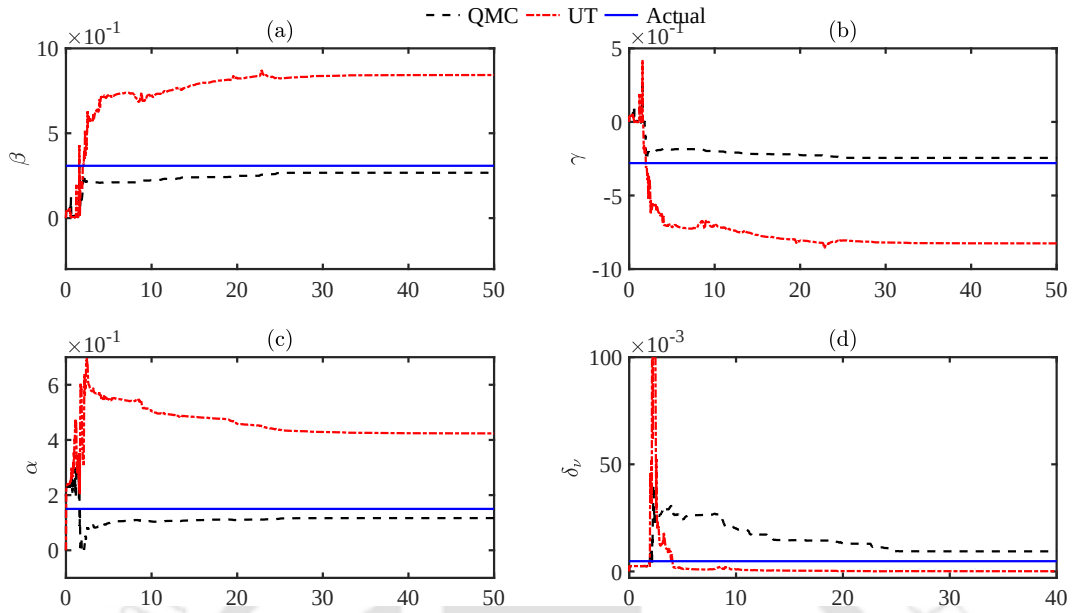

Figure 3.22: Identified hysteretic parameters for 2-DOF BWBN model for 5% measurement noise; (a) β, (b) γ, (c) α and (d) δ_ν

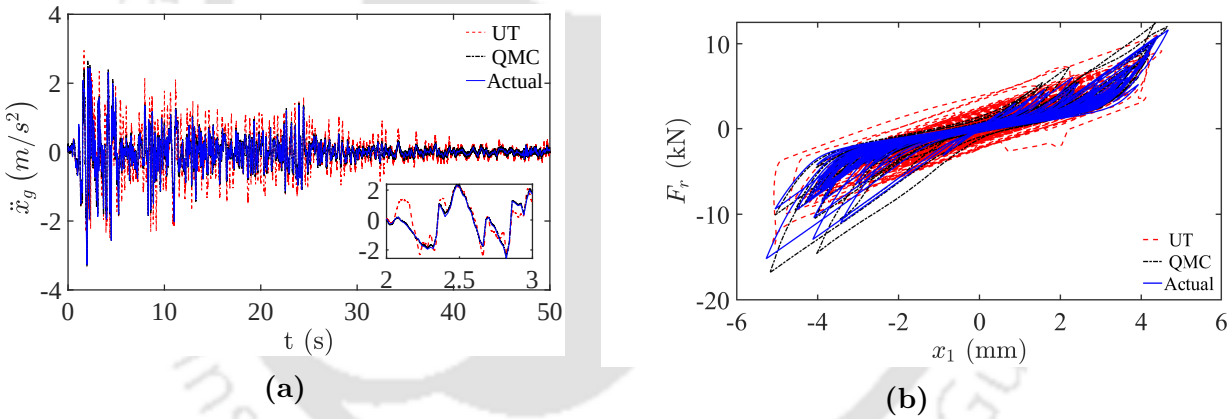

Figure 3.23: Estimation of input and BWBN parameters for 5% noise; (a) support excitation and (b) hysteresis.

maintained. Once the algorithm is validated, its performance is further demonstrated using experimental results of a full-scale bridge pier. Although unscented points perform well, it may not be adequate to approximate the statistical moments due to its ability to produce only a few sigma points. To address this problem, a quasi Monte Carlo point generation scheme is introduced based on the stochastic integration rule, which shows significant advantage over the unscented points. The Numerical results presented in this chapter clearly show the robustness of the proposed, which can identify both hysteretic properties and input excitation with a sufficient level of accuracy.

Chapter 4

Damage Estimation of RC Structures

4.1 Overview

Damage estimation of any structure after an earthquake is one of the primary concerns for civil engineers to ensure safety and serviceability. A common practice in this context is to estimate the damage by measuring the changes in modal frequencies and damping characteristics before and after the event. However, in reinforced concrete (RC) structures, the above procedure may not provide satisfactory results as they are designed to undergo inelastic deformation during an earthquake [184]. Therefore, the severity of damage is underestimated when quantified in terms of change in natural frequencies and damping [185, 186]. Thus, damage estimation based on engineering demand parameters (EDP) such as peak displacement, inter-storey drift, hysteretic energy provides robust insight into the level of deterioration induced in it. Further, EDP-based damage estimation offers a powerful scientific basis for improving structural performance against seismic risk and serves as a foundation for performance-based earthquake engineering in both design and post-event maintenance. Among different EDPs, cumulative hysteretic energy-based damage quantification provides better estimation than other instantaneous parameters, e.g., peak roof displacement and peak inter-storey displacement [187, 188].

This non-linear hysteretic behaviour of RC structures under moderate to severe ground excitation imposes huge inelastic demand. It is often manifested in the cracking of concrete and yielding of reinforcement. The relationship between the restoring force and the output state variable in such structures is memory-based, i.e., the output depends upon the instantaneous state and its history. Due to this reason, modeling the hysteretic behaviour of RC structure offers serious challenges. Besides modeling, measuring the restoring force acting in an existing system using instrumentation is also a daunting task. In the absence of measured restoring force, engineers often use the total inertia force acting on the structure under base excitation as the restoring force [184, 189]. It is incorrect since the contribution from the inherent damping of the structure is not decoupled. Thus, estimating the actual restoring force of a real-life structural system has a growing appeal to the research community. To address this issue, several parametric identification techniques have been demonstrated in the literature [190]. Among them, recursive Kalman filter-based estimations are preferred by the researcher as they can utilize the available information (i.e. measurements) more

efficiently. In these techniques, measurements are used to update the numerical model of the structure. Wu and Smyth [96] have compared the performance of Extended Kalman filter (EKF) and Unscented Kalman filter (UKF) to identify the parameters of Bouc-Wen hysteretic SDOF structure and found that UKF offered a better estimation. Similarly, Song and Dyke [191] have estimated the parameters of the modified Bouc-Wen model from the experimental response of a scaled (1/10) single storey shear building frame subjected to base excitation. A different approach than the traditional UKF based identification technique has been developed by Bisht and Singh [192], where they have adjusted the covariance matrix to track any sudden change in stiffness. Zhang et al. [193] have proposed improved EKF with Tikhonov regularization to identify the damage of a 7-storied structure.

Besides time-domain techniques, several other approaches are available in the literature for damage assessment of concrete structures. One of the commonly used techniques is based on acoustics emission, where deterioration in concrete is analyzed to trace the process of failure progression [194]. For rapid assessment, non-destructive evaluation techniques are commonly used, which are based on electrical resistivity (ER), impact echo (IE), ground-penetrating radar (GPR), and ultrasonic surface waves (USW) method [195]. Nowadays, cost-effective Lead Zirconate Titanate (PZT) transducers are extensively used for damage detection of a concrete structure. In this context, Tzoura et al. [196] have utilized PZT sensors to measure the extent of damage in a concrete column for retrofitting. They have found that the electro-mechanical impedance provides more insight into the damage incurred in the structure. The studies demonstrate the necessity behind condition assessment of reinforced concrete structures.

Although these non-destructive tests provide valuable information about damage, they are not sufficient to characterize the phenomenological behavior, which is essential for deciding appropriate rehabilitation work. The literature review presented above mainly focuses on two aspects - (i) time-domain recursive identification of hysteretic systems and (ii) damage mechanism with its quantification in the analysis and design of the reinforced concrete structure. In this context, it can be observed that the Kalman filter or its advanced versions for system identification are well developed. Multiple researchers have extensively studied this inverse parameter identification strategy and have proposed different modifications to make their algorithm robust. Their studies mainly focus on the filtering aspect involving various support point generation schemes or other regularization techniques for variance reduction of the error covariance matrix. Most of these studies are validated with simulation-based synthetic experiments or small-scale laboratory tests in a controlled environment. However, these variants of Kalman filters have more significant potential for parametric identification of non-linear behaviour often encountered in actual full-scale structure. One such example is the reinforced concrete structures that undergo inelastic deformation during seismic events. Thus, accurate estimation of model parameters defining the inelastic behaviour is a precondition for any reasonable retrofitting measure. This aspect of system identification in the light of Gaussian filtering is less represented in the literature. Besides inelastic parametric identification, estimation of input excitation is equally crucial as it helps cross-verify the original structure's designed demand. In this chapter, Kalman filter techniques for the identification of hysteretic structure are provided for known input situations followed by unknown input cases.

4.2 Damage Estimation with Known Input

In this section, the performance of the UKF algorithm has been demonstrated for damage estimation RC structure, which possesses non-linear hysteresis behaviour. The proposed constrained iterated unscented Kalman filter (CIUKF) is used to quantify the incurred damage in the RC column with the help of an energy-based damage index. The column is modeled in Opensees, incorporating non-linear material properties of concrete and reinforcement. The response obtained from the numerical analysis is used for damage quantification. However, the proposed algorithm utilizes the Bouc-Wen model as the underlying mathematical model instead of the Opensees model during the identification process. The results show that the proposed CIUKF algorithm can quantify the damage with an acceptable level of accuracy. A brief description of the proposed constrained iterated unscented Kalman filter (CIUKF) is presented in the following section.

4.2.1 Constrained Iterated Unscented Kalman Filter

The UKF algorithm is one of the most popular methods in time domain estimation theory due to its ability to track non-linear systems without calculating the partial derivative, i.e., gradient vector [191]. Moreover, the UKF algorithm is computationally less expensive than the Monte-Carlo simulation-based Bayesian filtering [97]. This computational efficiency is due to fewer sample points in UKF for moment estimation compared to the Monte-Carlo simulation. In this study, the CIUKF algorithm is proposed augmenting the conventional UKF with the constraint condition presented in the previous chapter. Theoretically, to achieve convergence of system parameters in UKF, an extended duration response is necessary, which may not be available all the time. Thus, the system weighted global iteration technique has been incorporated in the algorithm [197] to deal with the non-convergence problem in a short-duration response. The proposed approach is demonstrated with the help of an n degree of freedom (DOF) non-linear structural system, whose governing equation can be expressed as

$$\mathbf{M}\ddot{\mathbf{x}}\left(t\right)+\mathbf{F}\left[\mathbf{x}\left(t\right),\dot{\mathbf{x}}\left(t\right),\boldsymbol{\Theta}\right]=\mathbf{B}\mathbf{f}\left(t\right) \tag{4.1}$$

where $\mathbf{x}\in\mathbb{R}^n$, $\dot{\mathbf{x}}\in\mathbb{R}^n$, and $\ddot{\mathbf{x}}\in\mathbb{R}^n$ are the displacement, velocity, and acceleration vectors of the structure. In Eq. 4.1, $\boldsymbol{\Theta}=[\theta_1,\theta_2,.....\theta_m]$ are n parametric vector composed of unknown parameters of the structure, which includes stiffness, damping, and other hysteretic parameters. The mass of the structure can be fairly estimated using the geometries and material property. Hence, mass matrix $\mathbf{M}$ is considered to be known. The restoring force $\mathbf{F}\left[\mathbf{x}\left(t\right),\dot{\mathbf{x}}\left(t\right),\boldsymbol{\Theta}\right]$ is the non-linear function of displacement, velocity, and hysteretic parameters of the structure, and $\mathbf{B}$ is the influence matrix associated with the external force vector $\mathbf{f}\left(t\right)$. The unknown system parameters are included in the state vector to execute the Kalman filter-based estimation algorithm, and the corresponding extended state vector can be expressed as

$$\mathbf{Z}=\left\{\mathbf{Z_1^T},\mathbf{Z_2^T},\mathbf{Z_3^T}\right\}^T \tag{4.2}$$

where $\mathbf{Z_1}=\mathbf{x}^T$; $\mathbf{Z_2}=\dot{\mathbf{x}}^T$ and $\mathbf{Z_3}=\boldsymbol{\Theta}^T$. The extended state vector in Eq. 4.2 consists of two parts - time-dependent state vector, i.e $\left\{\mathbf{Z_1}^T\mathbf{Z_2}^T\right\}^T$ and time-invariant parameter vector i.e.

$\dot{\mathbf{\Theta}} = 0_{mx1}$. Now 4.1 can be written in state space form as

$$\begin{Bmatrix} \dot{\mathbf{Z}}_1 \\ \dot{\mathbf{Z}}_2 \\ \dot{\mathbf{Z}}_3 \end{Bmatrix} = \begin{Bmatrix} \mathbf{Z_2} \\ \mathbf{M}^{-1}\left\{\mathbf{Bf}\left(t\right) - \mathbf{F}\left[{\mathbf{Z_1}}^T\left(t\right), {\mathbf{Z_2}}^T\left(t\right), {\mathbf{Z_3}}^T\left(t\right)\right]\right\} \\ 0_{m\times 1} \end{Bmatrix} \tag{4.3}$$

As seen from Eq. 4.3, the unknown parameters and the state vectors are coupled non-linearly in the extended state-space equation. Therefore, Eq. 4.3 can be represented in the general form of non-linear differential state equation in continuous time as

$$\dot{\mathbf{Z}}(t) = \mathbf{G}\left(\mathbf{Z}(t), \mathbf{f}(t)\right) \tag{4.4}$$

Although the system equation is defined in continuous time state space in Eq.4.4, the system responses are measured in discrete time in practice. The system equation is expressed in discrete time to implement the identification algorithm with the real-time measurements as follows

$$\mathbf{z}_k = \mathbf{z}_{k-1} + \int_{(k-1)\Delta t}^{k\Delta t} \mathbf{G}\left(\mathbf{Z}\left(t\right), \mathbf{f}\left(t\right)\right)dt = \mathbf{g}\left(\mathbf{z}_{k-1}, \mathbf{f}_{k-1}\right) \tag{4.5}$$

The discretized observation equation at any time $t = k\Delta t$ can be expressed by a non-linear function $\mathbf{h}$ as follows

$$\mathbf{y}_k = \mathbf{h}\left(\mathbf{z}_k, \mathbf{f}_k,\right) + \mathbf{v}_k \tag{4.6}$$

In the above equation, $\mathbf{z}_k$ and $\mathbf{f}_k$ are the state vector, known input vector at $t = k\Delta t$ respectively where, Δt is the sampling period. $\mathbf{v}_k$ is the random measurement noise which is assumed to be a zero mean Gaussian process with known covariance $\mathbb{E}\left[\mathbf{v}_k\mathbf{v}_k^T\right] = \mathbf{R}_k$. Now, the extended state vector is concatenated to implement the parameter constraints in the following way

$$\mathbf{Z} = \begin{bmatrix} \mathbf{X} & \mathbf{\Lambda} & \mathbf{w} \end{bmatrix}^T \tag{4.7}$$

where, vector is $\mathbf{X} = \begin{bmatrix} \mathbf{Z_1} & \dot{\mathbf{Z}}_\mathbf{1} \end{bmatrix}^T$, vector $\mathbf{\Lambda} = [\lambda_1, \lambda_2, \lambda_3 ..... \lambda_n]^T$ is the parameters having constraints and $\mathbf{w} = [w_1, w_2, w_3 ..... w_n]^T$ denotes the parameter vector without constraints. The constraint conditions implemented in here are according to Eq.3.4 and Eq.3.5.

The proposed CIUKF method estimates both system state $\mathbf{X}$ and the parameters $\begin{bmatrix} \mathbf{\Lambda} & \mathbf{w} \end{bmatrix}^T$ based on the sequential measurements $\{\mathbf{y}_1, \mathbf{y}_2, ...\mathbf{y}_k\}$ provided with the unbiased estimate of initial state $\tilde{\mathbf{Z}}_{0|0}$ and corresponding covariance matrix $\mathbf{P}^{\mathbf{z}}_{0|0}$ using the UKF algorithm, which is explained in section 2.4. The traditional UKF estimates the parameters of the structural system by a single global iteration. However, dealing with the experimental response of the structural system, convergence issues have been encountered. These issues may arise due to the selection of an initial estimate of the mean and the covariance far away from the expected values. Thus, a weighted global iteration technique is introduced to obtain a stable and optimal solution. Such a weighted global iteration approach helps obtain a correct estimate of the structural parameter even if the incorrect estimate of parameters is obtained during the

first global iteration. In this approach, the estimated mean and corresponding covariance at the end of the one global iteration is again introduced to the UKF algorithm with a small amplification to the diagonal elements of the covariance matrix. The amplification is provided utilizing a weight factor κ, which is applied on the diagonal element of the covariance matrix corresponding to the system parameters. In contrast, the element corresponding to the system state remains intact. This weight causes a small change in parameter estimates between the initial and the end of the global iteration, which helps to attain the correct optimal estimate. The convergence criteria are selected so that the hysteretic energy (E_H) content estimated between two consecutive global iterations remains within a tolerance limit (ε). It is found that tolerance of 5% relative percentage error in hysteretic energy provides good estimation parameters without imposing a significant computational burden. The flowchart of the proposed CIUKF algorithm is shown in Fig. 4.1. Following this approach, the initial values of state and covariance are presented using the following relation

$$\mathbf{Z}^{j}_{0|0} = \begin{bmatrix} \mathbf{X}_{0|0} & \mathbf{\Lambda}_{0|0} & \mathbf{w}_{0|0} \end{bmatrix} \tag{4.8a}$$

$$\mathbf{P}^{j}_{0|0} = \begin{bmatrix} \mathbf{P}^{z}_{0|0} & 0 & 0 \\ 0 & \kappa * \mathbf{P}^{\Lambda}_{0|0} & 0 \\ 0 & 0 & \kappa * \mathbf{P}^{\mathbf{w}}_{0|0} \end{bmatrix} \tag{4.8b}$$

where $j = 2, 3, 4...m$ denotes the global iteration count.

4.2.2 Damage Quantification

Damage quantification plays a vital role in post-earthquake decision-making procedures based on which appropriate measures are taken. It involves repairing and/or strengthening the structure and predicting its remaining service life. Condition assessment using the Damage index (DI) is convenient because it can realistically measure the damage level of the system by a dimensionless number. In general, DI are mathematical functions based on some representative variables to quantify the damage of a structure or its components. These variables are generally related to irrecoverable or inelastic deformations such as strains, curvatures, rotations, displacements, and sometimes forces (e.g., base shears, member resistances, or energy dissipated inelastic reversed cyclic loading). Different types of DI have been reported in the literature for damage estimation of RC structures [198]. An in-depth description of other types of DI used for RC bridge pier can be found in Mahboubi and Shiravand [199]. In this section, the damage has been quantified by the energy-based damage index proposed by Williams and Sexsmith [198]. The idea behind this DI is based on the distribution of input earthquake energy (E_I) to the structure in the from of kinetic energy (E_k), damping energy (E_d), strain energy (E_s), and hysteretic energy (E_h), which can be expressed as follows

$$E_I = E_k + E_d + E_s + E_h \tag{4.9}$$

Among these components of total energy, hysteretic energy (E_h) represents the energy dissipated during the repeated loading cycles, which is associated with the damage induced in the structure. So, damage can be quantified as the ratio of hysteretic energy to the earthquake

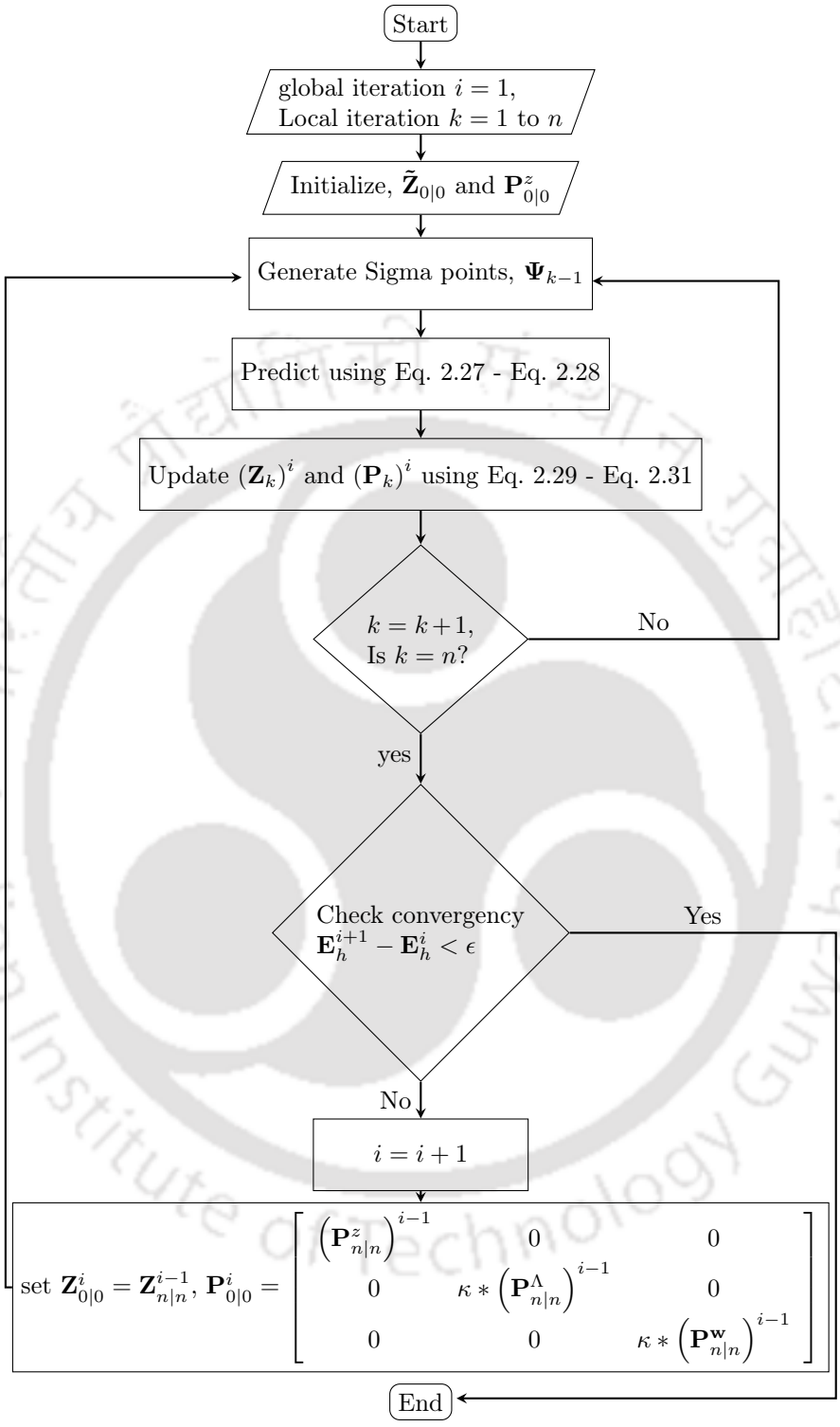

Figure 4.1: Flow chart of CIUKF algorithm

energy (i.e. input) as proposed by Mahboubi and Shiravand [199]

$$DI = \frac{E_h}{E_I} \tag{4.10}$$

In general, the hysteretic energy can not be obtained directly from the measurements. Nevertheless, it can be estimated by rearranging Eq. 4.9 i.e.

$$E_h = E_I - E_k - E_d - E_s \tag{4.11}$$

However, to obtain E_h from the equation mentioned above, other components must be known beforehand. Further, damping and strain energy requires an accurate estimation of the stiffness and damping coefficients of the structure. Typical expressions for strain and damping energy of an SDOF system are given below

$$\begin{aligned} E_d &= \int_0^x c\dot{x}dx \\ E_s &= \int_0^x k_t x dx \end{aligned} \tag{4.12}$$

Where, c and k_t represent the damping and tangent stiffness of the system, respectively. Researchers estimate these parameters from the finite element model in practice, which are expected to match the experimental results closely. Usually, this tuning process consists of adjusting the parameters in the finite element model (i.e., element size, length of plastic hinge length, etc.) by trial and error. The hysteretic energy can be directly estimated from the measurement using the constrained iterated unscented Kalman filter to avoid this practice.

4.2.3 Numerical Investigation

In this section, numerical results show the effectiveness of the proposed method for damage estimation RC structure under earthquake excitation. For this purpose, fiber discriticized single RC column is modeled in Open System for Earthquake Engineering Simulation (i.e., OpenSees) program, as shown in Fig. 4.2. A point load of 100 kN is applied at the free end to simulate the superimposed load. It is assumed that the column undergoes idealized cantilever behaviour due to the earthquake applied at the base. Concentrated plasticity is adopted using the beam-with-hinges element to model the non-linear behaviour of the column, assuming the hinge is located near the point of fixity. The length of the plastic hinge (L_p) is defined according to the Caltrans Seismic Design Criteria [200], which is given by

$$L_p = 0.08L + 0.022 f_{ye} d_{bl} \geq 0.044 f_{ye} d_{bl} \tag{4.13}$$

where L is the length of the column. f_{ye} denotes yield strength of longitudinal reinforcement having nominal bar diameter d_{bl}. The cross section of the column is divided into a number of fiber cells and material properties are defined accordingly. The material stress-strain property is defined in three different regions, i.e., unconfined concrete, confined concrete and longitudinal steel reinforcement. In this study, *Concrete07* model is used to simulate the inelastic behaviour of the concrete, where *ReinforcingSteel* material model is used for the rebars.

4.2.4 Damage Estimation Results

The RC column is modeled as an SDOF non-linear Bouc-Wen oscillator as described in section 2.5.1. The governing equations of motion can be expressed using Eq. 2.34 and Eq. 2.35. The restoring force F_r generated by the applied load can be separated into elastic and hysteretic components, as shown in Eq. 3.1a. Now, substituting Eq. 3.1a in Eq. 2.34 and dividing both side by m gives the following expression

$$\ddot{x}(t) + 2\xi\omega_0\dot{x}(t) + \alpha\omega_0^2 x(t) + (1-\alpha)\omega_0^2 z(t) = f(t) \tag{4.14}$$

where ξ is the linear damping ratio, $\omega_0 = \sqrt{\frac{k}{m}}$ is the pre-yield natural frequency and $f(t)$ is the mass normalized forcing function. The numerical simulation study is carried out to generate the responses from the Opensees model using different earthquake records (viz. El centro, Loma Prieta, Chile, Chichi). The acceleration at the free end of the column is used for parameter identification. To apply the constraint conditions, the extended state vector for the system can be expressed as $\mathbf{Z} = \begin{bmatrix} \mathbf{X} & \mathbf{\Lambda} & \mathbf{w} \end{bmatrix}^T$. Here, $\mathbf{X} = \begin{bmatrix} x & \dot{x} \end{bmatrix}^T$ is the state vector, where $\mathbf{\Theta} = \begin{bmatrix} \alpha & \beta & \gamma & n \end{bmatrix}^T$ and $\mathbf{W} = [\omega_0]^T$. The constraint conditions are the same as in Section 3.4.1. As stated earlier four ground motions are selected and responses are simulated using Opensees to show the performance of the proposed algorithm. To maintain uniformity in analysis, all the ground motions are scaled up to the same PGA, and 2% zero-mean Gaussian white noise is added to the response. The damage quantification is carried out using Eq. 4.10. The actual hysteretic energy E_h is evaluated as the area under the force-deformation acquired from the Opensees recorders. The performance of the proposed technique (i.e., hysteretic energy) and DI estimation is presented in Table 4.1. The estimated hysteretic energy $E_h{}'$ is obtained from the proposed algorithm using the Bouc-Wen hysteretic model. Similarly, the estimated Damage index DI' is compared with the actual DI (refer to Table 4.1). This table shows that the proposed technique captures the inherent non-linear behaviour of the RC column modeled in Opensees. The acceleration response and the hysteretic response of the Opensees model match satisfactorily with the estimates provided by the inverse technique, which is shown in Fig. 4.3 and Fig. 4.4.

Table 4.1: Damage Estimation Results

Record Name	Year	Scale	E_h (KNm)	$E_h{}'$(KNm)	DI	DI'
El Centro	1940	0.50	912.97	1110.90	0.72	0.87
Loma Prieta	1989	0.50	2863.70	2452.40	0.86	0.74
Chile	1985	0.50	9933.30	11336.00	0.81	0.92
Chichi	1999	0.50	1491.20	1644.80	0.70	0.77

4.3 Damage Estimation under Unknown Input

Once the performance of the sigma point approach for damage quantification is established under known input, it is further extended for unknown input. The damage quantification is

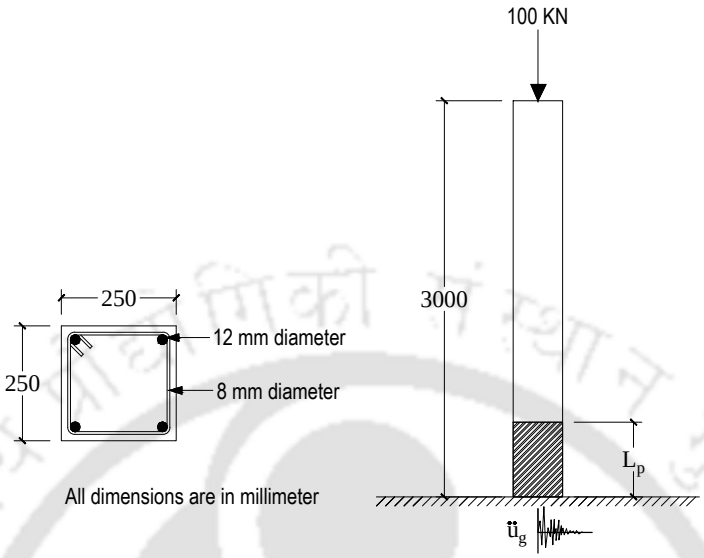

Figure 4.2: Opensees model of RC column

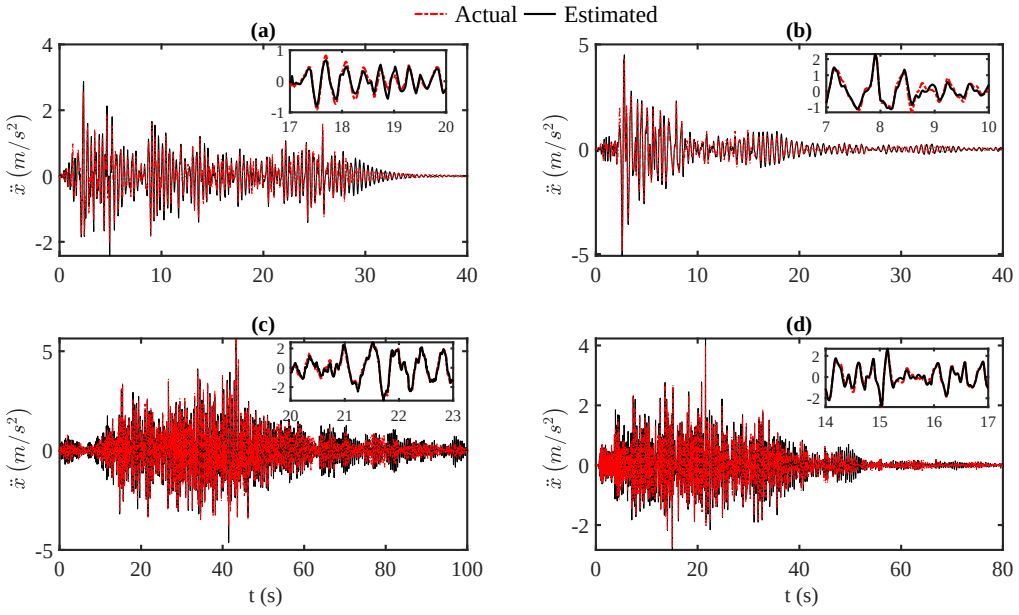

Figure 4.3: Comparison of estimated and actual acceleration of top node of column for different earthquake; (a) El-Centro, (b) Loma Prieta, (c) Chile and (d) Chichi

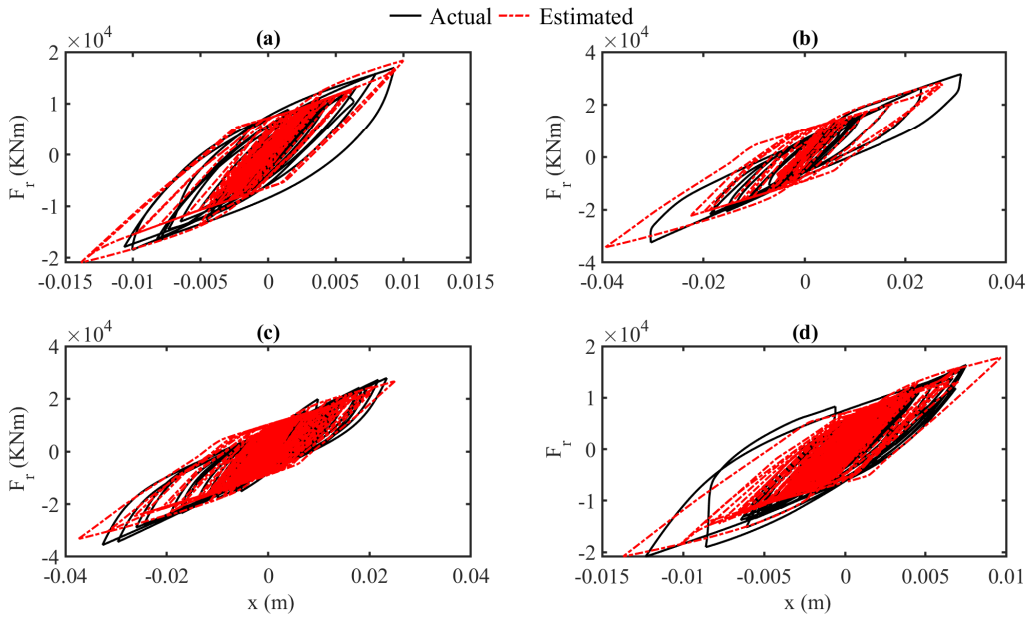

Figure 4.4: Comparison of estimated and actual hysteresis plot for different earthquake (a) El-Centro (b) Loma Prieta (c) Chile and (d) Chichi

carried out using Park and Ang index, a non-dimensional number between zero to one. In the following section, a brief introduction of the Park and Ang damage index is presented.

4.3.1 Park and Ang Damage Index

Although the energy-based damage indices (e.g., Eq. 4.10) can estimate the incurred damage in RC structure, it may not be accurate for a structure having plastic deformation. For such situations, cumulative damage indices are suitable alternatives, which are primarily defined as a function of accumulated plastic deformation and can incorporate seismically absorbed hysteresis energy. Among them, the most widely used modified Park and Ang [201] DI is selected here for its ability to provide the best correlation with the laboratory results [188]. It has been accepted worldwide that the damage induced in a structure during an earthquake depends on the maximum deformation and the hysteretic energy dissipated during the load cycles. The modified Park and Ang DI combines these two aspects to provide a better characterization of the damage. In this model, both ductility demand and cumulative hysteretic energy demand are incorporated as a linear combination of normalized deformation and hysteretic energy adsorption, i.e.

$$DI = \frac{\delta_m - \delta_y}{\delta_u - \delta_y} + \beta_d \frac{\int dE_h}{F_y \delta_u} \tag{4.15}$$

where δ_m, δ_u and δ_y are the maximum displacement, ultimate displacement and yield displacement, respectively and F_y is the yield force. At the same time, $\int dE_h$ is the dissipated hysteresis energy in each loading cycle. The nonzero positive parameter β_d refers to the strength degradation of the structural member. However, evaluation of the dissipated hys-

teresis energy is not straight forward since it can not be obtained directly from the measurement itself. In practice, researchers used to get this from the updated finite element model such that the response generated by the model matches with the experiment within an acceptable range of accuracy. Although the forward problem is well-posed, the inverse problem to estimate them is difficult. In this study, the hysteretic energy is estimated from the identified Bouc-Wen model using the algorithm mentioned above. For this purpose, the measurements obtained from the system are provided to the constrained minimum variance unbiased estimator and the parameters related to hysteretic energy are subsequently estimated. The proposed algorithm is first validated using a synthetic experiment, which is followed by the full-scale test of a bridge pier on the shake table. These are discussed in the following section.

4.3.2 Synthetic Experiment for Engineering Demand Parameter Estimation

The 2-DOF structure, as shown in Fig. 3.20, is considered to simulate the hysteretic response. Here, BWBN hysteretic model is used as explained in section 3.5.1 to simulate the actual behaviour of the RC structure under extreme loading. The main aim of this study is the estimation of engineering damage parameters (EDP) used in the Park and Ang damage index, i.e., maximum displacement (δ_m) and dissipated hysteretic energy ($\int dE_h$). The capacity-related parameters such as ultimate displacement (δ_m) and yield force (F_y) remained unchanged in this estimation. Hence, only the engineering damage parameters are responsible for the damage index value obtained after any seismic event. The comparison of estimated and actual engineering damage parameters is provided in Table 4.2 for 2% RMS noise. The small percentage error between the estimated and actual values of engineering damage parameters signifies the performance of the proposed algorithm, which can be further utilized for the Park and Ang damage index calculation. This is otherwise difficult to quantify using other non-destructive or destructive tests. It is the main objective of this study, which augments the decision-making process for rehabilitation and retrofitting.

Table 4.2: Comparison of simulated and estimated EDPs

${\delta_m}^{sim}$(mm)	${\delta_m}^{est}$ (mm)	$\in_{\delta_m}$(%)	$\int {dE_h}^{sim}$ (kNmm)	$\int {dE_h}^{est}$ (kNmm)	$\in_{E_h}$(%)
5.2725	5.2751	0.0493	1.6583E+05	1.6473E+05	0.6632

NB: superscripts *sim* and *est* stand for simulated and estimated cases

4.3.3 Full-Scale Bridge Pier Test

Once the performance of the proposed algorithm is established using simulated Bouc-Wen hysteretic response, it is further used for damage estimation of a full-scale structure under earthquake excitation. In this case, the experimental data of the circular reinforced concrete

bridge pier, as shown in Fig. 3.15, is used. The structure was subjected to different earthquake ground excitations in succession, which correspond to the different intensity levels. In this study, the EQ5-EQ8 sequences are selected for damage estimation purposes. The details of these ground motions are presented in Table 4.3. One of the significant advantages of the

Table 4.3: Ground motion details

Tests	Earthquake	Year	Station	Moment Magnitute	Scale	PGA
EQ5	Kobe	1995	Takatori	6.9	-0.8	-0.533
EQ6	Loma Prieta	1989	LGPC	6.9	1	-0.512
EQ7	Kobe	1995	Takatori	6.9	-1.2	0.646
EQ8	Kobe	1995	Takatori	6.9	1	-0.829

proposed method is its ability to estimate the restoring force acting on the structure, which is otherwise difficult to quantify. In the absence of restoring force measurement, designers often assume the total inertia force as the base shear acting on the structure. A similar practice was observed in Shan et al. [189] for the same EQ5 sequence used in this study. The comparison between the proposed method and the hysteresis plot obtained by following the assumption in Shan et al. [189] is shown in Fig. 4.5. A distinct difference between the nature of hysteresis plots is observed in both of these approaches. The proposed algorithm can capture the actual nature of the hysteresis plot while the other approach, as adopted by Shan et al. [189], fails to do so. The main difference arises due to the contribution of inherent damping of the structure, which is balanced by the total inertia force along with the non-linear spring force, and hence, the estimation of the restoring force is incorrect, which leads to the hysteresis plot as shown in Fig. 4.5.

4.3.3.1 Validation of Proposed Method with Strain Measurement

The strain data acquired during the experiment has been considered to validate the proposed algorithm further. These are obtained from the gauges installed on the longitudinal reinforcements on the opposite sides of the specimen in a plane parallel to the loading direction. The strain measurements are utilized to obtain the curvature (ϕ_c) of the section from the following expression

$$\phi_c = \frac{\varepsilon_2 - \varepsilon_1}{D} \tag{4.16}$$

where ε_1 and ε_2 are the strain measurements obtained at section AA using strain gauges with an effective gauge length of 5mm, as shown in Fig. 4.6. D is the distance between the gauge mounting points. Further, the curvature time history obtained using Eq. 4.16 has been employed to calculate the moment time-history using the monotonic moment-curvature relationship. It is assumed that the moment at section AA is due to the response of the SDOF system, whose mass is lumped at the top. By this assumption, the force experienced at section AA is calculated from moment time history using the force-moment relationship of a cantilever column. The comparison of estimated restoring force by the proposed method and the same obtained from the strain measurements is shown in Fig.4.7. Although they

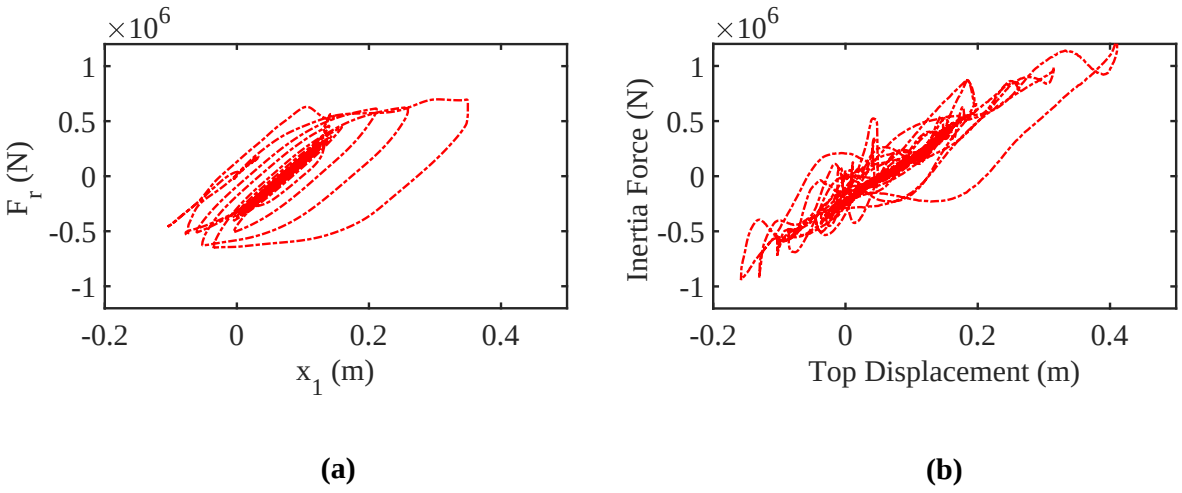

Figure 4.5: Comparison of hysteresis for EQ5 case; (a) proposed CMVU method, and (b) using total inertia force as base shear

differ marginally for the initial few seconds, an excellent match is observed beyond 50s. During the initial few seconds, the structure experiences very high inelastic demand, which compels the sectional curvature demand to go beyond its elastic range. Hence, the linear relationship fails to accurately capture the actual restoring force. However, as long as the sectional curvature is within the elastic range (i.e., beyond 50s), a satisfactory match in terms of amplitude and frequency is observed between them.

4.3.3.2 Park and Ang Damage Index Estimation

In this subsection, the Park and Ang damage index is estimated for the EQ5-EQ8 earthquake sequences, as shown in Table 4.4. The capacity-related parameters, i.e., yield force F_y, yield displacement δ_y and ultimate displacement δ_u are taken from the PEER report no. 2015/02 [180], which are given as F_y = 781.8 (kN), δ_y=88 (mm) and δ_u = 506 (mm). To calculate the β_d parameter involved in the Park and Ang DI, the following equation is used in this study [201]

$$\beta_d = \left(-0.447 + 0.073\frac{l}{d} + 0.24n_o + 0.314p_t\right) \times 0.7^{\rho_w} \tag{4.17}$$

where $\frac{l}{d}$ is the shear span ratio, n_o is the normalized axial stress, p_t is the longitudinal steel ratio, and ρ_w is the confinement ratio. The demand-related parameters used in this process are obtained from the proposed method for three ground motion sequences (i.e. EQ6-EQ8), shown in Fig. 4.8. Since the performance of the proposed technique has been already discussed in the previous chapter for the EQ5 case, the results for the remaining

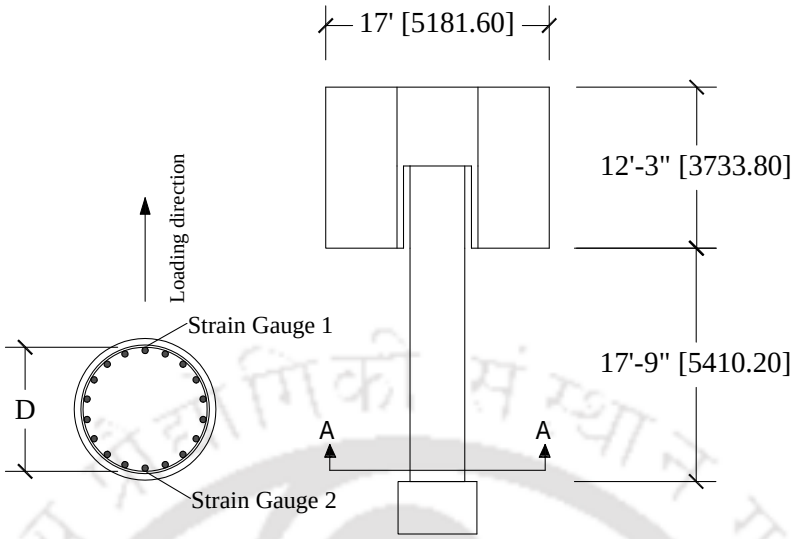

Figure 4.6: Schematic diagram showing strain gauge locations

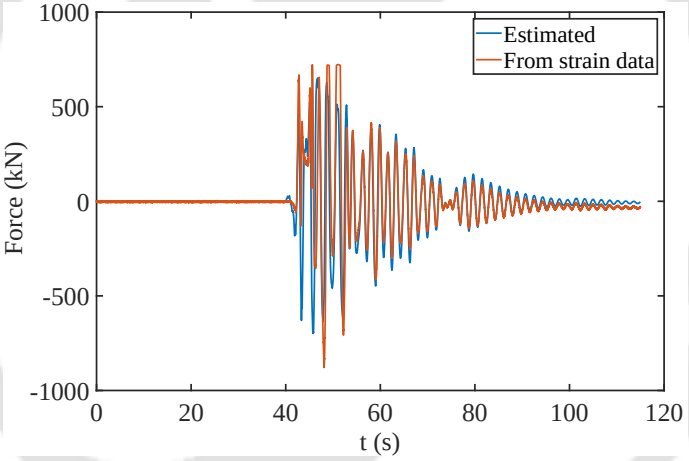

Figure 4.7: Estimated force from strain data for EQ5 case

ground motion sequence are shown here. The engineering damage parameters are obtained using the proposed algorithm, which is further utilized for damage index estimation as shown in Table 4.4. During the EQ5 event, spalling of cover concrete was observed. However, no damage in core concrete had occurred during the experiment. In the next two events (i.e., EQ6 and EQ7), spalling of cover concrete intensified and longitudinal reinforcements were exposed to the environment. At the end of the EQ8 event, some damage took place at the core concrete and the loss of integrity of the confining reinforcements. This gradual increase in damage state is also reflected in the commutative damage index, as shown in Table 4.4. Here, EQ5 offers the least value of damage while EQ8 corresponds to the highest level, consistent with the observed damage state, as shown in Fig. 4.9.

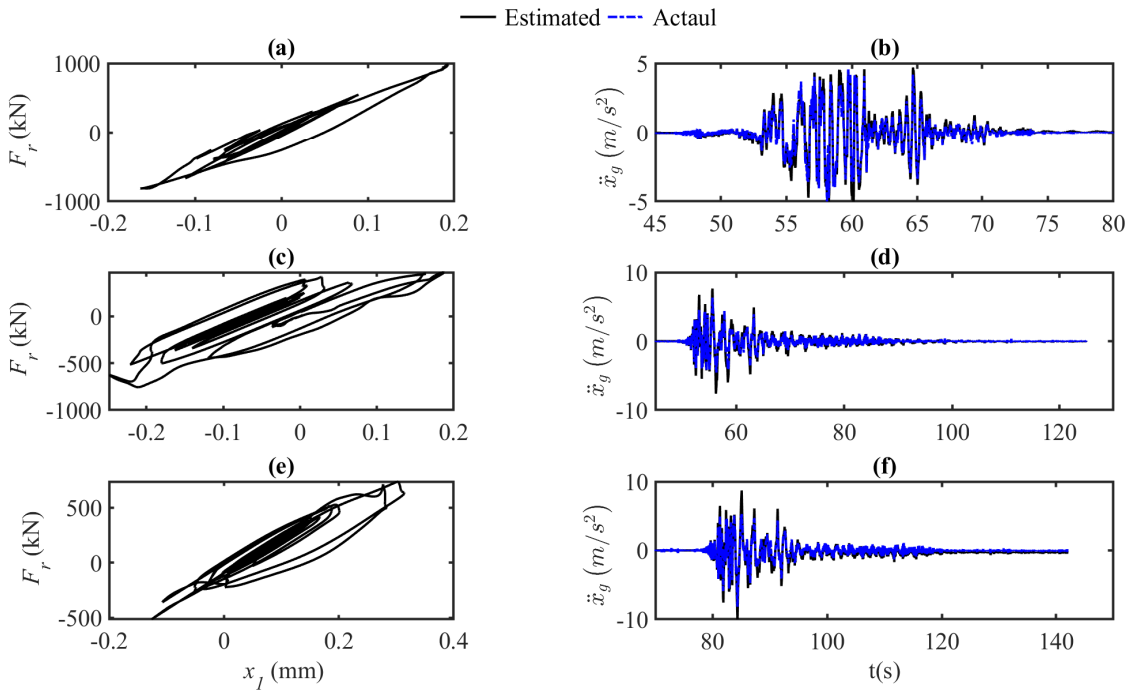

Figure 4.8: Estimated hystresis and input ground motion for different events; (a) EQ6 hysteresis, (b) EQ6 input ground motion (c) EQ7 hysteresis, (d) EQ7 input ground motion (e) EQ8 hysteresis, and (f) EQ8 input ground motion

Table 4.4: Estimated cumulative damage index for EQ5-EQ8 sequence

Event	F_y (KN)	δ_m (m)	β_d	$\int dE_h$ (kNm)	DI	Remark
EQ5	782	0.35	0.04	6.65E+02	0.69	Spalling of cover concrete
EQ6	782	0.19	0.04	1.04E+02	0.70	Spalling of cover concrete
EQ7	782	0.24	0.04	2.45E+02	0.73	Reinforcement exposed
EQ8	782	0.31	0.04	2.69E+02	0.75	Cracks in core-concrete

Figure 4.9: Damage during shake table test for different sequence; (a) EQ5, (b) EQ6, (c) EQ7, and (d) EQ8

4.4 Summary

Inverse analysis of non-linear reinforced concrete bridge pier using recursive Gaussian filtering for in-situ condition assessment is the central theme of this chapter. The uniqueness of this inverse analysis lies in updating engineering demand parameters, where appropriate bound and constraint conditions are introduced to ensure numerical stability and convergence. First, the proposed constraint strategy is tested with the CIUKF algorithm with known input to investigate its efficiency. Finally, the CMVU algorithm using unscented sigma points is the applied on the test data of a full-scale bridge pier to study its in-situ condition in terms of Park and Ang damage index. Also, the identified seismic input possesses an added advantage for the structures where no dedicated sensor for seismic measurement is available. Overall the study shows the augmented Gaussian filtering based recursive time-marching algorithm for non-linear system identification to estimate the engineering damage parameters that are the basic information necessary for any future decision making for retrofitting/rehabilitation.

Chapter 5

Non-linear Finite Element Model Updating

5.1 Overview

Finite element (FE) modelling plays a crucial role in high fidelity structural analysis under different loading conditions. Besides response prediction, it can be used for condition assessment and impact analysis of damage, if any. For design and other decision-making processes, FE analysis is indispensable to ensure the safety of the structure under anticipated static and dynamic loads. However, discrepancies between the FE model and the actual structure due to inaccurate idealization/discretization, and erroneous assumptions of model properties [202] affect the whole purpose. To overcome this problem, FE model updating is carried out where model parameters are adjusted so that the deviation between the measured response and that obtained from the FE model is minimum. The updated FE model serves as a digital twin for damage prediction during an anticipated catastrophic event. One of the major advantages of model updating is that it can provide important information, such as location, extent and type of damage incurred in the structure. A comprehensive review of recent advancements for damage assessment of structure by FE model updating can be found in Simoen et al. [31, 203]. These studies are focused on identifying the modal properties (i.e., natural frequencies and mode shapes) of the structure from the recorded vibration before and after any event. Finally, the damage is quantified using a suitable objective function, e.g., difference between the modal properties obtained from the FE model and the same derived from the measurements. Besides these initial attempts, numerous studies have been conducted in the recent past on FE model updating. In this context, Clementi et al. [204] demonstrated a modal frequency-based model updating technique of masonry building damaged during an earthquake. Likewise, Gharechahi et al. [205] presented a model updating technique for damage detection using eigenvalues and eigenvectors of the intact and the damaged structure. The importance of detailed FE analysis for model updating of an actual structure was presented by Kodikara et al. [206], where they had successfully implemented the algorithm for two different structures using both automated and manual procedures. The efficiency of the sensitivity based model updating technique using wavelet coefficients was presented by Mansourabadi and Esfandiari [207] using numerical examples of 2D and

3D truss. Mahato and Chakraborty [208] developed an advanced synchrosqueezed wavelet based modal identification for FE model updating of a structure. The recent advancement of the computational facility has influenced model updating with data driven techniques, e.g., machine learning, neural network. A comparison between physics-based models and data-driven models offers contrasting results, where the physics-based approach is more efficient in identifying the modal parameters [209]. Here, the nomenclature physics based model refers to any explicit characterization of the mechanics behind the structural response. The damage estimated from the identified linear systems as the loss of effective stiffness may not be appropriate to quantify the actual case due to non-linear behaviour [210]. To address this limitation, non-linear FE model updating has become a viable option to the researchers, which was pioneered by Distefano and his coworkers [211, 212].

Among different techniques for damage quantification, the recursive Gaussian filtering based algorithms are more efficient in incorporating measurements. Commonly used Gaussian filtering techniques for non-linear FE model updating are extended Kalman filter [143, 213], Unscented Kalman filter [143, 214], and particle filter [106, 215]. EKF utilizes the Taylor series expansion of the non-linear state and observation equations to fit into the Kalman filter [122]. However, the derivation of the gradient vector to linearize a non-linear systems is an arduous task. Moreover, the linearization process itself introduces significant error, which leads to inaccurate parameter estimation. To address these problems, Julier and Uhlmann [140] have proposed UKF, which utilizes sigma points to propagate the non-linearity through the FE models. It quantifies the Gaussian distribution of the state variables accurately up to third-order for non-linearity [96]. Unlike EKF and UKF, where the assumption of Gaussianity is inherent, particle filter utilizes sample points generated from the actual distribution relaxing this assumption. Although frameworks of UKF and PF are somewhat similar, there is a conceptual difference between them. Chatzi and Smyth [97] conducted numerical experiments to compare these two techniques, where time-invariant parameters of a 3-DOF hysteretic structural system were estimated using both these techniques. They found that UKF is computationally efficient for real time applications, while PF provided a more accurate estimation of the structural parameters. Astroza et al. [216] demonstrated the estimation of material parameters of a non-linear FE model from the noisy measurements using UKF. Recently, a comparative study has been carried to investigate the relative performance of UKF, EKF, and iterated-EKF for non-linear model updating problems using reinforced concrete (RC) frame, and the results have shown the superiority of UKF over others [143].

5.1.1 Problem Formulation

From the above discussion, it can be observed that a significant amount of research works have been directed towards FE model updating. Although most of them are focused on linear models, some efforts have been made for mechanics-based non-linear FE model updating [**?**, 217, 218]. Among them, a few are focused on dealing with damage estimation and their impact on structural performance [219]. However, most of these studies aim to estimate phenomenological behaviour (often characterized by Bouc-Wen hysteresis) at the global level. In particular, damage estimation of reinforced concrete structure under earthquake excitation using a full-scale model needs further attention to study the efficiency of the up-

dating procedure, which is the main objective of this work. These updated mechanics-based non-linear FE models allow post-event damage assessment that serves as the foundation for decision making related to retrofitting and rehabilitation.

In general, designers use various finite element packages to model the structure where material parameters are selected accordingly to reproduce the actual behaviour. Contrary to this approach, researchers in the non-linear system identification community use the standard Bouc-Wen model or its advanced variants. These non-linear models can not be used directly within the finite element analysis used by the designers, where different material level models are used for analysis. To address this issue, the present study aims to use a constrained unscented Kalman filter algorithm to identify these non-linear material parameters directly. The optimized values of these parameters are expected to remain within the feasible domain, which the traditional UKF algorithm can not ensure. To address this issue, constraint conditioned are introduced within the unscented Kalman filter framework to ensure the stability of the identification process. With these in view, the following objectives are set for this work

1. Develop CUKF algorithm for finite element model updating using mechanics-based approach. In this process, constraint conditions are introduced to maintain the numerical stability of the filtering algorithm.

2. This unique effort for non-linear parameter estimation at the material level opens the possibility of damage quantification in a more precise manner, particularly for a reinforced concrete structure. For this purpose, a modified Park and Ang damage index is utilized for local and global condition assessment.

3. Validate the proposed damage estimation framework using the simulated response of a 2D reinforced concrete frame, which is modelled using fiber discretized distributed-plasticity elements. The damage incurred due to ground excitation is estimated from the updated FE model to investigate its efficiency and accuracy.

4. Finally, demonstrate the efficiency of the proposed framework using the test data obtained from the shake table experiment of a full-scale reinforced concrete bridge pier.

5.2 Non-linear Finite Element Modeling of Reinforced concrete structures

Modelling and analysis of non-linear behaviour of RC structures have witnessed significant development in the recent past. Most of these works use phenomenological models (e.g. Bouc-Wen [125] model) which is intended to capture the macro level non-linear hysteretic behaviour of a structure [220]. Although these models are excellent to capture the input-output relationship of a hysteretic structure, they are not adequate to model the damage mechanism of a complex system in terms of its location, type, and extent. Therefore, detailed material level non-linear finite element modeling is essential for damage assessment of reinforced concrete structures. In general, non-linear finite element models of reinforced

concrete can be broadly classified into two categories - distributed plasticity model and lumped plasticity model based on how the non-linearity is introduced into the element. In this paper, distributed plasticity is used due to its excellent capability in replicating the experimental non-linear behaviour of RC structures [221]. The hierarchical levels of non-linear FE modeling of RC frame are presented in Fig.5.1, which consists of an assembly of interconnected frame elements, modelled using force-based distributed plasticity. Accurate

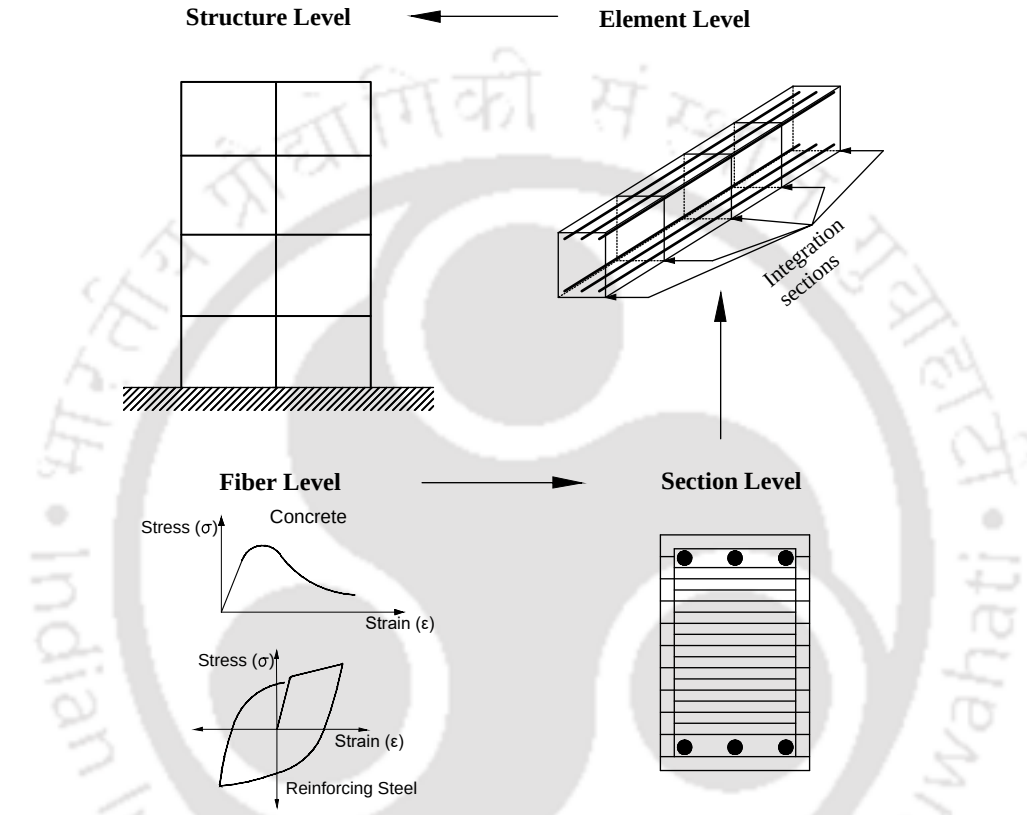

Figure 5.1: Hierarchy of non-linear FE modeling

calibration of these elements is essential for the proper implementation of non-linear behaviour. The best way to characterize them is done by the classical plastic theory using the material stress-strain behaviour at the critical sections [222, 223]. For this purpose, uniaxial material constitutive models for both concrete and reinforcement are used to form the fiber section of the beam and column elements. This type of analysis can efficiently capture the local stress-strain behaviour of an RC frame, which has significance in defining the damage state of a material. To address this issue, fiber discretized sections are employed in this study using open-sourced finite element modelling package Open System for Earthquake Engineering Simulation (OpenSees) [224]. The weighted integration of the sectional responses governs the behaviour at the element level, where the weights depend on the type of integration scheme used in the analysis. The fiber model of the element cross-sections is defined by dividing it into several strips depending upon the sectional geometry and number of steel

bars, followed by assigning the material properties to the individual fibers. Thus the section is classified into three different regions - cover concrete, core concrete, and reinforcements.

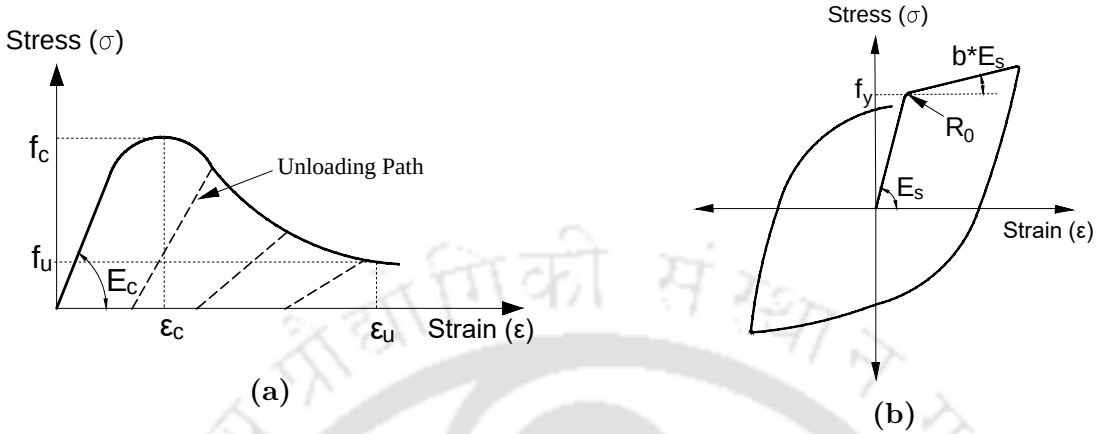

Figure 5.2: Material constitutive models; (a) concrete and (b) reinforcement

The accuracy of the fiber model while replicating the non-linear behaviour of the RC section depends on the constitutive material models [225]. Due to this reason, the material constitutive parameters of the concrete and steel need to be updated for damage quantification. In this study, the non-linear characteristics of concrete are modelled by Popovics-Saenz [226] material constitutive model, defined by *concrete04* in the *Opensees* platform. In general, the core and cover concrete behaviour are different under extreme loading conditions, where the nature of the core concrete is more ductile compared to the cover concrete. Therefore, they are modelled separately, where the ductile core concrete is modelled by the confinement factor as proposed by Mander et. al [227]. In this model, the stress-strain in compression envelope follows the non-linear Popovics concrete model [226] during loading, which is followed by linear unloading, where the slope is provided by the Karsan-Jirsa model [228] and the tensile characteristics are modelled with the help of an exponential function (refer to Appendix B). The behaviour of this model is governed by five material parameters i.e. modulus of elasticity (E_c), compressive strength (f_c), strain at the maximum compressive strength (ϵ_c), crushing strength (f_u), and strain at the crushing strength (ϵ_u) as shown in Fig. 5.2a. In the *concrete04* material model, the confined and unconfined compressive strengths are assumed to be unknown, which are updated directly. This model considers ϵ_c, f_u and ϵ_u as free parameters, among others. Moreover, the overall behaviour under the present level of shaking is not sensitive to these parameters. Hence, they are assumed to be constants and kept outside the identification loop to avoid over-fitting. The constant values of these parameters are provided in the numerical results and discussion. Further, E_c is modeled as a function of f'_c i.e. $E_c = 5000\sqrt{f'_c}$ as per the Indian design code [229]. However, the proposed identification algorithm does not demand this dependency. Hence, it is excluded from the updating procedure, and the only unknown concrete model parameter considered in this inverse formulation is f'_c. Similarly, the non-linear behaviour of reinforcement is defined by the Giuffre-Menegotto-Pinto (GMP) [230] constitutive model to account for isotropic hardening (refer to Appendix B). This model is governed by a combination of physical and empirical parameters to match the experimental behaviour of steel [231]. The remaining physical

time-invariant parameters are - modulus of elasticity (E_s), initial yield strength (f_y), strain hardening ratio (b) and elastoplastic transition parameter R_0 that regulate the backbone curve as shown in Fig. 5.2b. Among them, E_s is assumed to remain constant since it has a little variation for different grades of steel and manufacturer [232]. The other three unknown physical parameters are updated in this study keeping all other parameters known. Apart from these parameters, Rayleigh damping in the form of modal damping ratios (ξ_i) is also considered as one of the unknown parameters. Altogether, five parameters constitute the unknown parameter vector $\mathbf{\Theta}$, which can be written as

$$\mathbf{\Theta} = \begin{bmatrix} f_y & R_0 & b & f_c & \xi_i \end{bmatrix}^T \tag{5.1}$$

In the following section, updating procedure of the unknown parameter vector Θ are explained using modified Kalman filter theory.

5.3 Finite Element Model Updating Using Constrained Unscented Kalman Filter

The equilibrium equation of a non-linear reinforced concrete structure after assembling the beam-column elements using distributed plasticity is expressed by Eq. 4.1, where Θ represents unknown material parameters as shown in Eq. 5.1. This equation is expressed by augmenting the state-vector with unknown parameters as (refer to section 4.2.1

$$\begin{Bmatrix} \dot{\mathbf{Z}}_1 \\ \dot{\mathbf{Z}}_2 \\ \dot{\mathbf{Z}}_3 \end{Bmatrix} = \begin{Bmatrix} \mathbf{Z_2} \\ \mathbf{M}^{-1}\left\{\mathbf{B}\mathbf{f}\left(t\right) - \mathbf{F}\left[{\mathbf{Z_1}}^T\left(t\right), {\mathbf{Z_2}}^T\left(t\right), {\mathbf{Z_3}}^T\left(t\right)\right]\right\} \\ 0_{m\times 1} \end{Bmatrix} \tag{5.2}$$

where, $\mathbf{Z_1} = \mathbf{x}^T$; $\mathbf{Z_2} = \dot{\mathbf{x}}^T$ and $\mathbf{Z_3} = \mathbf{\Theta}^T$. The extended state vector in Eq. 4.2 consists of two parts - time-dependent state vector, i.e $\left\{{\mathbf{Z_1}}^T{\mathbf{Z_2}}^T\right\}^T$ and time-invariant parameter vector i.e. $\dot{\mathbf{\Theta}} = 0_{mx1}$. Eq. 4.6 represents the corresponding measurement equation used in this problem. This formulation of non-linear FE model updating is convenient for practical application since the parameters to be identified are included in the state vector and any measured response quantity (e.g. acceleration,velocity, displacement, strain etc.) can be incorporated into this format. It is worthy to mention that during the model updating process, the domain of these parameters must be realistic. For example, the strain hardening ratio (b) of the steel should be within 0 to 1. Any value of b out of this domain can cause a run-time error in the solver. However, the original formulation of Gaussian filtering can not take into account any algebraic bounds on a system variable [165]. To address this issue, the authors have proposed a constrained UKF (CUKF) algorithm so that the respective bounds can be assigned to each parameter to avoid any instability issue. The implementation of parameter bounds in the state-space model has already been explained in section 3.2.

5.3.1 Damage Quantification

Once the non-linear model of the reinforced concrete structure is updated based on the actual measurements, it can be further utilized to quantify the in-situ damage incurred into

a structure. In this study, the damage is quantified using a non-dimensional damage index (DI) due to its ability to correlate the damaged state of the structure. A review of different indices used for damage estimation of a reinforced concrete structure can be found in [198]. Among them, the modified Park and Ang damage index is chosen in this study due to its efficiency and excellent correlation with the laboratory test results [188]. The damage of a structure during an earthquake can be characterized by the combined action of maximum deformation and hysteretic energy dissipation during the loading cycles. The modified Park and Ang damage index combines these two aspects as a linear combination of normalized deformation and hysteretic energy adsorption, making it one of the suitable candidates for damage quantification. The expression for this damage index at any section of an element is given by [233]

$$DI_L = \frac{\theta_m - \theta_y}{\theta_u - \theta_y} + \beta \frac{\int dE}{M_y \theta_u} \tag{5.3}$$

where θ_m, θ_u and θ_y are the maximum, ultimate, and yield rotation, respectively, while M_y is the yield moment and $\int dE$ is the dissipated hysteresis energy in each loading cycle. The nonzero positive parameter β in Eq. 5.3 refers to cyclic degradation. In this study, the value of this parameter is assumed to be 0.1 as recommended by IDARC 3.0 [233]. Using sectional data, the global damage index (DI_G) of a structure can be evaluated as a weighted average of the local damage indices (DI_L), considering dissipated energy as the weight function [234]. Thus, the global damage index can be mathematically expressed as

$$DI_G = \frac{\sum_{i=1}^{N} (DI_L)_i E_i}{\sum_{i=1}^{N} E_i} \tag{5.4}$$

where $(DI_L)_i$ denotes the local damage index at the i^{th} section of an element and N represents the total number of sections considered in the structure.

5.4 Numerical Validation

In this section, the constrained unscented Kalman filter is used for damage assessment of a reinforced concrete bridge pier. However, the methodology is validated first using a synthetic experiment before the condition assessment of a bridge pier, which is discussed below.

5.4.1 Validation Exercise

The numerical validation example consists of a two-dimensional 3-storey-2-bay reinforced concrete frame subjected to ground excitation. The width of each bay is 4 m and the height of each storey is 3 m. The dead load and the live load acting on this structure are assumed to be a uniformly distributed load of 36 kN/m over the beams and the corresponding seismic masses are computed according to IS-1893 [235]. The reinforcements are designed as per IS 456 [229] and IS 13920 [236], which are shown in Fig. 5.3. Distributed plasticity-based

beam-column elements with five integration points are used in the FE model as explained in section 5.2. Rayleigh damping with critical damping ratios ξ_1 and ξ_2 are assumed in the first two modes to simulate the structural response. In this context, the stiffness matrix at the last-committed state is used to define the Rayleigh damping in the Opensees framework. Further, the core concrete of each beam and column elements are discretized into 40 layers, which is also followed by the cover concrete. The size of the columns is (280×400) mm^2 with 6-16mm diameter bars as the main reinforcement and 2-legged 8 mm dia bar placed at 100 mm distance are considered as transverse reinforcement. Similarly for beams, the dimension is (350×350) mm^2 having 8-20mm diameter bars as main reinforcement with additional transverse rebars consisting of 2-legged 8 mm diameter bars spaced at 100 mm intervals. The sectional view of the beams and columns are shown in Fig. 5.3. The non-linear behaviour of reinforcements in beams and columns are modeled as a single layer having a uni-axial Giuffre-Menegotto-Pinto [230] material constitutive model.

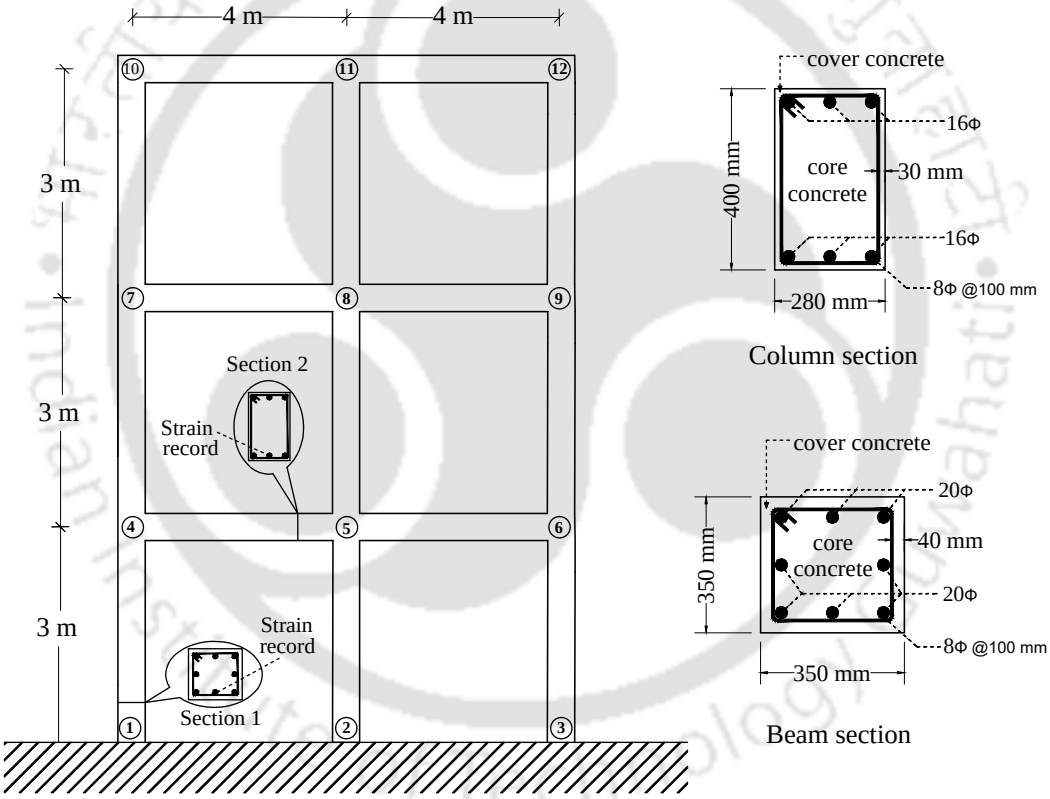

Figure 5.3: Multi-storey RC frame with reinforcement details

In this numerical example, the structural response is generated using scaled El-Centro ground excitation ($\ddot{u}_g$) acting at the base with a sampling rate of 200 Hz, as shown in Fig. 5.4. The scaling factor of the ground motion is selected so that the frame experiences non-linear deformation. The true value of the concrete material parameters used in this simulation are taken from Mackie et al. [237] and the parameters of the reinforcement are selected from the PEER report 2010/103 [238], which are $f_y = 487.45$ MPa, $R_0 = 15$, $b = 0.025$, $\xi_1 = 5\%$, $\xi_2 = 4\%$ and unconfined compressive strength $f'_c = 27.58$ MPa with

ϵ_c=0.002. The compressive strength of the unconfined concrete (f'_c) is factored as per Mander et al. [227] to obtain the core concrete strength (f_{cc}) for any flexural member. This factor depends on f'_c, yield strength of the transverse reinforcement and its given configuration. The reinforcement configuration for a particular structure is known (either from the design detailing or from the non-destructive tests). The variation of confinement factor for beams and columns due to the variation of f'_c and f_y of transverse reinforcement are obtained as 1.26±0.04 and 1.40±0.05 within the bounds of the respective parameter. Since the change of confinement factor is negligible, it is kept unchanged during the identification. Their values are assumed to be based on the nominal values of material parameters i.e. $f'_c = 27.58MPa$ and $f_y = 487.45MPa$. The properties of confined and unconfined concrete are shown in Table 5.1. However, the proposed identification algorithm does not impose any restriction on the choice of the confinement factor, which can be incorporated within the identification loop, if the need be. Thus, the compressive strength of the unconfined concrete (f'_c) is the only unknown parameter used to update *concrete04* material properties for both confined and unconfined concrete during the identification process.

Table 5.1: Properties of *concrete04* material model

Concrete Type	f'_c(MPa)	Confinement factor	f_{cc} (MPa)	ϵ_c	ϵ_u	E (MPa)
Unconfined	27.58	1.00	27.58	0.002	0.004	26258.33
Confined beam	27.58	1.26	35.01	0.00469	0.00902	26258.33
Confined column	27.58	1.40	38.81	0.00607	0.0131	26258.33

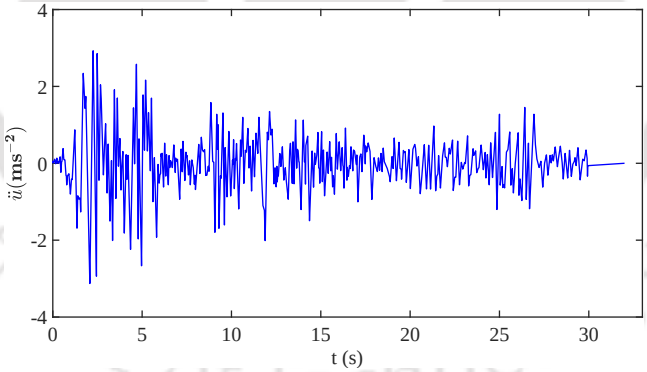

Figure 5.4: El-Centro ground motion

The seismic response of the structure is assumed to be known only at a few degrees of freedom, which are the relative accelerations at nodes 4, 7 and 12 as marked in Fig. 5.3. Besides acceleration response, the rebar strains at critical locations are also assumed to be known, which are marked as section 1 and section 2 in Fig. 5.3.

The proposed algorithm recursively estimates the unknown FE model parameters based on the sequential measurements. During this estimation process, the FE model needs to be run depending upon the number of unknown parameters. The number of sigma points generated at each time step is $(2n + 1)$, where n is the number of unknown parameters in

the vector $\boldsymbol{\Theta}$. Thus, the FE model needs to be run for $(2 \times 6 + 1) = 13$ times at every time step to estimate the updated parameters. At time t_k, the time history analysis is carried out from time zero to t_k, as proposed by Astroza et al. [216]. In this process, the bounds corresponding to each parameter are incorporated into the sigma point generation step with the help of Eq.3.4 to avoid numerical instability. The bounds for the material parameters f_y and f'_c are considered to be 400 MPa $\leq f_y \leq$ 600 MPa and 15 MPa $\leq f'_c \leq$ 30 MPa, respectively. Being the ratio between the post-yield tangent and initial elastic tangent, the parameter b must be within [0,1]. Similarly, the value of R_0 is assumed to remain within $10 \leq R_0 \leq 20$ and the damping ratio is assumed to be within the range $0 \leq \xi_i \leq 0.1$.

The initial Guess of these parameters are f_y=570 MPa, $R_0 = 18.48$, $b = 0.01$, $f'_c = 29.8$ MPa and $\xi_i = 0.01$. The process noise $\mathbf{Q}_k$ is considered to be a diagonal matrix with each term equal to 10^{-8}. Similarly, measurement noise is assumed to be a diagonal matrix whose each term corresponds to the variance of the zero-mean white noise process. It is assumed that initial state covariance is a diagonal matrix $\mathbf{P}_0 = diag\begin{pmatrix} 1.5 \times 10^4 & 150 & 0.0015 & 100 & 0.1 \end{pmatrix}$, which corresponds to the state variable in Eq.5.1 . In this study, two cases are considered based on the type of responses used in the measurement vector. In case 1, only acceleration responses are considered while in case 2 reinforcement strain time histories are included in addition to the acceleration time histories. These simulated acceleration time histories are polluted with zero-mean Gaussian white noise with two different intensities (i.e. 2% & 5% RMS noise) to account for the measurement noise. Fig.5.5 shows the updated FE model parameters using the proposed algorithm for the two cases with 2% RMS noise. Here, it is observed that the estimated parameters are stable and converged to their true values. Further, in most of these convergence plots in Fig.5.5, the inclusion of strain measurement in case 2 increases the efficiency of the algorithm as it takes fewer iterations to converge to their true values compared to case 1. The comparison of nodal responses is presented in Fig.5.6, demonstrating the efficiency of the finite element model updating algorithm. The accuracy of these updated parameters are present in Table 5.2 in terms of relative percentage error for each case, which is defined as $\frac{|\Theta_{est} - \Theta_{true}|}{\Theta_{true}} \times 100$. Here, Θ_{est} represents the estimate of any parameter, whereas Θ_{true} denotes the actual value of this parameter. The convergence plots for the 5% noise case are not presented to avoid repetition, though the results are included in Table 5.2. The relative percentage error of the estimated parameters for both these cases are comparable. However, the inclusion of the strain data in the measurement vector improves the efficiency of the proposed algorithm. The inset in Fig. 5.5b shows that the strain data faster convergence of model parameters. In general, the relative percentage errors of these parameters are below 5% irrespective of the measurement type, which proves the accuracy and robustness of the proposed algorithm for non-linear finite element model updating. A comparison of the sample moment-curvature (M-ϕ_c) relationship at two different sections is shown in Fig. 5.7. A close match is observed in these figures between the actual and the estimated quantities, which also establishes the accuracy of the constrained unscented Kalman filter algorithm used at the sectional level. In this context, it may be noted that the shear hinge formation is restricted by the capacity based design against seismic input. So, shear hinge formation has not been considered in the inverse identification of structural parameters. Moreover, this study aims to identify small to moderate levels of damage where bond-slip and anchorage failure are unlikely to occur. Hence, these effects are not included in the parameter estimation.

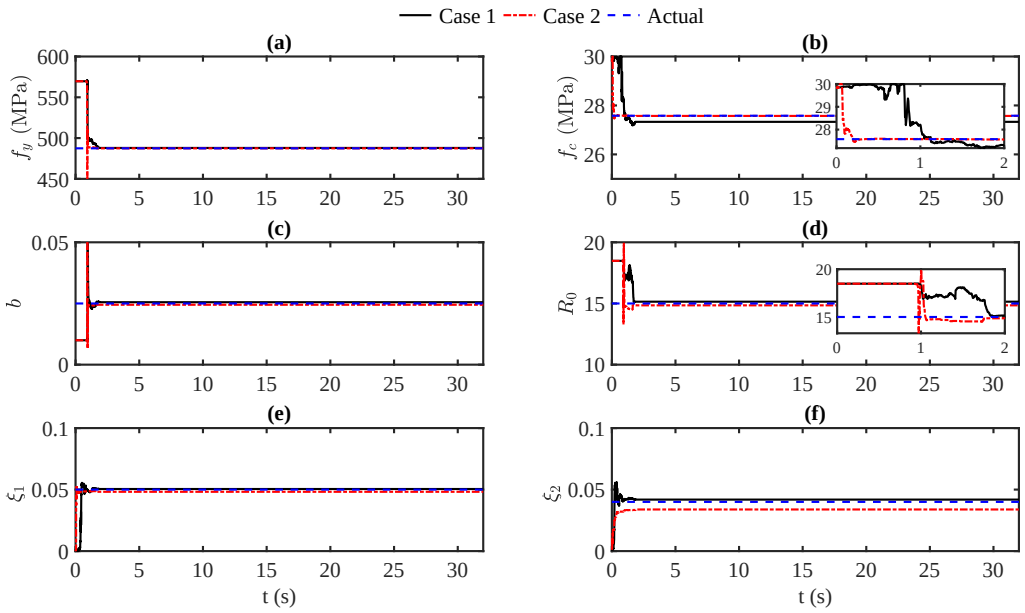

Figure 5.5: Updated FE model parameters for 2% noise; (a) f_y, (b) f_c', (c) b (d) R_0 (e) ξ_1 and (f) ξ_2

Table 5.2: Estimation error in % for updated FE model parameters

Noise level	Measurement Type	Relative Percentage Error					
		f_y	f_c	b	R_0	ξ_1	ξ_2
2%	Case 1	0.01	0.91	2.06	0.97	1.01	3.57
	Case 2	0.01	0.03	2.11	1.02	0.97	3.72
5%	Case 1	1.35	2.73	6.18	2.21	3.39	0.88
	Case 2	0.21	0.62	2.66	1.05	1.32	3.56

5.4.2 Damage estimation using modified Park and Ang index

In this subsection, the proposed algorithm is used for damage estimation of the frame, which is the main aim of this work. The global damage index is estimated for different cases and the results are summarized in Table 5.3. From this table, it can be observed that the proposed framework can estimate the global damage state directly from the recorded responses. Also, very small percentage error in the estimation of the global damage index (DI_G) in Table 5.3 demonstrates the high level of accuracy and robustness of the proposed bounded non-linear FE model updating using constrained unscented Kalman filter.

5.5 Experimental Validation

Once the performance of the proposed approach for damage estimation is established using a simulated example, it is further used for damage estimation of a full-scale bridge pier under

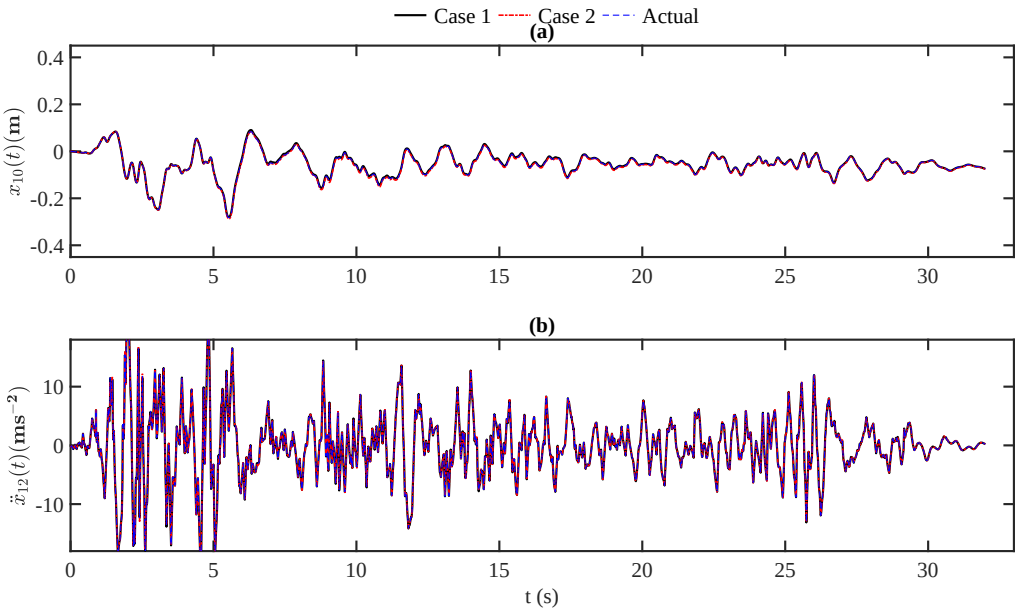

Figure 5.6: Comparison of actual and estimated responses for 2% noise; (a) $x_{10}(t)$ and (b) $\ddot{x}_{12}(t)$

Table 5.3: Estimated global damage index

Noise	Measurement Type	DI_G Estimate	DI_G Actual	% Error
2%	Case 1	0.3856	0.4056	4.90
	Case 2	0.4041	0.4056	0.36
5%	Case 1	0.4083	0.4056	0.66
	Case 2	0.3922	0.4056	3.30

earthquake excitation. In this study, the experimental result of a circular reinforced concrete bridge pier under uniaxial ground excitation is used. This test was carried out in the NEES-UCSD large High-Performance Outdoor Shake Table facility as shown in Fig.3.15a and test data are available in the public domain [179], i.e., DESIGNSAFE-CI platform [239] under the project name NEES-2010-0987. The diameter of this bridge pier is 1.22 m, which has a length of 7.32 m. To simulate the mass of the superstructure, a concrete block weighing 2245 kN is placed on top of the column. The PEER report no. 2015/02 [180] has all the necessary information regarding the instrumentation and the loading protocol. For experimental validation, the test data corresponding to EQ3 and EQ5 sequences are used in this work due to its distinguishable non-linear behaviour observed during the experiment in the form of damage. The schematic diagram of this test setup is presented in Fig. 5.8, along with the sensor placements. It should be noted that the naming of the sensors is kept consistent with the original data file available in the DESIGNSAFE-CI platform. The corresponding Opensees model of this bridge pier is shown in Fig. 5.9a. The bridge pier is modelled with *nonlinearBeamColumn* elements with five integration points such that the measurements corresponding to different heights of the pier can be utilized. The reinforcement details as

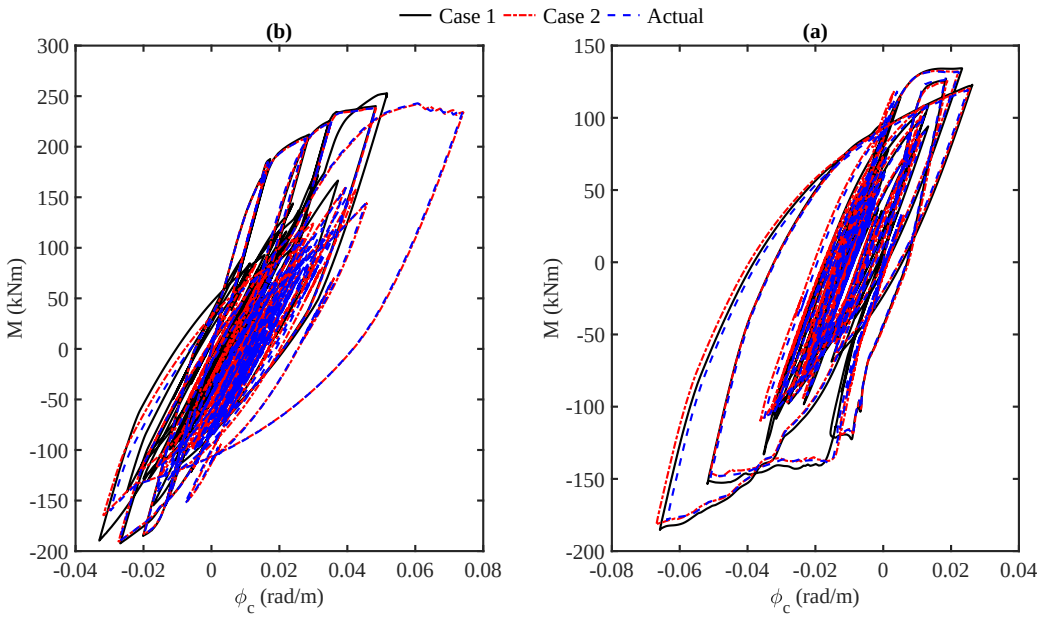

Figure 5.7: Comparison of moment-curvature (M-ϕ_c) relation for 5% noise; (a) section 1 and (b) section 2

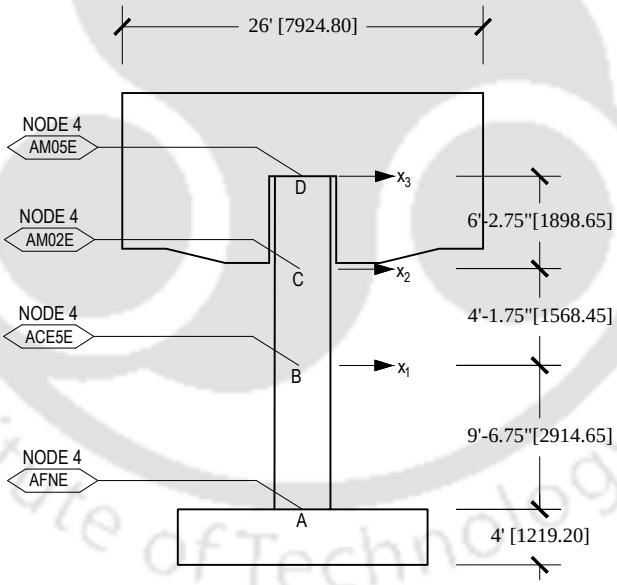

Figure 5.8: Schematic diagram of bridge pier for non-linear FE modeling

well as all other necessary information required in the FE modelling are adopted from the PEER report [180]. The mass of the concrete block resting on this pier is represented by an equivalent weight in the Opensees model. Similar to the previous example, damping is quantified using Rayleigh's model. Hence, ξ_i (i.e., critical damping ratio in the rst two modes), $i = 1, 2$ are the unknown damping parameters in the identification algorithm.

To apply the proposed algorithm, a parameter vector ($\boldsymbol{\Theta}$) is formed, which is similar to

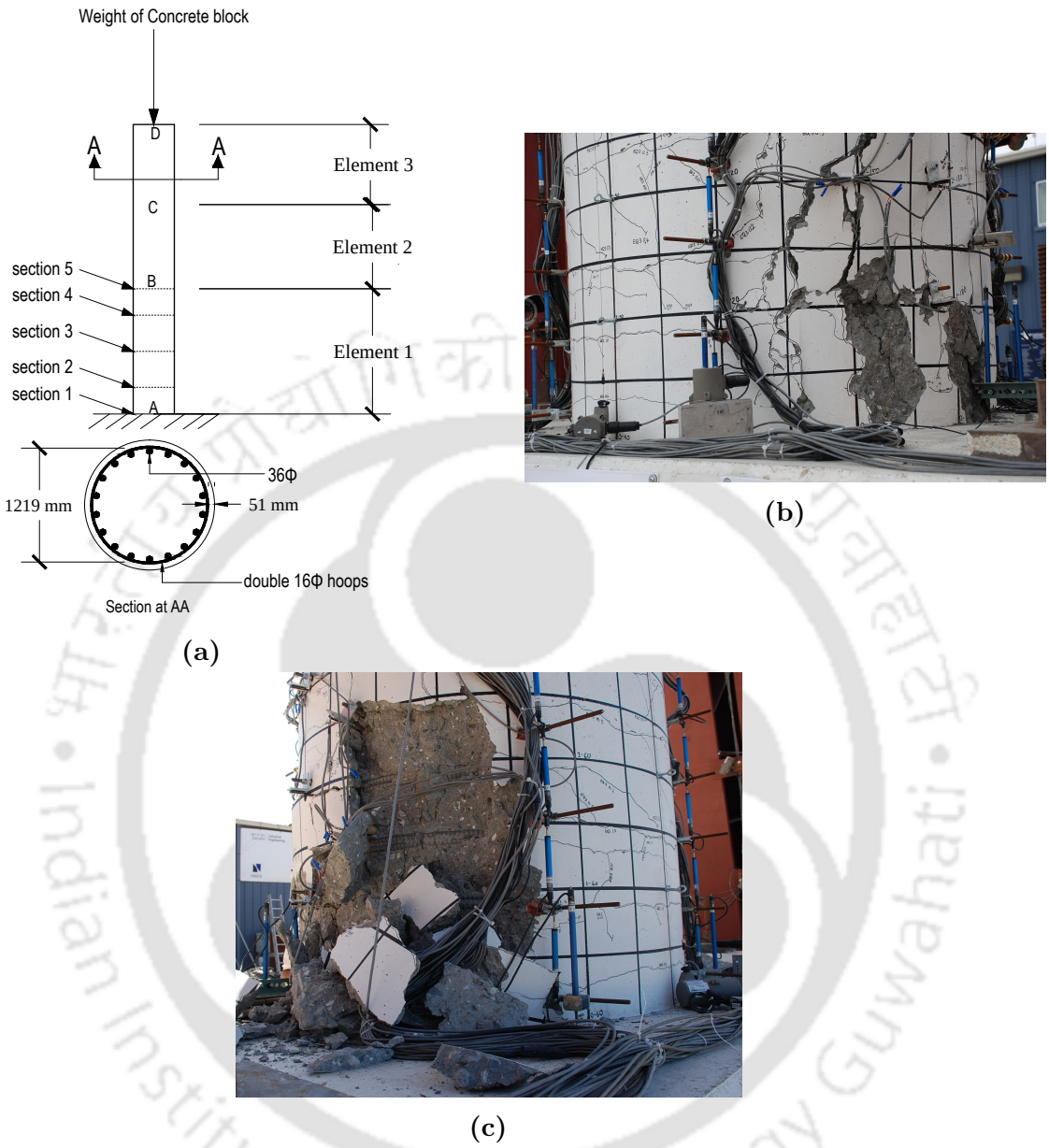

Figure 5.9: Details of bridge pier; (a) structural parameters, (b) damage during EQ3, and (c) damage during EQ5

the previous example i.e. $\mathbf{\Theta} = [f_y, R_0, b, f_c', \xi_i]$. The initial guess for the parameters in this model are f_y=500 MPa, $R_0 = 20$, $b = 0.01$ $f_c' = 40$ MPa and $\xi_i = 0.06$. Next, the parameter bounds are incorporated using Eq.3.4, which can be presented as 450 MPa $\leq f_y \leq$ 550 Mpa, 30 MPa $\leq f_c' \leq$ 50 Mpa, $0 \leq b \leq 1$, $10 \leq R_0 \leq 20$ and $0 \leq \xi_i \leq 0.1$. The measurement vector consists of acceleration responses at the degree of freedom (DOF) x_1, x_2 and x_3 as shown in Fig. 5.8. The process noise $\mathbf{Q}_k$ is assumed same as in previous example. The measurement noise covariance matrix $\mathbf{R_k}$ is a diagonal matrix, whose elements are evaluated from the pre-event measurement (i.e. when no excitation is applied). Also, the

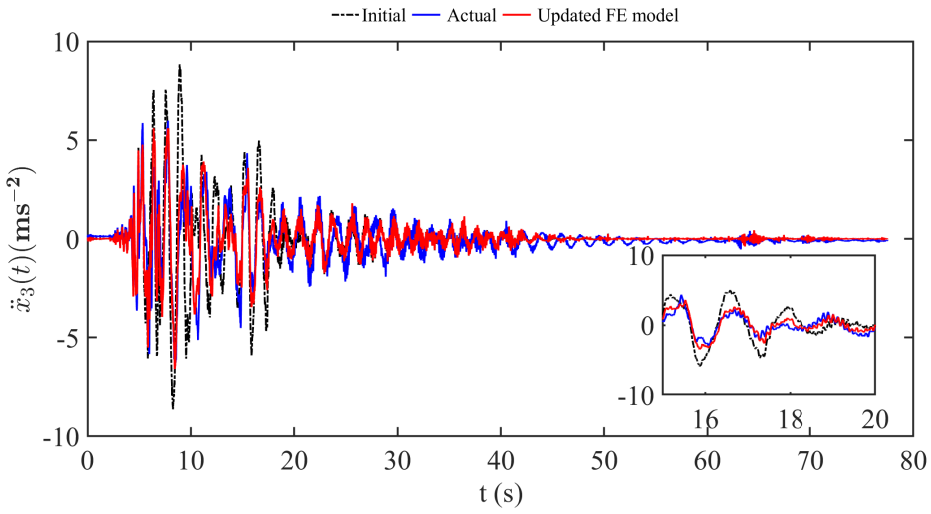

Figure 5.10: Comparison of initial and updated response of the FE model for EQ5 case

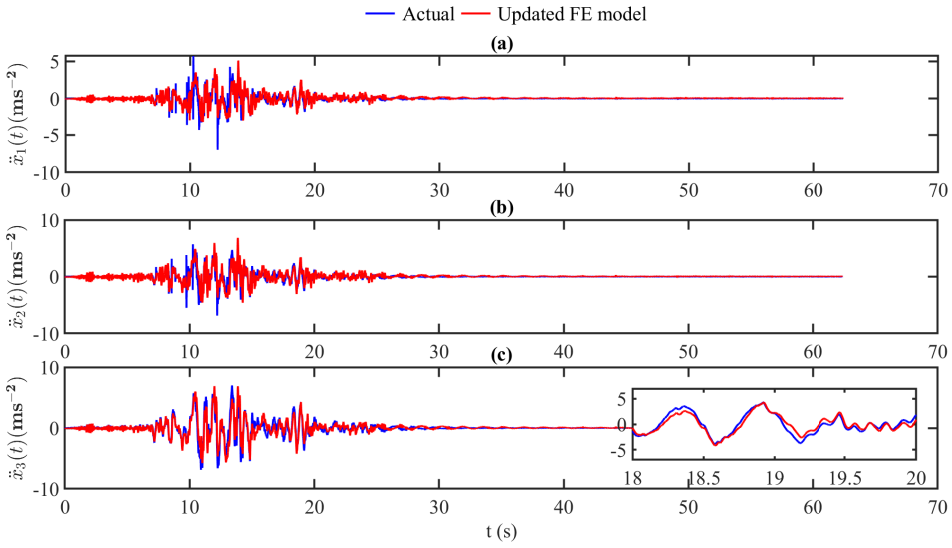

Figure 5.11: Comparison of response for EQ3 case; (a) $\ddot{x}_1(t)$, (b) $\ddot{x}_2(t)$ and (c) $\ddot{x}_3(t)$,

initial state covariance matrix is assumed to be $\mathbf{P}_0 = diag\begin{pmatrix} 4\times10^4 & 200 & 0.03 & 200 & 0.1 \end{pmatrix}$. Fig.5.12 shows the performance of the algorithm in terms of the convergence plot of the parameters. The proposed algorithm has shown satisfactory performance by converging all the model parameters without any instability. The parameter estimation results for both EQ3 and EQ5 cases are summarized in Table 5.4. The degradation of material strength can be observed from this table as the final estimated values of the parameters f_c and f_y marginally deteriorating from EQ3 to EQ5 case. The effectiveness of the proposed technique can be observed from Fig 5.10, where the response obtained from the FE model using the initial guess of the parameters is compared with the updated model. It shows the error in response prediction has been significantly improved with the updated parameters. Further,

the response of the updated FE model is compared with the recorded data, as shown in Fig.5.11. The close match between the acceleration response of the updated model with the measurement demonstrates the accuracy of the proposed algorithm.

Similar to the validation exercise, the modified Park and Ang damage index is also employed to estimate the damage state of this bridge pier. The capacity related parameters i.e. yield moment M_y, yield curvature ϕ_y and ultimate curvature ϕ_u are taken from the PEER report no. 2015/02 [180], which are given by M_y = 5793 (kNm), ϕ_y= 4.73×10^{-3} (rad/m) and ϕ_u = 7.56 × 10^{-2} (rad/m). It is observed from the updated model that the damage is concentrated to element 1 as shown in Fig. 5.9b and the remaining elements are found to be undamaged. The local damage index calculated at each section of element 1 is presented in Table 5.5. Section 1, 2 and 3 show substantial damage due to the earthquake excitation while section 5 remains undamaged (i.e. $DI_L = 0$). The damaged state in sections 1 and 2 can also be observed from the non-linear moment-curvature relationships, as shown in Fig. 5.13. The estimated damage at these sections conforms to the observed damage state of the pier as shown in Fig. 5.9b, where damage is confined near the bottom of the bridge pier. The damage states are compared using the damage index values, as shown in Table 5.5, it is observed that the global damage index for the EQ5 event is greater than the EQ3 event. Fig 5.9b and Fig 5.9c show that the spalling of cover concrete started during the EQ3 event, which was later intensified during the EQ5 event. The estimated global damage index values for these two events reflect this trend. Overall, substantial damage is incurred during these two events in the form of extensive damage in cover concrete, which is well estimated by the global damage index (DI_G).

Table 5.4: Estimated parameters for bridge pier

Parameters	EQ3	EQ5
f'_c	46.44 MPa	45.81 MPa
f_y	462.78 MPa	450.10 MPa
b	0.29	0.07
R_0	15.10	18.75
ξ_1	0.064	0.063
ξ_2	0.070	0.071

The proposed technique utilizes a constrained unscented Kalman filter for model updating of RC structure. Contrary to the traditional UKF, the proposed technique has adopted a unique approach to pre-define the feasible domain to the unknown parameters. This strategy is essential for the model updating of actual structures as the Kalman filter approach does not allow bounds to the state variable. The proposed technique can be readily used taking advantage of the existing FE package for model updating. The numerical exercise shows that the proposed technique is highly accurate as the percentage errors are insignificant (i.e., below 5%). Also, the damage state estimated using the damage index shows a minimal difference from the actual value as the percentage error is very low. Later, the applicability of the proposed technique is demonstrated using a full-scale bridge pier experiment. Stable convergence is achieved for the parameters using the proposed constrained UKF algorithm

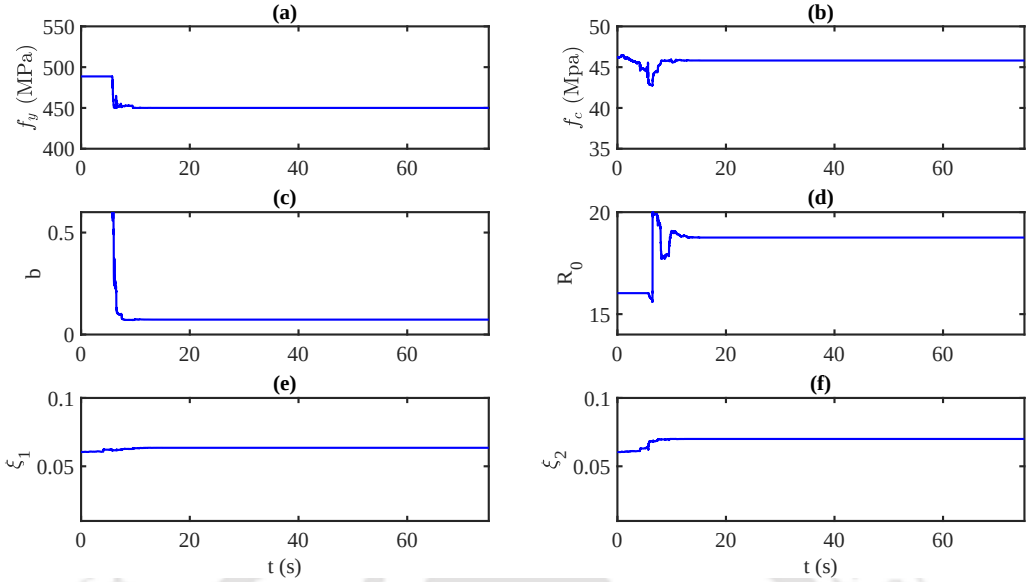

Figure 5.12: Updated Parameters of the bridge pier for EQ3 event; (a) f_y, (b) f'_c, (c) b (d) R_0 (e) ξ_1 and (f) ξ_2

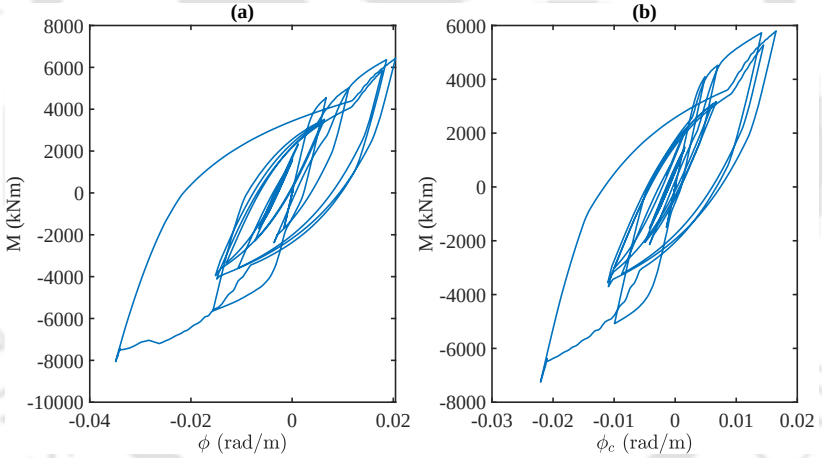

Figure 5.13: Non-linear moment-curvature relationship for EQ5 event; (a) section 1 and (b) section 2

while the estimate of the unconstrained UKF diverges from the actual one, as shown in Fig.5.14. Due to this divergence in f_y (below zero), the solver faces instability and stops. It shows the importance of the proposed CUKF algorithm to solve practical problems. Also, the location of damage obtained from the CUKF technique match satisfactorily with the observed one. The extent of damage predicted by the updated model shows good resemblance, where the increasing trend of damage from EQ3 to EQ5 is captured through the estimated global damage index. Further, the efficiency of this technique can be observed from the satisfactory match between the of predicted response and the measurements, as shown in Fig. 5.11.

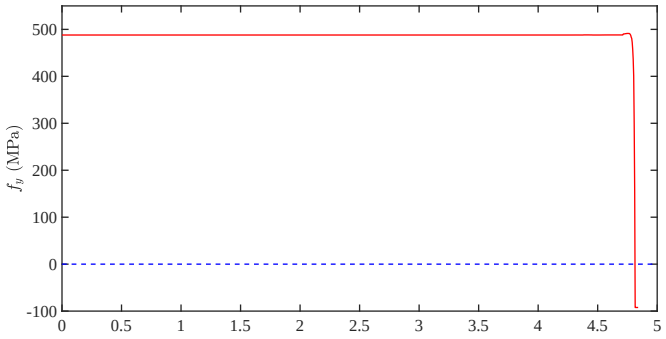

Figure 5.14: Estimation of f_y using unconstrained UKF for EQ5 event

Table 5.5: Estimated damage index for bridge pier experiment

Event	Section	DI_L	DI_G
EQ3	section 1	0.393	0.328
	section 2	0.339	
	section 3	0.148	
	section 4	0.040	
	section 5	0.00	
EQ5	section 1	0.565	0.443
	section 2	0.322	
	section 3	0.173	
	section 4	0.001	
	section 5	0.00	

5.6 Summary

This study presents a new framework for material level system identification for damage assessment of a reinforced concrete structure using a modified version of the unscented Kalman filtering technique. The complete framework is based on non-linear finite element model updating using constrained conditions, where the sigma points are generated within a predefined domain of the respective model parameters. The proposed framework updates the parameters using noisy measurements (i.e., acceleration, strain history, etc.), which are used for condition assessment using modified Park and Ang damage index. First, the proposed algorithm is validated using the simulated response of a multistory 2D moment-resisting frame. This numerical analysis show the efficiency of the proposed methodology for estimating the damage state of the structure excited by seismic ground motion. Finally, the performance of the proposed damage estimation algorithm is demonstrated using full-scale test results of a reinforced concrete bridge pier. It clearly shows the possibility to update element-level material parameters, which is the main aim of this study. This element-level parameter identification helps to quantify both in-situ local and global damage, which can be further utilized for decision-making before retrofitting/rehabilitation.

Chapter 6

Conclusions and Future Work

The work presented in this thesis primarily contributes toward the development of the Kalman filter algorithm and its application in structural health assessment. The focus of this work is mainly aimed at hysteretic structures, which possess a unique set of challenges. Several studies have been conducted to identify hysteretic systems using filtering algorithms. However, they are dedicated to estimating phenomenological parameters using simulated examples or small scale laboratory experiments. The performance of these algorithms has not been tested extensively for full-scale reinforced concrete structures. Thus, an effort has been made in this thesis towards the identification and damage estimation of hysteretic systems. Significant emphasis is given to the tuning of different algorithms for condition assessment of the full-scale structure. The important contributions of this work and their possible extension for future research are reported in the following sections.

6.1 Summary and Conclusions

A novel filtering based identification strategy has been developed in this thesis to estimate hysteretic structure incorporating the prior knowledge of the system and some constrained conditions. Overall, this work proposes different adaptive versions of sigma point-based recursive filtering for various applications, i.e., identifying phenomenological models (e.g. Bouc-Wen hysteresis) to mechanics-based material characterization for non-linear FE models. The major observations from the numerical works presented in this thesis are reported below

- The sigma point-based CMVU algorithm is developed for simultaneous identification of hysteretic parameters and input excitation. The numerical instability in this process is taken care of by the efficient use of BIBO property within the CMVU algorithm using suitable constraint conditions. This BIBO property is essential for structural or mechanical hysteretic systems to maintain realistic response and energy dissipation characteristics. In general, the traditional Kalman filter theory does not impose algebraic bounds on its state variables. To address this problem, the author has provided a novel solution by treating the state variable as a function of another auxiliary variable whose functional value is bounded. In contrast, the underlying auxiliary variable remains unbounded. This constraint implementation allows providing bounds on the hysteretic parameters, which facilitates the convergence to its optimal value. In a

nutshell, both parameter bounds and BIBO constrained conditions have helped in the iterative identification process, where non-linearity is propagated through the sigma points. Further, the proposed CMVU algorithm can estimate the input force acting on the system, which is helpful for structures having no sensor dedicated for input measurement.

- The proposed CMVU algorithm is successfully validated using the simulated response of a 3-DOF hysteretic system whose extended Bouc-Wen parameters (including degradation and pinching) are obtained from the actual behaviour of an RC frame. The rationality behind this modelling approach is to replicate the actual non-linear material behaviour instead of using hypothetical values of the hysteretic parameters. The results of this synthetic experiment show the efficiency of the proposed algorithm for simultaneous input and parameter estimation. It is worth noting that between the two different sigma point generation schemes, unscented points are more accurate and robust in dealing with measurement noise by its additional central point, absent in the cubature quadrature scheme. Although the performance of unscented points is satisfactory, the moment estimation using these points is still inaccurate due to the limited number of sigma points in this scheme. Thus, a quasi-Monte Carlo point generation scheme based on a stochastic integration rule is presented, outperforming the unscented points.

- The experimental validation of the CMVU algorithm is demonstrated using full-scale test results of a reinforced concrete bridge pier. This study establishes the applicability of the proposed algorithm for the estimation of hysteretic parameters in the absence of recorded input, i.e., earthquake. The sensitivity analysis (i.e., the performance comparison with the other established technique) show the superiority of the proposed algorithm in dealing with numerical instability. The parameters of the hysteretic systems have converged to their optimal values, and the estimated input time-history shows good matching with the actual record.

- One of the significant advantages of the proposed constraint conditions is that it can be applied to any sigma point-based Kalman filtering algorithm, which provides numerical stability to the identification problem. The CIUKF algorithm has been developed to quantify the parameters of a hysteretic RC structure under known input to demonstrate its numerical performance. The results show the ability of the proposed technique for damage quantification using an energy-based damage index. Once validated with known input, it is further extended for simultaneous estimation of input and damage state of the hysteretic structure. In this context, the CMVU algorithm estimates the hysteretic energy dissipated by the system after any seismic event, which is a critical engineering damage parameter. These results are also validated with the recorded strain data, proving the accuracy of this algorithm for full-scale structures. The cumulative damage index (Park and Ang) is obtained for the bridge pier based on the estimated engineering damage parameters. It establishes a good correlation with the observed damage state, which can be extremely useful in the decision-making process.

- A damage estimation framework has been proposed for RC structures based on the material level non-linear finite element model updating using a modified version of the unscented Kalman filter. The fibre discretized distributed plasticity elements used in this study facilitate non-linearity at the material level using constitutive models. Here, the time-invariant model parameters are estimated using a constrained unscented Kalman filtering algorithm, where previously explained bounds are assigned to each parameter to avoid any numerical instability. The updated FE model is further utilized for the damage estimation in terms of modified Park and Ang damage index from the section level responses of the FE model. The proposed framework is first validated numerically for a reinforced concrete frame, followed by the experimental validation using shake table test results of a full-scale RC bridge pier. The location and extent of the damage obtained from the updated model of this bridge pier conform closely with the actual damage observed during the experiment. This result establishes the efficiency and robustness of the proposed damage estimation methodology, which can be helpful for rehabilitation/retrofitting of the structures after any seismic event.

6.2 Future Scope for Further Research

This work presented in this thesis clearly outlines the theoretical background of the Kalman filter and some of its advanced variants using different sigma point generation schemes. It also proposes efficient constrained conditions and parameter bounds, which are demonstrated using full-scale structural test results. The numerical examples presented in this thesis prove the efficiency and accuracy of the improved Kalman filter algorithm (particularly the CMVU estimator) to identify non-stationary input and non-linear hysteretic behaviour of RC structures. Although different engineering applications are demonstrated in this thesis satisfactorily, the proposed algorithms have room for further developments. With this in view, the following avenues are identified for further research -

- This study employed three different sigma point generation schemes (i.e., Unscented points, Cubature quadrature points, and quasi-Monte Carlo points) to estimate the statistical moments where the state variables undergo non-linear transformation. There are several sigma point generation schemes available in the literature (viz. Gauss-Hermite scheme, central difference scheme). The performance of the proposed algorithms using these sigma point generation schemes can be compared to study their efficiency for non-linear system identification and condition assessment.

- The algorithms proposed in this study have a common assumption that the measurement noises are modelled as a set of uncorrelated Gaussian white noise processes. However, measurement noises may not follow these assumptions always. Besides correlation and non-Gaussianity, the assumptions of additive noise, as in this case, may not be valid always. Therefore, there is a constant need to develop the Kalman filter or its advanced variant to deal with those situations.

- In this study, the mathematical developments of the Kalman filter and Its advanced variants are purely based on mono-component earthquake ground motion. The pro-

posed modification for the CMVU algorithm can be extended for structures experiencing multi-component earthquake ground motions. In this context, the mathematical model for multi-component input estimation needs to be developed considering coherence and other critical features of multi-component ground motions.

- The proposed CMVU algorithm characterizes structural non-linearity using Bouc-Wen hysteresis. It can be further modified to incorporate other mechanics-based material models available in different finite element modelling packages (e.g., Opensees, Ansys, Abaqus).

- The finite element updating framework presented in this study is focused on the RC structure. However, the performance of the same algorithm needs to be verified for other types of systems (e.g., steel-concrete composite). Although the basic CMVU algorithm used in this work does not change with different materials used in the modelling, its performance still needs to be verified using different types of structures as they involve various other challenges in their modelling.

- The study reported in this thesis considers condition assessment of RC structures under earthquake excitation only. The performance of the proposed technique needs to be verified for different loading other than earthquake ground motion. As stated earlier, the sigma point generation scheme and its use in the identification algorithm do not depend on the type of loading on the structure. However, the algorithm needs to be tuned for different structural, material, loading types on a case-to-case basis due to the complexities associated with them. Thus, suitable adjustments can be made to these algorithms depending upon the structures exposed to specific external events (e.g., explosions, fires, impacts, hurricanes, tsunamis).

Appendix A

Optimal Gain Matrix

The CMVU algorithm needs optimal gain matrix $\mathbf{L}_k$ to estimate the state $\tilde{\mathbf{Z}}_k$ without any bias. It is obtained by minimizing the trace of the covariance matrix $\mathbf{P}^{\mathbf{Z}}_{k|k}$, subjected to the condition $\mathbf{L}_k\mathbf{H}_k = 0$. The total Lagrangian for this constrained minimization problem takes the following form [240]

$$\begin{aligned}\Gamma\left(\mathbf{L}_k, \mathbf{\Lambda}_k\right) &= trace\left(\mathbf{P}^{\mathbf{Z}}_{k|k}\right) - trace\left(\mathbf{L}_k\mathbf{H}_k\mathbf{\Lambda}_k^T\right) \\ &= trace\left(\mathbf{P}^{\mathbf{Z}}_{k|k-1} - \mathbf{L}_k\mathbf{P}^{\mathbf{eZ}}_{k|k-1} - \mathbf{P}^{\mathbf{eZ}}_{k|k-1}\mathbf{L}_k^T\right) - trace\left(\mathbf{L}_k\mathbf{H}_k\mathbf{\Lambda}_k^T\right) \end{aligned} \tag{A.1}$$

where $\mathbf{\Lambda_k} \in \mathbb{R}^{n\times p}$ is the Lagrange multiplier. The 1^{st} derivative of the Lagrangian with respect to $\mathbf{L}_k$ and $\mathbf{\Lambda}_K$ are equal to zero for the optimal solution, i.e.,

$$\begin{bmatrix} \mathbf{P}^e_k & -\mathbf{H}_k \\ \mathbf{H}_k^T & 0 \end{bmatrix} \begin{bmatrix} \mathbf{L}_k^T \\ \mathbf{\Lambda}_k^T \end{bmatrix} = \begin{bmatrix} \mathbf{P}^{\mathbf{eZ}}_{k|k-1} \\ 0 \end{bmatrix} \tag{A.2}$$

Eq. A.2 offers unique solution for $\mathbf{P}^e_k > 0$ provided the following condition is satisfied

$$\mathbf{S} = \mathbf{H}_k^T\left(\mathbf{P}^e_k\right)\mathbf{H}_k \tag{A.3}$$

the schur coefficient $\mathbf{S}$ of the error covariance matrix is $\mathbf{P}^e_k > 0$ is non-singular. All this conditions lead to the solution of Eq. A.2 in the following form

$$\begin{aligned}\begin{bmatrix} \mathbf{L}_k^T \\ \mathbf{\Lambda}_k^T \end{bmatrix} &= \begin{bmatrix} \mathbf{P}^e_k & -\mathbf{H}_k \\ \mathbf{H}_k^T & 0 \end{bmatrix}^{-1} \begin{bmatrix} \mathbf{P}^{\mathbf{eZ}}_{k|k-1} \\ 0 \end{bmatrix} \\ &= \begin{bmatrix} (\mathbf{P}^e_k) - (\mathbf{P}^e_k)^{-1}\mathbf{H}_k\mathbf{S}^{-1}\mathbf{H}_k^T(\mathbf{P}^e_k)^{-1} & (\mathbf{P}^e_k)^{-1}\mathbf{H}_k S^{-1} \\ -\mathbf{S}^{-1}\mathbf{H}_k^T(\mathbf{P}^e_k)^{-1} & \mathbf{S}^{-1} \end{bmatrix} \end{aligned} \tag{A.4}$$

The above equation yields the optimal gain matrix $\mathbf{L}_k$. Substituting $\mathbf{L}_k$ into Eq. 3.29, the covariance matrix $\mathbf{P}^{\mathbf{Z}}_k$ of the CMVU state estimator $\tilde{\mathbf{Z}}_k$ can be obtained as

$$\mathbf{P}^{\mathbf{Z}}_{k|k} = \mathbf{P}^{\mathbf{Z}}_{k|k-1} - \mathbf{K}_k\left(\mathbf{P}^{\mathbf{e}}_k - \mathbf{H}_k\mathbf{P}^{\mathbf{f}}_k\mathbf{H}_k^T\right)\mathbf{K}_k^T \tag{A.5}$$

Appendix B

Material Models

The behaviour of the fiber beam-column element nonlinear behavior depends on the nonlinear characteristics exhibit at the fiber level. Thus, selection of material constitutive model for the fibers is crucial for replicating the actual behaviour. The critical aspect of these models is that strain at every fiber should be an explicit function of stress that will be reflected in sectional deformation. This thesis used two material models - one for concrete and another for reinforcing steel whose descriptions are given below.

B.1 Material Model for Reinforcement

Menegotto and Pinto [241] nonlinear model is used in this thesis to explain the stress-strain behavior of reinforcing steel, which was updated by Filippou et al. [230] to incorporate isotropic strain hardening. The stress-strain relationship of Menegotto and Pinto model can be expressed as

$$\sigma^* = b\varepsilon^* + \frac{(1-b)\,\varepsilon^*}{(1+\varepsilon^*)^{1/R}} \tag{B.1}$$

where $\varepsilon^* = \frac{\varepsilon-\varepsilon_r}{\varepsilon_0-\varepsilon_r}$ and $\sigma^* = \frac{\sigma-\sigma_r}{\sigma_0-\sigma_r}$. The above equation represents the stress-strain curve transition from straight line asymptotic with slope E_0 to another asymptote with slope E_1, as shown in Fig. B.1. In this figure, point A denotes the meeting point of two asymptotes under consideration and point B represents the last strain reversal point. The strain hardening ratio b represent the ratio of the slope E_1 and E_0 while R is responsible for the shape of the transition zone. The expression of R is given by

$$R = R_0\left(1 - \frac{cR_1\xi}{cR_2+\xi}\right) \tag{B.2}$$

where ξ denotes the normalized plastic deformation range controlling R, which is defined as

$$\xi = \left|\frac{\varepsilon_p - \varepsilon_0}{\varepsilon_y}\right| \tag{B.3}$$

In the above expression, ϵ_p is maximum recorded strain in the loading direction and ϵ_0 denotes current yield-strain updated after the reversal at ϵ_r. Despite its simplicity, isotropic

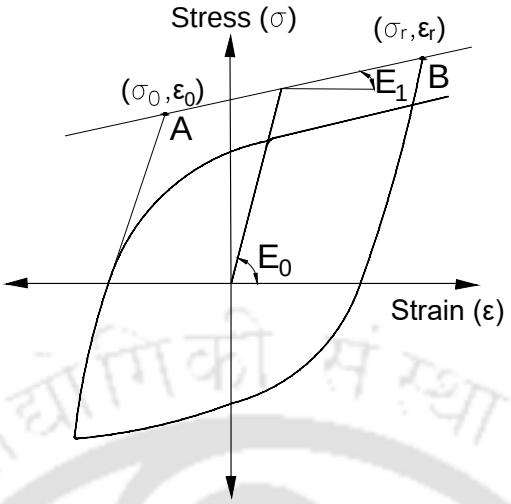

Figure B.1: Menegotto and Pinto steel model

hardening phenomenon can not be captured by this model. To address this issue, Filippou et al. [230] introduced this effect to the formulation by using a function to shift stress identified by the asymptotes. This shifted stress (σ_{st}) can be expressed as

$$\frac{\sigma_{st}}{\sigma_y} = a_1 \left(\frac{\varepsilon_{\max}}{\varepsilon_y} - a_2 \right) \tag{B.4}$$

where ϵ_{max} is the maximum strain at strain reversal. σ_y and ϵ_y are the stress and strain at yielding while a_1 and a_2 are two experimentally determined parameter.

B.2 Material Model for Concrete

The material model for concrete (i.e., *concrete04*) used in this thesis follows the Popovic's model [226] where the unloading slope is defined by Karsan-Jirsa model [228]. The relationship between stress (f) and strain (ϵ) obtained from the Popovic's model can be expressed as

$$f = f_c \left(\frac{\varepsilon}{\varepsilon_c} \right) \frac{n}{n - 1 + \left(\frac{\varepsilon}{\varepsilon_c} \right)^n} \tag{B.5}$$

where ε_c represents the strain corresponding to characteristic strength f_c, while the parameter n represents the following ratio

$$n = \frac{E_c}{E_c - E_{\text{sec}}} \tag{B.6}$$

Usually, the modulus of Elasticity E_c is defined by Mander et al. [227] and the secant modulus of elasticity, i.e., E_{sec} is defined at each time step i by the following formula.

$$E_{sec} = \frac{f_i}{\varepsilon_i} \tag{B.7}$$

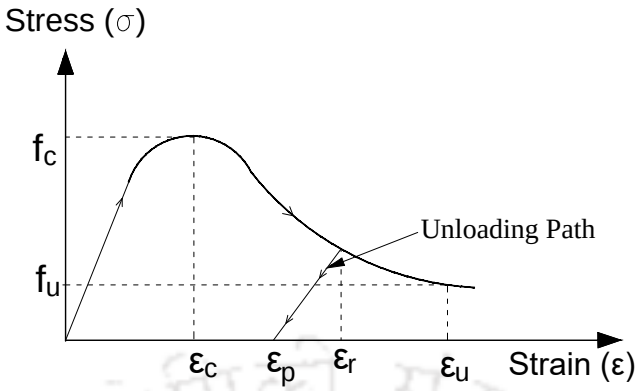

Figure B.2: *Concrete04* material model

The unloading path during a cyclic excursion is determined using Karsan-Jirsa model [228]. It takes place in a straight line from point ϵ_r on the envelope curve to ϵ_p (refer to Fig. B.2) on the strain axis using the following formulae

$$\frac{\varepsilon_p}{\varepsilon_c} = 0.145\left(\frac{\varepsilon_r}{\varepsilon_0}\right)^2 + 0.13\left(\frac{\varepsilon_r}{\varepsilon_0}\right) \quad \text{for} \left(\frac{\varepsilon_r}{\varepsilon_0}\right) < 2 \tag{B.8a}$$

$$\frac{\varepsilon_p}{\varepsilon_c} = 0.707\left(\frac{\varepsilon_r}{\varepsilon_0} - 2\right) + 0.834 \quad \text{for} \left(\frac{\varepsilon_r}{\varepsilon_0}\right) \geq 2 \tag{B.8b}$$

Thus, *Concrete04* material property is composed of Popovic's model and Karsen-Jirsa formulation for better representation of the experimental behaviour.

References

[1] "Infrastructure outlook." http://https://outlook.gihub.org/. accessed on: 27-06-2021.

[2] G. I. Outlook, "Infrastructure investment needs 50 countries, 7 sectors to 2040," *July, A G20 Initiative. Sydney: Global Infrastructure Hub*, 2017.

[3] "Earthquake disaster risk index report 50 towns and 1 district in seismic zones iii, iv and v," tech. rep., National Disaster Management Authority, Government of India, 2019.

[4] American Society of Civil Engineers (ASCE), "Report Card for America's infrastructure," 2017. https://www.infrastructurereportcard.org/.

[5] Intelligent Sensing for Innovative Structures, "Reinforcing concrete structures with fibre-reinforced polymers," 2007. ISIS Canada Research Network, Design Manual No.3, University of Manitoba, Manitoba, Canada.

[6] The American Road and Transportation Builders Association, "Bridge conditions report," 2021. https://artbabridgereport.org/reports/2021-ARTBA-Bridge-Report.pdf.

[7] Sumitomo Australia Pty Ltd, "Bridge repair market statistics," 2011. http://www.iceng.com.au/files/link/Bridge-market-statistics.pdf.

[8] C. R. Farrar, S. W. Doebling, and D. A. Nix, "Vibration–based structural damage identification," *Philosophical Transactions of the Royal Society of London A: Mathematical, Physical and Engineering Sciences*, vol. 359, no. 1778, pp. 131–149, 2001.

[9] C. Farrar and L. A. N. Laboratory, *Damage Prognosis: Current Status and Future Needs*. LA (Series) (Los Alamos, N.M.), Los Alamos National Laboratory, 2003.

[10] A. Rytter, *Vibrational based inspection of civil engineering structures*. PhD thesis, Dept. of Building Technology and Structural Engineering, Aalborg University, 1993.

[11] H. Sohn, C. R. Farrar, F. M. Hemez, D. D. Shunk, D. W. Stinemates, B. R. Nadler, and J. J. Czarnecki, "A review of structural health monitoring literature: 1996–2001," *Los Alamos National Laboratory*, 2003.

[12] K. Worden and J. M. Dulieu-Barton, "An overview of intelligent fault detection in systems and structures," *Structural Health Monitoring*, vol. 3, no. 1, pp. 85–98, 2004.

[13] K. Worden, C. R. Farrar, G. Manson, and G. Park, "The fundamental axioms of structural health monitoring," in *Proceedings of the Royal Society of London A: Mathematical, Physical and Engineering Sciences*, vol. 463, pp. 1639–1664, The Royal Society, 2007.

[14] C.-P. Fritzen and P. Kraemer, "Self-diagnosis of smart structures based on dynamical properties," *Mechanical Systems and Signal Processing*, vol. 23, no. 6, pp. 1830–1845, 2009.

[15] S. Park, C. Lee, and H. Sohn, "Reference-free crack detection using transfer impedances," *Journal of Sound and Vibration*, vol. 329, no. 12, pp. 2337–2348, 2010.

[16] E. S. Sazonov, P. Klinkhachorn, U. B. Halabe, and H. V. GangaRao, "Non-baseline detection of small damages from changes in strain energy mode shapes," *Nondestructive Testing and Evaluation*, vol. 18, no. 3-4, pp. 91–107, 2002.

[17] S. Patil, B. Karkare, and S. Goyal, "Corrosion induced damage detection of in-service rc slabs using acoustic emission technique," *Construction and Building Materials*, vol. 156, pp. 123–130, 2017.

[18] J. Tian, P.-F. Zhu, Y.-Y. Wang, and H.-F. Guo, "Experimental study and application of magnetic bridge double-loop main flux detection method," *Insight-Non-Destructive Testing and Condition Monitoring*, vol. 62, no. 2, pp. 98–103, 2020.

[19] D. Shoukroun, L. Massimi, F. Iacoviello, M. Endrizzi, D. Bate, A. Olivo, and P. Fromme, "Enhanced composite plate impact damage detection and characterisation using x-ray refraction and scattering contrast combined with ultrasonic imaging," *Composites Part B: Engineering*, vol. 181, p. 107579, 2020.

[20] G. Kerschen, K. Worden, A. F. Vakakis, and J.-C. Golinval, "Past, present and future of nonlinear system identification in structural dynamics," *Mechanical systems and signal processing*, vol. 20, no. 3, pp. 505–592, 2006.

[21] Y. Huang, C. Shao, B. Wu, J. L. Beck, and H. Li, "State-of-the-art review on bayesian inference in structural system identification and damage assessment," *Advances in Structural Engineering*, vol. 22, no. 6, pp. 1329–1351, 2019.

[22] S. W. Doebling, C. R. Farrar, M. B. Prime, and D. W. Shevitz, "Damage identification and health monitoring of structural and mechanical systems from changes in their vibration characteristics: a literature review," 1996.

[23] J. Penny, D. Wilson, and M. Friswell, "Damage location in structures using vibration data," in *PROCEEDINGS-SPIE THE INTERNATIONAL SOCIETY FOR OPTICAL ENGINEERING*, pp. 861–861, SPIE INTERNATIONAL SOCIETY FOR OPTICAL, 1993.

[24] Y.-S. Lee and M.-J. Chung, "A study on crack detection using eigenfrequency test data," *Computers & structures*, vol. 77, no. 3, pp. 327–342, 2000.

[25] D. Patil and S. Maiti, "Detection of multiple cracks using frequency measurements," *Engineering Fracture Mechanics*, vol. 70, no. 12, pp. 1553–1572, 2003.

[26] J.-T. Kim and N. Stubbs, "Crack detection in beam-type structures using frequency data," *Journal of Sound and Vibration*, vol. 259, no. 1, pp. 145–160, 2003.

[27] S. Zhong, S. O. Oyadiji, and K. Ding, "Response-only method for damage detection of beam-like structures using high accuracy frequencies with auxiliary mass spatial probing," *Journal of Sound and Vibration*, vol. 311, no. 3, pp. 1075–1099, 2008.

[28] C. Farrar and G. James III, "System identification from ambient vibration measurements on a bridge," *Journal of Sound and Vibration*, vol. 205, no. 1, pp. 1–18, 1997.

[29] X. Hua, *Structural health monitoring and condition assessment of bridge structures*. PhD thesis, The Hong Kong Polytechnic University, 2006.

[30] J. Ko, C. Wong, and H. Lam, "Damage detection in steel framed structures by vibration measurement approach," in *Proceedings-SPIE the International Society For Optical Engineering*, pp. 280–280, SPIE INTERNATIONAL SOCIETY FOR OPTICAL, 1994.

[31] A. Tatar, A. Niousha, and F. R. Rofooei, "Damage detection in existing reinforced concrete building using forced vibration test based on mode shape data," *Journal of Civil Structural Health Monitoring*, vol. 7, no. 1, pp. 123–135, 2017.

[32] Z. Shi, S. Law, and L. Zhang, "Damage localization by directly using incomplete mode shapes," *Journal of Engineering Mechanics*, vol. 126, no. 6, pp. 656–660, 2000.

[33] P. M. Pawar, K. Venkatesulu Reddy, and R. Ganguli, "Damage detection in beams using spatial fourier analysis and neural networks," *Journal of Intelligent Material Systems and Structures*, vol. 18, no. 4, pp. 347–359, 2007.

[34] L. Hadjileontiadis, E. Douka, and A. Trochidis, "Fractal dimension analysis for crack identification in beam structures," *Mechanical Systems and Signal Processing*, vol. 19, no. 3, pp. 659–674, 2005.

[35] I. Duvnjak, D. Damjanović, M. Bartolac, and A. Skender, "Mode shape-based damage detection method (msdi): Experimental validation," *Applied Sciences*, vol. 11, no. 10, p. 4589, 2021.

[36] O. Huth, G. Feltrin, J. Maeck, N. Kilic, and M. Motavalli, "Damage identification using modal data: Experiences on a prestressed concrete bridge," *Journal of Structural Engineering*, vol. 131, no. 12, pp. 1898–1910, 2005.

[37] M. A. Wahab and G. De Roeck, "Damage detection in bridges using modal curvatures: application to a real damage scenario," *Journal of Sound and vibration*, vol. 226, no. 2, pp. 217–235, 1999.

[38] A. Pandey, M. Biswas, and M. Samman, "Damage detection from changes in curvature mode shapes," *Journal of sound and vibration*, vol. 145, no. 2, pp. 321–332, 1991.

[39] C. P. Ratcliffe, "A frequency and curvature based experimental method for locating damage in structures," *TRANSACTIONS-AMERICAN SOCIETY OF MECHANICAL ENGINEERS JOURNAL OF VIBRATION AND ACOUSTICS*, vol. 122, no. 3, pp. 324–329, 2000.

[40] A. Dutta and S. Talukdar, "Damage detection in bridges using accurate modal parameters," *Finite Elements in Analysis and Design*, vol. 40, no. 3, pp. 287–304, 2004.

[41] Z. Shi, S. Law, and L. Zhang, "Structural damage detection from modal strain energy change," *Journal of engineering mechanics*, vol. 126, no. 12, pp. 1216–1223, 2000.

[42] H. Li, H. Yang, and S.-L. J. Hu, "Modal strain energy decomposition method for damage localization in 3d frame structures," *Journal of engineering mechanics*, vol. 132, no. 9, pp. 941–951, 2006.

[43] R. Janeliukstis, S. Rucevskis, M. Wesolowski, and A. Chate, "Experimental structural damage localization in beam structure using spatial continuous wavelet transform and mode shape curvature methods," *Measurement*, vol. 102, pp. 253–270, 2017.

[44] S. M. H. Pooya and A. Massumi, "A novel and efficient method for damage detection in beam-like structures solely based on damaged structure data and using mode shape curvature estimation," *Applied Mathematical Modelling*, vol. 91, pp. 670–694, 2021.

[45] C. Modena, D. Sonda, and D. Zonta, "Damage localization in reinforced concrete structures by using damping measurements," in *Key engineering materials*, vol. 167, pp. 132–141, Trans Tech Publ, 1999.

[46] S. D. Panteliou, T. G. Chondros, V. Argyrakis, and A. Dimarogonas, "Damping factor as an indicator of crack severity," *Journal of Sound and Vibration*, vol. 241, no. 2, pp. 235–245, 2001.

[47] H. Yamaguchi, Y. Matsumoto, K. Kawarai, A. J. Dammika, S. Shahzad, and R. Takanami, "Damage detection based on modal damping change in bridges," 2013.

[48] M. Cao, G. Sha, Y. Gao, and W. Ostachowicz, "Structural damage identification using damping: a compendium of uses and features," *Smart Materials and Structures*, vol. 26, no. 4, p. 043001, 2017.

[49] A. M. Ay, S. Khoo, and Y. Wang, "Probability distribution of decay rate: a statistical time-domain damping parameter for structural damage identification," *Structural Health Monitoring*, vol. 18, no. 1, pp. 66–86, 2019.

[50] A. Pandey and M. Biswas, "Damage detection in structures using changes in flexibility," *Journal of sound and vibration*, vol. 169, no. 1, pp. 3–17, 1994.

[51] J. Zhao and J. T. DeWolf, "Sensitivity study for vibrational parameters used in damage detection," *Journal of structural engineering*, vol. 125, no. 4, pp. 410–416, 1999.

[52] M. Salehi, S. Z. Rad, M. Ghayour, and M. Vaziry, "A non model-based damage detection technique using dynamically measured flexibility matrix," *Iranian Journal of Science and Technology. Transactions of Mechanical Engineering*, vol. 35, no. M1, p. 1, 2011.

[53] A. C. Altunışık, F. Y. Okur, S. Karaca, and V. Kahya, "Vibration-based damage detection in beam structures with multiple cracks: modal curvature vs. modal flexibility methods," *Nondestructive Testing and Evaluation*, vol. 34, no. 1, pp. 33–53, 2019.

[54] P. Caravani, M. Watson, and W. Thomson, "Recursive least-squares time domain identification of structural parameters," 1977.

[55] M. A. Torkamani and A. K. Ahmadi, "Stiffness identification of two-and three-dimensional frames," *Earthquake engineering & structural dynamics*, vol. 16, no. 8, pp. 1157–1176, 1988.

[56] D. Wang and A. Haldar, "Element-level system identification with unknown input," *Journal of Engineering Mechanics*, vol. 120, no. 1, pp. 159–176, 1994.

[57] M. Hoshiya and O. Maruyama, "Identification of running load and beam system," *Journal of engineering mechanics*, vol. 113, no. 6, pp. 813–824, 1987.

[58] E. Şafak, "Adaptive modeling, identification, and control of dynamic structural systems. i: Theory," *Journal of Engineering Mechanics*, vol. 115, no. 11, pp. 2386–2405, 1989.

[59] S. R. Ibrahim, "Time-domain quasilinear identification of nonlinear dynamic systems," *AIAA journal*, vol. 22, no. 6, pp. 817–823, 1984.

[60] P. Spanos, "Time domain method for parameter system identification," *Journal of Vibration and Acoustics*, vol. 112, p. 281, 1990.

[61] W. Tsai, D. Kung, and J. Yang, "Application of system identification technique to damage detection and location in offshore platform," in *Proceedings of the Seventh Offshore Mechanics and Arctic Engineering Conference, Houston*, pp. 77–83, 1988.

[62] X. Ling and A. Haldar, "Element level system identification with unknown input with rayleigh damping," *Journal of engineering mechanics*, vol. 130, no. 8, pp. 877–885, 2004.

[63] H. Katkhuda, R. Martinez, and A. Haldar, "Health assessment at local level with unknown input excitation," *Journal of Structural Engineering*, vol. 131, no. 6, pp. 956–965, 2005.

[64] H. Katkhuda and A. Haldar, "Defect identification under uncertain blast loading," *Optimization and Engineering*, vol. 7, no. 3, pp. 277–296, 2006.

[65] P. H. Vo and A. Haldar, "Health assessment of beams-experimental investigations," *Journal of Structural Engineering (Madras)*, vol. 31, no. 1, pp. 23–30, 2004.

[66] J. N. Yang, H. Huang, and S. Lin, "Sequential non-linear least-square estimation for damage identification of structures," *International Journal of Non-linear mechanics*, vol. 41, no. 1, pp. 124–140, 2006.

[67] E. A. Johnson, H.-F. Lam, L. S. Katafygiotis, and J. L. Beck, "Phase i iasc-asce structural health monitoring benchmark problem using simulated data," *Journal of engineering mechanics*, vol. 130, no. 1, pp. 3–15, 2004.

[68] J. N. Yang and H. Huang, "Sequential non-linear least-square estimation for damage identification of structures with unknown inputs and unknown outputs," *International Journal of Non-linear mechanics*, vol. 42, no. 5, pp. 789–801, 2007.

[69] X.-J. Wang and J. Cui, "A two-step method for structural parameter identification with unknown ground motion," in *Proceeding of the 14th World Conference on Earthquake Engineering (14-WCEE)*, vol. 1, pp. 12–19, 2008.

[70] Y. M. Choi, H. N. Cho, Y. B. Kim, and Y. K. Hwang, "Structural identification with unknown input excitation," *KSCE Journal of Civil Engineering*, vol. 5, no. 3, pp. 207–213, 2001.

[71] J. Chen and J. Li, "Simultaneous identification of structural parameters and input time history from output-only measurements," *Computational Mechanics*, vol. 33, no. 5, pp. 365–374, 2004.

[72] S. Sandesh and K. Shankar, "Time domain identification of structural parameters and input time history using a substructural approach," *International journal of structural stability and dynamics*, vol. 9, no. 02, pp. 243–265, 2009.

[73] R. Garrido and F. J. Rivero-Angeles, "Hysteresis and parameter estimation of mdof systems by a continuous-time least squares method," *Journal of earthquake engineering*, vol. 10, no. 02, pp. 237–264, 2006.

[74] B. Xu, J. He, R. Rovekamp, and S. J. Dyke, "Structural parameters and dynamic loading identification from incomplete measurements: approach and validation," *Mechanical systems and signal processing*, vol. 28, pp. 244–257, 2012.

[75] A. Aloisio, R. Alaggio, and M. Fragiacomo, "Dynamic identification of a masonry façade from seismic response data based on an elementary ordinary least squares approach," *Engineering Structures*, vol. 197, p. 109415, 2019.

[76] C.-B. Yun and M. Shinozuka, "Identification of nonlinear structural dynamic systems," *Journal of Structural Mechanics*, vol. 8, no. 2, pp. 187–203, 1980.

[77] M. Hoshiya and E. Saito, "Structural identification by extended kalman filter," *Journal of Engineering Mechanics*, vol. 110, no. 12, pp. 1757–1770, 1984.

[78] K. TOKI, T. SATO, and J. KIYONO, "Identification of structural parameters and input ground motion from response time histories," *Doboku Gakkai Ronbunshu*, vol. 1989, no. 410, pp. 243–251, 1989.

[79] N. Ott and H. Meder, "The kalman filter as a prediction error filter," *Geophysical Prospecting*, vol. 20, no. 3, pp. 549–560, 1972.

[80] L. Jeen-Shang and Z. Yigong, "Nonlinear structural identification using extended kalman filter," *Computers & Structures*, vol. 52, no. 4, pp. 757–764, 1994.

[81] A. W. Oreta and T.-a. Tanabe, "Localized identification of structures by kalman filter," *Doboku Gakkai Ronbunshu*, vol. 1993, no. 459, pp. 19–27, 1993.

[82] D. Wang and A. Haldar, "System identification with limited observations and without input," *Journal of Engineering Mechanics*, vol. 123, no. 5, pp. 504–511, 1997.

[83] H. Katkhuda and A. Haldar, "A novel health assessment technique with minimum information," *Structural Control and Health Monitoring*, vol. 15, no. 6, pp. 821–838, 2008.

[84] A. K. Das, *Health assessment of three dimensional large structural systems using limited uncertain dynamic response information*. The University of Arizona, 2012.

[85] R. Martinez-Flores, H. Katkhuda, and A. Haldar, "A novel health assessment technique with minimum information: verification," *International Journal of Performability Engineering*, vol. 4, no. 2, pp. 121–140, 2008.

[86] C.-K. Ma and C.-C. Ho, "An inverse method for the estimation of input forces acting on non-linear structural systems," *Journal of Sound and Vibration*, vol. 275, no. 3, pp. 953–971, 2004.

[87] J. N. Yang, S. Lin, H. Huang, and L. Zhou, "An adaptive extended kalman filter for structural damage identification," *Structural Control and Health Monitoring*, vol. 13, no. 4, pp. 849–867, 2006.

[88] Y. Lei, Y. Jiang, and Z. Xu, "Structural damage detection with limited input and output measurement signals," *Mechanical Systems and Signal Processing*, vol. 28, pp. 229–243, 2012.

[89] S. Sen and B. Bhattacharya, "Online structural damage identification technique using constrained dual extended kalman filter," *Structural Control and Health Monitoring*, vol. 24, no. 9, p. e1961, 2017.

[90] D. Li and Y. Wang, "Parameter identification of a differentiable bouc-wen model using constrained extended kalman filter," *Structural Health Monitoring*, vol. 20, no. 1, pp. 360–378, 2021.

[91] D. Y. Yun, T. Hong, D.-E. Lee, and H. S. Park, "Structural damage identification with a tuning-free hybrid extended kalman filter," *Structural Engineering International*, pp. 1–15, 2020.

[92] S. J. Julier, J. K. Uhlmann, and H. F. Durrant-Whyte, "A new approach for filtering nonlinear systems," in *American Control Conference, Proceedings of the 1995*, vol. 3, pp. 1628–1632, IEEE, 1995.

[93] A. Sitz, U. Schwarz, J. Kurths, and H. U. Voss, "Estimation of parameters and unobserved components for nonlinear systems from noisy time series," *Physical review E*, vol. 66, no. 1, p. 016210, 2002.

[94] C. Popescu and Y. Wong, "The unscented and extended kalman filter for systems with polynomial restoring forces," in *44th AIAA/ASME/ASCE/AHS/ASC Structures, Structural Dynamics, and Materials Conference*, p. 1410, 2003.

[95] S. Mariani and A. Ghisi, "Unscented kalman filtering for nonlinear structural dynamics," *Nonlinear Dynamics*, vol. 49, no. 1, pp. 131–150, 2007.

[96] M. Wu and A. W. Smyth, "Application of the unscented kalman filter for real-time nonlinear structural system identification," *Structural Control and Health Monitoring*, vol. 14, no. 7, pp. 971–990, 2007.

[97] E. N. Chatzi and A. W. Smyth, "The unscented kalman filter and particle filter methods for nonlinear structural system identification with non-collocated heterogeneous sensing," *Structural control and health monitoring*, vol. 16, no. 1, pp. 99–123, 2009.

[98] E. N. Chatzi, A. W. Smyth, and S. F. Masri, "Experimental application of on-line parametric identification for nonlinear hysteretic systems with model uncertainty," *Structural Safety*, vol. 32, no. 5, pp. 326–337, 2010.

[99] E. Ghorbani and Y.-J. Cha, "An iterated cubature unscented kalman filter for large-dof systems identification with noisy data," *Journal of Sound and Vibration*, vol. 420, pp. 21–34, 2018.

[100] M. Sheibani and G. Ou, "A bayesian optimized framework for successful application of unscented kalman filter in parameter identification of mdof structures," *Journal of Low Frequency Noise, Vibration and Active Control*, p. 14613484211014316, 2021.

[101] M. Cheng and T. C. Becker, "Performance of unscented kalman filter for model updating with experimental data," *Earthquake Engineering & Structural Dynamics*, vol. 50, no. 7, pp. 1948–1966, 2021.

[102] G. Evensen, "Sequential data assimilation with a nonlinear quasi-geostrophic model using monte carlo methods to forecast error statistics," *Journal of Geophysical Research: Oceans*, vol. 99, no. C5, pp. 10143–10162, 1994.

[103] R. Ghanem and G. Ferro, "Health monitoring for strongly non-linear systems using the ensemble kalman filter," *Structural control and health monitoring*, vol. 13, no. 1, pp. 245–259, 2006.

[104] W. Slika and G. Saad, "An ensemble kalman filter approach for service life prediction of reinforced concrete structures subject to chloride-induced corrosion," *Construction and Building Materials*, vol. 115, pp. 132–142, 2016.

[105] C. Manohar and D. Roy, "Monte carlo filters for identification of nonlinear structural dynamical systems," *Sadhana*, vol. 31, no. 4, pp. 399–427, 2006.

[106] H. Nasrellah and C. Manohar, "Finite element method based monte carlo filters for structural system identification," *Probabilistic Engineering Mechanics*, vol. 26, no. 2, pp. 294–307, 2011.

[107] B. Radhika and C. Manohar, "Nonlinear dynamic state estimation in instrumented structures with conditionally linear gaussian substructures," *Probabilistic Engineering Mechanics*, vol. 30, pp. 89–103, 2012.

[108] E. N. Chatzi and A. W. Smyth, "Particle filter scheme with mutation for the estimation of time-invariant parameters in structural health monitoring applications," *Structural Control and Health Monitoring*, vol. 20, no. 7, pp. 1081–1095, 2013.

[109] D. Sen, K. Erazo, and S. Nagarajaiah, "Bayesian estimation of acoustic emissions source in plate structures using particle-based stochastic filtering," *Structural Control and Health Monitoring*, vol. 24, no. 11, p. e2005, 2017.

[110] Z. Wan, T. Wang, S. Li, and Z. Zhang, "A modified particle filter for parameter identification with unknown inputs," *Structural Control and Health Monitoring*, vol. 25, no. 12, p. e2268, 2018.

[111] J. Li and W. Liu, "Seismic ground motion model," in *Lifeline Engineering Systems*, pp. 25–44, Springer, 2021.

[112] E. Lourens, C. Papadimitriou, S. Gillijns, E. Reynders, G. De Roeck, and G. Lombaert, "Joint input-response estimation for structural systems based on reduced-order models and vibration data from a limited number of sensors," *Mechanical Systems and Signal Processing*, vol. 29, pp. 310–327, 2012.

[113] S. E. Azam, E. Chatzi, and C. Papadimitriou, "A dual kalman filter approach for state estimation via output-only acceleration measurements," *Mechanical Systems and Signal Processing*, vol. 60, pp. 866–886, 2015.

[114] K. Maes, A. Smyth, G. De Roeck, and G. Lombaert, "Joint input-state estimation in structural dynamics," *Mechanical Systems and Signal Processing*, vol. 70, pp. 445–466, 2016.

[115] S. Gillijns and B. De Moor, "Unbiased minimum-variance input and state estimation for linear discrete-time systems," *Automatica*, vol. 43, no. 1, pp. 111–116, 2007.

[116] S. Gillijns and B. De Moor, "Unbiased minimum-variance input and state estimation for linear discrete-time systems with direct feedthrough," *Automatica*, vol. 43, no. 5, pp. 934–937, 2007.

[117] P. K. Kitanidis, "Unbiased minimum-variance linear state estimation," *Automatica*, vol. 23, no. 6, pp. 775–778, 1987.

[118] W. Song, "Generalized minimum variance unbiased joint input-state estimation and its unscented scheme for dynamic systems with direct feedthrough," *Mechanical Systems and Signal Processing*, vol. 99, pp. 886–920, 2018.

[119] R. E. Kalman, "A New Approach to Linear Filtering and Prediction Problems," *Journal of Basic Engineering*, vol. 82, pp. 35–45, 03 1960.

[120] P. S. Maybeck, *Stochastic models, estimation, and control*, vol. 3. Academic press, 1982.

[121] A. J. Haug, *Bayesian estimation and tracking: a practical guide*. John Wiley & Sons, 2012.

[122] R. E. Kalman *et al.*, "A new approach to linear filtering and prediction problems," *Journal of basic Engineering*, vol. 82, no. 1, pp. 35–45, 1960.

[123] R. E. Kalman and R. S. Bucy, "New results in linear filtering and prediction theory," *Journal of basic engineering*, vol. 83, no. 3, pp. 95–108, 1961.

[124] S. J. Julier and J. K. Uhlmann, "New extension of the kalman filter to nonlinear systems," in *Signal processing, sensor fusion, and target recognition VI*, vol. 3068, pp. 182–194, International Society for Optics and Photonics, 1997.

[125] R. Bouc, "Forced vibrations of mechanical systems with hysteresis," in *Proc. of the Fourth Conference on Nonlinear Oscillations, Prague, 1967*, 1967.

[126] A. G. Chassiakos, S. F. Masri, A. Smyth, and J. C. Anderson, "Adaptive methods for identification of hysteretic structures," in *Proceedings of 1995 American Control Conference - ACC'95*, vol. 3, pp. 2349–2353, June 1995.

[127] C.-Y. Peng and W. Iwan, "An identification methodology for a class of hysteretic structures," *Earthquake engineering & structural dynamics*, vol. 21, no. 8, pp. 695–712, 1992.

[128] A. Calabrese, S. Strano, and M. Terzo, "Adaptive constrained unscented kalman filtering for real-time nonlinear structural system identification," *Structural Control and Health Monitoring*, vol. 25, no. 2, p. e2084, 2018.

[129] Y. Ni, J. Ko, and C. Wong, "Nonparametric identification of nonlinear hysteretic systems," *Journal of engineering mechanics*, vol. 125, no. 2, pp. 206–215, 1999.

[130] E. Kosmatopoulos, A. Smyth, S. Masri, and A. Chassiakos, "Robust adaptive neural estimation of restoring forces in nonlinear structures," *Journal of applied mechanics*, vol. 68, no. 6, pp. 880–893, 2001.

[131] M. Yar and J. Hammond, "Parameter estimation for hysteretic systems," *Journal of sound and vibration*, vol. 117, no. 1, pp. 161–172, 1987.

[132] A. Smyth, S. Masri, A. Chassiakos, and T. Caughey, "On-line parametric identification of mdof nonlinear hysteretic systems," *Journal of Engineering Mechanics*, vol. 125, no. 2, pp. 133–142, 1999.

[133] J.-W. Lin, R. Betti, A. W. Smyth, and R. W. Longman, "On-line identification of non-linear hysteretic structural systems using a variable trace approach," *Earthquake engineering & structural dynamics*, vol. 30, no. 9, pp. 1279–1303, 2001.

[134] C. Koh and L. See, "Identification and uncertainty estimation of structural parameters," *Journal of Engineering Mechanics*, vol. 120, no. 6, pp. 1219–1236, 1994.

[135] H. Zhang, G. C. Foliente, Y. Yang, and F. Ma, "Parameter identification of inelastic structures under dynamic loads," *Earthquake engineering & structural dynamics*, vol. 31, no. 5, pp. 1113–1130, 2002.

[136] Y. Lei, F. Chen, and H. Zhou, "An algorithm based on two-step kalman filter for intelligent structural damage detection," *Structural Control and Health Monitoring*, vol. 22, no. 4, pp. 694–706, 2015.

[137] S. Li, Y. Suzuki, and M. Noori, "Identification of hysteretic systems with slip using bootstrap filter," *Mechanical systems and signal processing*, vol. 18, no. 4, pp. 781–795, 2004.

[138] J. Ching, J. L. Beck, and K. A. Porter, "Bayesian state and parameter estimation of uncertain dynamical systems," *Probabilistic engineering mechanics*, vol. 21, no. 1, pp. 81–96, 2006.

[139] M. S. Arulampalam, S. Maskell, N. Gordon, and T. Clapp, "A tutorial on particle filters for online nonlinear/non-gaussian bayesian tracking," *IEEE Transactions on signal processing*, vol. 50, no. 2, pp. 174–188, 2002.

[140] S. Julier, J. Uhlmann, and H. F. Durrant-Whyte, "A new method for the nonlinear transformation of means and covariances in filters and estimators," *IEEE Transactions on automatic control*, vol. 45, no. 3, pp. 477–482, 2000.

[141] K. Erazo and S. Nagarajaiah, "An offline approach for output-only bayesian identification of stochastic nonlinear systems using unscented kalman filtering," *Journal of Sound and Vibration*, vol. 397, pp. 222–240, 2017.

[142] K. Erazo and S. Nagarajaiah, "Bayesian structural identification of a hysteretic negative stiffness earthquake protection system using unscented kalman filtering," *Structural Control and Health Monitoring*, vol. 25, no. 9, p. e2203, 2018.

[143] R. Astroza, H. Ebrahimian, and J. P. Conte, "Performance comparison of kalman-based filters for nonlinear structural finite element model updating," *Journal of Sound and Vibration*, vol. 438, pp. 520–542, 2019.

[144] H. U. Voss, J. Timmer, and J. Kurths, "Nonlinear dynamical system identification from uncertain and indirect measurements," *International Journal of Bifurcation and Chaos*, vol. 14, no. 06, pp. 1905–1933, 2004.

[145] M. Wu and A. Smyth, "Real-time parameter estimation for degrading and pinching hysteretic models," *International Journal of Non-Linear Mechanics*, vol. 43, no. 9, pp. 822–833, 2008.

[146] E. Lourens, E. Reynders, G. De Roeck, G. Degrande, and G. Lombaert, "An augmented kalman filter for force identification in structural dynamics," *Mechanical Systems and Signal Processing*, vol. 27, pp. 446–460, 2012.

[147] Q. Zhang, Z. Duan, *et al.*, "Simultaneous identification of excitation time histories and parametrized structural damages," *Mechanical Systems and Signal Processing*, vol. 33, pp. 56–68, 2012.

[148] F. Naets, J. Croes, and W. Desmet, "An online coupled state/input/parameter estimation approach for structural dynamics," *Computer Methods in Applied Mechanics and Engineering*, vol. 283, pp. 1167–1188, 2015.

[149] S. E. Azam, V. Dertimanis, E. Chatzi, and C. Papadimitriou, "Output-only schemes for joint input-state-parameter estimation of linear systems," in *Proceedings of the 1st ECCOMAS Thematic Conference on Uncertainty Quantification in Computational Sciences and Engineering (UNCECOMP15)*, pp. 497–510, 2015.

[150] S. Pan, D. Xiao, S. Xing, S. Law, P. Du, and Y. Li, "A general extended kalman filter for simultaneous estimation of system and unknown inputs," *Engineering Structures*, vol. 109, pp. 85–98, 2016.

[151] Y. Lei, Y. Wu, and T. Li, "Identification of non-linear structural parameters under limited input and output measurements," *International Journal of Non-Linear Mechanics*, vol. 47, no. 10, pp. 1141–1146, 2012.

[152] J. N. Yang, S. Pan, and H. Huang, "An adaptive extended kalman filter for structural damage identifications ii: unknown inputs," *Structural Control and Health Monitoring: The Official Journal of the International Association for Structural Control and Monitoring and of the European Association for the Control of Structures*, vol. 14, no. 3, pp. 497–521, 2007.

[153] Y. Lei, D. Xia, K. Erazo, and S. Nagarajaiah, "A novel unscented kalman filter for recursive state-input-system identification of nonlinear systems," *Mechanical Systems and Signal Processing*, vol. 127, pp. 120–135, 2019.

[154] Z. Lai and S. Nagarajaiah, "Sparse structural system identification method for nonlinear dynamic systems with hysteresis/inelastic behavior," *Mechanical Systems and Signal Processing*, vol. 117, pp. 813–842, 2019.

[155] Z. Lai and S. Nagarajaiah, "Semi-supervised structural linear/nonlinear damage detection and characterization using sparse identification," *Structural Control and Health Monitoring*, vol. 26, no. 3, p. e2306, 2019.

[156] K. Erazo, B. Moaveni, and S. Nagarajaiah, "Bayesian seismic strong-motion response and damage estimation with application to a full-scale seven story shear wall structure," *Engineering Structures*, vol. 186, pp. 146–160, 2019.

[157] P. Sengupta and B. Li, "Hysteresis modeling of reinforced concrete structures: State of the art," *ACI Structural Journal*, vol. 114, no. 1, p. 25, 2017.

[158] Y.-K. Wen, "Method for random vibration of hysteretic systems," *Journal of the engineering mechanics division*, vol. 102, no. 2, pp. 249–263, 1976.

[159] F. Ikhouane, V. MañOsa, and J. Rodellar, "Adaptive control of a hysteretic structural system," *Automatica*, vol. 41, no. 2, pp. 225–231, 2005.

[160] F. Ikhouane and J. Rodellar, "On the hysteretic bouc–wen model," *Nonlinear dynamics*, vol. 42, no. 1, pp. 63–78, 2005.

[161] C. V. Rao, J. B. Rawlings, and D. Q. Mayne, "Constrained state estimation for nonlinear discrete-time systems: Stability and moving horizon approximations," *IEEE transactions on automatic control*, vol. 48, no. 2, pp. 246–258, 2003.

[162] P. Vachhani, R. Rengaswamy, V. Gangwal, and S. Narasimhan, "Recursive estimation in constrained nonlinear dynamical systems," *AIChE Journal*, vol. 51, no. 3, pp. 946–959, 2005.

[163] R. Mandela, V. Kuppuraj, R. Rengaswamy, and S. Narasimhan, "Constrained unscented recursive estimator for nonlinear dynamic systems," *Journal of Process Control*, vol. 22, no. 4, pp. 718–728, 2012.

[164] Y. Yang and F. Ma, "Constrained kalman filter for nonlinear structural identification," *Modal Analysis*, vol. 9, no. 12, pp. 1343–1357, 2003.

[165] R. Kandepu, L. Imsland, and B. A. Foss, "Constrained state estimation using the unscented kalman filter," in *2008 16th Mediterranean Conference on Control and Automation*, pp. 1453–1458, IEEE, 2008.

[166] F. Ikhouane, V. Mañosa, and J. Rodellar, "Dynamic properties of the hysteretic bouc-wen model," *Systems & control letters*, vol. 56, no. 3, pp. 197–205, 2007.

[167] I. Arasaratnam, S. Haykin, and R. J. Elliott, "Discrete-time nonlinear filtering algorithms using gauss–hermite quadrature," *Proceedings of the IEEE*, vol. 95, no. 5, pp. 953–977, 2007.

[168] I. Arasaratnam and S. Haykin, "Cubature kalman filters," *IEEE Transactions on automatic control*, vol. 54, no. 6, pp. 1254–1269, 2009.

[169] S. Bhaumik, "Cubature quadrature kalman filter," *IET Signal Processing*, vol. 7, no. 7, pp. 533–541, 2013.

[170] T. T. Baber and Y.-K. Wen, "Random vibration hysteretic, degrading systems," *Journal of the Engineering Mechanics Division*, vol. 107, no. 6, pp. 1069–1087, 1981.

[171] T. T. Baber and M. N. Noori, "Random vibration of degrading, pinching systems," *Journal of Engineering Mechanics*, vol. 111, no. 8, pp. 1010–1026, 1985.

[172] P. Sengupta and B. Li, "Modified bouc–wen model for hysteresis behavior of rc beam–column joints with limited transverse reinforcement," *Engineering Structures*, vol. 46, pp. 392–406, 2013.

[173] G. C. Foliente, "Hysteresis modeling of wood joints and structural systems," *Journal of Structural Engineering*, vol. 121, no. 6, pp. 1013–1022, 1995.

[174] V. L. Nithin, *Stochastic simulation of main shock-aftershock sequences and their use in damage-based seismic design of reinforced concrete structures*. PhD thesis, Indian Institute of Technology Guwahati, India, 2021.

[175] G. A. Ortiz, D. A. Alvarez, and D. Bedoya-RuíZ, "Identification of bouc–wen type models using multi-objective optimization algorithms," *Computers & Structures*, vol. 114, pp. 121–132, 2013.

[176] C.-H. Loh, C.-H. Mao, J.-R. Huang, and T.-C. Pan, "System identification and damage evaluation of degrading hysteresis of reinforced concrete frames," *Earthquake Engineering & Structural Dynamics*, vol. 40, no. 6, pp. 623–640, 2011.

[177] Z. Ding and B. Balaji, "Comparison of the unscented and cubature kalman filters for radar tracking applications," 2012.

[178] E. M. Rathje, C. Dawson, J. E. Padgett, J.-P. Pinelli, D. Stanzione, A. Adair, P. Arduino, S. J. Brandenberg, T. Cockerill, C. Dey, *et al.*, "Designsafe: new cyberinfrastructure for natural hazards engineering," *Natural Hazards Review*, vol. 18, no. 3, p. 06017001, 2017.

[179] M. J. Schoettler, J. Restrepo, G. Guerrini, D. E. Duck, and F. Carrea, "Large-scale validation of seismic performance of bridge columns [dataset]." https://doi.org/10.17603/DS2-D232. DesignSafe-CI, 2010.

[180] M. J. Schoettler, J. Restrepo, G. Guerrini, D. E. Duck, and F. Carrea, "A full-scale, single-column bridge bent tested by shake-table excitation," *Center for Civil Engineering Earthquake Research, Department of Civil Engineering, University of Nevada*, 2012.

[181] J. Duník, O. Straka, and M. Šimandl, "The development of a randomised unscented kalman filter," *IFAC Proceedings Volumes*, vol. 44, no. 1, pp. 8–13, 2011.

[182] A. Genz and J. Monahan, "Stochastic integration rules for infinite regions," *SIAM journal on scientific computing*, vol. 19, no. 2, pp. 426–439, 1998.

[183] V. L. Nithin, *Stochastic simulation of main shock-aftershock sequences and their use in damage-based seismic design of reinforced concrete structures*. PhD thesis, Indian Institute of Technology Guwahati, 2019.

[184] C. A. Gaviria and L. A. Montejo, "Monitoring physical and dynamic properties of reinforced concrete structures during seismic excitations," *Construction and Building Materials*, vol. 196, pp. 43 – 53, 2019.

[185] M. I. Todorovska and M. D. Trifunac, "Earthquake damage detection in the imperial county services building i: The data and time–frequency analysis," *Soil Dynamics and Earthquake Engineering*, vol. 27, no. 6, pp. 564–576, 2007.

[186] E. M. Hernandez and G. May, "Dissipated energy ratio as a feature for earthquake-induced damage detection of instrumented structures," *Journal of Engineering Mechanics*, vol. 139, no. 11, pp. 1521–1529, 2012.

[187] T. F. Zahrah and W. J. Hall, "Earthquake energy absorption in sdof structures," *Journal of structural Engineering*, vol. 110, no. 8, pp. 1757–1772, 1984.

[188] S. Ghosh, D. Datta, and A. A. Katakdhond, "Estimation of the parkang damage index for planar multi-storey frames using equivalent single-degree systems," *Engineering Structures*, vol. 33, no. 9, pp. 2509 – 2524, 2011.

[189] J. Shan, Y. Ouyang, H. Zhang, and W. Shi, "Model-reference damage tracking and evaluation of hysteretic structures with test validation," *Mechanical Systems and Signal Processing*, vol. 118, pp. 443 – 460, 2019.

[190] C.-M. Chang, S. Strano, and M. Terzo, "Modelling of hysteresis in vibration control systems by means of the bouc-wen model," *Shock and Vibration*, vol. 2016, 2016.

[191] W. Song and S. Dyke, "Real-time dynamic model updating of a hysteretic structural system," *Journal of Structural Engineering*, vol. 140, no. 3, p. 04013082, 2013.

[192] S. S. Bisht and M. P. Singh, "An adaptive unscented kalman filter for tracking sudden stiffness changes," *Mechanical Systems and Signal Processing*, vol. 49, no. 1, pp. 181 – 195, 2014.

[193] C. Zhang, J.-Z. Huang, G.-Q. Song, L. Dai, and H.-K. Li, "Detection of structural damage via free vibration responses by extended kalman filter with tikhonov regularization scheme," *Structural Monitoring and Maintenance*, vol. 3, no. 2, pp. 115–127, 2016.

[194] A. Nair, C. Cai, F. Pan, and X. Kong, "Acoustic emission monitoring of damage progression in cfrp retrofitted rc beams," *Struct Monit Maintenance*, vol. 1, no. 1, pp. 111–130, 2014.

[195] N. Gucunski, S. Kee, H. La, B. Basily, and A. Maher, "Delamination and concrete quality assessment of concrete bridge decks using a fully autonomous rabit platform," *Structural Monitoring and Maintenance*, vol. 2, no. 1, pp. 19–34, 2015.

[196] E. A. Tzoura, T. C. Triantafillou, C. Providakis, A. Tsantilis, C. G. Papanicolaou, and D. Karabalis, "Damage detection of reinforced concrete columns retrofitted with frp jackets by using pzt sensors," *Struct. Monit. Maint*, vol. 2, pp. 165–180, 2015.

[197] A. Al-Hussein and A. Haldar, "Unscented kalman filter with unknown input and weighted global iteration for health assessment of large structural systems," *Structural Control and Health Monitoring*, vol. 23, no. 1, pp. 156–175, 2016.

[198] M. S. Williams and R. G. Sexsmith, "Seismic damage indices for concrete structures: a state-of-the-art review," *Earthquake spectra*, vol. 11, no. 2, pp. 319–349, 1995.

[199] S. Mahboubi and M. R. Shiravand, "Proposed input energy-based damage index for RC bridge piers," *Journal of Bridge Engineering*, vol. 24, p. 04018103, jan 2019.

[200] S. Caltrans, "Caltrans seismic design criteria version 1.6," *California Department of Transportation, Sacramento*, 2010.

[201] Y.-J. Park and A. H.-S. Ang, "Mechanistic seismic damage model for reinforced concrete," *Journal of structural engineering*, vol. 111, no. 4, pp. 722–739, 1985.

[202] J. E. Mottershead, M. Link, and M. I. Friswell, "The sensitivity method in finite element model updating: A tutorial," *Mechanical systems and signal processing*, vol. 25, no. 7, pp. 2275–2296, 2011.

[203] E. Simoen, G. De Roeck, and G. Lombaert, "Dealing with uncertainty in model updating for damage assessment: A review," *Mechanical Systems and Signal Processing*, vol. 56, pp. 123–149, 2015.

[204] F. Clementi, A. Pierdicca, A. Formisano, F. Catinari, and S. Lenci, "Numerical model upgrading of a historical masonry building damaged during the 2016 italian earthquakes: the case study of the podestà palace in montelupone (italy)," *Journal of Civil Structural Health Monitoring*, vol. 7, no. 5, pp. 703–717, 2017.

[205] A. Gharechahi and M. J. Ketabdari, "A novel method for selecting measurement points in structural model updating and damage detection," *Journal of Civil Structural Health Monitoring*, vol. 7, no. 4, pp. 471–482, 2017.

[206] K. Kodikara, T. H. Chan, T. Nguyen, and D. P. Thambiratnam, "Model updating of real structures with ambient vibration data," *Journal of Civil Structural Health Monitoring*, vol. 6, no. 3, pp. 329–341, 2016.

[207] A. S. Mansourabadi and A. Esfandiari, "Structural model updating using sensitivity of wavelet transform coefficients of incomplete structural response," *Journal of Civil Structural Health Monitoring*, vol. 9, no. 1, pp. 37–51, 2019.

[208] S. Mahato and A. Chakraborty, "Sequential clustering of synchrosqueezed wavelet transform coefficients for efficient modal identification," *Journal of Civil Structural Health Monitoring*, vol. 9, no. 2, pp. 271–291, 2019.

[209] A. Sabamehr, C. Lim, and A. Bagchi, "System identification and model updating of highway bridges using ambient vibration tests," *Journal of Civil Structural Health Monitoring*, vol. 8, no. 5, pp. 755–771, 2018.

[210] R. Astroza and A. Alessandri, "Effects of model uncertainty in nonlinear structural finite element model updating by numerical simulation of building structures," *Structural Control and Health Monitoring*, vol. 26, no. 3, p. e2297, 2019.

[211] N. Distefano and A. Rath, "System identification in nonlinear structural seismic dynamics," *Computer methods in applied mechanics and engineering*, vol. 5, no. 3, pp. 353–372, 1975.

[212] N. Distefano and A. Rath, "Sequential identification of hysteretic and viscous models in structural seismic dynamics," *Computer Methods in Applied Mechanics and Engineering*, vol. 6, no. 2, pp. 219–232, 1975.

[213] H. Ebrahimian, R. Astroza, and J. P. Conte, "Extended kalman filter for material parameter estimation in nonlinear structural finite element models using direct differentiation method," *Earthquake Engineering & Structural Dynamics*, vol. 44, no. 10, pp. 1495–1522, 2015.

[214] R. Astroza, A. Alessandri, and J. P. Conte, "A dual adaptive filtering approach for nonlinear finite element model updating accounting for modeling uncertainty," *Mechanical Systems and Signal Processing*, vol. 115, pp. 782–800, 2019.

[215] W. Song, S. Dyke, and T. Harmon, "Application of nonlinear model updating for a reinforced concrete shear wall," *Journal of Engineering Mechanics*, vol. 139, no. 5, pp. 635–649, 2013.

[216] R. Astroza, H. Ebrahimian, and J. P. Conte, "Material parameter identification in distributed plasticity fe models of frame-type structures using nonlinear stochastic filtering," *Journal of Engineering Mechanics*, vol. 141, no. 5, p. 04014149, 2015.

[217] E. Asgarieh, B. Moaveni, and A. Stavridis, "Nonlinear finite element model updating of an infilled frame based on identified time-varying modal parameters during an earthquake," *Journal of Sound and Vibration*, vol. 333, no. 23, pp. 6057–6073, 2014.

[218] S. G. Shahidi and S. N. Pakzad, "Generalized response surface model updating using time domain data," *Journal of Structural Engineering*, vol. 140, no. 8, p. A4014001, 2014.

[219] H. Ebrahimian, R. Astroza, J. P. Conte, and C. Papadimitriou, "Bayesian optimal estimation for output-only nonlinear system and damage identification of civil structures," *Structural Control and Health Monitoring*, vol. 25, no. 4, p. e2128, 2018.

[220] G. Miraglia, E. Lenticchia, C. Surace, and R. Ceravolo, "Seismic damage identification by fitting the nonlinear and hysteretic dynamic response of monitored buildings," *Journal of Civil Structural Health Monitoring*, pp. 1–13, 2020.

[221] R.-Y. Wu and C. P. Pantelides, "Concentrated and distributed plasticity models for seismic repair of damaged rc bridge columns," *Journal of Composites for Construction*, vol. 22, no. 5, p. 04018044, 2018.

[222] F. A. Charney and V. V. Bertero, "An evaluation of the design and analytical seismic response of a seven-story reinforced concrete frame-wall structure," *STIN*, vol. 83, p. 29470, 1982.

[223] A. Babazadeh, R. Burgueño, and P. F. Silva, "Use of 3d finite-element models for predicting intermediate damage limit states in rc bridge columns," *Journal of Structural Engineering*, vol. 141, no. 10, p. 04015012, 2015.

[224] F. McKenna, "Opensees: a framework for earthquake engineering simulation," *Computing in Science & Engineering*, vol. 13, no. 4, pp. 58–66, 2011.

[225] S. K. Kunnath, Y. Heo, and J. F. Mohle, "Nonlinear uniaxial material model for reinforcing steel bars," *Journal of Structural Engineering*, vol. 135, no. 4, pp. 335–343, 2009.

[226] S. Popovics, "A numerical approach to the complete stress-strain curve of concrete," *Cement and concrete research*, vol. 3, no. 5, pp. 583–599, 1973.

[227] J. B. Mander, M. J. Priestley, and R. Park, "Theoretical stress-strain model for confined concrete," *Journal of structural engineering*, vol. 114, no. 8, pp. 1804–1826, 1988.

[228] I. D. Karsan and J. O. Jirsa, "Behavior of concrete under compressive loadings," *Journal of the Structural Division*, 1969.

[229] *PLAIN AND REINFORCED CONCRETE DESIGN*. New Delhi India: Bureau of Indian Standards, 2000.

[230] F. C. Filippou, E. P. Popov, and V. V. Bertero, "Effects of bond deterioration on hysteretic behavior of reinforced concrete joints," 1983.

[231] F. Taucer, E. Spacone, and F. C. Filippou, *A fiber beam-column element for seismic response analysis of reinforced concrete structures*, vol. 91. Earthquake Engineering Research Center, College of Engineering, University , 1991.

[232] Z. Chen, U. Gandhi, J. Lee, and R. Wagoner, "Variation and consistency of youngs modulus in steel," *Journal of Materials Processing Technology*, vol. 227, pp. 227–243, 2016.

[233] S. K. Kunnath, A. M. Reinhorn, and R. Lobo, *IDARC Version 3.0: A program for the inelastic damage analysis of reinforced concrete structures*. National Center for Earthquake Engineering Research Buffalo, NY, 1992.

[234] Y.-J. Park, A. H.-S. Ang, and Y. K. Wen, "Seismic damage analysis of reinforced concrete buildings," *Journal of Structural Engineering*, vol. 111, no. 4, pp. 740–757, 1985.

[235] "Criteria for earthquake resistant. design of structures. part 1 general provisions," standard, Bureau of Indian Standards, New Delhi India, 2002.

[236] "Ductile design and detailing of reinforced concrete structures subjected to seismic force," standard, Bureau of Indian Standards, New Delhi India, 2016.

[237] K. R. Mackie, M. H. Scott, K. Johnsohn, M. Al-Ramahee, M. Steijlen, *et al.*, "Nonlinear time history analysis of ordinary standard bridges," tech. rep., California. Dept. of Transportation. Division of Engineering Services, 2017.

[238] V. Terzic, B. Stojadinovic, *et al.*, "Post-earthquake traffic capacity of modern bridges in california," tech. rep., University of California, Berkeley. Earthquake Engineering Research Center, 2010.

[239] E. M. Rathje, C. Dawson, J. E. Padgett, J.-P. Pinelli, D. Stanzione, A. Adair, P. Arduino, S. J. Brandenberg, T. Cockerill, C. Dey, *et al.*, "Designsafe: new cyberinfrastructure for natural hazards engineering," *Natural Hazards Review*, vol. 18, no. 3, p. 06017001, 2017.

[240] D. P. Bertsekas, *Constrained optimization and Lagrange multiplier methods*. Academic press, 2014.

[241] M. Menegotto, "Method of analysis for cyclically loaded rc plane frames including changes in geometry and non-elastic behavior of elements under combined normal force and bending," in *Proc. of IABSE symposium on resistance and ultimate deformability of structures acted on by well defined repeated loads*, pp. 15–22, 1973.